Carbonation of Peridotite in The Oman Ophiolite

Elisabeth Streit Falk

Submitted in partial fulfillment of the
requirements for the degree of
Doctor of Philosophy
in the Graduate School of Arts and Sciences

COLUMBIA UNIVERSITY

2014

ABSTRACT

Carbonation of Peridotite in The Oman Ophiolite

Elisabeth Streit Falk

The formation of carbonate minerals during alteration of ultramafic rocks represents a geological analogue of mineral carbon sequestration. In the Oman Ophiolite, these carbonation reactions are manifested in (1) active, on-going low-temperature systems involving meteoric water, which result in serpentinization, carbonate vein formation, and travertine precipitation at alkaline springs, and (2) older, higher-temperature systems, which resulted in completely carbonated peridotite, known as listvenite. Employing electron microprobe analysis, x-ray diffraction, stable and clumped isotope thermometry, Sr isotope geochemistry, and geochemical modeling, this study seeks to constrain the conditions under which natural carbonation has occurred in the Oman ophiolite, with the broader goal of understanding what factors and feedbacks control efficient carbonation of peridotite.

Near low-temperature alkaline springs emanating from peridotite in Oman, networks of young carbonate veins are prevalent in highly serpentinized peridotite. A notable feature in some carbonate-veined serpentinite samples is the coexistence of Fe-rich serpentine and quartz. At a given pressure, the formation of iron-rich serpentine at the expense of magnetite should be favored at lower temperatures. Calculations of thermodynamic equilibria in the MgO-SiO_2-H_2O-CO_2 system show that serpentine + quartz is stable assemblage at sufficiently low temperatures (e.g., less than ~15-50°C), and is stabilized to higher temperatures by preferential cation substitutions in serpentine

over talc. Thus, the observed serpentine + quartz assemblages could result from serpentinization at near-surface temperatures. Clumped isotope thermometry of carbonate veins yields temperatures within error of the observed temperatures in Oman groundwater, while the $\delta^{18}O$ of water calculated to be in equilibrium with carbonate precipitated at those temperatures is within error of the observed isotopic composition of Oman groundwater. As groundwater geochemistry suggests that carbonate precipitation and serpentinization occur concomitantly, this indicates that both hydration and carbonation of peridotite are able to produce extensive alteration at the relatively low temperatures of the near-surface weathering environment in Oman.

Along some locations near the basal thrust of the ophiolite, hydrothermal alteration of peridotite in the Samail Ophiolite of Oman has resulted in the formation of listvenite, characterized by complete carbonation, in which all of the Mg and much of the Fe has been incorporated into carbonate minerals, resulting in a rock composed primarily of magnesite (and/or dolomite where Ca has been added) + quartz. Mineral parageneses and clumped isotope data from magnesite and dolomite suggest that carbonate phases within the listvenite formed at peak temperatures ~100°C. CO_2-enriched fluids were likely derived from underlying calcite-bearing sediment during emplacement of the ophiolite. Initial $^{87}Sr/^{86}Sr$ values in the listvenite vary from 0.7085 to 0.7135, mostly significantly higher than seawater values, and are consistent with values within the underlying allochthonous and autochthonous metasediments. An internal Rb-Sr isochron from one listvenite sample yields an age of 97 ± 29 Ma, consistent with the timing of emplacement of the ophiolite. Release of pore fluid during compaction of subducted

sediments may result in similar carbonation of peridotite in the shallow hanging wall of other subduction/obduction environments.

These natural systems demonstrate that significant carbonation of peridotite may occur even at low temperatures, but can be much more efficient at higher temperatures. Furthermore, complete carbonation of peridotite may be achieved, in spite of the potential for armoring of reactive surfaces and reduction of permeability, as demonstrated by the formation listvenite. These natural processes of hydrothermal alteration and weathering could potentially be accelerated to provide a permanent storage solution for the disposal of CO_2 via the in situ formation of solid carbonate minerals in peridotite.

TABLE OF CONTENTS

List of tables ii

List of figures iii

Acknowledgments vi

Dedication viii

Chapter 1: Introduction 1

References 11

Chapter 2: Coexisting serpentine and quartz from carbonate-bearing serpentinized peridotite in the Samail Ophiolite, Oman 25

References 49

Chapter 3: Assessment of the clumped isotope paleothermometer for magnesite 71

References 89

Chapter 4: Geochemistry and petrology of listvenite in the Oman Ophiolite 100

References 133

Appendices 180

LIST OF TABLES

Chapter 2: Coexisting serpentine and quartz from carbonate-bearing serpentinized peridotite in the Samail Ophiolite, Oman

Table 1. Bulk rock major element chemistry and mineralogy of carbonate-veined serpentinites 57

Table 2. Electron microprobe analyses of quartz compared to thin section glass 59

Table 3. Electron microprobe analyses of serpentine 60

Table 4. Clumped isotope data from carbonate veins 61

Chapter 3: Assessment of the clumped isotope paleothermometer for magnesite

Table 1. Clumped isotopic data for calcite standards 93

Table 2. Clumped isotopic data for magnesite samples formed at known T 94

Chapter 4: Geochemistry and petrology of listvenite in the Oman Ophiolite

Table 1. Mineral parageneses 140

Table 2. Electron microprobe analyses of carbonates 142

Table 3. Electron microprobe analyses of chlorite, serpentine, and talc 144

Table 4. Electron microprobe analyses of olivine 145

Table 5. Electron microprobe analyses of spinels 146

Table 6. Electron microprobe analyses of miscellaneous minor and trace phases 147

Table 7. Bulk Sr isotopic data 148

Table 8. Rb-Sr data from OM10-26 149

Table 9. Clumped isotope data for listvenites and associated lithologies 150

Table 10. $\delta^{18}O$ in quartz from listvenites 151

LIST OF FIGURES

Chapter 1: Introduction

Figure 1. Evolution of groundwater in peridotite aquifers 21

Figure 2. Map of the Samail Ophiolite 22

Figure 3. Emplacement of the ophiolite..... 23

Figure 4. Olivine carbonation rates..... 24

Chapter 2: Coexisting serpentine and quartz from carbonate-bearing serpentinized peridotite in the Samail Ophiolite, Oman

Figure 1. X-ray diffraction spectrum of quartz-bearing carbonate-veined serpentinized peridotite 62

Figure 2. Back-scattered electron image of co-existing serpentine+quartz..... 63

Figure 3. Histogram of iron content in serpentine 64

Figure 4. WDS element map of Fe in serpentine co-existing with quartz..... 65

Figure 5. MgO-FeO-SiO_2 ternary plot of serpentine compositions..... 66

Figure 6. T-XCO_2 diagram of phase relations between magnesite, chrysotile, talc, and quartz, 5 bars pressure..... 67

Figure 7. T-XCO_2 plot of the magnesite-chrysotile-talc-quartz invariant point, at 3.5-1000 bars..... 68

Figure 8. Clumped isotope and $\delta^{18}O$ data for carbonate veins 69

Chapter 3: Assessment of the clumped isotope paleothermometer for magnesite

Figure 1. Rate of phosphoric acid dissolution of magnesite..... 95

Figure 2. Residual $\Delta 47$ values from calcite standards..... 96

Figure 3. Residual $\delta^{18}O$ and $\delta^{13}C$ of calcite standards 97

Figure 4. $\Delta 47$ values in magnesite samples vs. $10^6/T^2$ 99

Chapter 4: Geochemistry and petrology of listvenite in the Oman Ophiolite

Figure 1. Map of listvenite localities 152

Figure 2. Zoned soapstone reaction fronts in Wadi Abyad 153

Figure 3. Geologic map of listvenite locality at Wadi Mansah 154

Figure 4. Listvenite outcrops in Wadi Mansah 156

Figure 5. Volatile-free molar Mg, Si, and Fe in listvenites compared to typical Oman peridotite 157

Figure 6. Volatile-free major element composition of listvenites relative to typical Oman peridotite 160

Figure 7. Isocon diagrams for select listvenite samples and ambient peridotite 161

Figure 8. Micro-textures in listvenite and transitional zones, BSE 163

Figure 9. Cross-cutting relationships between carbonate minerals 165

Figure 10. BSE and WDS elemental maps of partially serpentinized peridotite 166

Figure 11. Fe# histograms for serpentine, talc, and magnesite in carbonate-veined serpentinite, listvenite, and soapstone 167

Figure 12. Fuchsite after Cr-spinel in OM10-26, BSE 168

Figure 13. Fuchsite & spinel Cr# vs Mg# 169

Figure 14. Sr isotope ratios for listvenites and underlying metasediments 170

Figure 15. Internal Rb-Sr isochron for OM10-26 172

Figure 16. Ar-Ar data for OM10-26 173

Figure 17. Clumped and stable isotopes in listvenite and associated lithologies 174

Figure 18. $\delta^{18}O$ in quartz vs. $\delta^{18}O$ in carbonate 175

Figure 19. T-XCO_2 phase diagram for magnesite, antigorite, talc, and quartz at 2 kb pressure 176

Figure 20. T-XCO_2 phase boundaries for the reaction 3 magnesite + 4 quartz + H_2O = talc + 3 CO_2, 0.1-10kbar pressure 177

Figure 21. Fluid $\delta^{18}O$ from carbonate and quartz versus carbonate $\delta^{18}O$ at temperatures of 80-110°C 178

Figure 22. Carbon concentration in pore-water saturated in sediment 179

Acknowledgments

The completion of this thesis would not have been possible without the support of many colleagues, mentors, and friends. I have been very lucky to have an enthusiastic, challenging, and supportive advisor in Peter Kelemen. Hundreds of hours of stimulating conversation with Peter have shaped both this thesis and my development as a scientist. Peter has encouraged me to think broadly, and his unfettered approach to science has allowed me to gain experience with a wide range of geochemical tools and always be ready to try something new. Peter's passion is infectious, and his support has been indispensible.

I owe a great debt of gratitude to other mentors and collaborators, at Lamont and beyond. Juerg Matter, Marc Spiegelman, Dave Walker, Steve Goldstein, Craig Manning, Bernard Evans, Sobhi Nasir, Frieder Klein, and George Harlow offered crucial input, advice, and assistance. A huge portion of this thesis would not have been possible without the help of John Eiler, who allowed me to complete the clumped isotope work in his lab. Even with John's generous guidance and insight, the clumped isotope analysis would not have been possible without the friendly assistance of many staff, postdocs, and students at Caltech: Nami Kitchen, Kristin Bergmann, Aradhna Tripati, Magali Bonifacie, Daniel Stolper, Alison Piasecki, and Katie Snell. Greg Dipple and Ian Power, Eric Oelkers and Quentin Gautier, Marco Mazzotti and Mischa Werner, John Ferry, and J.C. Deelman graciously shared their magnesite samples for assessment of the clumped isotope thermometer. I'm very grateful to Juliane Gross, Charlie Mandeville, Joe Boesenberg, and Beth Goldoff for their cheerful and skilled assistance with the electron

microprobe at AMNH. Zhengrong Wang was very welcoming in allowing me to measure oxygen isotopes in his lab at Yale, and Tommy Winger and Ben Parks were a huge help in the lab there.

I also need to thank all the other grad students who spent hours helping me in the lab, repeatedly looked after my cats for me, and shared their friendship: Jason Jweda, Merry Cai, Will Jacobson, Rachel Lupien, Cathleen Doherty, Jill VanTongeren; Elizabeth Pierce, Kat Allen, Meghan Crowley, Evelyn Mervine, Claire Bendersky, Alex Lloyd, Cassy Rose, Ellen Crapster-Pregont, Anastasia Yanchilina, Amelia Paukert, Jesse Farmer, and Rafael Almeida, among others.

Finally, I would like to thank my family for their unfaltering love and encouragement. My parents, Tom and Chris, have always been nothing but supportive in every aspect of my life, and my sisters, Becky and Laura, have routinely provided the healthy dose of laughter necessary to survive grad school. Thanks also to my mother-in-law, Debbie, for improving my science communication skills by repeatedly making me explain my research to her over many long car trips. Above all, I thank my husband, Tony, for his encouragement, patience, and love.

This work was supported in part by a National Science Foundation Graduate Research Fellowship under Grant No. DGE-07-0742, and by research grants to Peter Kelemen and co-workers from the National Science Foundation, the Department of Energy, and Columbia University.

To my family

Chapter 1: Introduction

This thesis addresses the conditions under which carbonate minerals form during alteration of tectonically exposed peridotite in the Oman Ophiolite, a process that serves as a natural analog for mineral carbon sequestration. Because peridotite is far from equilibrium with CO_2-bearing surface- and ground-waters, its exposure near the surface represents a vast reservoir of available chemical potential energy to drive hydration and carbonation reactions. By examining natural carbonation reactions in hydrothermal and weathering environments, I seek to better constrain their role in the global carbon cycle and to evaluate the potential promises and pitfalls of using enhanced *in situ* carbonation of peridotite for CO_2 capture and storage.

1. Alteration of ultramafic rocks

Hydrothermal alteration and weathering of ultramafic rocks have attracted increasing attention over the past twenty years, as researchers have recognized the potentially important consequences of these reactions for global carbon cycles, engineered solutions for carbon capture and storage, hydrogen generation, extremophile communities, and perhaps even the origin of life. Natural CO_2 uptake via carbonation of peridotite on the seafloor is a significant carbon sink and an important element of the carbon cycle (e.g., Früh-Green et al. 2004; Kelemen et al. 2011; Schwarzenbach et al. 2013). It has even been proposed that the emergence of large areas of ultramafic seafloor in the New Caledonia region was responsible for rapid CO_2 drawdown leading to profound climate change (Reusch 2011).

The fate of carbon in these environments is closely linked with hydration of peridotite. H_2-rich fluids resulting from serpentinization act as a reductant for abiotic synthesis of hydrocarbons (e.g., Sleep et al. 2004; Proskurowski et al. 2008; McCollom et al. 2010), may provide chemical energy for microbial communities and were perhaps vital in the emergence of early life (e.g., Schulte et al. 2006; McCollom and Bach 2009; Holm and Neubeck 2009; Sleep et al. 2011). Serpentinization and carbonation of peridotite are exothermic, and heat released by serpentinization of seafloor peridotite may contribute to hydrothermal circulation (Schuiling 1964; Fyfe 1974; Kelley et al. 2001; Emmanuel and Berkowitz 2006).

Most studies of peridotite-hosted hydrothermal systems have focused on serpentinization near mid-ocean ridges (e.g., Früh-Green et al. 1996; Agrinier and Cannat 1997; Kelley et al. 2001; Charlou et al. 2002; Schmidt et al. 2007). Carbonation of seafloor peridotite is most stunningly manifested in tall carbonate chimneys the off-axis Lost City hydrothermal field (Kelley et al. 2001; Früh-Green et al. 2003), but diffuse interactions seawater and seafloor peridotite may be more significant globally (Kelemen et al. 2011). In submarine forearc environments, reaction of hanging wall peridotite above subduction zones with hydrothermal fluids is evidenced by serpentine mud volcanoes and associated carbonate chimneys (e.g., Hensen et al. 2004; Mottl et al. 2004). Near-shore and on-land peridotite-hosted systems share many of the same chemical characteristics of hydrothermal systems in seafloor peridotite: reaction with peridotite leads to the development of high-pH, low-Eh fluids, production of hydrogen and methane, and precipitation of abundant carbonate (e.g., Barnes and O'Neil 1969;

Neal and Stanger 1985; Peretti et al. 1992; Bruni et al. 2002; Kelley et al. 2005; McCollom and Bach 2009).

On-land, hydration and carbonation result from low-temperature reaction of meteoric water with peridotite in three steps (Figure 1), first described in Northern California (Barnes and O'Neil 1969; Barnes et al. 1967), and recognized in exposed peridotite bodies worldwide (Barnes et al. 1978; Neal and Stanger 1985; Bruni et al. 2002; Cipolli et al. 2004; Kelemen and Matter 2008; Paukert et al. 2012). In the first step, meteoric water reacts with peridotite in shallow aquifers in an open system with atmospheric levels of CO_2 and O_2, resulting in Mg^{2+}-HCO_3^- waters. When this water infiltrates to deeper depths cut off from atmospheric CO_2 and O_2, the water evolves to a highly alkaline Ca^{2+}-OH^- groundwater, with virtually no Mg^{2+} or dissolved inorganic carbon, as continued reaction with peridotite results in precipitation of serpentine and carbonate minerals. Finally, when these alkaline waters return to the surface with the atmosphere or mix with shallow groundwater, the addition of CO_2 results in calcite precipitation in the form of travertine terraces, stream conglomerates, or shallow veins. This model suggests the presence of Ca^{2+}-OH^- groundwater issuing from ultramafic bodies is evidence of linked, on-going serpentinization and carbonation.

Extreme carbonate-alteration of peridotite results in the formation of talc-carbonate rocks (soapstone) and quartz-carbonate rocks (listvenite), which form at higher CO_2 partial pressures and higher temperatures (e.g., 75-450°C) than the shallow groundwater reactions described above (e.g., Schandl and Naldrett 1992; Auclair et al. 1993; Hansen et al. 2005; Akbulut et al. 2006; Nasir et al. 2007; Damdinov et al. 2007; Likhoidov et al. 2007; Lutkov et al. 2007; Plissart et al. 2009; Yigit 2009; Kelemen et al.

2011). Listvenites represent complete carbonation of peridotite, with all Mg in carbonate minerals and all Si in quartz. So complete is this transformation that relict chromian spinels are often one of the only indications of the peridotite protolith and these carbonate-silica rocks have been mistaken for metasediments until only recently (e.g., Santti et al. 2006). Listvenite deposits have historically attracted attention primarily for their association with gold mineralization and other economically-valuable hydrothermal deposits (first noted by Rose 1837), but more recently have been highlighted as a natural analog to mineral carbon storage (Hansen et al. 2005; Kelemen et al. 2011; Beinlich et al. 2012) and as a window into peridotite carbonation processes in the hanging wall of subduction zones (Kelemen et al., 2011).

2. Geologic setting

In Oman, carbonate-altered peridotite is present as (a) travertine and carbonate veins in serpentinized peridotite associated with active, ongoing "low T" systems involving meteoric water, and (b) fully-carbonated listvenite, representing older, fossil "high T" systems.

The Samail Ophiolite, located in the Sultanate of Oman and the United Arab Emirates (Figure 2), is the largest and best-exposed ophiolite in the world. The ophiolite is a thrust sheet of oceanic crust and upper mantle that was emplaced onto the Arabian continental margin during the closure of the Tethyan ocean in the late Cretaceous, beginning ~95 Ma (Figure 3) (Coleman 1981; Hacker et al. 1996). The mantle section is underlain by the metamorphic sole, consisting of a thin sheet of metamorphosed oceanic sediments and volcanic rocks heated and welded against the mantle during initiation of

intraoceanic thrusting, the relatively unmetamorphosed oceanic sediments and volcanic rocks of the allochthonous Hawasina nappes, which were bulldozed in front of and beneath the leading edge of the advancing ophiolite, and finally the autochthonous continental shelf and parautochthonous continental slope deposits, thick carbonate deposits which rest on pre-Permian crystalline basement (Glennie et al. 1974). Tilting and erosion has exposed ophiolite sections from 0 to 15km below the paleo-seafloor, providing outcrop exposures of igneous and hydrothermal processes at oceanic spreading centers (e.g., Pallister and Hopson 1981; Gregory and Taylor 1981; Kelemen et al. 1995; 1997; Van Tongeren et al. 2008).

While the Oman ophiolite has been the site of important studies of hydrothermal processes in the lower crust, there has been relatively little work on mantle peridotite hydration and carbonation. Most of these studies have focused on the active, low-temperature system. Dewandel et al. (2005), Weyhenmeyer (2000), Weyhenmeyer et al. (2002), and Matter et al. (2006) studied the hydrology of parts of the ophiolite and peridotite alluvium. Stanger and co-workers wrote several papers on the geochemistry of groundwater and mineral deposits associated with alkaline springs formed by peridotite alteration (Neal and Stanger 1983, 1984, 1985; Stanger 1986; Stanger et al. 1988; Stanger and Neal 1994). Clark and co-workers studied the stable isotope and radiocarbon record of travertine formation from peridotite-hosted alkaline springs (Clark and Fontes 1990; Clark et al. 1992). Recent studies have investigated these alkaline systems in greater detail, adding extensive mineralogical analyses, isotopic data, quantitative estimates of carbonation rates and geochemical reaction path models (e.g., Kelemen and Matter 2008; Matter and Kelemen 2009; Kelemen et al. 2011; Monnin et al. 2011; Paukert et al. 2012;

Chavagnac et al. 2013). Mineralogical studies of serpentinization in Oman include recent, detailed investigations of serpentinite replacement textures by Boudier et al. (2010), and two short papers on native metal alloys in Oman serpentinites (Lorand 1987; Leblanc et al. 1991). There have been some, mainly descriptive, studies of the listvenites in Oman (Stanger 1985; Wilde et al. 2002; Nasir et al. 2007; Rajendran et al. 2013), but few constraints have been placed on the conditions of their formation (e.g., temperatures, fluid compositions).

Recently, Kelemen and co-workers have proposed that the natural mineral carbonation systems in Oman can provide insights into the design of engineered systems for carbon capture and storage (Kelemen and Matter 2008; Matter and Kelemen 2009; Kelemen et al. 2011; Paukert et al. 2012; Mervine et al. in press). Detailed mapping of travertine, mass balance calculations and ^{14}C dating in travertine and carbonate veins in peridotite indicate that ~10^4 to 10^5 tons of atmospheric CO_2 are converted to solid carbonate minerals annually via alteration of peridotite in Oman. These rates are surprisingly rapid, and the carbon storage potential of the Oman ophiolite is vast—adding 1 wt% CO_2 to the peridotite would consume an amount roughly equivalent to the increase since the industrial revolution.

3. *In situ* mineral carbon sequestration

Stabilizing CO_2 concentrations in the atmosphere over the next century will likely require implementation of carbon capture and storage (CCS) (e.g., Metz et al. 2005; Lackner et al. 2012). Storage of CO_2 in solid carbonate minerals via reaction with ultramafic materials has been championed on the basis that the waste product is

thermodynamically stable and environmentally neutral, thus allowing CO_2 to be safely sequestered for thousands of years without the need for long-term monitoring (e.g., Seifritz 1990; Lackner et al. 1995; Lackner et al. 1997).

Peridotite is an ideal substrate for mineral carbon sequestration because its primary component, olivine, has the greatest CO_2 storage potential of major rock-forming minerals (e.g., Xu et al. 2004), and the dissolution and carbonation rates of olivine are faster than those of other silicate minerals (e.g., as summarized in Matter and Kelemen (2009) and Kelemen et al. (2011)). While more efficient industrial processes are being developed (e.g., Park and Fan 2004), *ex situ* carbonation of peridotite, either "at the smokestack" or via weather of dispersed olivine powders, entails high costs of mining, transporting, and processing reactant peridotite (e.g., Lackner et al. 1997; Schuiling and Krijgsman 2006). *In situ* reaction of peridotite with injected CO_2 or thermally convecting seawater offers a slower, but lower-cost alternative (Cipolli et al. 2004; Hansen et al. 2005; Kelemen and Matter 2008; Kelemen et al. 2011). Although carbonation rates observed in the active system in Oman are significantly slower than laboratory carbonation reactions, reaction rates could be enhanced over several orders of magnitude under optimal conditions (Kelemen and Matter 2008).

Direct olivine carbonation experiments indicate that peak reaction rates are achieved at temperatures ~185°C and that reaction rate increases with partial pressure of CO_2 (Chizmeshya et al. 2007; O'Connor et al. 2005), as shown in Figure 4 (fit by Kelemen and Matter (2008)). When grain size effects are taken into account, natural peridotite carbonation rates in Oman agree surprisingly well with experimental data from O'Connor et al. (2005) (Kelemen et al. 2011). At the optimal temperature of 185°C,

reaction rates are expected to be ~10^6 times faster than in the active, low-temperature system, and increasing the CO_2 partial pressure to over 100 bars increases the reaction rate by a factor of almost 10^3. Because the carbonation reactions are exothermic, self-heating may be able to sustain high reaction rates at temperatures near the optimum of 185°C (Kelemen and Matter 2008). In another positive feedback mechanism, reaction progress could be further self-sustained by reaction-driven cracking, wherein solid volume increases during hydration and carbonation reactions could cause fracture formation, thereby maintaining or increasing permeability and availability of reactive surfaces (MacDonald and Fyfe 1985; Jamtveit et al. 2008; Rudge et al. 2010; Kelemen and Hirth 2012).

However, these solid volume increases could potentially lead to armoring of reactive surfaces and reductions in porosity and permeability, thereby limiting reaction progress. Experimental studies of olivine hydration and carbonation have noted decreases in reaction rates with time (Martin and Fyfe 1970; O'Connor et al. 2005), and armoring of reactive surfaces has been observed in the form of silica "passivating" layers on olivine during carbonation reactions (Chizmeshya et al. 2007; Andreani et al. 2009). Nonetheless, extensive outcrops of completely hydrated peridotite (serpentinite) and completely carbonated peridotite (listvenite) attest to the fact that olivine hydration and carbonation reactions are not always self-limiting.

4. Outline of thesis

This thesis examines the conditions of peridotite carbonation and hydration in the Oman ophiolite in order to understand the chemical and physical processes that lead to

rapid and extensive peridotite carbonation. I focus on petrologic and geochemical evidence for the timing, temperature, and fluid compositions of on-going and ancient peridotite carbonation in Oman. All rock samples used in this study, collected during fieldwork in Oman in January of 2007, 2008, 2009, 2010, and 2011, are listed in Appendix 1, which includes field descriptions, GPS locations, and major phases.

Chapter 2 presents the results of mineralogical analyses and clumped isotope thermometry in carbonate-veined serpentinite from the active, low-temperature system. The presence of iron-rich serpentine and the coexistence of lizardite + quartz in these rocks suggests low temperatures of serpentinization, consistent with clumped isotope temperatures in carbonate veins and observed groundwater temperatures. The results of this chapter provide further evidence that present-day serpentinization and carbonation of peridotite are occurring at ambient temperatures in a shallow weathering horizon in the Oman ophiolite.

Chapter 3 contains an assessment of the application of the carbonate clumped isotope paleothermometer to magnesite. Clumped isotope thermometry provides a method of determining the temperature of formation of carbonate minerals independent of the isotopic composition of the fluid from which they formed, making it a valuable tool where constraints on the isotopic composition of the fluid are limited, for example, in ancient hydrothermal systems such as those involved in listvenite formation. However, clumped isotope analysis of magnesite, the most abundant carbonate mineral in listvenite, presents unique challenges, and the clumped isotope thermometer has not been previously calibrated for magnesite. This chapter verifies the reliability of the carbonate

clumped isotope paleothermometer for natural and synthetic magnesite samples formed at known temperature ranging from ~5-250°C.

Chapter 4 investigates the temperatures, timing, and fluid compositions involved in the formation of listvenite in Oman. The results of electron microprobe analyses, x-ray diffraction, Sr isotope geochemistry, carbonate clumped isotope thermometry, oxygen isotope analyses in quartz, and thermodynamic and geochemical modeling are considered. These mineralogical and isotopic data support the hypothesis that magnesite-quartz listvenites formed at temperatures around 100°C during obduction of the Oman ophiolite, as slightly CO_2-enriched fluids derived from underlying sediments metasomatized hanging wall peridotite.

Overall, natural peridotite carbonation processes in Oman highlight the promise of enhanced *in situ* mineral carbon storage in peridotite. Extensive outcrops of fully carbonated listvenite demonstrate that complete carbonation of peridotite is attainable, and on-going, low-temperature carbonation shows that these systems can be sustained for tens of thousands of years. This work provides further evidence for the link between low-temperature alkaline springs, serpentinization, and formation of carbonate veins in serpentinite, additionally validating the carbonation rates estimated by Kelemen and Matter (2008). Even though results indicate that listvenites formed at temperatures below those corresponding to peak carbonation rates and CO_2 concentrations were likely moderate, the inferred conditions of listvenite formation correspond to carbonation rates at least 2-4 orders of magnitude faster than rates of ongoing peridotite carbonation. Thus rapid and complete carbonation of peridotite may be attainable via relatively low-cost *in situ* methods of carbon capture and storage in peridotite.

References

Agrinier P, Cannat M (1997) Oxygen-isotope constraints on serpentinization processes in ultramafic rocks from the Mid-Atlantic Ridge (23°N)). In: Karson JA, Cannat M, Miller DJ, Elthon D (eds) Proc. ODP, Sci. Results, vol 153. Ocean Drilling Program, College Station, TX, pp 381-388. Available at http://www-odp.tamu.edu/publications/153_SR/VOLUME/CHAPTERS/sr153_320.pdf. doi:doi:10.2973/odp.proc.sr.153.033.1997

Akbulut M, Piskin O, Karayigit AI (2006) The genesis of the carbonatized and silicified ultramafics known as listvenites: a case study from the Mihaliccik region (Eskisehir), NW Turkey. Geological Journal 41 (5):557-580. doi:10.1002/gj.1058

Andreani M, Luquot L, Gouze P, Godard M, Hoisé E, Gibert B (2009) Experimental study of carbon sequestration reactions controlled by the percolation of CO2-rich brine through peridotites. Environ Sci Technol 43:1226-1231

Auclair M, Gauthier M, Trottier J, Jébrak M, Chartrand F (1993) Mineralogy, geochemistry, and paragenesis of the Eastern Metals serpentinite-associated Ni-Cu-Zn deposit, Quebec Appalachians. Econ Geol 88:123-138

Barnes I, LaMarche VC, Himmelberg G (1967) Geochemical evidence of present-day serpentinization. Science 156 (3776):830-832

Barnes I, O'Neil JR (1969) Relationship between fluids in some fresh alpine-type ultramafics and possible modern serpentinization, western United States. GSA Bull 80 (10):1947-1960

Barnes I, O'Neil JR, Trescases JJ (1978) Present Day Serpentinization in New-Caledonia, Oman and Yugoslavia. Geochim Cosmochim Acta 42 (1):144-145

Beinlich A, Plumper O, Hovelmann J, Austrheim H, Jamtveit B (2012) Massive serpentinite carbonation at Linnajavri, N-Norway. Terra Nova 24 (6):446-455. doi:10.1111/j.1365-3121.2012.01083.x

Boudier F, Baronnet A, Mainprice D (2010) Serpentine mineral replacements of natural olivine and their seismic implications: Oceanic lizardite versus subduction-related antigorite. J Petrol 51:495-512

Bruni J, Canepa M, Chiodini G, Cioni R, Cipolli F, Longinelli A, Marini L, Ottonello G, Zuccolini MV (2002) Irreversible water-rock mass transfer accompanying the generation of the neutral, Mg-HCO3 and high-pH, Ca-OH spring waters of the Genova province, Italy. Applied Geochem 17 (4):455-474

Charlou JL, Donval JP, Fouquet Y, Jean-Baptiste P, Holm N (2002) Geochemistry of high H-2 and CH4 vent fluids issuing from ultramafic rocks at the Rainbow hydrothermal field (36 degrees 14 ' N, MAR). Chemical Geology 191 (4):345-359

Chavagnac V, Ceuleneer G, Monnin C, Lansac B, Hoareau G, Boulart C (2013) Mineralogical assemblages forming at hyperalkaline warm springs hosted on ultramafic rocks: A case study of Oman and Ligurian ophiolites. Geochemistry Geophysics Geosystems 14 (7):2474-2495. doi:10.1002/ggge.20146

Chizmeshya AVG, McKelvy MJ, Squires K, Carpenter RW, Béarat H (2007) DOE Final Report 924162: A novel approach to mineral carbonation: Enhancing carbonation while avoiding mineral pretreatment process cost 29 pages plus appendices. Arizona State University, Tempe, AZ

Cipolli F, Gambardella B, Marini L, Ottonello G, Zuccolini MV (2004) Geochemistry of high-pH waters from serpentinites of the Gruppo di Voltri (Genova, Italy) and reaction path modeling of CO2 sequestration in serpentinite aquifers. Applied Geochem 19 (5):787-802

Clark ID, Fontes JC (1990) Paleoclimatic reconstruction in northern Oman based on carbonates from hyperalkaline groundwaters. Quaternary Res 33 (3):320-336

Clark ID, Fontes JC, Fritz P (1992) Stable isotope disequilibria in travterine from high pH-waters - Laboratory investigations and field observations from Oman. Geochim Cosmochim Acta 56 (5):2041-2050

Coleman RG (1981) Tectonic setting for ophiolite obduction in Oman. Journal of Geophysical Research 86 (NB4):2497-2508. doi:10.1029/JB086iB04p02497

Damdinov BB, Mironov AG, Borovikov AA, Guntypov BB, Karmanov NS, Borisenko AS, Garmaev BL (2007) Composition and conditions of formation of gold-telluride mineralization in the Tissa-Sarkhoi gold-bearing province (East Sayan). Russian Geology and Geophysics 48:643-655. doi:10.1016/j.rgg.2006.11.001

Dewandel B, Lachassagne P, Boudier F, Al-Hattali S, Ladouche B, Pinault JL, Al-Suleimani Z (2005) A conceptual hydrogeological model of ophiolite hard-rock aquifers in Oman based on a multiscale and a multidisciplinary approach. Hydrogeology J 13 (5-6):708-726

Früh-Green GL, Connolly JAD, Plas A, Kelly DS, Groberty B (2004) Serpentinization of oceanic peridotites: Implications for geochemical cycles and biological activity. In: Wilcock WD, Kelley DS, DeLong E, Cary C (eds) The Subseafloor Biosphere at Mid-Ocean Ridges. AGU Geophysical Monograph, vol 144. Washington, D.C., pp 119-136

Früh-Green GL, Kelley DS, Bernasconi SM, Karson JA, Ludwig KA, Butterfield DA, Boschi C, Proskurowski G (2003) 30,000 years of hydrothermal activity at the Lost City vent field. Science 301 (5632):495-498

Früh-Green GL, Plas A, Lécuyer C (1996) Petrologic and stable isotope constraints on hydrothermal alteration and serpentinization of the EPR shallow mantle at Hess Deep (Site 895). Proc. ODP, Sci. Results, vol 147. Ocean Drilling Program, College Station, TX. doi:10.2973/odp.proc.sr.147.016.1996

Glennie KW, Bouef MGA, Hughes-Clarke MW, Moody-Stuart M, Pilaar WFH, Reinhardt BM (1974) Geology of the Oman Mountains, vol 31. Verhundelingen van het koninklijk Nederlnnds Geologisch-Mijnbouwkundig Genootschap.

Gregory RT, Taylor HP (1981) An oxygen isotope profile in a section of Cretaceous oceanic crust, Samail Ophiolite, Oman - Evidence for delta-18O buffering of the oceans by deep (less than 5 km) seawater-hydrothermal circulation at mid-ocean ridges. Journal of Geophysical Research 86 (NB4):2737-2755

Hacker BR, Mosenfelder JL, Gnos E (1996) Rapid emplacement of the Oman ophiolite: Thermal and geochronologic constraints. Tectonics 15 (6):1230-1247. doi:10.1029/96tc01973

Hansen LD, Dipple GM, Gordon TM, Kellett DA (2005) Carbonated serpentinite (listwanite) at Atlin, British Columbia: A geological analogue to carbon dioxide sequestration. Can Mineral 43:225-239

Hensen C, Wallmann K, Schmidt M, Ranero CR, Suess E (2004) Fluid expulsion related to mud extrusion off Costa Rica - A window to the subducting slab. Geology 32 (3):201-204. doi:10.1130/g20119.1

Holm NG, Neubeck A (2009) Reduction of nitrogen compounds in oceanic basement and its implications for HCN formation and abiotic organic synthesis. Geochemical Transactions 10. doi:10.1186/1467-4866-10-9

Jamtveit B, Malthe-Sorenssen A, Kostenko O (2008) Reaction enhanced permeability during retrogressive metamorphism. Earth Planet Sci Lett 267:620-627

Kelemen PB, Hirth G (2012) Reaction-driven cracking during retrograde metamorphism: Olivine hydration and carbonation. Earth and Planetary Science Letters 345:81-89. doi:10.1016/j.epsl.2012.06.018

Kelemen PB, Koga K, Shimizu N (1997) Geochemistry of gabbro sills in the crust-mantle transition zone of the Oman ophiolite: Implications for the origin of the oceanic lower crust. Earth and Planetary Science Letters 146 (3-4):475-488

Kelemen PB, Matter J (2008) In situ carbonation of peridotite for CO2 storage. Proc Natl Acad Sci U S A 105 (45):17295-17300. doi:10.1073/pnas.0805794105

Kelemen PB, Matter J, Streit EE, Rudge JF, Curry WB, Bluztajn J (2011) Rates and mechanisms of mineral carbonation in peridotite: Natural processes and recipes for enhanced, in situ CO2 capture and storage. Ann Rev Earth Planet Sci 39:545-576

Kelemen PB, Shimizu N, Salters VJM (1995) Extraction of mid-ocean ridge basalt from the upwelling mantle by focused flow of melt in dunite channels. Nature 375:747-753

Kelley DS, Karson JA, Blackman DK, Fruh-Green GL, Butterfield DA, Lilley MD, Olson EJ, Schrenk MO, Roe KK, Lebon GT, Rivizzigno P (2001) An off-axis hydrothermal vent field near the Mid-Atlantic Ridge at 30 degrees N. Nature 412 (6843):145-149

Kelley DS, Karson JA, Früh-Green GL, Yoerger DR, Shank TM, Butterfield DA, Hayes JM, Schrenk MO, Olson EJ, Proskurowski G, Jakuba M, Bradley A, Larson B, Ludwig K, Glickson D, Buckman K, Bradley AS, Brazelton WJ, Roe K, Elend MJ, Delacour A, Bernasconi SM, Lilley MD, Baross JA, Summons RT, Sylva SP (2005) A serpentinite-hosted ecosystem: The lost city hydrothermal field. Science 307 (5714):1428-1434. doi:10.1126/science.1102556

Lackner KS, Brennan S, Matter JM, Park A-HA, Wright A, van der Zwaan B (2012) The urgency of the development of CO2 capture from ambient air. Proceedings of the National Academy of Sciences 109 (33):13156-13162. doi:10.1073/pnas.1108765109

Lackner KS, Butt DP, Wendt CH (1997) Progress on binding CO2 in mineral substrates. Energy Conversion & Management 38:S259-S264

Lackner KS, Wendt CH, Butt DP, Joyce EL, Sharp DH (1995) Carbon-dioxide disposal in carbonate minerals. Energy 20 (11):1153-1170

Leblanc M, Ceuleneer G, Alazri H, Jedwab J (1991) Hydrothermal Concentration of Palladium and Platinum in Mantle Peridotites from the Oman Ophiolite. Comptes Rendus De L Academie Des Sciences Serie Ii 312 (9):1007-1012

Likhoidov GG, Plyusnina LP, Shcheka ZA (2007) The behavior of gold during listvenitization: Experimental and theoretical simulation. Doklady Earth Sciences 415 (5):723-726. doi:10.1134/s1028334x07050145

Lorand JP (1987) A New Occurrence of Native Iron in a Serpentinized Mantle Peridotite - Maqsad, Sumail Massif, Semail Ophiolite (Southern Oman). Comptes Rendus De L Academie Des Sciences Serie Ii 304 (13):703-706

Lutkov VS, Mogarovskii VV, Lutkova VY (2007) Petrogeochemistry and genesis of listwaenite xenoliths in the alkali basalts of the southern Tien Shan. Geochemistry International 45 (8):733-743. doi:10.1134/s0016702907080010

MacDonald AH, Fyfe WS (1985) Rate of serpentinization in seafloor environments. Tectonophys 116 (1-2):123-135

Martin B, Fyfe WS (1970) Some experimental and theoretical observations on kinetics of hydration reactions with particular reference to serpentinization. Chem Geol 6 (3):185-202

Matter JM, Assayag N, Goldberg D (2006) Basaltic rocks and their potential to permanently sequester industrial carbon dioxide emissions. GHGT-8:https://events.adm.ntnu.no/ei/viewpdf.esp?id=24&file=d%23A%25CAmlink%25CEVENTWIN%25Cdocs%25Cpdf%25C950Final00411%00412Epdf

Matter JM, Kelemen PB (2009) Permanent CO2 storage and mineral carbonation in geologic reservoirs. Nature Geoscience 2:837-841

McCollom TM, Bach W (2009) Thermodynamic constraints on hydrogen generation during serpentinization of ultramafic rocks. Geochim Cosmochim Acta 73:856-875

McCollom TM, Lollar BS, Lacrampe-Couloume G, Seewald JS (2010) The influence of carbon source on abiotic organic synthesis and carbon isotope fractionation under hydrothermal conditions. Geochim Cosmochim Acta 74 (9):2717-2740. doi:10.1016/j.gca.2010.02.008

Mervine EM, Humphris SE, Sims KWW, Kelemen PB, Jenkins WJ (in press) Carbonation Rates of Peridotite in the Samail Ophiolite, Sultanate of Oman, Constrained Through 14C Dating and Stable Isotopes. Geochim Cosmochim Acta. doi:http://dx.doi.org/10.1016/j.gca.2013.11.007

Metz B, Davidson O, de Coninck H, Loos M, Meyer L (eds) (2005) IPCC Special Report on Carbon Dioxide Capture and Storage. Cambridge University Press, New York

Monnin C, Chavagnac V, Ceuleneer G, Boulart C, Hoareau G (2011) Characterization of Hyperalkaline Fluids Produced by Serpentinization of Mantle Peridotites in Oman and in Liguria (Northern Italy). Mineralogical Magazine 75 (3):1490

Mottl MJ, Wheat G, Fryer P, Gharib J, Martin JB (2004) Chemistry of springs across the Mariana forearc shows progressive devolatilization of the subducting plate. Geochim Cosmochim Acta 68:4915-4933

Nasir S, Al Sayigh AR, Al Harthy A, Al-Khirbash S, Al-Jaaldi O, Musllam A, Al-Mishwat A, Al-Bu'saidi S (2007) Mineralogical and geochemical characterization of listwaenite from the Semail Ophiolite, Oman. Chemie Der Erde-Geochemistry 67 (3):213-228. doi:10.1016/j.chemer.2005.01.003

Neal C, Stanger G (1983) Hydrogen generation from mantle source rocks in Oman. Earth Planet Sci Lett 66 (1-3):315-320

Neal C, Stanger G (1984) Calcium and magnesium-hydroxide precipitation from alkaline groundwaters in Oman, and their significance to the process of serpentinization. Min Mag 48 (347):237-241

Neal C, Stanger G (1985) Past and present serpentinization of ultramafic rocks: An example from the Semail ophiolite nappe of northern Oman. In: Drewer JI (ed) The Chemistry of Weathering. D. Reidel Publishing Company, Holland, pp 249-275

O'Connor WK, Dahlin DC, Rush GE, Gerdemann SJ, Nilsen DN (2005) Final report: Aqueous mineral carbonation, DOE/ARC-TR-04-002. Office of Process Development, Albany Research Center, Office of Fossil Energy, US DOE, Albany, OR

Pallister JS, Hopson CA (1981) Samail ophiolite plutonic suite: Field relations, phase variation, cryptic variation and layering, and a model of a spreading ridge magma chamber. J Geophys Res 86:2593-2644

Park AHA, Fan LS (2004) CO2 mineral sequestration: physically activated dissolution of serpentine and pH swing process. Chemical Engineering Science 59 (22-23):5241-5247

Paukert AN, Matter JM, Kelemen PB, Shock EL, Havig JR (2012) Reaction path modeling of enhanced in situ CO2 mineralization for carbon sequestration in the peridotite of the Samail Ophiolite, Sultanate of Oman. Chemical Geology 330–331 (0):86-100. doi:http://dx.doi.org/10.1016/j.chemgeo.2012.08.013

Peretti A, Dubessy J, Mullis J, Frost BR, Trommsdorff V (1992) Highly reducing conditions during alpine metamorphism of the Malenco peridotite (Sondrio, northern Italy) indicated by mineral paragenesis and H2 in fluid inclusions. Contributions to Mineralogy and Petrology 112 (2-3):329-340

Plissart G, Femenias O, Maruntiu M, Diot H, Demaiffe D (2009) Mineralogy and geothermometry of gabbro-derived listvenites in the Tisovita-Iuti Ophiolite, southwestern Romania. Canadian Mineralogist 47 (1):81-105. doi:10.3749/canmin.47.1.81

Proskurowski G, Lilley MD, Seewald JS, Frueh-Green G, Olson EJ, Lupton JE, Sylva SP, Kelley DS (2008) Abiogenic hydrocarbon production at Lost City hydrothermal field. Science 319:604-607

Rajendran S, Nasir S, Kusky TM, Ghulam A, Gabr S, El-Ghali MAK (2013) Detection of hydrothermal mineralized zones associated with listwaenites in Central Oman

using ASTER data. Ore Geology Reviews 53 (0):470-488. doi:http://dx.doi.org/10.1016/j.oregeorev.2013.02.008

Reusch DN (2011) New Caledonian carbon sinks at the onset of Antarctic glaciation. Geology 39 (9):807-810. doi:10.1130/g31981.1

Rose G (1837) Mineralogisch-geognostiche Reise nach dem Ural, dem Altai und dem Kaspischen Meere. Volume 1: Reise nach dem nördlichen Ural und dem Altai. G.E. Reimer (Verlag der Sanderschen Buchhandlung), Berlin

Rudge JF, Kelemen PB, Spiegelman M (2010) A simple model of reaction-induced cracking applied to serpentinization and carbonation of peridotite. Earth Planet Sci Lett 291 (1-4):215-227

Santti J, Kontinen A, Sorjonen-Ward P, Johanson B, Pakkanen L (2006) Metamorphism and chromite in serpentinized and carbonate-silica–altered peridotites of the Paleoproterozoic Outokumpu-Jormua Ophiolite Belt, Eastern Finland. Int Geol Rev 48:494-546

Schandl ES, Naldrett AJ (1992) CO2 metasomatism of serpentinites, south of Timmins, Ontario. Canadian Mineralogist 30:93-108

Schmidt K, Koschinsky A, Garbe-Schonberg D, de Carvalho LM, Seifert R (2007) Geochemistry of hydrothermal fluids from the ultramafic-hosted Logatchev hydrothermal field, 15 degrees N on the Mid-Atlantic Ridge: Temporal and spatial investigation. Chemical Geology 242 (1-2):1-21

Schuiling RD, Krijgsman P (2006) Enhanced weathering: An effective and cheap tool to sequester CO2. Clim Change 74:349-354

Schulte M, Blake D, Hoehler T, McCollom TM (2006) Serpentinization and its implications for life on the early Earth and Mars. Astrobiology 6:364–376

Schwarzenbach EM, Fruh-Green GL, Bernasconi SM, Alt JC, Plas A (2013) Serpentinization and carbon sequestration: A study of two ancient peridotite-hosted hydrothermal systems. Chemical Geology 351:115-133. doi:10.1016/j.chemgeo.2013.05.016

Seifritz W (1990) CO2 disposal by means of silicates. Nature 345:486

Sleep NH, Bird DK, Pope EC (2011) Serpentinite and the dawn of life. Philosophical Transactions of the Royal Society B-Biological Sciences 366 (1580):2857-2869. doi:10.1098/rstb.2011.0129

Sleep NH, Meibom A, Fridriksson T, Coleman RG, Bird DK (2004) H-2-rich fluids from serpentinization: Geochemical and biotic implications. Proc Natl Acad Sci U S A 101 (35):12818-12823

Stanger G (1985) Silicified serpentinite in the Semail nappe of Oman. Lithos 18 (1):13-22

Stanger G (1986) The Hydrogeology of the Oman Mountains. The Open University, Durham, UK

Stanger G, Laver J, Neal C (1988) Black Carbonaceous Calcite Associated with Serpentinite from Oman. Mineralogical Magazine 52 (366):403-408

Stanger G, Neal C (1994) The occurrence and chemistry of huntite from Oman. Chem Geol 112:274-254

Van Tongeren JA, Kelemen PB, Hanghoj K (2008) Cooling rates in the lower crust of the Oman ophiolite: Ca in olivine, revisited. Earth Planet Sci Lett 267:69-82

Weyhenmeyer C, Burns SJ, Waber HN, Macumber PG, Matter A (2002) Isotope study of moisture sources, recharge areas, and groundwater flow paths within the eastern Batinah coastal plain, Sultanate of Oman. Water Res J 38:1184, doi:1110.1029/2000WR000149

Weyhenmeyer CE (2000) Origin and evolution of groundwater in the alluvial aquifer of the eastern Batinah coastal plain, Sultanate of Oman: A hydrogeochemical approach. Universität Bern, Bern, Switzerland

Wilde A, Simpson L, Hanna S (2002) Preliminary study of Cenozoic hydrothermal alteration and platinum deposition in the Oman Ophiolite. J of the Virtual Explorer 6:7-13

Xu TF, Apps JA, Pruess K (2004) Numerical simulation of CO2 disposal by mineral trapping in deep aquifers. Applied Geochemistry 19 (6):917-936. doi:10.1016/j.apgeochem.2003.11.003

Yigit O (2009) Mineral Deposits of Turkey in Relation to Tethyan Metallogeny: Implications for Future Mineral Exploration. Economic Geology 104 (1):19-51

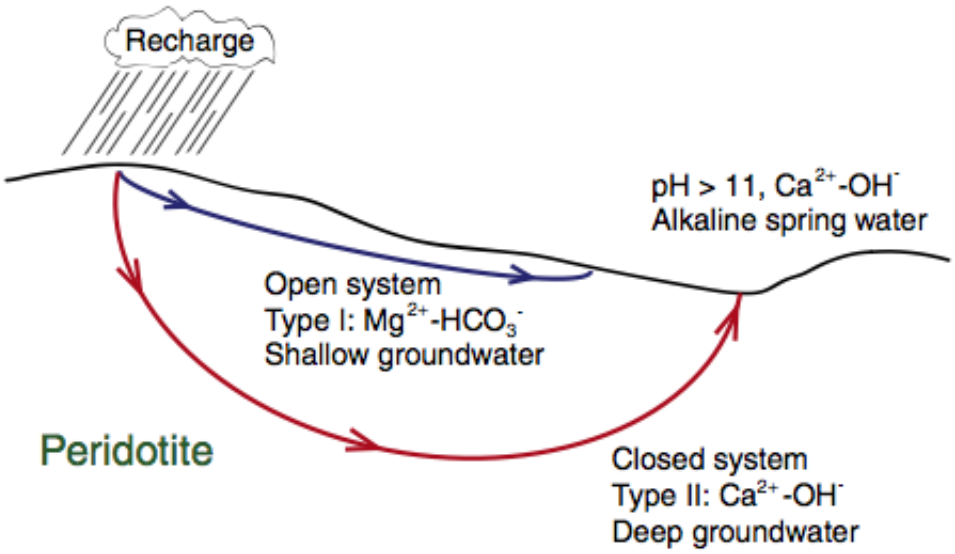

Figure 1. Evolution of groundwater in peridotite aquifers (Paukert et al. 2012, Fig. 1)

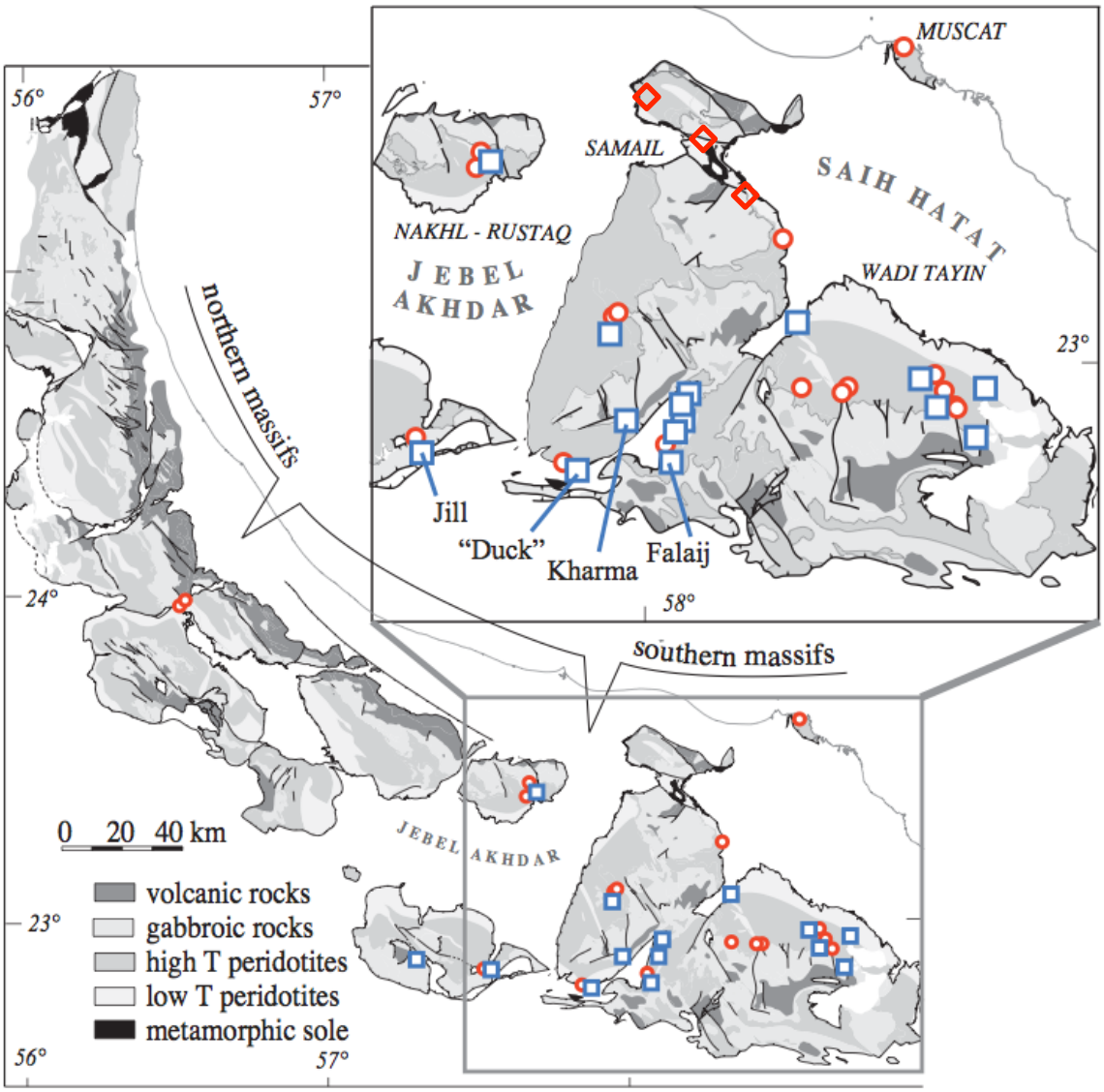

Figure 2. Map of the Samail ophiolite, major sites of peridotite carbonation indicated. Blue squares = alkaline springs and travertines, red circles = carbonate veins in serpentinized peridotite, red diamonds = listvenite. (modified from Kelemen and Matter 2008, Fig. 2)

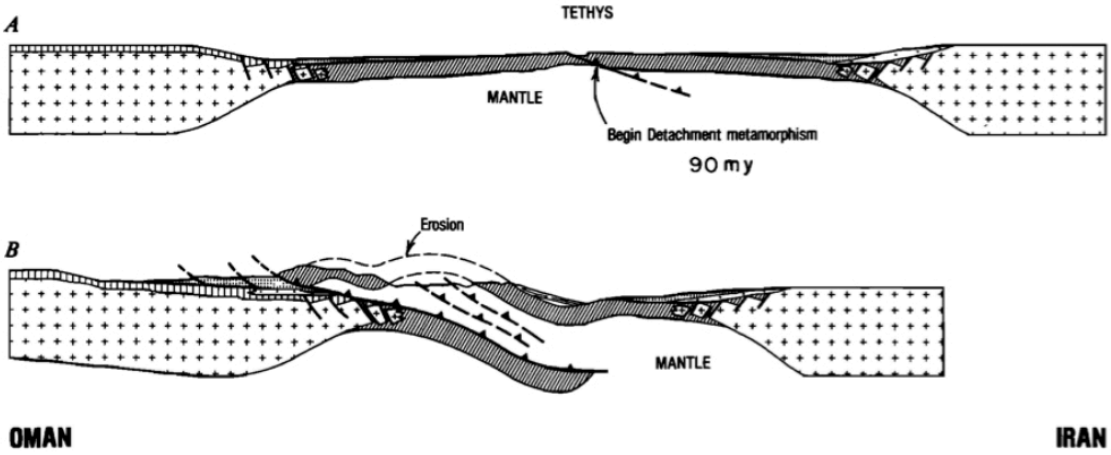

Figure 3. Emplacement of the Oman ophiolite (Coleman 1981, Fig. 6)

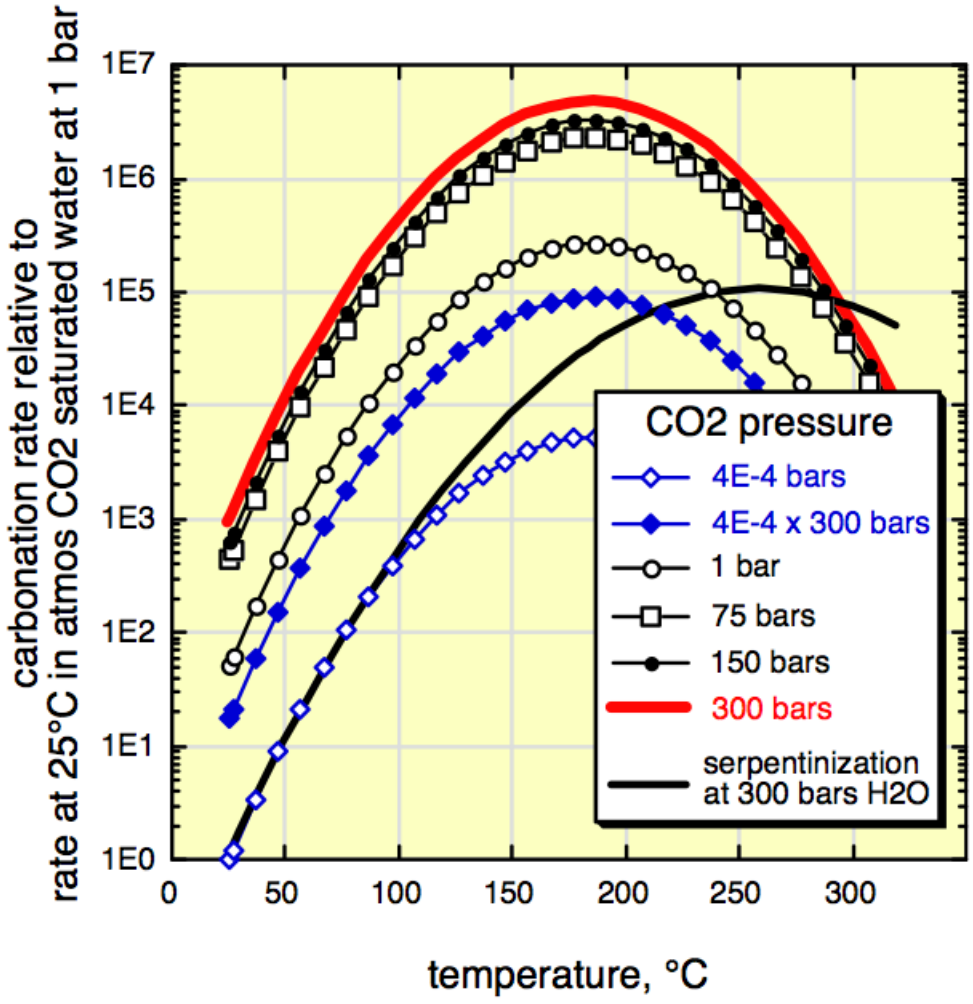

Figure 4. Olivine carbonation rates (Kelemen and Matter 2008, Fig. 5)

Chapter 2: Coexisting serpentine and quartz from carbonate-bearing serpentinized peridotite in the Samail Ophiolite, Oman

This chapter has been published in *Contributions to Mineralogy and Petrology.* The final publication is available at http://link.springer.com/article/10.1007/s00410-012-0775-z

Abstract

Tectonically exposed mantle peridotite in the Oman Ophiolite is variably serpentinized and carbonated. Networks of young carbonate veins are prevalent in highly serpentinized peridotite, particularly near low-temperature alkaline springs emanating from the peridotite. An unusual feature in some samples is the coexistence of serpentine and quartz, which is not commonly observed in serpentinites. This assemblage is unstable with respect to serpentine + talc or talc + quartz under most conditions. Serpentine in the carbonated serpentinites in this study is more iron-rich than in most serpentinites reported in previous studies, and samples with co-existing quartz contain the most iron-rich serpentines. Calculations of thermodynamic equilibria in the MgO-SiO_2-H_2O-CO_2 system suggest that serpentine + quartz may be a stable assemblage at low temperatures (e.g., less than ~15-50°C), and is stabilized to higher temperatures by preferential cation substitutions in serpentine over talc. Based on these calculations, serpentine + quartz assemblages could result from serpentinization at near-surface temperatures. Clumped isotope thermometry of carbonate veins yields temperatures within error of the observed temperatures in Oman groundwater for all samples analyzed, while the $\delta^{18}O$ of water calculated to be in equilibrium with carbonate precipitated at those temperatures is within error of the observed isotopic composition of Oman groundwater for the majority of

samples analyzed. As groundwater geochemistry suggests that carbonate precipitation and serpentinization occur concomitantly, this indicates that both hydration and carbonation of peridotite are able to produce extensive alteration at the relatively low temperatures of the near-surface weathering environment.

1. Introduction

Mantle peridotite is far from thermodynamic equilibrium with the atmosphere and surface waters, and peridotite exposed at Earth's surface reacts readily with aqueous fluids to form products including serpentine and carbonate minerals. Carbonation of exposed mantle peridotite may therefore provide effective means of permanent carbon storage (e.g., Seifritz 1990). It has been demonstrated that *in situ* carbonation of peridotite has the potential to store large amounts of CO_2 as stable carbonate minerals (Kelemen and Matter 2008). The efficiency of peridotite carbonation depends on temperature, pressure, water composition, and reactions involving the magnesium silicates that are dissolved and precipitated during alteration of peridotite (e.g., O'Connor et al. 2004; Hansen et al. 2005; Chizmeshya et al. 2007). Thus, understanding the circumstances of carbonation of peridotite during natural alteration can constrain the optimal conditions and limitations of mineral carbon sequestration in peridotite.

High degrees of carbonation and serpentinization are observed in carbonate-bearing serpentinized peridotite in the Samail Ophiolite of Oman. The extent of serpentinization in the tectonically exposed mantle section of ophiolites is typically 30-60%, reaching 100% in some cases (Boudier et al. 2010). In peridotite that hosts abundant carbonate veins in the Samail Ophiolite, we commonly observe 100% serpentinization, and relict olivine is rare. Most of the sub-surface carbonate veins now

exposed by erosion are relatively young, with 95% of 40 samples yielding ^{14}C ages ranging from 0 to 50,000 years (Clark and Fontes 1990; Kelemen and Matter 2008; Kelemen et al. 2010). Low-temperature alkaline springs emanating from the peridotite, as well as the spectacular travertine terraces that precipitate around these springs, are also linked to ongoing carbonation and serpentinization. Ca-OH^--rich, carbon-poor waters are formed as groundwater reacts with peridotite isolated from the atmosphere and precipitate calcite and dolomite as they emerge at the surface to react with atmospheric CO_2 or mix with Mg-HCO_3^- waters (Barnes and O'Neil 1969; Neal and Stanger 1985; Bruni et al. 2002; Kelemen and Matter 2008). Spring water temperatures are ~30°C, similar to the mean annual air temperature in Oman. Kelemen et al. (2011) report $d^{18}O$ values in peridotite-hosted carbonate veins and travertines that are consistent with equilibrium with Oman groundwater and spring-water at near-surface temperatures. Together, carbonate ages, geochemical trends in groundwater, and preliminary stable isotope thermometry suggest that low-temperature serpentinization and carbonation in these rocks has been ongoing for more than 50,000 years and continues to the present day.

The products of ongoing alteration of peridotite at near-surface temperatures in Oman are primarily serpentine + magnesite, dolomite, or calcite, with calcite more prevalent near alkaline springs and associated travertine deposits. Talc is very rare in our carbonate-veined, altered peridotite samples, found only as scattered grains in one sample (OM07-28A). However, we observe the surprising occurrence of abundant quartz + serpentine without talc in two of our samples (OM08-206A and OM08-206D). Here we discuss mineral parageneses and thermometry in low temperature carbonated and

serpentinized peridotite from the Samail Ophiolite in Oman and consider the implications for conditions of alteration.

2. Analytical Methods

Samples were studied by petrographic microscope, powder X-ray diffraction (XRD), X-ray fluorescence (XRF), and electron microprobe. Powdered samples were analyzed by X-ray diffraction using a Philips Model 1830 X-ray diffractometer located at Woods Hole Oceanographic Institution and peaks for constituent minerals were identified using MacDiff and Match! Software. Whole rock major and trace element composition were determined by X-ray fluorescence at the Washington State University GeoAnalytical Lab, where loss on ignition (LOI), primarily $H_2O + CO_2$, was also measured (http://www.sees.wsu.edu/Geolab/equipment/xrf.html). Polished thin sections were quantitatively analyzed with a 5-spectrometer Cameca SX-100 electron microprobe located at the American Museum of Natural History in New York, using a 10μm beam diameter, with 15kV accelerating voltage, 10nA current, and 20-30 second peak time, to analyze the major element composition of phases in thin section in terms of Si, Ti, Al, Cr, Fe, Mn, Mg, Ca, and Ni, using natural and synthetic standards. To correct for matrix effects in serpentine, Si and Mg concentrations in serpentine analyses were corrected using a calibration based on analyses of reference antigorite standard, BM66586. The reported analytical precision is based on replicate analyses of this reference material. Calibration information for each measured oxide, including spectrometer crystal, calibration standard, peak time, wt% in antigorite sample, standard deviation, and post-measurement corrections, are shown in the supplementary table in Online Resource 1.

Clumped isotope and conventional $\delta^{18}O$ carbonate-water exchange thermometry were employed to determine the temperature of carbonate precipitation during alteration of peridotite. Clumped isotope thermometry is a relatively new carbonate paleothermometer based on temperature-dependent "clumping" of ^{13}C and ^{18}O relative to a stochastic distribution in CO_2 released by acid digestion of carbonate, and does not depend on the bulk isotopic composition of the fluid from which the carbonate minerals precipitated (Ghosh et al. 2006; Eiler 2007; Huntington et al. 2009). CO_2 was extracted from carbonate minerals in our samples by phosphoric acid digestion, with samples containing only calcite veins reacting at 25°C for 12-16 hours in sealed vessels (OM08-01 and OM09-130) or at 90°C for 20 minutes with evolved CO_2 continuously trapped cryogenically (samples OM08-206D and OM10-34B), samples containing only dolomite veins reacting at 90°C for 20 minutes in sealed vessels, and samples containing magnesite veins reacting at 80°C for 2-3 days in sealed vessels. Samples containing more than one carbonate mineral were subjected to a stepped phosphoric acid digestion procedure following the method of Guo (2008). The extracted gas was purified by cryogenic separation and gas chromatography, and analyzed by gas-source isotope ratio mass spectrometry using a modified Thermo-Finnegan 253 in the laboratories for stable isotope geochemistry at Caltech to simultaneously make measurements of clumped isotope ratios, reported as $\Delta 47$ values (Ghosh et al. 2006), $\delta^{13}C$, and $\delta^{18}O$.

Clumped isotope analytical methods and data processing were carried out according to the protocols described in Huntington et al. (2009). $\Delta 47$ values were normalized based on analysis of heated CO_2 gases with a stochastic distribution of isotopologues, and were corrected for fractionation during phosphoric acid digestion at

temperatures above that of the original calibration (25°C) (Ghosh et al. 2006) via linear interpolation between that and the experimentally-determined correction factor of 0.081‰ at 90°C (Passey et al. 2010). This agrees relatively well with the theoretically predicted correction of 0.0078‰ for phosphoric digestion of calcite at 90°C (Guo et al. 2009). Although Guo et al. (2009) predict different (slightly non-linear) hot acid fractionation corrections for calcite, dolomite, and magnesite, the difference between those corrections and the experimental value does not result in significantly different clumped isotope temperatures (~3°C higher for magnesite digested at 90°C, ~2°C higher for dolomite digested at 90°C, and ~1°C lower for calcite and dolomite digested at 50°C for low-temperature carbonates).

Clumped isotope temperatures were calculated using a polynomial fit to the experimental calcite calibration data between 1 and 50°C and at 1100°C from Ghosh et al. (2006) and experimental dolomite calibration data between 25 and 350°C (Bonifacie et al. 2011; Bristow et al. 2011; M. Bonifacie, manuscript in preparation). The synthetic dolomite data are consistent with inorganic calcite calibrations as well as the theoretical dolomite calibration of Guo et al. (2009). Although experimental calibration data are not available for magnesite, Guo et al. (2009) calculate a temperature dependence of Δ47 in magnesite that is indistinguishable from that in dolomite. Varying the choice of equation used for Δ47 temperature-dependence (single polynomial fit to all available calibration data (Bristow et al. 2011), separate fits to calibration data for calcite and dolomite (Ghosh et al. 2006; M. Bonifacie et al., manuscript in preparation), or separate theoretical calibrations for each mineral (Guo et al. 2009)) results in less than 4°C variation in the calculated temperatures of carbonate precipitation at low temperatures, which is similar

in magnitude to the analytical error. As such, a single polynomial fit is used for all three minerals.

Oxygen isotope ratios of water in equilibrium with the carbonates at these clumped isotope temperatures were calculated using the calcite-water fractionation factors from Kim and O'Neil (1997), dolomite-water fractionation factors from Vasconcelos et al. (2005), and magnesite-water fractionation factors calculated ratioing the reduced partition function ratios for magnesite and water from, Schauble et al. (2006) and Rosenbaum (1997), respectively. Since experimental data are not available for magnesite-water oxygen isotope fractionation, and different theoretical calculations of fractionation factors can yield significantly different results (Schauble et al. 2006; Chacko and Deines 2008; Zheng 2011), less confidence can be given to the $\delta^{18}O_{water}$ values derived from magnesite.

3. Results

3.1 Mineralogy

Most samples have mesh textures typical of serpentine replacing olivine (Wicks and Whittaker 1977; O'Hanley 1996). Rare olivine relicts are present in only a few carbonate-veined serpentinite samples, with sparse pyroxene the most common relict primary silicate phase. X-ray diffraction (XRD) analysis was employed to identify the major minerals in most of the samples. XRD, combined with optical petrography, reveals that serpentine is composed of lizardite and chrysotile, and the vein carbonates are primarily dolomite and magnesite. However, in some veins near active alkaline springs, calcite is the most abundant carbonate mineral. Minerals other than serpentine and carbonate commonly reported in carbonate-bearing serpentinized peridotites during low-

temperature alteration and weathering of peridotite, such as brucite, talc, and hydrated carbonates including hydromagnesite, nesquehonite, dypingite, and huntite (e.g., Stanger and Neal 1994; Wilson et al. 2006; Klein et al. 2009; Bach and Klein 2009)), are not present in sufficient quantities (more than 5 to 10%) in our samples to be identified in XRD, nor were they found by electron microprobe in most samples. Our samples are chemically heterogeneous, as magnesium and calcium are mobilized in the fluid during serpentinization and precipitated elsewhere in millimeter-to-decimeter-scale carbonate veins. Bulk-rock chemistry and mineralogy is presented in Table 1.

The fine-grained nature of most of our samples limits the usefulness of the petrographic microscope for identifying phases and observing textures. Electron microprobe analysis, including both point measurements and elemental mapping, and back-scattered electron (BSE) imaging are therefore valuable for distinguishing different types of carbonates in situ, observing fine-scale textural relationships between minerals, identifying accessory minerals, and determining the composition of the minerals in our samples.

Accessory minerals in carbonate-veined serpentinites identified using the electron microprobe include chromian spinel, magnetite, hematite, goethite, olivine, diopside, enstatite, talc, quartz, ankerite, barite, gypsum, pyrite, and silver sulfide, as summarized in Table 1. Hydrated carbonates and brucite can be distinguished from their anhydrous counterparts (including magnesite) using the microprobe totals. Hydrated carbonate phases are not observed in any of our samples, and brucite is found at only a single point, in keeping with the likelihood of brucite breakdown to form magnesium carbonates via reactions such as $Mg(OH)_2 + CO_2 = MgCO_3 + H_2O$. Minor phases show signs of

disequilibrium. For example, in isolated, small veins and vugs up to ~50 μm in size, some apparently late-forming calcite is found in contact with magnesite, which under equilibrium conditions should lead to the formation of dolomite. Many studies have emphasized the role of magnetite in serpentinization (e.g., Hansen et al. 2005; Klein et al. 2009), since serpentines generally accommodate less iron than their precursor silicate minerals (Trommsdorff and Evans 1972; Vance and Dungan 1977), making it possible in some cases to use magnetic susceptibility as an indicator of the extent of serpentinization (Toft et al. 1990; Hansen et al. 2005; Bach et al. 2006). In some of our samples, scattered magnetite grains are found with serpentine, but in most samples magnetite occurs only as rims on relict chromian spinels, if at all, and hematite is more common than magnetite, while other samples have essentially no iron oxides. Our data are consistent with the observation that hematite, rather than magnetite, is common in carbonate-altered peridotites worldwide (Eckstrand 1975; Frost 1985).

The presence of minerals such as hematite and sulfates in many of our samples suggests that oxygen fugacity was relatively high, at least locally, despite the reducing nature of serpentinization reactions that commonly reduce H_2O while oxidizing Fe^{2+} from olivine (Frost 1985). In some samples hematite and magnetite are present in the same thin section, implying buffering along redox reactions, localized heterogeneities in oxygen fugacity, or disequilibrium.

A surprising assemblage observed in a few samples is coexisting serpentine + quartz. In two samples, OM08-206A and OM08-206D, quartz makes up a large enough proportion of the rock to be identifiable by XRD (Figure 1). Small amounts of a pure silica phase were also detected by electron microprobe in a third serpentinite sample,

OM08-01. In OM08-206A and OM08-206D, microcrystalline quartz is found in the cores of mesh-texture serpentine in 5-10 mm wide, formerly pyroxene-rich bands that still contain relatively abundant relict pyroxene. ~30 volume % of these bands is composed of quartz. The bands are also evident in outcrop morphology and comprise ~10 volume % of the outcrop.

Although the silica appears isotropic in thin section, XRD spectra of OM08-206A and OM08-206D show the silica phase to be quartz, and not opal or amorphous silica. Unlike some silica reported in weathered and silicified serpentinites elsewhere (O'Hanley 1996; Tsikouras et al. 2006; Boschi et al. 2009), the texture of coexisting serpentine and quartz in our samples is similar to serpentine mesh texture. Boschi et al. (2009) report chalcedony rimming carbonates, which in turn surround serpentine relicts, without direct contact between chalcedony and serpentine. Tsikouras et al. (2006) report microcrystalline quartz surrounding relict serpentine. In our quartz-bearing serpentinite samples, serpentine forms a meshwork that surrounds cores of quartz (Figure 2), whereas in a typical mesh serpentine the mesh centers are composed of relict olivine or late-forming serpentine that statically replaces olivine (O'Hanley 1996). Beinlich et al. (2010) report a similar occurrence of quartz filling mesh cells defined by serpentine veins, formed during low temperature, near-surface weathering of ultramafic clasts in a sedimentary basin.

Carbonate-free, partially serpentinized peridotite found at the same location as our quartz-bearing serpentinite has a similar mesh texture with serpentine surrounding olivine, as well as surrounding epoxy-filled holes in the thin section. However, the serpentine meshwork surrounding quartz commonly includes a layer of more iron-rich

serpentine rims surrounding the quartz cores, whereas the serpentine mesh surrounding olivine or epoxy-filled holes does not. The cryptocrystalline quartz is commonly very finely inter-grown with sub-micron-sized iron compounds, which results in up to 25 wt% FeO* in some mixed analyses. Aside from this variable iron component, microprobe analyses show that quartz regions are nearly pure SiO_2 and cannot be confused with the soda lime glass slides on which the thin sections are mounted (Table 2). Although serpentine + quartz is unstable under typical metamorphic conditions with respect to serpentine + talc or talc + quartz (Evans and Guggenheim 1988), the low temperatures of ongoing serpentinization in Oman could allow this assemblage to coexist stably, as discussed below.

3.2 Iron in serpentine

Average serpentine compositions for each sample are reported in Table 3, and a complete table of all electron microprobe analyses of serpentine can be found in Online Resource 2. Serpentine in our carbonated serpentinite samples from Oman is, on average, slightly more iron-rich than lizardite from serpentinized mantle peridotites compiled from the literature by Evans et al. (2009), and the serpentine in our quartz-bearing samples is significantly more iron-rich, as shown in Figure 3. Lizardite analyses from the literature have an average X_{Fe} = molar Fe/[molar Fe + Mg] of 5.7%, serpentines in our quartz-free serpentinite samples have an average X_{Fe} of 6.3%, and serpentines in our samples containing coexisting serpentine + quartz have an average X_{Fe} of 10.1%. The iron content of much of the serpentine in our samples, particularly serpentine coexisting with quartz, exceeds the iron content of the relict olivine (X_{Fe} ~9.0%) and pyroxene (X_{Fe} ~8.1%) found in these samples and elsewhere in the ophiolite (Hanghoj et al. 2010).

Variation in serpentine composition across the boundaries between serpentine and quartz is evident in WDS elemental maps of Fe (Figure 4), with serpentine forming Fe-rich rims around quartz containing fine-grained Fe-compounds.

Projection of our serpentine microprobe analyses onto a molar MgO-SiO_2-FeO ternary diagram (Figure 5), reveals that, in addition to higher than normal Fe-content, several of our serpentine analyses are also anomalously silica-rich. This may be due to the presence of talc inter-layers within the serpentine structure (Veblen and Buseck 1979). Fe substitution and/or the presence of talc interlayers may stabilize serpentine relative to talc, and may help explain why end-member talc is so rarely observed in our samples.

Many studies model iron substitution in serpentine as if all iron in serpentine is Fe(II) on M sites to produce $Fe_3^{2+}Si_2O_5(OH)_4$ (e.g., Frost and Beard 2007; McCollom and Bach 2009), but significant Fe(III) substitution is also possible (Wicks and Plant 1979; O'Hanley and Dyar 1993; Klein et al. 2009) and perhaps is dominant in many lizardites (Evans 2008, 2010; Evans et al. 2009). Evans (2008) emphasized the importance of ferric iron substitution in serpentine, primarily in the form of a ferri-Tschermak substitution, as proposed by Wicks and Plant (1979), where Fe^{3+} substitutes on both M sites and T sites to form a cronstedtite component of serpentine, producing an end-member serpentine with the stoichiometry $(Mg_2Fe^{3+})(Fe^{3+}Si)O_5(OH)_4$. In some cases ferric iron may substitute only on the M site, charge balanced by M site vacancies, yielding an end-member ferrian serpentine with the formula $(\square Fe_2^{3+})Si_2O_5(OH)_4$ (Wicks and Plant 1979; Evans 2008; Evans et al. 2009). Comparison of the compositions

of serpentine from our samples with these end-members (Figure 5), suggests that all three substitution mechanisms may be present in our serpentines.

Regardless of the particular iron substitution mechanism in serpentine, the reaction of magnetite with water and aqueous silica to produce an Fe component of serpentine will be favored at lower temperatures because the reaction involves a net consumption of volatiles (given nearly constant pressure in the near-surface alteration environment). For example,

(R1) $Fe^{2+}Fe_2^{3+}O_4 + 2\ SiO_{2\ aq} + H_2O + H_{2\ aq} = Fe_3^{2+}Si_2O_5(OH)_4$
magnetite — ferroan lizardite

(R2) $2\ Fe^{2+}Fe_2^{3+}O_4 + 6\ SiO_{2\ aq} + 7\ H_2O = 3(\square\ Fe_2^{3+})Si_2O_5(OH)_4 + H_{2\ aq}$
magnetite — vacancy-coupled Fe^{3+}lizardite

(R3) $4\ Fe^{2+}Fe_2^{3+}O_4 + 3\ SiO_{2\ aq} + 5\ H_2O + H_{2\ aq} = 3\ (Fe_2^{2+}Fe^{3+})(Fe^{3+}Si)O_5(OH)_4$
magnetite — cronstedtite

The source of aqueous SiO_2 in these reactions can be understood as the result of incongruent carbonation of silicates, e.g., olivine, serpentine, pyroxene, or talc + CO_2 = magnesite + SiO_{2aq}. The observation that the formation of iron-rich serpentine should be favored at lower temperatures is borne out in geochemical reaction path models by Klein et al. (2009), which calculate decreasing magnetite and increasing iron in serpentine with decreasing temperature.

The samples containing abundant quartz + serpentine also have the lowest bulk rock Mg#'s of our samples (87.2 for OM08-206A and 82.7 for OM08-206D), slightly lower than in typical Oman mantle peridotite, while relict clinopyroxenes in these samples have typical mantle Mg#'s of 91-93. The low bulk rock Mg# is probably due to small amounts of Mg-extraction during alteration (e.g., Snow and Dick 1995). Even so,

the average Fe-content of serpentine in these samples (X_{Fe} ~11%) is still higher than would be predicted (X_{Fe} ~6%) for antigorite serpentine in Fe/Mg exchange equilibrium with Mg# 82-87 olivine (Trommsdorff and Evans 1972). We infer that the high Fe content of serpentine in these samples is due mainly to low temperature reactions consuming Fe-oxides (e.g., reactions R1-R3), and not to the slightly Fe-rich bulk compositions.

3.3 Stability of coexisting serpentine + quartz at low temperatures

T-X diagrams for end-member reactions in the system MgO-SiO_2-H_2O-CO_2 were calculated at constant pressure using THERMOCALC (Holland and Powell 1998). Thermodynamic data are not available for lizardite, and chrysotile and lizardite have very similar free energy (Evans 2004), so the stability of both phases is modeled using thermodynamic data for chrysotile. Calculations were done under fluid saturated conditions to produce T-X diagrams for Mg-end-member magnesite (mgs), chrysotile (chr), talc (ta), and quartz (q), at a variety of near-surface pressures and mineral activities.

For pure Mg-end-members (unit activities of Mg-components in all minerals), the isobaric invariant point involving magnesite, chrysotile, talc, quartz, and fluid is predicted to be at 15°C, which is slightly lower than observed ground- and surface-water temperatures of 17-40°C in Oman (Neal and Stanger 1985; Matter 2001, 2005; Dewandel et al. 2005; our unpublished data). Increasing pressure does not have a significant effect on the temperature of the invariant point, but shifts it to lower values of X_{CO2}, from $\log(X_{CO2})$ of -5.06 at 3.5 bars to -6.6 at 1kbar. T-X_{CO2} phase relations for magnesite, chrysotile, talc, and quartz with unit activities are plotted at 5 bars pressure in Figure 6.

The temperature of the invariant point on the T-X_{CO2} plot is controlled mainly by the reaction chrysotile + 2 quartz = talc + H_2O, which is not sensitive to X_{CO2} over the range considered. THERMOCALC output reports the uncertainty of the temperature of this reaction as ± 4°C (one sigma). However, the THERMOCALC database also lists uncertainties for the standard enthalpies of each mineral. If the standard enthalpies are allowed to vary by two standard deviations, the temperature of this reaction for pure end-members at 1 bar can be as low as -33°C or as high as 65°C. Note that these extreme bounds arise via taking the 2 sigma high values of enthalpy for reactants (4% probability) and the 2 sigma low values for products (also 4% probability), or vice versa. Thus, the resulting temperature extremes lie well outside 2 sigma bounds for the reaction temperature. Using other internally-consistent thermodynamic databases further illustrates the uncertainty associated with these calculations; using the thermodynamic data of Gottschalk (1997) yields a temperature of 46°C, while using that of Berman (1988) yields a temperature of 37°C, not only illustrating the uncertainty associated with choosing a thermodynamic database, but also suggesting that the temperatures calculated by THERMOCALC may be low.

Additionally, the single parameter activity model used by THERMOCALC for H_2O-CO_2 activity is calibrated over the *PT* range of 0.5–20 kbar, 400–1,000 °C, and is likely to be imprecise near the solvus involving immiscible H_2O- and CO_2-rich fluids (Holland and Powell 2003). Applying THERMOCALC to our low-pressure, low-temperature system is thus an approximation that will become less accurate near the solvus. For calculations at pressures greater than 3.5 bars, serpentine + quartz are predicted to be stable when X_{CO2} in fluid is more than one order of magnitude lower than

the solubility limit of CO_2 in aqueous fluid (Duan and Sun 2003). Even so, because the non-ideal behavior of H_2O-CO_2 fluids at these low temperatures and pressures may not be well fit by the activity model used in THERMOCALC, the results of our thermodynamic calculations in this section should be viewed as illustrative, rather than fully quantitative.

Serpentine accommodates more iron than does talc (Trommsdorff and Evans 1972), and thus adding FeO to MgO-SiO_2-H_2O-CO_2 stabilizes serpentine with respect to talc. A T-X diagram for magnesite-chrysotile-talc-quartz was calculated with reduced activities for chrysotile and talc based on an ideal mixing-on-sites model (Spear 1993). Magnesite in our serpentinite samples contains very little iron (less than 0.5 wt% on average), so magnesite was modeled with unit activity. The average Mg# of our (limited number of) of talc analyses was about 95.5, which is approximately consistent with Fe partitioning between talc and antigorite observed by Trommsdorff and Evans (1972). A fit to their data predicts an Mg# of 96.4 for talc when antigorite has an Mg# of 92.8, the average Mg# of serpentine in our single talc-bearing sample, OM07-28A. We therefore used the fit of Trommsdorff and Evans (1972) to predict the Mg# of talc that could coexist with our higher-Fe serpentine. While iron is the most abundant element substituting into serpentine and talc, the concentrations of aluminum and chromium present in these minerals are also considered in the activity model. Serpentine in quartz-bearing samples has an average Mg# of 89.9 and an average chrysotile activity of 0.710. Based on the partitioning data of Trommsdorff and Evans (1972), talc in Fe/Mg exchange equilibrium with this serpentine should have an Mg# of 94.9, giving an Mg-end-member talc activity of 0.856. When the T-X phase diagram is recalculated with these reduced

activities, the invariant point is predicted by THERMOCALC to be at 19°C. While this temperature is no doubt imprecise, it does reflect the fact that preferential Fe, Al and Cr substitution into serpentine will raise the temperature of the invariant point, compared to the MgO-SiO_2-H_2O-CO_2 system. An average composition of the three most iron-rich serpentine analyses in our samples yields a chrysotile activity of 0.236 and a theoretical talc activity of 0.474, which places the calculated invariant point at a temperature of 28°C. The location of the calculated invariant point for the range of chrysotile activities observed in our samples is plotted for pressures between 3.5 bars and 1 kbar in Figure 7.

Again, because the H_2O-CO_2 fluid model used in THERMOCALC is uncertain at low temperature and pressure, and because different methods of fitting and extrapolating the available thermodynamic data result in invariant point temperatures that vary by more than 30°C, the calculated temperatures reported in this section should be viewed as approximate. However, they demonstrate that serpentine + quartz could be stable during near-surface weathering of Oman peridotite. Also, even if talc were stable with respect to serpentine + quartz at, e.g., 30°C and 50 bars, these calculations demonstrate that the thermodynamic driving force for talc crystallization would be very low under these conditions, and this could enhance kinetic inhibition of talc formation.

3.4 Clumped isotope thermometry in carbonate veins

Results of clumped isotope analysis of carbonate veins in serpentinized peridotite from the Oman ophiolite are presented in Table 4, including: the CO2 clumped isotope index $\Delta 47$ (a measure of the enrichment in mass 47 isotopologues relative to a stochastic composition); temperature corresponding to the $\Delta 47$ value (based on calibration of the relationship between carbonate growth temperature and the $\Delta 47$ value of CO_2 extracted

from carbonate by phosphoric acid dissolution); bulk isotopic composition of extracted CO_2 in terms of $\delta^{13}C$ and $\delta^{18}O$; the calculated bulk $\delta^{18}O$ of the carbonate mineral (i.e., correcting for the acid dissolution fractionation); and the calculated $\delta^{18}O$ of water in equilibrium with the carbonate at the calculated clumped isotope temperature. Clumped isotope temperatures range from 23°C to 43°C, placing all samples within error of the observed temperatures of shallow groundwater and surface water in Oman, ~17-40°C (Neal and Stanger 1985; Matter 2001, 2005; Dewandel et al. 2005; our unpublished data). $\delta^{13}C$ ranges from -11.4‰ to 0.3‰ (V-PDB), and $\delta^{18}O$ of the carbonates range from 26.4‰ to 38.8‰ (VSMOW). We believe the $\delta^{18}O$ data for magnesite presented here are more accurate than those presented in Kelemen et al. (2011), as those were derived from magnesite reacted for only 10 minutes at 70°C, so that much of the CO_2 could have been produced by dissolution of dolomite rather than magnesite. $\delta^{18}O$ values of water calculated to be in equilibrium with the carbonate at the measured clumped isotope temperature range from -7.7‰ to 8.0‰ (VSMOW), with the majority of samples falling within error of the -2.1‰ to 3.6‰ (VSMOW) range of $\delta^{18}O$ observed in Oman groundwater (Neal and Stanger 1985; Clark et al. 1992; Matter 2005; J. Matter, pers. comm. 2012), as shown in Figure 8.

4. Discussion

The observation of high Fe content in serpentines and the coexistence of serpentine and quartz are consistent with low-temperature serpentinization. This supports the hypothesis that serpentine in our samples formed at lower temperatures than most lizardite and chrysotile whose compositions are published. Oxygen isotope fractionation between serpentine and magnetite in drilled and dredged samples of seafloor outcrops

suggests serpentinization occurred at temperatures of ~130-400°C (Wenner and Taylor 1971; Früh-Green et al. 1996; Barnes et al. 2009). Continental lizardites and chrysotiles yield serpentine-magnetite temperatures above 85°C (Wenner and Taylor 1971).

Johannes (1969) placed the reaction serpentine + 2 quartz = talc + H_2O at ~300°C at 2 kbar for Mg-end-member minerals. However, the experiments to determine the equilibrium conditions for this reaction were unsuccessful in that study, and serpentinite is observed to have altered to talc during formation of listvenite at temperatures less than 300°C (e.g., Hansen et al. 2005). Tsikouras et al. (2006) attributed the coexistence of serpentine + quartz in their samples to Mg loss to an extremely CO_2-rich fluid at temperatures below 500°C, via the reaction chrysotile = 2 SiO_2 + 3 MgO(aq) + 2 H_2O, but our calculations suggest that serpentine + quartz is unstable at all X_{CO2} above ~ 50°C. This low-temperature interpretation is also consistent with the formation of mesh-texture serpentine + quartz during surface and near-surface weathering of ultramafic clasts, as reported by Beinlich et al. (2010). Our calculations show that serpentine coexists stably with quartz at low temperatures, from a calculated temperature of ~15 to 46°C for Mg end-members, extending to slightly higher temperatures for bulk compositions containing iron, in which Fe partitions preferentially into serpentine rather than talc. Thus the presence of serpentine + quartz supports the hypothesis that serpentinization is ongoing in the Samail ophiolite in Oman, in a low-temperature weathering horizon (Neal and Stanger 1985; Barnes and O'Neil 1969; Bruni et al. 2002; Kelemen and Matter 2008; Kelemen et al. 2011).

The low temperatures required for serpentine + quartz stability are within the range of carbonate crystallization temperatures derived from conventional carbonate-

water oxygen isotope thermometry and clumped stable isotope thermometry, and of observed groundwater temperatures in Oman. Clumped isotope thermometry yields carbonate crystallization temperatures of 23-43°C (Fig. 8), consistent with the observed temperatures of shallow groundwater and surface water in Oman, ~17-40°C (Neal and Stanger 1985; Matter 2001, 2005; Dewandel et al. 2005; our unpublished data). Similarly, Kelemen et al. (2011) used observed $\delta^{18}O$ in monomineralic magnesite and calcite samples, together with the observed range of $\delta^{18}O$ in Oman ground water and spring water and the water-carbonate oxygen isotope thermometer of Chacko and Deines (2008) to determine crystallization temperatures of 23-60°C. This is consistent with our observation that calculated values of $\delta^{18}O$ for water in equilibrium with carbonate are mostly consistent with the observed modern range of -2.1 to 3.6‰ (VSMOW) in groundwater, surface waters, and alkaline springs in peridotite catchments in Oman (Neal and Stanger 1985; Clark et al. 1992; Matter 2005; J. Matter, pers. comm. 2012). The agreement of carbonate stable isotope data with temperatures and $\delta^{18}O$ values in modern groundwater demonstrates that alteration in the form of carbonate vein precipitation in peridotite occurred under conditions similar to those in the modern environment. Together with geochemical trends in groundwater (Barnes and O'Neil 1969; Neal and Stanger 1985; Bruni et al. 2002; Kelemen and Matter 2008; Paukert et al. 2012), this suggests that carbonation and serpentinization may be occurring simultaneously via reactions between modern groundwater and peridotite, as proposed by Kelemen and Matter (2008) and Barnes and O'Neil (1969).

The range of fluid X_{CO2} within the serpentine + quartz stability field is also consistent with observed groundwater compositions in the Samail Ophiolite, which range

from a mole fraction of ~$10^{-3.5}$ in neutral to slightly alkaline groundwater to below detection limits (less than 10^{-5}) in alkaline springs (Neal and Stanger 1985; Matter 2001, 2005; Dewandel et al. 2005; E. Shock, pers. comm., 2011). Groundwater at the high X_{CO2} end of this range would be too CO_2-rich for serpentine + quartz to coexist stably according to our calculations. However, the presence of calcite in our quartz-bearing serpentinites, together with the observation that calcite veins in serpentine are abundant in the vicinity of alkaline springs, suggests that alteration occurred in the presence of Ca-OH^- type waters, which have exceptionally low dissolved CO_2 contents in peridotite catchments worldwide (Barnes and O'Neil 1969; Barnes et al. 1978; Bruni et al. 2002; Kelemen and Matter 2008). Thus, these samples were likely subject to alteration under conditions of low fluid CO_2 concentrations, favorable for serpentine + quartz stability.

It is likely that serpentinization of peridotite in Oman began during hydrothermal alteration of shallow suboceanic mantle prior to obduction (Boudier et al. 2010). Some of this may have occurred at higher temperatures, in the ~130-400°C range inferred from $\delta^{18}O$ in ocean-floor serpentinites (e.g., Wenner and Taylor 1971; Früh-Green et al. 1996; Barnes et al. 2009). This initial, oceanic serpentinization may have yielded Fe-poor serpentine and magnetite, as is observed in a partially serpentinized peridotite sample (OM08-206I), collected at the same location as samples with serpentine + quartz. During later alteration at lower temperature, early magnetite may have been consumed to form more Fe-rich serpentine as in reactions R1-R3 in Section 3.2. Much of the Fe-rich serpentine we observe could represent re-equilibration of the products of previous serpentinization rather than direct serpentinization of olivine, particularly where serpentine is locally more Fe-rich than the initial olivine in the peridotite.

Elevated silica activity may favor the formation of iron-rich serpentine (Frost and Beard 2007), as in reactions R1-3, thus indirectly stabilizing the serpentine + quartz assemblage. If the initial peridotite is harzburgite or lherzolite rather than dunite, the presence of pyroxene will shift the bulk composition towards silica. We infer that clinopyroxene dissolution is occurring during present-day serpentinization of peridotite due to the generation of Ca-OH fluid (Barnes and O'Neil 1969; Neal and Stanger 1985; Bruni et al. 2002). In the samples where we see coexisting serpentine + quartz, calcite is the most abundant carbonate phase, and relict clinopyroxenes are observed. Centimeter-scale pyroxene-rich bands comprise ~10% of the outcrop where serpentine + quartz assemblage and found, and quartz is restricted to these bands. Small-scale heterogeneities in fluid composition due to pyroxene dissolution may shift the silica activity to higher values, locally stabilizing Fe-rich serpentine and thereby expanding the stability of serpentine + quartz.

Precipitation of magnesite and dolomite veins could also introduce heterogeneities that would favor the local formation of Fe-rich serpentine in some areas. Serpentine is more silica-rich than olivine, so during alteration of olivine alone without SiO_2 mass transfer, it must coexist with a less silica-rich Mg phase, such as magnesite, dolomite, or brucite e.g.,

(R4) $2\ Mg_2SiO_4 + 2\ H_2O + CO_2 = Mg_3Si_2O_5(OH)_4 + MgCO_3$
forsterite serpentine magnesite

Higher concentrations of CO_2 favor additional magnesium carbonate precipitation, thereby raising the silica activity of the fluid. In Oman, dense networks of magnesite veins constitute large volume proportions in serpentinized peridotite at meter

scales, indicating that silica activity was elevated, at least locally. Additionally, magnesium dissolution and removal during alteration (e.g., Snow & Dick, 1995) may have produced slightly lower bulk Mg# in the quartz-bearing samples, compared to typical Oman mantle peridotite. Both lower bulk Mg# and elevated silica could favor the formation of Fe-rich serpentine, and as a result, stabilize the serpentine + quartz assemblage. However, as discussed in Section 3.3 above, the main factor leading to the absence of talc in our samples is low temperature, stabilizing serpentine + quartz even in MgO-SiO_2-H_2O-CO_2, and leading to reactions producing Fe-rich serpentine from magnetite + Fe-poor serpentine.

5. Conclusions

Some samples of serpentinized peridotite in the Oman ophiolite contain the unusual assemblage, serpentine + quartz, instead of talc. Phase equilibrium calculations suggest that this assemblage is stable at low temperature, below approximately 15 to 46°C in an Fe-free system depending on the thermodynamic data used. Consistent with this low inferred temperature, clumped isotope analyses of carbonate veins minerals in these and other, similar samples yield temperature estimates of 15 to 50°C. Serpentine in serpentinized peridotite with carbonate veins in the Oman Ophiolite is relatively Fe-rich in comparison with other serpentinites. The formation of high-Fe serpentine rather than magnetite is favored at low temperatures, at a given pressure, and at high silica activities. Thus the presence of Fe-rich serpentine is another indicator of low-temperature alteration. Also, because Fe partitions into serpentine relative to talc, relatively high Fe content can help to stabilize serpentine + quartz. Temperatures and oxygen isotope compositions of fluids, inferred from phase equilibria and clumped isotope data, are consistent with the

range measured in groundwater and alkaline spring water in peridotite catchments in Oman. These data all support the hypothesis that serpentinization and carbonation of peridotite are occurring at ambient temperatures in a shallow weathering horizon in the Oman Ophiolite.

References

Bach W, Klein F (2009) The petrology of seafloor rodingites: Insights from geochemical reaction path modeling. Lithos 112:103-117

Bach W, Paulick H, Garrido CJ, Ildefonse B, Meurer WP, Humphris SE (2006) Unraveling the sequence of serpentinization reactions: petrography, mineral chemistry, and petrophysics of serpentinites from MAR 15 degrees N (ODP Leg 209, Site 1274). Geophysical Research Letters 33 (13)

Barnes I, O'Neil JR (1969) Relationship between fluids in some fresh alpine-type ultramafics and possible modern serpentinization, western United States. GSA Bull 80 (10):1947-1960

Barnes I, O'Neil JR, Trescases JJ (1978) Present Day Serpentinization in New-Caledonia, Oman and Yugoslavia. Geochim Cosmochim Acta 42 (1):144-145

Barnes JD, Paulick H, Sharp ZD, Bach W, Beaudoin G (2009) Stable isotope (delta(18)O, delta D, delta(37)Cl) evidence for multiple fluid histories in mid-Atlantic abyssal peridotites (ODP Leg 209). Lithos 110 (1-4):83-94. doi:10.1016/j.lithos.2008.12.004

Beinlich A, Austrheim H, Glodny J, Erambert M, Andersen TB (2010) CO2 sequestration and extreme Mg depletion in serpentinized peridotite clasts from the Devonian Solund basin, SW-Norway. Geochim Cosmochim Acta 74 (24):6935-6964. doi:10.1016/j.gca.2010.07.027

Berman RG (1988) Internally-consistent thermodynamic data for minerals in the system NA2O-K2O-CAO-MGO-FEO-FE2O3-AL2O3-SIO2-TIO2-H2O-CO2. Journal of Petrology 29 (2):445-522

Bonifacie M, Ferry JM, Horita J, Vasconcelos C, Passey BH, Eiler JM (2011) Calibration and applications of the dolomite clumped isotope thermometer to high temperatures. 75 (3):551

Boschi C, Dini A, Dallai L, Ruggieri G, Gianelli G (2009) Enhanced CO2-mineral sequestration by cyclic hydraulic fracturing and Si-rich fluid infiltration into serpentinites at Malentrata (Tuscany, Italy). Chem Geol 265:209-226

Boudier F, Baronnet A, Mainprice D (2010) Serpentine mineral replacements of natural olivine and their seismic implications: Oceanic lizardite versus subduction-related antigorite. J Petrol 51:495-512

Bristow TF, Bonifacie M, Derkowski A, Eiler JM, Grotzinger JP (2011) A hydrothermal origin for isotopically anomalous cap dolostone cements from south China. Nature 474 (7349):68-U92. doi:10.1038/nature10096

Bruni J, Canepa M, Chiodini G, Cioni R, Cipolli F, Longinelli A, Marini L, Ottonello G, Zuccolini MV (2002) Irreversible water-rock mass transfer accompanying the generation of the neutral, Mg-HCO3 and high-pH, Ca-OH spring waters of the Genova province, Italy. Applied Geochem 17 (4):455-474

Chacko T, Deines P (2008) Theoretical calculation of oxygen isotope fractionation factors in carbonate systems. Geochim Cosmochim Acta 72:3642-3660

Chizmeshya AVG, McKelvy MJ, Squires K, Carpenter RW, Béarat H (2007) DOE Final Report 924162: A novel approach to mineral carbonation: Enhancing carbonation while avoiding mineral pretreatment process cost 29 pages plus appendices. Arizona State University, Tempe, AZ

Clark ID, Fontes JC (1990) Paleoclimatic reconstruction in northern Oman based on carbonates from hyperalkaline groundwaters. Quaternary Res 33 (3):320-336

Clark ID, Fontes JC, Fritz P (1992) Stable Isotope disequilibria in travertine from high pH waters: Laboratory investigations and field observations from Oman. Geochim Cosmochim Acta 56 (5):2041-2050

Das Sharma S, Patil DJ, Gopalan K (2002) Temperature dependence of oxygen isotope fractionation of CO2 from magnesite-phosphoric acid reaction. Geochim Cosmochim Acta 66:589-593

Dewandel B, Lachassagne P, Boudier F, Al-Hattali S, Ladouche B, Pinault JL, Al-Suleimani Z (2005) A conceptual hydrogeological model of ophiolite hard-rock aquifers in Oman based on a multiscale and a multidisciplinary approach. Hydrogeology J 13 (5-6):708-726

Downs R The RRUFF Project: an integrated study of the chemistry, crystallography, Raman and infrared spectroscopy of minerals. In: Program and Abstracts of the 19th General Meeting of the International Mineralogical Association, Kobe, Japan, 2006.

Duan ZH, Sun R (2003) An improved model calculating CO2 solubility in pure water and aqueous NaCl solutions from 273 to 533 K and from 0 to 2000 bar. Chemical Geology 193 (3-4):257-271

Eckstrand OR (1975) Dumont Serpentinite - Model for control of nickeliferous opaque mineral assemblages by alteration reactions in ultramafic rocks. Economic Geology 70 (1):183-201

Eiler J (2007) "Clumped-isotope" geochemistry: The study of naturally occurring, multiply-substituted isotopologues. Earth Planet Sci Lett 262:309-327

Emmanuel S, Berkowitz B (2006) Suppression and stimulation of seafloor hydrothermal convection by exothermic mineral hydration. Earth Planet Sci Lett 243 (3-4):657-668

Evans BW (2004) The serpentinite multisystem revisited: Chrysotile is metastable. Int Geol Rev 46 (6):479-506

Evans BW (2008) Control of the products of serpentinization by the Fe2+Mg-1 exchange potential of olivine and orthopyroxene. J Petrol 49:1873-1887

Evans BW (2010) Lizardite versus antigorite serpentinite: Magnetite, hydrogen, and life(?). Geology 38 (10):879-882. doi:10.1130/g31158.1

Evans BW, Guggenheim S (1988) Talc, pyrophyllite, and related minerals. In: Bailey SW (ed) Hydrous Phyllosilicates (Exclusive of Micas). Reviews in Mineralogy, vol 19. Mineralogical Society of America, Washington, D.C., pp 225-294

Evans BW, Kuehner SM, Chopelas A (2009) Magnetite-free, yellow lizardite serpentinization of olivine websterite, Canyon Mountain complex, NE Oregon. American Mineralogist 94 (11-12):1731-1734. doi:10.2138/am.2009.3301

Frost BR (1985) On the Stability of Sulfides, Oxides, and Native Metals in Serpentinite. Journal of Petrology 26 (1):31-63

Frost BR, Beard JS (2007) On silica activity and serpentinization. J Petrol 48:1351-1368

Früh-Green GL, Connolly JAD, Plas A, Kelly DS, Groberty B (2004) Serpentinization of oceanic peridotites: Implications for geochemical cycles and biological activity. In: Wilcock WD, Kelley DS, DeLong E, Cary C (eds) The Subseafloor Biosphere at Mid-Ocean Ridges. AGU Geophysical Monograph, vol 144. Washington, D.C., pp 119-136

Früh-Green GL, Plas A, Lécuyer C (1996) Petrologic and stable isotope constraints on hydrothermal alteration and serpentinization of the EPR shallow mantle at Hess Deep (Site 895). Proc. ODP, Sci. Results, vol 147. Ocean Drilling Program, College Station, TX. doi:10.2973/odp.proc.sr.147.016.1996

Fyfe WS (1974) Heats of chemical reactions and submarine heat production. Geophys J Roy Astr Soc 37 (1):213-215

Ghosh P, Adkins J, Affek H, Balta B, Guo W, Schauble EA, Schrag D, Eiler JM (2006) 13C–18O bonds in carbonate minerals: A new kind of paleothermometer. Geochim Cosmochim Acta 70:1439-1456

Gottschalk M (1997) Internally consistent thermodynamic data for rock-forming minerals in the system SiO2-TiO2-Al2O3-Fe2O3-CaO-MgO-FeO-K2O-Na2O-H2O-CO2. European Journal of Mineralogy 9:175-223

Guo W (2008) Carbonate clumped isotope thermometry : application to carbonaceous chondrites and effects of kinetic isotope fractionation., California Institute of Technology, Pasadena

Guo WF, Mosenfelder JL, Goddard WA, Eiler JM (2009) Isotopic fractionations associated with phosphoric acid digestion of carbonate minerals: Insights from first-principles theoretical modeling and clumped isotope measurements. Geochim Cosmochim Acta 73 (24):7203-7225. doi:10.1016/j.gca.2009.05.071

Hanghoj K, Kelemen PB, Hassler D, Godard M (2010) Composition and Genesis of Depleted Mantle Peridotites from the Wadi Tayin Massif, Oman Ophiolite; Major and Trace Element Geochemistry, and Os Isotope and PGE Systematics. Journal of Petrology 51 (1-2):201-227. doi:10.1093/petrology/egp077

Hansen LD, Dipple GM, Gordon TM, Kellett DA (2005) Carbonated serpentinite (listwanite) at Atlin, British Columbia: A geological analogue to carbon dioxide sequestration. Can Mineral 43:225-239

Holland T, Powell R (2003) Activity-composition relations for phases in petrological calculations: an asymmetric multicomponent formulation. Contributions to Mineralogy and Petrology 145 (4):492-501. doi:10.1007/s00410-003-0464-z

Holland TJB, Powell R (1998) An internally consistent thermodynamic data set for phases of petrological interest. Journal of Metamorphic Geology 16 (3):309-343

Huntington KW, Eiler JM, Affek HP, Guo W, Bonifacie M, Yeung LY, Thiagarajan N, Passey B, Tripati A, Daëron M, Came R (2009) Methods and limitations of 'clumped' CO2 isotope (Δ47) analysis by gas-source isotope ratio mass spectrometry. Journal of Mass Spectrometry 44 (9):1318-1329. doi:10.1002/jms.1614

Johannes W (1969) An experimental investigation of the system MgO-SiO2-H2O-CO2. Am J Sci 267 (9):1083-&

Kelemen PB, Matter J, Streit EE, Rudge JF, Curry WB, Blusztajn J (2011) Rates and Mechanisms of Mineral Carbonation in Peridotite: Natural Processes and Recipes for Enhanced, in situ CO(2) Capture and Storage. In: Jeanloz R, Freeman KH (eds) Annual Review of Earth and Planetary Sciences, Vol 39, vol 39. Annual Review of Earth and Planetary Sciences. pp 545-576. doi:10.1146/annurev-earth-092010-152509

Kelemen PB, Matter JM (2008) In situ carbonation of peridotite for CO2 storage. Proc Nat Acad Sci USA 105:17,295-217,300

Kelemen PB, Streit L, Mervine E, Matter JM, Eiler J, Shock E (2010) Oxygen and carbon isotope systematics during natural mineral carbonation in peridotite of the Samail Ophiolite, Oman. Geochim Cosmochim Acta 74 (12):A504-A504

Kelley DS, Karson JA, Blackman DK, Fruh-Green GL, Butterfield DA, Lilley MD, Olson EJ, Schrenk MO, Roe KK, Lebon GT, Rivizzigno P (2001) An off-axis hydrothermal vent field near the Mid-Atlantic Ridge at 30 degrees N. Nature 412 (6843):145-149

Kim ST, O'Neil JR (1997) Equilibrium and nonequilibrium oxygen isotope effects in synthetic carbonates. Geochim Cosmochim Acta 61 (16):3461-3475. doi:10.1016/s0016-7037(97)00169-5

Klein F, Bach W, Jons N, McCollom T, Moskowitz B, Berquo T (2009) Iron partitioning and hydrogen generation during serpentinization of abyssal peridotites from 15 degrees N on the Mid-Atlantic Ridge. Geochim Cosmochim Acta 73 (22):6868-6893

Matter JM (2001) Geochemical evolution and hydrodynamics of groundwaters in the alluvial aquifer of the Dakhiliya Area, Sultanate of Oman. ETH-Zurich,

Matter JM (2005) Recharge areas and geochemical evolution of groundwater in an alluvial aquifer system in the Sultanate of Oman. Hydrogeology J 14:203-224

McCollom TM, Bach W (2009) Thermodynamic constraints on hydrogen generation during serpentinization of ultramafic rocks. Geochim Cosmochim Acta 73:856-875

McCollom TM, Lollar BS, Lacrampe-Couloume G, Seewald JS (2010) The influence of carbon source on abiotic organic synthesis and carbon isotope fractionation under hydrothermal conditions. Geochim Cosmochim Acta 74 (9):2717-2740. doi:10.1016/j.gca.2010.02.008

Neal C, Stanger G (1985) Past and present serpentinization of ultramafic rocks: An example from the Semail ophiolite nappe of northern Oman. In: Drewer JI (ed) The Chemistry of Weathering. D. Reidel Publishing Company, Holland, pp 249-275

O'Connor WK, Dahlin DC, Rush GE, Gerdemann SJ, Nilsen DN (2004) Final report: Aqueous mineral carbonation, DOE/ARC-TR-04-002. Office of Process Development, Albany Research Center, Office of Fossil Energy, US DOE, Albany, OR

O'Hanley DS (1996) Serpentinite: Records of tectonic and petrological history. Oxford University, New York

O'Hanley DS, Dyar MD (1993) The composition of lizardite 1T and, the formation of magnetite in serpentinites. American Mineralogist 78 (3-4):391-404

Passey BH, Levin NE, Cerling TE, Brown FH, Eiler JM (2010) High-temperature environments of human evolution in East Africa based on bond ordering in

paleosol carbonates. Proc Natl Acad Sci U S A 107 (25):11245-11249. doi:10.1073/pnas.1001824107

Paukert AP, Matter JM, Kelemen PB, Shock EL, Havig JR (2012) Reaction path modeling of enhanced in situ CO2 mineralization for carbon sequestration in the peridotite of the Samail Ophiolite, Sultanate of Oman. Chem Geol submitted

Reusch DN (2011) New Caledonian carbon sinks at the onset of Antarctic glaciation. Geology 39 (9):807-810. doi:10.1130/g31981.1

Rosenbaum JM (1997) Gaseous, liquid, and supercritical fluid H2O and CO2: Oxygen isotope fractionation behavior. Geochim Cosmochim Acta 61 (23):4993-5003. doi:10.1016/s0016-7037(97)00362-1

Schauble EA, Ghosh P, Eiler JM (2006) Preferential formation of C-13-O-18 bonds in carbonate minerals, estimated using first-principles lattice dynamics. Geochim Cosmochim Acta 70 (10):2510-2529. doi:10.1016/j.gca.2006.02.011

Schuiling RD (1964) Serpentization as a possible cause of high heat-flow values in and near the oceanic ridges. Nature 201:807-808

Schulte M, Blake D, Hoehler T, McCollom TM (2006) Serpentinization and its implications for life on the early Earth and Mars. Astrobiology 6:364–376

Seifritz W (1990) CO2 disposal by means of silicates. Nature 345 (6275):486-486

Sleep NH, Meibom A, Fridriksson T, Coleman RG, Bird DK (2004) H-2-rich fluids from serpentinization: Geochemical and biotic implications. Proc Natl Acad Sci U S A 101 (35):12818-12823

Snow JE, Dick HJB (1995) Pervasive magnesium loss by marine weathering of peridotite. Geochim Cosmochim Acta 59:4219-4235

Spear FS (1993) Metamorphic Phase Equilibria and Pressure-Temperature-Time Paths. Mineralogical Society of America, Washington, D. C.

Stanger G, Neal C (1994) The occurrence and chemistry of huntite from Oman. Chem Geol 112:274-254

Toft PB, Arkani-Hamed J, Haggerty SE (1990) The effects of serpentinization on density and magnetic susceptibility: a petrophysical model. Physics of The Earth and Planetary Interiors 65 (1-2):137-157

Trommsdorff V, Evans BW (1972) Progressive metamorphism of antigorite schists in the Bergell tonalite aureole (Italy). Am J Sci 272 (5):423-437

Tsikouras B, Karipi S, Grammatikopoulos TA, Hatzipanagiotou K (2006) Listwaenite evolution in the ophiolite melange of Iti Mountain (continental Central Greece). Eur J Mineral 18 (2):243-255. doi:10.1127/0935-1221/2006/0018-0243

Vance JA, Dungan MA (1977) Formation of peridotites by deserpentinization in Darrington and Sultan areas, Cascade Mountains, Washington. Geol Soc Am Bull 88 (10):1497-1508

Vasconcelos C, McKenzie JA, Warthmann R, Bernasconi SM (2005) Calibration of the d18O paleothermometer for dolomite precipitated in microbial cultures and natural environments. Geology 33:317-320

Veblen DR, Buseck PR (1979) Serpentine minerals: Intergrowths and new combination structures. Science 206 (4425):1398-1400

Wenner DB, Taylor HP (1971) Temperatures of serpentinization of ultramafic rocks based on O18/O16 fractionation between coexisting serpentine and magnetite. Contributions to Mineralogy and Petrology 32 (3):165-&

Wicks FJ, Plant AG (1979) Electron microprobe and X-ray microbeam studies of serpentine textures. Canadian Mineralogist 17:785-830.

Wicks FJ, Whittaker EMJ (1977) Serpentine textures and serpentinization. Canadian Mineralogist 15 (4):459-488

Wilson SA, Raudsepp M, Dipple GM (2006) Verifying and quantifying carbon fixation in minerals from serpentine-rich mine tailings using the Rietveld method with X-ray powder diffraction data. Am Min 91:1331–1341

Zheng YF (2011) On the theoretical calculations of oxygen isotope fractionation factors for carbonate-water systems. Geochem J 45 (4):341-354

Electronic Supplementary Materials

Available with the online version of this article published in Contributions to Mineralogy and Petrology (doi:10.1007/s00410-012-0775-z)

Online Resource 1 Electron microprobe calibration setup for serpentine analysis

Online Resource 2 All electron microprobe analyses of serpentine in our Oman serpentinites and antigorite standard BM66586. Analyses have been corrected based on repeat analyses of the antigorite standard, as in Online Resource 1. Points close to the edge of serpentine grains that appear to include mixed analyses with Fe-oxides or carbonates, points with totals <73%, and points with >0.3 Al atoms per formula unit (most likely chlorite) have been excluded.

Table 1 Bulk rock mineralogy and major element chemistry of Oman serpentinite samples

Sample	OM07-05	OM07-17	OM07-27	OM07-28A	OM07-34A	OM07-39	OM07-53	OM07-54	OM08-01
UTM[a] E	451254	586007	598089	598021	608365	634006	640914	646240	608957
UTM N	2652948	2523245	2555805	2555719	2526870	2571609	2533993	2537136	2529931
Mineralogy[b]									
serp	**X**	**X**	x	**X**	tr	x	**X**	**X**	**X**
mgs				**X**		**X**			
dol	**X**	**X**	**X**	**X**	**X**	x	**X**	**X**	tr
cc	x	**X**	x		**X**	x	x	tr	**X**
other trace minerals:	ank	Cr-sp, Fe-ox, AgS, hal	Cr-sp, chl, di, hem, bar	Cr-sp, tc, di	bar, gyp	Cr-sp	chl, di	hem, chl, mgt, Cr-sp, en, AgS	cr-sp, qtz, chl
wt%									
SiO2	19.78	10.22	7.82	-	2.25	1.09	20.30	21.46	28.10
TiO2	0.01	0.03	0.04	-	0.02	0.00	0.20	0.13	0.02
Al2O3	0.34	0.48	1.12	-	0.39	0.01	3.22	2.27	0.80
FeO*	3.37	1.79	2.12	-	0.16	0.27	4.67	1.91	4.10
MnO	0.08	0.02	0.04	-	0.00	0.01	0.09	0.08	0.07
MgO	28.25	18.49	21.78	-	3.11	44.94	23.00	29.30	26.94
CaO	17.54	31.09	26.45	-	52.28	2.97	20.23	15.00	16.45
Na2O	0.02	0.07	0.01	-	0.02	0.01	0.04	0.02	0.04
K2O	0.00	0.06	0.07	-	0.01	0.00	0.05	0.00	0.02
P2O5	0.01	0.01	0.01	-	0.01	0.00	0.01	0.01	0.01
LOI (%)	29.92	37.14	39.38	-	41.71	48.68	27.51	29.02	22.84
Total	99.32	99.41	98.84	-	99.96	97.99	99.34	99.19	99.38
Mg #	0.94	0.95	0.95		0.97	1.00	0.90	0.96	0.92

Table 1 (*Continued*)

Sample	OM08-201	OM08-206A	OM08-206D	OM08-206I	OM09-13	OM09-121	OM09-122	OM09-129	OM09-130
UTM E	600090	596370	596370	596370	621536	487520	487520	487520	487520
UTM N	2528421	2531270	2531270	2531270	2585653	2576000	2576000	2576000	2576000
Mineralogy									
serp	X	X	X	X	X	X	X	X	X
mgs							x	x	
dol	x					X	X		
cc	X	X	X			x	tr	X	X
qtz		x	x						
ol				X					
other trace minerals:	Cr-sp, hem, pyr	di, Fe-ox, Cr-sp	di, Fe-ox, Cr-sp, en	mgt, Cr-sp, chl	Cr-sp, goeth, chl, bar	mgt, Cr-sp, di	hem	mgt	Cr-sp, hem, mgt
wt%									
SiO2	19.36	27.80	25.29	37.77	40.04	22.93	18.12	27.49	23.59
TiO2	0.01	0.02	0.01	0.01	0.03	0.01	0.01	0.01	0.01
Al2O3	0.95	0.54	0.75	1.65	1.47	0.41	0.33	0.36	0.36
FeO*	3.12	6.29	6.47	8.09	6.80	4.62	1.68	5.90	5.13
MnO	0.06	0.09	0.11	0.10	0.08	0.05	0.04	0.10	0.08
MgO	18.95	23.96	17.37	36.10	38.12	28.97	27.02	30.17	23.67
CaO	28.35	17.13	24.17	0.21	0.38	15.62	20.12	12.51	21.06
Na2O	0.15	0.06	0.04	0.06	0.03	0.05	0.33	0.07	0.14
K2O	0.01	0.03	0.02	0.00	0.00	0.01	0.04	0.00	0.01
P2O5	0.01	0.01	0.02	0.01	0.01	0.02	0.01	0.00	0.01
LOI (%)	29.70	23.27	25.87	13.94	13.26	26.70	32.50	22.74	25.58
Total	100.70	99.20	100.11	97.95	100.21	99.39	100.21	99.35	99.65
Mg #	0.92	0.87	0.83	0.89	0.91	0.92	0.97	0.90	0.89

[a] UTM coordinates are in zone 40Q.

[b] serp=serpentine, mgs=magnesite, dol=dolomite, cc=calcite, qtz=quartz, ol=olivine, Cr-sp=chromian spinel, chl=chlorite, tc=talc, hem=hematite, mgt=magnetite, goeth=goethite, Fe-ox=undetermined Fe-oxides, di=diopside, en=enstatite, ank=ankerite, hal=halite, bar=barite, gyp=gypsum. Large X indicates major phase, smaller x indicates minor phase, and 'tr' indicates only trace amounts of phase are present.

Table 2 Select electron microprobe analyses of quartz in Oman serpentinites compared to thin section slide glass

Sample	Slide glass	OM08-206A		OM08-206D		2σ
wt%						
SiO2	72.2	96.6	99.7	97.9	97.4	0.4
TiO2	--	0.00	0.00	0.00	0.01	0.06
Al2O3	1.20	0.02	0.00	0.02	0.00	0.02
FeO*	0.03	3.1	0.3	1.6	2.1	0.1
MgO	4.3	0.1	0.0	0.1	0.1	0.2
MnO	--	0.00	0.03	0.02	0.00	0.03
CaO	6.4	0.0	0.0	0.0	0.0	0.4
Na2O	14.30	0.02	0.01	0.04	0.01	0.09
K2O	1.20	0.03	0.02	0.01	0.01	0.01
Cr2O3	--	0.13	0.00	0.00	0.02	0.04
NiO	--	0.01	0.02	0.02	0.01	0.06
SO3	0.03	--	--	--	--	
Total	99.7	100.0	100.2	99.8	99.7	

Table 3 Serpentine analyses, averaged by sample

Sample #	OM07-05	OM07-17	OM07-27	OM07-28A	OM07-34A	OM07-39	OM07-53	OM07-54	OM08-01
n	6	111	19	2	3	6	2	59	49
wt%									
SiO2	42.0	42.0	42.1	44.9	47.7	42.4	40.3	42.0	40.7
TiO2	0.00	0.01	0.01	0.01	0.06	0.01	0.01	0.05	0.01
Al2O3	0.42	0.20	0.39	0.07	2.96	0.07	4.51	1.62	0.62
FeO	3.94	6.51	4.47	5.32	0.95	2.26	5.07	2.72	6.04
MnO	0.06	0.08	0.05	0.02	0.04	0.04	0.10	0.05	0.10
MgO	41.0	39.4	41.0	38.6	36.7	40.0	37.1	40.6	39.7
CaO	0.04	0.11	0.09	0.12	0.71	0.16	0.14	0.11	0.19
Cr2O3	0.05	0.02	0.01	0.01	0.04	0.01	0.03	0.09	0.13
NiO	0.09	0.03	0.15	0.53	0.03	0.08	0.22	0.13	0.26
Total	84.6	85.5	85.1	86.7	86.5	82.0	84.6	84.3	84.7
Mg#	0.95	0.92	0.94	0.93	0.99	0.97	0.93	0.96	0.92

Sample #	OM08-201	OM08-206A	OM08-206D	OM08-206I	OM09-13	OM09-121	OM09-122	OM09-129	OM09-130
n	101	27	69	25	4	29	17	13	40
wt%									
SiO2	40.3	40.8	42.1	41.2	42.2	43.2	43.1	41.1	42.1
TiO2	0.01	0.01	0.01	0.01	0.03	0.01	0.00	0.01	0.01
Al2O3	0.71	0.13	0.47	0.99	1.44	0.34	0.35	0.01	0.07
FeO*	5.85	7.65	7.42	4.77	4.11	2.19	2.40	3.69	3.89
MnO	0.08	0.08	0.05	0.05	0.05	N.A.	0.07	N.A.	0.05
MgO	39.8	38.1	37.1	40.7	40.4	42.1	42.1	42.2	41.7
CaO	0.06	0.20	0.26	0.05	0.04	0.12	0.03	0.06	0.05
Cr2O3	0.03	0.04	0.12	0.02	0.25	0.15	0.03	0.01	0.02
NiO	0.27	0.33	0.39	0.34	0.23	0.17	0.18	0.18	0.23
Total	84.2	84.0	85.0	84.5	85.6	85.1	85.1	84.0	85.0
Mg#	0.92	0.90	0.90	0.94	0.95	0.97	0.97	0.95	0.95

Table 4 Clumped isotope measurements of carbonate veins from Oman serpentinites

Sample	Min.	Digestion T, °C	Corrected $\Delta47$[a]	T, °C[b]	$\delta^{13}C$	$\delta^{18}O$ CO_2 VSMOW	$\delta^{18}O$ carbonate VSMOW[c]	$\delta^{18}O$ water VSMOW[d]
OM08-206D	cc	90	0.600 ± 0.005	38 ± 2	-9.003 ± 0.003	37.286 ± 0.005	28.874 ± 0.002	2.8 ± 0.3
OM08-206D	cc	90	0.635 ± 0.014	28 ± 4	-8.986 ± 0.002	37.285 ± 0.004	28.874 ± 0.001	0.8 ± 0.8
OM10-34B	cc	90	0.598 ± 0.010	39 ± 3	-9.090 ± 0.002	36.313 ± 0.005	27.909 ± 0.002	2.0 ± 0.6
OM10-34B	cc	90	0.604 ± 0.007	37 ± 2	-8.926 ± 0.004	37.840 ± 0.011	27.898 ± 0.002	1.6 ± 0.4
OM09-130	cc	25	0.594 ± 0.014	40 ± 5	-11.409 ± .001	36.897 ± 0.002	26.376 ± 0.002	0.7 ± 0.8
OM08-01	cc	50	0.625 ± 0.005	31 ± 2	-10.230 ± .001	37.840 ± 0.004	28.274 ± 0.004	0.7 ± 0.3
OM07-54	dol	90	0.630 ± 0.008	29 ± 2	-2.019 ± .001	48.166 ± 0.002	38.831 ± 0.002	8.0 ± 0.4
OM07-17	dol	50	0.587 ± 0.006	43 ± 2	0.343 ± .001	43.704 ± 0.002	33.203 ± 0.002	5.1 ± 0.3
OM08-01	dol	50	0.588 ± 0.010	42 ± 3	-10.173 ± .001	37.789 ± 0.002	27.348 ± 0.002	-0.7 ± 0.6
OM07-61a	dol	50	0.638 ± 0.009	27 ± 3	-4.933 ± .001	45.923 ± 0.005	35.400 ± 0.005	4.3 ± 0.5
OM07-61a	mgs	80	0.643 ± 0.008	26 ± 2	-8.666 ± .001	43.225 ± 0.001	33.146 ± 0.001	-4.9 ± 0.6
OM07-07	mgs	80	0.652 ± 0.007	23 ± 2	-9.944 ± .001	40.832 ± 0.001	30.776 ± 0.003	-7.7 ± 0.6

± uncertainties represent one standard error of the mean of all acquisitions for a sample

[a] $\Delta47$ corrected for mass spectrometer nonlinearity by normalization based on heated gas measurements (Huntington et al. 2009), and for fractionation during acid digestion at temperatures above 25°C (Passey et al. 2010). For these measurements, the linearity correction was given by:
$\Delta47$(corrected for linearity) = -0.8453/ -0.779*($\Delta47_{measured}$-(0.0076*δ47+ -0.779)) for the first four rows and
$\Delta47$(corrected for linearity) = -0.8453/ -0.815*($\Delta47_{measured}$-(0.0077*δ47+ -0.815)) for the remaining rows.

[b] Calculated from a polynomial fit to inorganic calcite and dolomite experimental calibration data (Ghosh et al. 2006; M. Bonifacie, in prep.)

[c] CO_2-carbonate $\delta^{18}O$ fractionation factors for phosphoric digestion from Das Sharma et al. (2002):

Calcite: $10^3 \ln\alpha_T = 5.608 * 10^5/T^2 + 3.89$,
Dolomite: $10^3 \ln\alpha_T = 5.858 * 10^5/T^2 + 5.51$,
Magnesite: $10^3 \ln\alpha_T = 6.845 * 10^5/T^2 + 4.22$,

where $10^3 \ln\alpha_T$ refers to fractionation at digestion temperatures T in Kelvin.

[d] Carbonate-water $\delta^{18}O$ fractionation factors for calcite from Kim and O'Neil (1997), for dolomite from Vasconcelos et al. (2005), and for magnesite from reduced partition coefficients from Schauble et al. (2006) and Rosenbaum (1997)

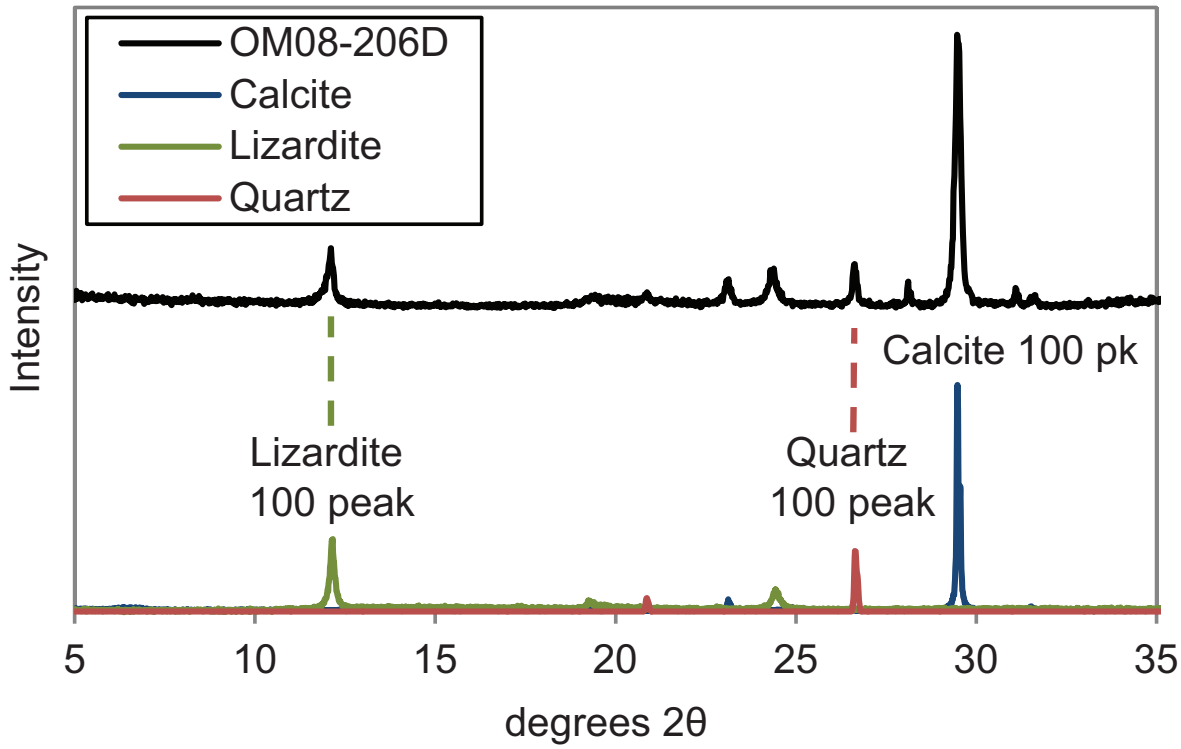

Fig. 1 XRD spectrum of quartz-bearing carbonate-veined serpentinized peridotite sample OM08-206D compared to XRD spectra for lizardite (RRUFFID=R060006), calcite (RRUFFID=R040070), and quartz (RRUFFID=R040031) from the RRUFF database, (Downs 2006), Cu-Kα X-ray radiation. Axes are intensity (counts) vs. degrees 2-theta

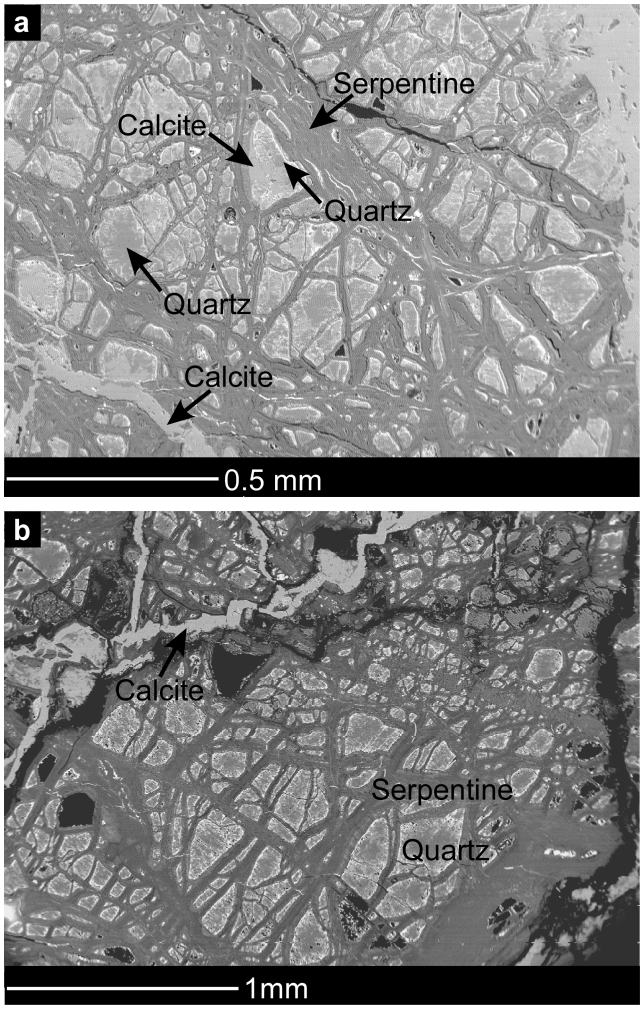

Fig. 2 Back-scattered electron image showing serpentine (dark grey), coexisting with quartz (light grey "islands") in (a) sample OM08-206A and (b) OM08-206D. The lighter grey veins in both images are calcite. Calcite is also found along with quartz in some of the cores of the mesh texture in OM08-206A

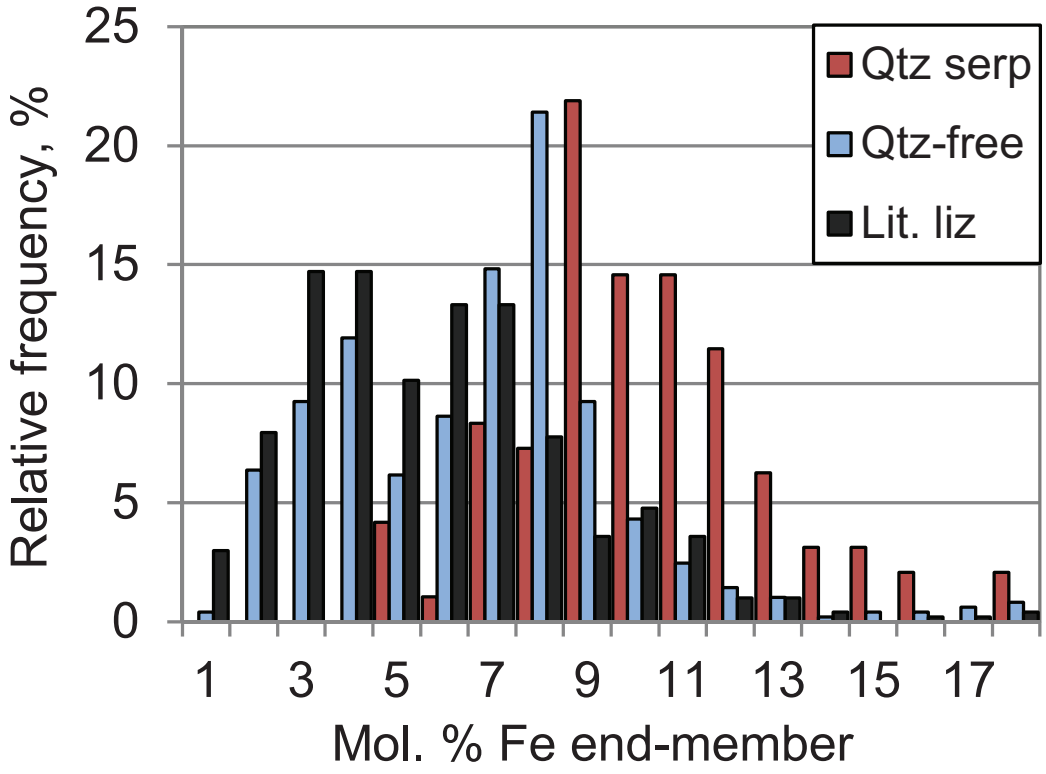

Fig. 3 Frequency histogram of total mol% Fe/[Fe + Mg] contents in serpentine from our quartz-bearing serpentinite (red, n= 96 analyses), our quartz-free carbonated serpentinite (blue, n=486 analyses), and lizardites from the literature (black, n=503 analyses) (Evans et al. 2009)

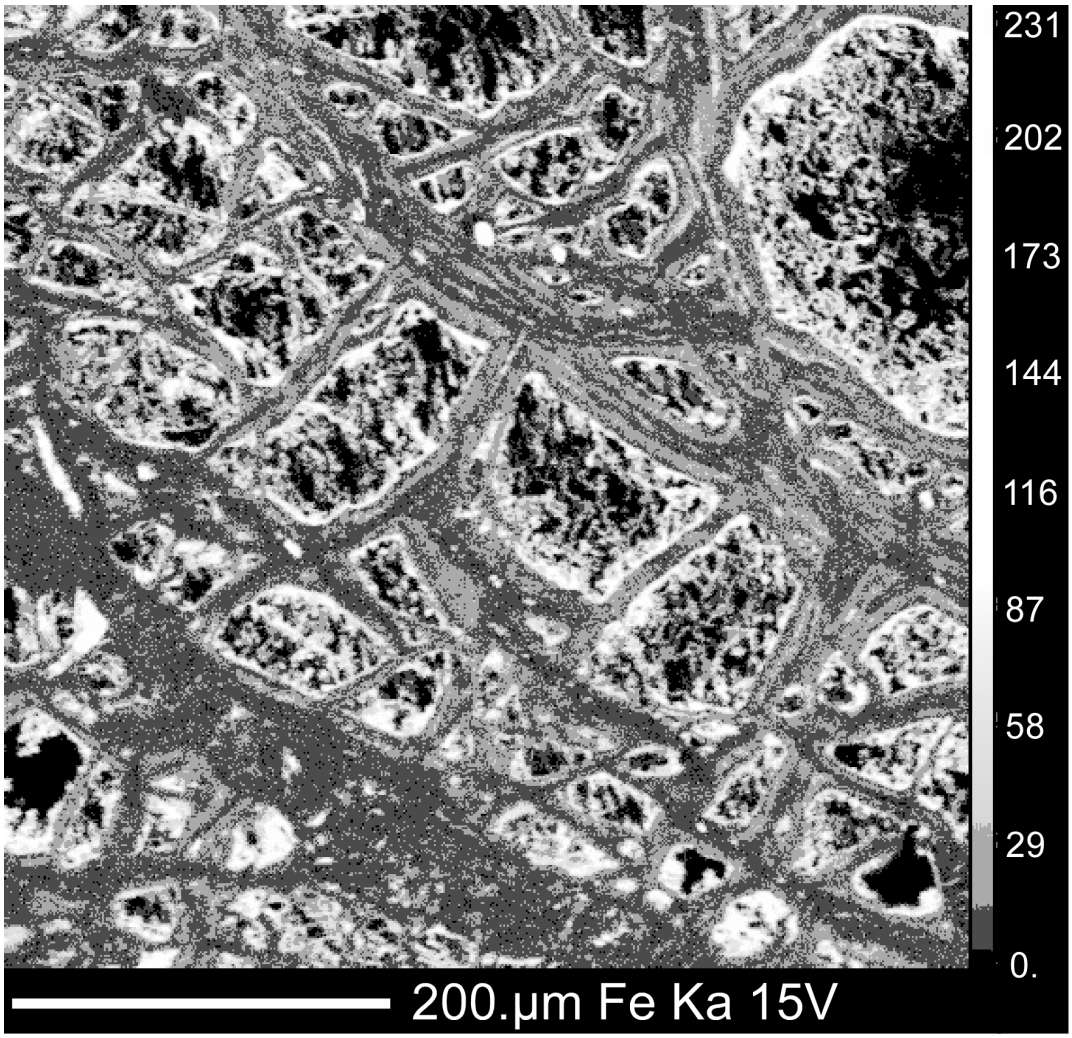

Fig. 4 WDS element map of Fe content in coexisting serpentine + quartz in sample OM08-206D. Strands of Fe-rich material (very light grey and white) are distributed within the quartz regions (black), concentrated at the edge of the quartz "mesh centers." Although the serpentine (grey) throughout these samples containing coexisting serpentine + quartz is already more Fe-rich than serpentine in other samples of carbonated serpentinites from Oman, the mesh serpentine surrounding these quartz regions forms even more Fe-rich rims (light grey) around the quartz mesh centers

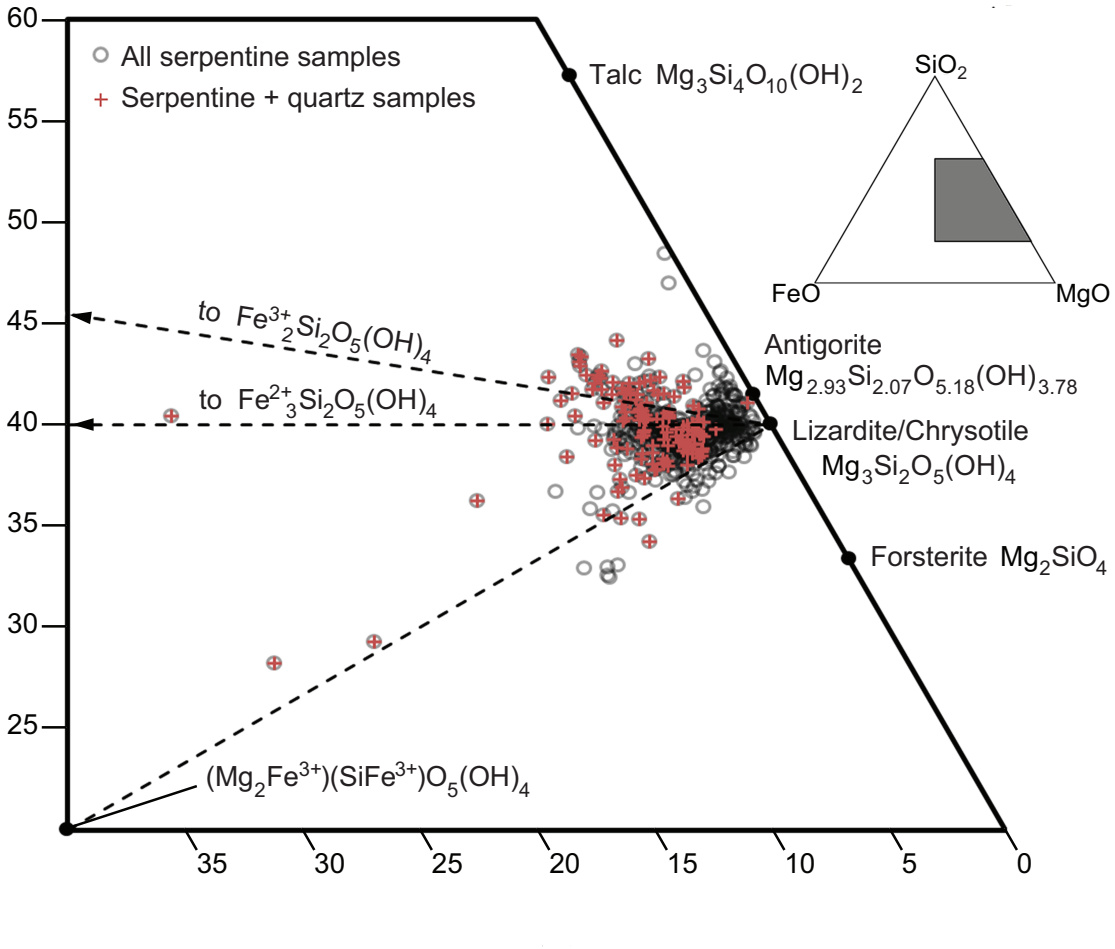

Fig. 5 Projection of all serpentine data and compositions of forsterite, talc, and serpentine end-members onto a ternary MgO-SiO_2-FeO diagram (molar proportions). Red crosses represent serpentine from samples that contain coexisting serpentine and quartz (OM08-206A, OM08-206D, OM08-01). The size of the circles representing these data approximates the uncertainty in these measurements, given as the 2σ of repeated measurements of antigorite standard BM66586 analyzed as unknown using the same calibrations used to analyze serpentine in our samples.

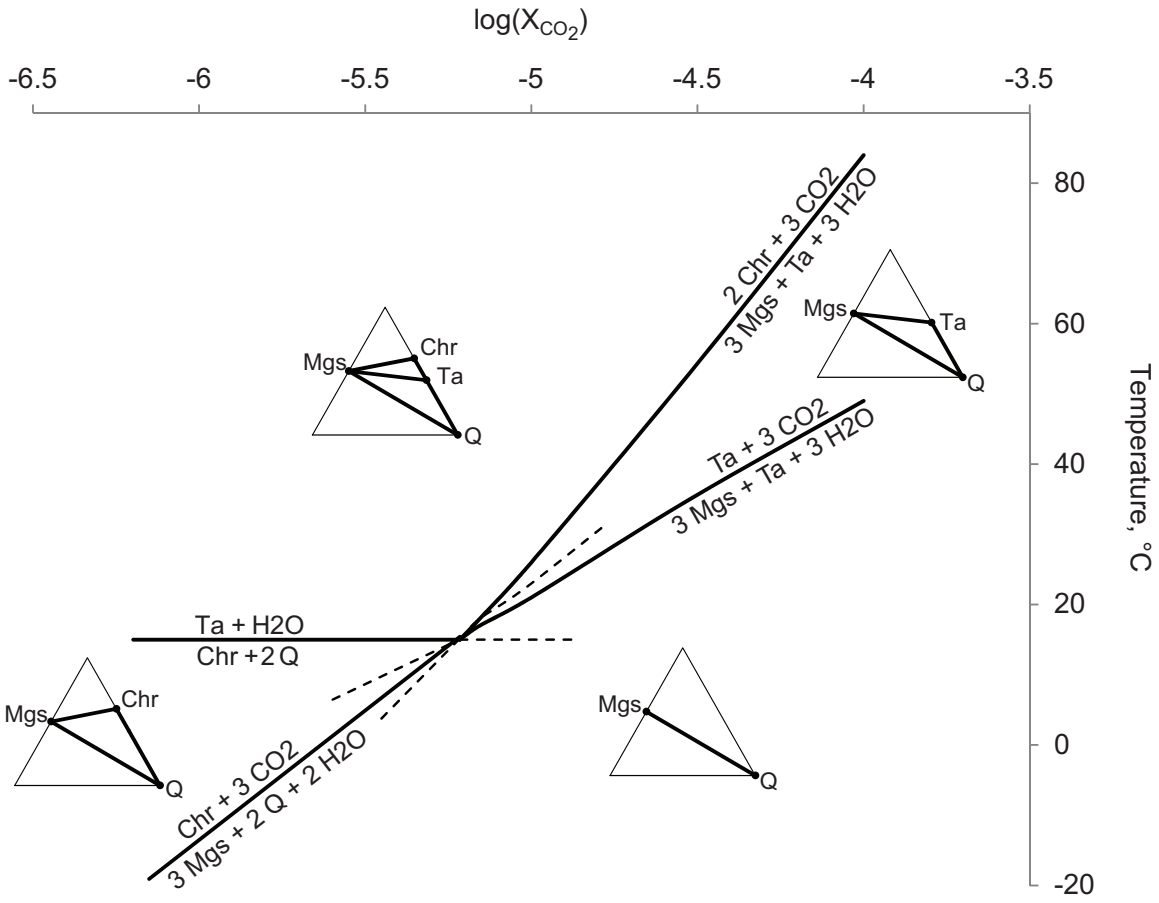

Fig. 6 T-X diagram of the phase relations between pure (activity =1) Mg end-member magnesite (Mgs), chrysotile (Chr), talc (Ta), and quartz (Q) at 5 bar

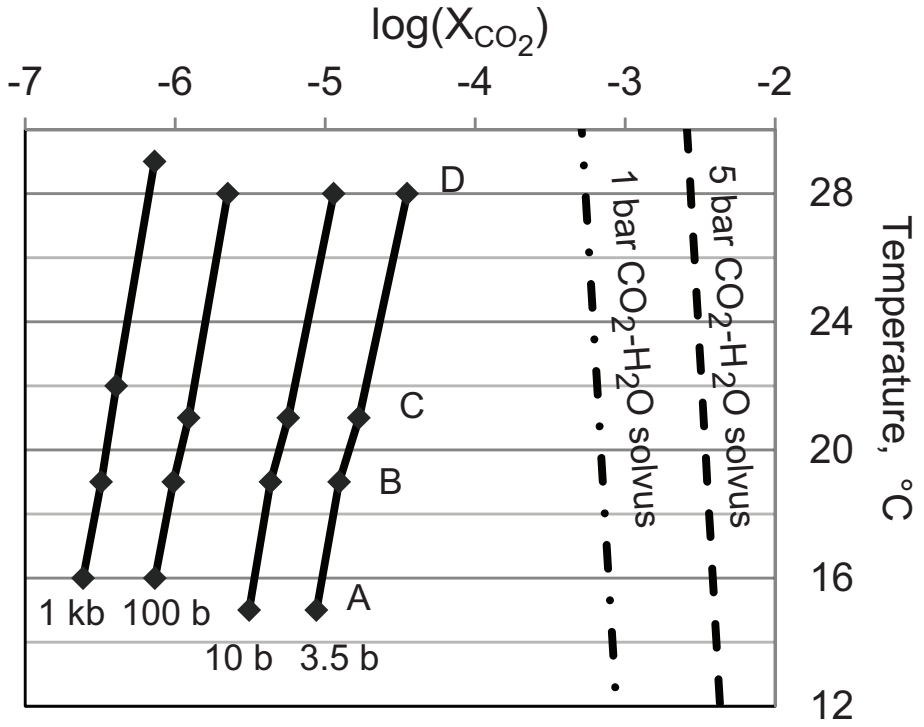

Fig. 7 Location of the invariant point for magnesite-chrysotile-talc-quartz calculated in THERMOCALC at pressures of 3.5, 10, 100 and 1000 bars, for chrysotile and talc activities corresponding to Fe-contents ranging from pure Mg end-members to our most Fe-rich serpentines (A through D). Talc activity was calculated from the predicted Mg# of talc coexisting with serpentine of a given Mg# based on the data of Trommsdorff and Evans (1972). (A) unit activities for all mineral phases (pure Mg end-members); (B) chrysotile activity = 0.71, talc activity = 0.86, corresponds to the average composition of serpentine coexisting with quartz; (C) chrysotile activity = 0.51, talc activity = 0.72, corresponds to the twenty most Fe-rich analyses of serpentine; D) chrysotile activity = 0.24, talc activity = 0.47, corresponds to the three most Fe-rich analysis of serpentine. The water-rich limb of the CO_2-H_2O solvus, as calculated by Duan and Sun (2003) is plotted as dashed lines, showing that even at the low pressures considered (>3.5 bar), unmixing should not occur in the H_2O-rich fluids in equilibrium with serpentine + quartz

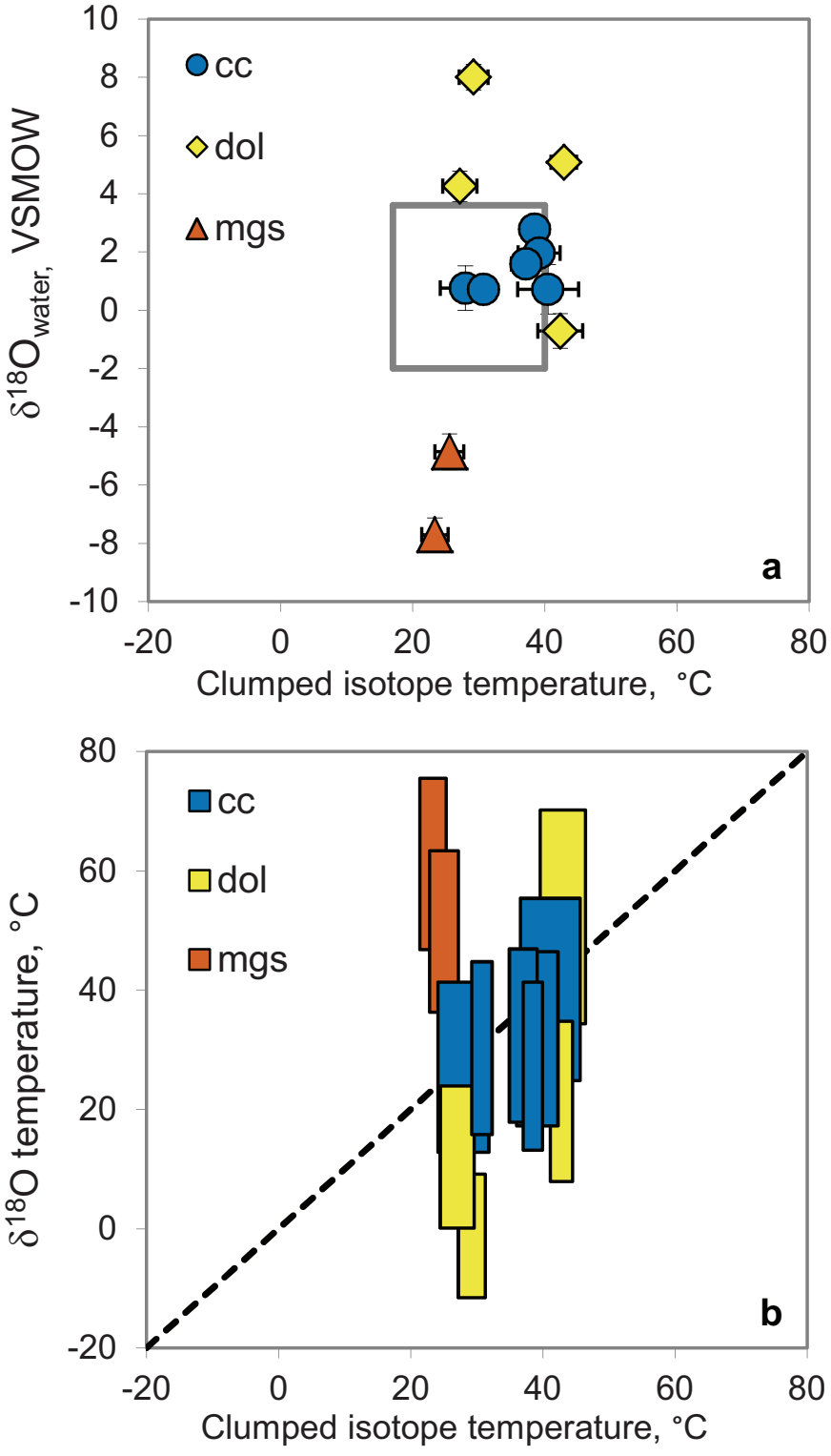
cc
dol
mgs
a
$\delta^{18}O_{water,}$ VSMOW
Clumped isotope temperature, °C
b
$\delta^{18}O$ temperature, °C
Clumped isotope temperature, °C

Fig. 8 (a) Calculated $\delta^{18}O$ of water from which carbonates precipitated, versus clumped isotope temperatures of carbonate veins; blue circles = calcite, yellow diamonds = dolomite, vermillion triangles = magnesite. Dashed and dotted lines connect different minerals from the same sample. Error bars represent one standard error of the mean. The grey box showing the range of temperatures and $\delta^{18}O$ measured in modern groundwater in Oman (Neal and Stanger 1985; Clark et al. 1992; Matter 2005; our unpublished data), is consistent with most clumped isotope temperatures and calculated fluid oxygen isotope compositions. (b) Temperatures calculated by conventional oxygen isotope thermometry, representing a range of $\delta^{18}O_{water}$ from -2.1 to +3.6, versus clumped isotope temperatures; blue boxes = calcite, yellow boxes = dolomite, vermillion boxes = magnesite. Box width represents two standard errors of the mean of clumped isotope temperature

Chapter 3. Assessment of the clumped isotope paleothermometer for magnesite

Abstract

Clumped isotope thermometry provides a method of determining the temperature of formation of carbonate minerals independent of the isotopic composition of the fluid from which they formed, making it a valuable tool for studies of paleoclimate, diagenesis, and low-temperature metamorphism, among other applications. Carbonate clumped isotope geochemistry has been studied primarily in calcite, with a limited number of studies in dolomite and siderite. Here we test the reliability of the carbonate clumped isotope paleothermometer for natural and synthetic magnesite samples formed at known temperature ranging from ~5-600°C. A challenge of analyzing the clumped isotopic signature of magnesite is the relatively long reaction times required for dissolution of magnesite in phosphoric acid. We find that complete digestion of magnesite requires about 17 hrs at 90°C, making "online" reaction, collection, and measurement of CO_2 impractical, whereas "offline" reaction in sealed vessels requires additional corrections to be made to clumped and bulk isotopic data and introduces significant scatter in the data. With adequate measurement of carbonate standards and appropriate corrections, clumped isotopic data for magnesite formed at temperatures below a blocking temperature of ~300°C are in good agreement with other calibration data on calcite and dolomite measured at the California Institute of Technology. At temperatures above 25°C, those calibration data agree with theoretical predictions and calcite calibration data measured at Harvard University but exhibit higher $\Delta 47$ values at low temperatures.

Introduction

Carbonate clumped isotope thermometry is a relatively new paleothermometer based on the tendency of ^{13}C and ^{18}O to preferentially bond to each other with decreasing temperature. This "clumping" of heavy isotopes is quantified in terms of Δ47, a measure of the excess abundance of mass-47 CO_2 (predominantly the doubly-substituted isotopologue $^{13}C^{18}O^{16}O$) evolved from acid dissolution of solid carbonate relative the abundance expected for a stochastic distribution in which the carbon and oxygen isotopes are randomly distributed among all isotopologues:

$$\Delta 47 = \left(\frac{R_{47}}{R_{47}^{*}} - 1 \right) \times 1000 \quad (‰) \qquad (1)$$

where R47 is the measured ratio of mass-47 CO_2 to mass 44 CO_2 and R47* is same ratio for the stochastic distribution (Wang et al. 2004; Ghosh et al. 2006). The temperature dependence of Δ47 has been empirically calibrated for synthetic and natural inorganic and biogenic calcite (Ghosh et al. 2006; Ghosh et al. 2007; Came et al. 2007; Dennis and Schrag 2010; Tripati et al. 2010; Thiagarajan et al. 2011; Henkes et al. 2013; Grauel et al. 2013), natural and synthetic dolomite (Ferry et al. 2011; M. Bonifacie, in prep.), and synthetic siderite (Fernandez et al. 2013), and predicted from first-principles theoretical models for calcite, aragonite, dolomite, magnesite, and witherite (Schauble et al. 2006; Guo et al. 2009). All of these calibration data and theoretical models agree within error for temperatures above ~20°C, but at lower temperatures, synthetic and biogenic calcite data from Caltech (Ghosh et al. 2006; Ghosh et al. 2007; Came et al. 2007; Tripati et al. 2010; Thiagarajan et al. 2011) and the ETH Zurich (Grauel et al. 2013) exhibit higher

Δ47 values than calcite samples of similar temperature measured at Harvard University (Dennis and Schrag 2010) and Johns Hopkins University (Henkes et al. 2013).

Conventional oxygen isotope thermometry is based on the temperature dependence of heterogeneous isotope exchange reactions, e.g., $CaC^{16}O_3 + H_2{}^{18}O \leftrightarrow CaC^{18}O^{16}O_2 + H_2{}^{16}O$, which requires knowledge of the oxygen isotopic composition of both the mineral and fluid phases. Clumped isotope thermometry is based on homogenous isotopic exchange reactions between isotopologues of a single phase, e.g., $Ca^{13}C^{16}O_3 + Ca^{12}C^{18}O^{16}O_2 \leftrightarrow Ca^{13}C^{18}O^{16}O_2 + Ca^{12}C^{16}O_3$, which are independent of the bulk isotopic composition of the mineral and the fluid from which it has precipitated. This feature of the clumped isotope paleothermometer makes it particularly appealing in geologic settings where there are limited constraints on the oxygen isotope composition of water and, furthermore, allows the $\delta^{18}O$ of the precipitating fluid to be calculated by applying conventional equilibrium carbonate-water oxygen isotope fractionations at clumped isotope-derived temperatures. Thus, the clumped isotope thermometer is a potentially valuable tool for constraining temperatures and the nature of precipitating fluids for studies of ancient marine environments, terrestrial paleoclimate, diagenesis, low-temperature metamorphism, extraterrestrial environments, and other environments. Application to higher temperature problems is limited to some extent by the $1/T^2$ dependence of the clumped isotope thermometer, resulting in increased relative temperature uncertainties with increasing temperatures, and in a more absolute sense by bond reordering due to diffusion at elevated temperatures, which results in apparent equilibrium temperatures of ~150-250°C for slowly cooled

calcite marbles and carbonatites (Ghosh et al. 2006; Dennis and Schrag 2010; Passey and Henkes 2012) and up to ~300°C for dolomite marbles (Ferry et al. 2011).

Magnesite occurs as strata-bound sedimentary deposits or ultramafic-hosted deposits, the origins of which remain uncertain (Pohl and Siegl 1986; Abu Jaber and Kimberley 1992). Temperatures of magnesite formation are often in question, as it is debated whether some ultramafic-hosted deposits formed in hydrothermal versus weathering environments. Low temperatures (~20-60°C) are calculated for oxygen isotope exchange between magnesite and observed surface water compositions, and these are consistent with ^{14}C ages and low temperature mineral parageneses (e.g., Kelemen & Matter 2008; Kelemen et al. 2011; Streit et al. 2012), whereas direct precipitation of magnesite at low temperatures has only been achieved in a limited number of laboratory experiments (Deelman 1999; dos Anjos et al. 2011). Instead, most experiments on solutions super-saturated in magnesite yield hydrated magnesium carbonates (e.g., Hänchen et al. 2008).

It is unclear whether large strata-bound magnesite deposits, which were common during the Precambrian but lack true analogs today, formed by direct precipitation in a marine environment, precipitation from hydrothermal-magmatic fluids, or metasomatic replacement of carbonate (Pohl and Siegl 1986; Aharon 1988; Frank and Fielding 2003). Magnesite has also been detected in extraterrestrial environments, including carbonaceous chondrites, the Martian meteor ALH84001, and the planet Mars itself (Endress and Bischoff 1996; Lee et al. 2012; Eiler et al. 2002; Ehlmann et al. 2008).

In most of the settings in which magnesite is found, formation temperatures have been debated and constraints on fluid isotopic compositions are lacking, making clumped

isotope thermometry an attractive method to address the continuing uncertainties. Clumped isotope thermometry has been applied to Fe-rich magnesites in CI chondrites and ALH84001 (Guo 2008; Halevy et al. 2011) and to ultramafic-hosted magnesite veins (Streit et al. 2012), but the reliability of calcite-based empirical calibrations or first-principles theoretical calibrations for magnesite has not been assessed. Here we present clumped isotope measurements natural and synthetic magnesite samples formed at known temperature ranging from ~5-600°C.

Methods

Magnesite samples with known precipitation temperatures

Because direct precipitation of magnesite is difficult to attain in laboratory experiments, most of the synthetic magnesite samples we analyzed were precipitated at temperatures of 120-250°C. Eric Oelkers provided us with four magnesite samples synthesized at the Laboratoire Géosciences Environnement Toulouse (GET) at temperatures of 150, 200, and 250 ± 0.5 °C as described in Saldi et al. (2010) and Saldi et al. (2012). XRD and granulometry measurements performed at GET indicate that these samples are pure magnesite with an average grain size <20μm (Q. Gautier, pers. comm. 2011). Marco Mazzotti of ETH provided us with magnesite sample ht-5 from Hänchen et al. (2008), synthesized at 120°C, the purity of which was verified by Raman spectroscopy and XRD during and immediately following its precipitation. J.C. Deelman provided us with a magnesium carbonate sample precipitated 40°C (Deelman 1999). However, XRD analysis of this sample at Lamont-Doherty Earth Observatory indicated

that minor amounts of calcite and dolomite are also present in this sample and the major peaks occurred at slightly lower 2θ than is expected for end-member magnesite.

Natural magnesite samples were provided to us by Greg Dipple of the University of British Columbia and John Ferry of Johns Hopkins University. The lowest temperature magnesites we analyze are two fine-grained, disaggregated samples from near-surface, modern playa deposits in Atlin, British Columbia. Magnesite precipitation temperatures are inferred to be ~5-10°C based on summer sub-surface temperature profiles (G. Dipple, pers. comm., 2011). It also remains possible that temperatures could be lower—less than 0°C—with magnesite precipitation caused by supersaturation in residual fluids during freezing, though mineral abundance and textural data suggest that is unlikely (G. Dipple, pers. comm., 2011). Because magnesite in these playas co-precipitates with hydromagnesite, these samples were reacted with 10% HCl for 24 hrs to remove hydromagnesite (Power et al. 2009; I. Power, pers. comm. 2012). Greg Dipple also provided us with a quartz-magnesite sample from a listvenite (magnesite + quartz) body in Atlin, British Columbia, described by Hansen et al. (2005), whose temperature of formation was constrained to be in the range of 210-180°C by fluid inclusion analysis (Andrew 1985). Magnesite-bearing metaperidotite from Val d'Efra, Switzerland, formed during Barrovian regional metamorphism at temperatures of 645 ± 10°C (Ferry et al. 2005), offers the possibility of estimating clumped isotope closure temperatures in slowly cooled magnesites.

Sample preparation and phosphoric acid digestion

Samples were analyzed over two sessions, in 2011 and 2012, at California Institute of Technology. Rock samples were crushed using a mortar and pestle and sieved to separate a 150-250 μm grain-size fraction. All samples were rinsed with ethyl alcohol and dried overnight in an oven at 40°C to remove water. To determine an appropriate reaction time for phosphoric acid digestion, OM10-03, a listvenite sample from Oman composed primarily of magnesite (69 wt%), quartz (26 wt%), and iron oxides (3 wt%) with no other carbonate minerals present (only 0.37 wt% CaO by XRF in bulk sample), was reacted with 100% phosphoric acid for up to 18 hours, while pressure increase due to evolved CO_2 was recorded as a measure of reaction progress. Three ~16 g aliquots of OM10-03 were reacted in sealed two-legged reaction vessels maintained at 90 ± 1°C in a water bath for 5.8, 15, and 18 hrs. Reaction vessels were pumped down under vacuum for 2-3 hours, then thermally equilibrated with the water bath for at least 1 hour before reacting. Another aliquot was reacted in a stirred reaction apparatus that allowed continuous cryogenic trapping of evolved CO_2 during phosphoric acid digestion at 90 ± 0.1°C (see extraction methods of Halevy et al. (2011)). Trapped CO_2 was thawed periodically to record the pressure over the course of ~7 hrs. Reaction progress as a function of time is plotted in Figure 1. A reaction time of 17 hours in sealed reaction vessels was chosen for all further magnesite digestions on the basis that over 90% of the magnesite should be reacted by this time.

Although continuous trapping of CO_2 would be preferable, as it minimizes the possibility of bond re-ordering among the CO_2 molecules before measurement, reacting each sample individually for 17 hours in an apparatus connected to a glass vacuum line would be impractical for analyzing a large number of samples. To account for the effects

of an “offline” reaction procedure on the clumped isotope signal, two calcite standards (Carrara marble and TV-01 travertine) were analyzed. “Online” standards were reacted using the automated online extraction system described in Passey et al. (2010), wherein samples are reacted for 20 minutes in a common acid bath maintained at 90°C with continuous cryogenic trapping of evolved CO_2 followed by further cryogenic and GC purification . “Offline” standards and magnesite samples were reacted in sealed vessels for 17 hrs at 90°C as described above. Following offline reaction, evolved CO_2 was cryogenically trapped with liquid nitrogen and purified by passing through a trap immersed in a slush of ethanol and dry ice to remove water as described in Ghosh et al. (2006). This cleaning step was performed three times before CO_2 was collected in glass break seals to be introduced on the heated gas port of the online system for further purification and introduction to the mass spectrometer. For magnesite samples that were potentially contaminated with calcite or dolomite, CO_2 evolved in the first 20 minutes of reaction was discarded. However, sample M223, the low temperature synthetic sample from Deelman (1999), reached almost complete digestion in this initial dissolution step, so it was instead reacted with 10% HCl at room temperature for <1 min, rinsed with DI water then with ethanol, and allowed to dry in an oven at 40°C overnight before being analyzed via the online system. Results from analysis of this sample are reported here, but it is not considered to be a true magnesite sample.

Isotopic analysis

Isotopic data were collected on a Thermo Finnigan MAT 253 gas source mass spectrometer at Caltech, employing standard published configurations and methods

(Huntington et al. 2009; Passey et al. 2010). Heated gas samples were analyzed daily to correct for instrument nonlinearity and "scale compression," allowing data to be normalized to the stochastic reference frame used for the original calibration of the clumped isotope thermometer reported in Ghosh et al. (2006). Following heated gas normalization, the empirically derived acid fractionation correction of +0.081‰ was added to Δ47 data to account for the difference between the phosphoric acid temperature of 90°C used in this study and the phosphoric acid temperature of 25°C used by Ghosh et al. (2006) in the original calibration (Passey et al. 2010).

Results

Effects of offline reaction

Leaking reaction vessels proved to be problematic for many of the offline reactions. The pressure of incondensable gases not frozen down when CO_2 was trapped with liquid nitrogen was taken as an indication of leaking, and pressure on the backspaces of reaction vessels was monitored before and after offline reaction as another possible warning of leaking. CO_2 samples with anomalously high pressures of incondensable gas were discarded, resulting in the loss of 10 out of 45 offline reactions during the 2012 session. Samples with backspace leaks were noted, but not excluded from the dataset.

Isotopic data from calcite standards are reported in Table 1 and plotted in Figure 2. Offline reaction results in significant offsets in Δ47, up to 0.1‰. During the 2011 session, offsets from accepted Δ47 values were negatively correlated with the accepted values for both online and offline standards (Figure 2a). To account for this effect, a correction of $0.154 \times \Delta47_{SA\text{-}HG,acid} - 0.093$, where $\Delta47_{SA\text{-}HG,acid}$ is the heated gas- and hot

acid-corrected Δ47, was added to all carbonate clumped isotope data collected in 2011. Following correction for online offsets, offline standards from 2011 had an average Δ47 offset of 0.035 ± 0.026‰ (1-s.d. uncertainty), and offline standards from 2012 had an average Δ47 offset of 0.083 ± 0.028‰, excluding Carrara standard "Rxn #12," which had a $\delta^{13}C$ value of 2.858‰, dramatically higher than the long-term average value of 2.34 ± 0.02‰ for all Carrara marble standards measured on that mass spectrometer between March 2010 and July 2011. There was no significant difference between the offsets in the Carrara marble and TV-01 calcite standards (homoscedastic t-test p = 0.65 in 2011, 0.63 in 2012). Although there were no notable changes in methodology for offline reactions between the two sessions, there is a significant difference in the offsets for offline standards measured in 2011 and those measured in 2012 (p = 0.02), so magnesite data from each session is treated separately.

Offline reaction also resulted in offsets in bulk isotopic data in calcite standards relative to long-term average values (Figure 3). Bulk isotopic values in calcite standards measured in the 2011 session are within error of their expected values, but $\delta^{13}C$ and $\delta^{18}O$ values in online calcite standards measured in 2012 are lower than expected, by an average of 0.098 ± 0.053‰ and 0.476 ± 0.086‰ (1-s.d. uncertainty), respectively. After correcting for this online offset, the average residuals for the 2012 offline standards were -0.587 ± 0.382‰ for $\delta^{18}O$ and +0.203 ± 0.077‰ for $\delta^{13}C$. The offline standards measured in 2011 had $\delta^{13}C$ values that were more scattered than, but not significantly offset from, the values measured online and had $\delta^{18}O$ values offset from expected values by an average of -0.500 ± 0.110‰. The highest deviations from expected bulk isotopic

values correspond to the highest Δ47 offsets (in the 2012 offline standards), but there is not a strong correlation overall.

Magnesite samples

Isotopic data from magnesite samples formed at known temperatures are reported in Table 2. The *slope* of the Δ47-temperature relationship, plotted in Figure 4, is consistent with previous calibrations of the clumped isotope thermometer (e.g., Ghosh et al. 2006; Guo et al. 2009; Dennis and Schrag 2010; Fernandez et al. 2013; M. Bonifacie in prep.). Following heated gas-, hot acid-, and online standard corrections, Δ47 *values* in magnesite are slightly higher than would be predicted by previous calibrations. However, if we subtract the offsets observed in the "offline" calcite standards, the Δ47 values in synthetic magnesites are lower than predicted by previous calibrations. This is not entirely surprising, as the offsets observed in samples reacted offline result from processes affecting the gas phase in the sealed reaction vessel. The calcite standards react very rapidly with phosphoric acid at 90°C, so the clumped isotopic signature of evolved CO_2 is subject to modification for the almost the entire 17 hour "reaction" period, whereas CO_2 is only gradually evolved over the reaction period for magnesite. Therefore, offsets observed in our offline calcite standards can bee seen as maximum potential offsets for magnesite samples. Actual offsets in Δ47 values due to offline reaction for magnesite are likely to be significantly smaller.

Based on the offline calcite standards, oxygen isotopic values are also expected to be offset due to offline reaction. True oxygen isotope values are likely to fall between the measured value and offset-corrected values that are ~0.5-0.6‰ higher. However, given

that the Δ47 offsets from previous calibrations are much smaller for magnesite samples than for offline calcite standards, the offsets in $\delta^{18}O$ may also be smaller for magnesite.

Discussion

Isotopic offsets in offline extractions

Δ47 offsets due to offline reaction may be much more significant for the calcite standards than for the magnesite samples, because evolved CO_2 was present in higher concentrations for longer periods of time following the rapid dissolution of calcite compared with the gradual dissolution of magnesite. If the offsets are generated by interactions between CO_2 molecules, then we would expect to see substantially higher offsets in the case of calcite because the cumulative number of interactions for rapidly formed CO_2 from calcite would be expected to be about triple that of gradually evolved CO_2 from magnesite. A similar observation could be made if the reactions generating the offsets are mediated by H_2O, since the partial pressure of H_2O will also increase during phosphoric acid digestion of carbonate, e.g., $CaCO_3 + H_3PO_4 \leftrightarrow CaHPO_4 + CO_2 + H_2O$.

One possible explanation for the observed offsets in Δ47 would be partial re-equilibration of the evolved CO_2. Affek (2013) studied the kinetics of water-catalyzed clumped isotopic equilibration, and found a log-linear relationship between equilibration reaction progress and time, i.e.,

$$\ln\left(\frac{\Delta_t - \Delta_{eq}}{\Delta_0 - \Delta_{eq}}\right) = -kt \qquad (2),$$

where Δ_t is the partially equilibrated Δ47 value at time t, Δ_{eq} is the equilibrium Δ47 value for CO_2 at the temperature of equilibration as calculated by Wang et al. (2004), Δ_0

is the initial Δ47 value, and *k* is a positive-valued constant with a values of 0.34 and 0.51/hr with shaking at 25°C and 42°C, respectively. Affek also shows that $\delta^{18}O$ follows the same relationship, with nearly identical slopes. Rearranging equation (2), we would expect offsets, *r*, due to re-equilibration to develop with time as follows:

$$r = \left(\Delta_{std} - \Delta_{eq}\right)(\exp(-kt) - 1) \qquad (3)$$

Thus, after re-equilibration at the same temperature and for the same amount of time, the offset for TV01 relative to Carrara would be:

$$\frac{r_{\text{TV01}}}{r_{\text{Carrara}}} = \frac{0.662 - \Delta_{eq}}{0.352 - \Delta_{eq}} \qquad (4)$$

At the 90°C acid digestion temperature, the equilibrium Δ47 value would be 0.651, so any re-equilibration offset for TV01 would be negative and very small. Even if temperatures in the headspace of the reaction vessel are cooler than 90°C, down to room temperature, we would expect to see at least twice as large an offset for Carrara compared with TV01, whereas we observe offsets that are indistinguishable for Carrara and TV01. Furthermore, the bulk isotopic offsets we observe are not consistent with water-mediated isotopic re-equilibration, which should produce $\delta^{18}O$ offsets correlated with Δ47 offsets and have no effect on bulk $\delta^{13}C$ values. Although the largest Δ47 offsets correspond to the largest offsets in $\delta^{18}O$ in the 2012 offline standards, there is not a strong correlation overall, and these extractions also had significant offsets in $\delta^{13}C$.

Although leaking reaction vessels were enough of a problem that several extractions were discarded, this does not appear to be the source of the offsets in the isotopic data for the offline standards either. If offsets were due to mixing with atmospheric CO_2 leaking into reaction vessels, we would expect increases in $\delta^{18}O$ and

decreases in $\delta^{13}C$, given that the $\delta^{18}O$ and $\delta^{13}C$ of ambient air in Pasadena are about 41‰ and -10‰, respectively (Affek and Eiler 2006), and the Carrara and TV01 standards have average $\delta^{13}C$ values of 2.3 and 2.5‰ and $\delta^{18}O$ values of 37.4 and 30.5‰, respectively. Diffusion of evolved CO_2 out of the reaction space should result in decreases in $\delta^{18}O$ and $\delta^{13}C$ and increases in $\Delta47$ (Saenger et al. 2012). In contrast to either of these processes, we observe decreases in $\delta^{18}O$ and either increases or no significant offset in $\delta^{13}C$, without significant correlations between $\delta^{18}O$, $\delta^{13}C$, and $\Delta47$ for offline standards.

Application of the clumped isotope thermometer to magnesite

Neglecting any corrections for offline reaction, synthetic magnesite samples grown at temperatures of 120-250°C yield $\Delta47$ values that are generally higher than, but within 2-SEM of, values predicted using the theoretical magnesite calibration of Guo et al. (2009) and the empirical dolomite calibration data of Bonifacie et al. (in prep.). $\Delta47$ values from the 210-280°C Atlin listvenite sample were higher than predicted for that temperature range, but it is possible that the quartz fluid inclusion data do not accurately reflect the temperature of magnesite precipitation in those listvenites (Andrew 1985). The low temperature playa magnesite samples yield $\Delta47$ values that diverge significantly from the theoretical calibration of Guo et al. (2009) and instead agree fairly well with low-temperature calcite calibrations developed at Caltech (Ghosh et al. 2006; Ghosh et al. 2007; Came et al. 2007; Tripati et al. 2010; Thiagarajan et al. 2011), falling within 2-SEM of the calibration of Ghosh et al. (2006).

If the playa magnesite crystallized from supersaturated solutions formed during freezing of water, as suggested above, then the data for this sample could fall close to the

Guo et al. theoretical magnesite calibration. Given the measured Δ47, the Guo et al. calibration would predict a temperature of about -15°C, close to the average temperature in Atlin in January (Power et al. 2009). In the case of cryogenic precipitation, the agreement with the Guo et al. theoretical calibration is likely to reflect kinetic depletions in Δ47 rather than a systematic difference between calcite and magnesite clumped isotope equilibrium at low temperature, as synthetic cryogenic calcites exhibit kinetic enrichments in $\delta^{18}O$ and $\delta^{13}C$ accompanied by depletions in Δ47 (Clark and Lauriol 1992; Guo 2008). Stable isotope results in Atlin playa magnesite do not appear to indicate cryogenic precipitation. $\delta^{18}O$ values in playa magnesite are ~16‰ (VSMOW), and summertime $\delta^{18}O$ values in groundwater at Atlin include values ranging from -21 to -18‰ (VSMOW) (G. Dipple, pers. comm., 2011). Given available magnesite-water $\delta^{18}O$ fractionation factors (Aharon 1988; Schauble et al. 2006; Chacko and Deines 2008), the measured $\delta^{18}O$ values in playa magnesite are already lower than would be expected for equilibration with observed groundwater at temperatures <10°C. In contrast, cryogenic carbonate precipitation has been shown to produce kinetic isotope *enrichments* in carbonate $\delta^{18}O$ (Clark and Lauriol 1992). However, *wintertime* $\delta^{18}O$ values in groundwater at Atlin might be expected to be significantly lower than summertime values due to preferential incorporation of ^{18}O into ice (O'Neil 1968), in which case the low $\delta^{18}O$ values in playa magnesite may still represent isotopic equilibrium or even enrichment. These questions highlight the importance of seasonality in terrestrial carbonate systems and potential pitfalls of the interpretation of conventional and clumped stable isotopes in terrestrial paleoenvironments, but we nonetheless tentatively favor an interpretation based

on summertime carbonate precipitation, leading to the conclusion that inter-laboratory differences in calibration of the clumped isotope thermometer are not material-specific.

The root mean square deviation, calculated relative to the theoretical calibration of Guo et al. (2009) for averaged synthetic magnesite samples, and calculated relative to the original calcite calibration of Ghosh et al. (2006) for averaged playa magnesite samples, is 0.017‰ without any offline corrections. This is reduced to 0.009‰ if offline standard offsets divided by a factor of 4.9 (chosen to minimize RMSD) are subtracted from the Δ47 data.

The metaperidotite sample from Val d'Efra records a Δ47 value of 0.310‰, corresponding to a temperature of 293°C (Guo et al. 2009), much lower than the 645°C experienced by the rock during regional metamorphism (Ferry et al. 2005). This "closure temperature" of ~300°C is similar to closure temperatures inferred from contact metamorphosed dolomite marbles (Ferry et al. 2011), carbonatites (Dennis and Schrag 2010), and slowly cooled marbles (Ghosh et al. 2006). Depending on the cooling rate following crystallization, clumped isotope thermometry can be expected record the temperature of magnesite precipitation (or recrystallization) up to ~300°C, with the theoretical calibration of Guo et al. (2009) accurately reflecting the relationship between Δ47 and temperature down to ~50°C.

At lower temperatures, Δ47-temperature calibrations for calcite diverge for different laboratories. Henkes et al. (2013) demonstrate that the potential effects of poor interlaboratory calibration and error in the acid temperature correction are not sufficient to explain these discrepancies. They also discuss a kinetic model in which rapidly growing carbonate inherits high clumped isotopic compositions from CO_2 without full

equilibration as CO_3^- but find that this model would require large kinetic fractionations in $\delta^{18}O$ and $\delta^{13}C$ as well, which were not observed in the carbonate from the Caltech calibrations. If the higher Δ47 values of low temperature carbonates in the Caltech calibrations were due to kinetic effects during the precipitation of low-temperature carbonates, then the same extent of kinetic fractionation would need to occur in biogenic calcite across different taxa (Ghosh et al. 2007; Came et al. 2007; Tripati et al. 2010; Thiagarajan et al. 2011; Grauel et al. 2013), in laboratory-grown calcite (Ghosh et al. 2006), and now, in natural playa magnesite. A very simple test of the source of these discrepancies would be to duplicate measurements of the same low-temperature carbonate samples in different laboratories. Although the reasons for these interlaboratory discrepancies remain unclear, they have been reproduced for varied materials and CO_2 extraction procedures, so the Caltech calibration line (Ghosh et al. 2006) can be expected to apply to any low-temperature carbonates (precipitated at T<50°C) analyzed at Caltech.

Conclusions

Sluggish magnesite dissolution in phosphoric acid creates challenges for applying the clumped isotope thermometer to magnesite samples. With complete dissolution requiring reaction times on the order of a day, continuous cryogenic trapping of evolved CO_2 using a specialized reaction apparatus (as in Halevy et al., (2011)) is impractical if a large number of extractions are required. However, phosphoric acid dissolution in sealed reaction vessels increases the risks of bond re-ordering in the evolved CO_2 and of leak development. In spite of these complications, Δ47 values from magnesite samples with

known growth temperatures are in fairly good agreement with values predicted from other calibrations (e.g., Ghosh et al. 2006; Guo et al. 2009; Dennis and Schrag 2010; Fernandez et al. 2013; M. Bonifacie in prep.).

References

Abu Jaber NS, Kimberley MM (1992) Origin of Ultramafic-Hosted Vein Magnesite Deposits. Ore Geology Reviews 7 (3):155-191

Affek HP (2013) Clumped isotopic equilibrium and the rate of isotope exchange between CO2 and water. Am J Sci 313 (4):309-325. doi:10.2475/04.2013.02

Affek HP, Eiler JM (2006) Abundance of mass 47 CO2 in urban air, car exhaust, and human breath. Geochim Cosmochim Acta 70 (1):1-12. doi:http://dx.doi.org/10.1016/j.gca.2005.08.021

Aharon P (1988) A stable-isotope study of magnesites from the Rum Jungle Uranium Field, Australia - Implications for the origin of strata-bound massive magnesites. Chemical Geology 69 (1-2):127-145. doi:10.1016/0009-2541(88)90164-7

Andrew K (1985) Fluid inclusion and chemical studies of gold--quartz veins in the Atlin Camp, Northwestern British Columbia. University of British Columbia, Vancouver, B.C.

Came RE, Eiler JM, Veizer J, Azmy K, Brand U, Weidman CR (2007) Coupling of surface temperatures and atmospheric CO2 concentrations during the Palaeozoic era. Nature 449 (7159):198-U193. doi:10.1038/nature06085

Chacko T, Deines P (2008) Theoretical calculation of oxygen isotope fractionation factors in carbonate systems. Geochim Cosmochim Acta 72:3642-3660

Clark ID, Lauriol B (1992) Kinetic enrichment of stable isotopes in cryogenic calcites. Chemical Geology 102 (1-4):217-228. doi:10.1016/0009-2541(92)90157-z

Deelman JC (1999) Low-temperature nucleation of magnesite and dolomite. Neues Jahrbuch Fur Mineralogie-Monatshefte (7):289-302

Dennis KJ, Schrag DP (2010) Clumped isotope thermometry of carbonatites as an indicator of diagenetic alteration. Geochim Cosmochim Acta 74 (14):4110-4122. doi:10.1016/j.gca.2010.04.005

dos Anjos APA, Sifeddine A, Sanders CJ, Patchineelam SR (2011) Synthesis of magnesite at low temperature. Carbonates and Evaporites 26 (3):213-215

Ehlmann BL, Mustard JF, Murchie SL, Poulet F, Bishop JL, Brown AJ, Calvin WM, Clark RN, Des Marais DJ, Milliken RE, Roach LH, Roush TL, Swayze GA, Wray JJ (2008) Orbital Identification of Carbonate-Bearing Rocks on Mars. Science 322 (5909):1828-1832. doi:10.1126/science.1164759

Eiler JM, Valley JW, Graham CM, Fournelle J (2002) Two populations of carbonate in ALH84001: Geochemical evidence for discrimination and genesis. Geochim Cosmochim Acta 66 (7):1285-1303. doi:10.1016/s0016-7037(01)00847-x

Endress M, Bischoff A (1996) Carbonates in CI chondrites: Clues to parent body evolution. Geochim Cosmochim Acta 60 (3):489-507

Fernandez A, Rosenheim B, Tang J (2013) Calibration of the siderite CO2 clumped isotope paleothermometer. Paper presented at the 3rd International Workshop on Clumped Iosotopes, Harvard University, Cambridge, MA, 10 Jan. 2013

Ferry JM, Passey BH, Vasconcelos C, Eiler JM (2011) Formation of dolomite at 40-80 degrees C in the Latemar carbonate buildup, Dolomites, Italy, from clumped isotope thermometry. Geology 39 (6):571-574. doi:10.1130/g31845.1

Ferry JM, Rumble D, Wing BA, Penniston-Dorland SC (2005) A new interpretation of centimetre-scale variations in the progress of infiltration-driven metamorphic reactions: Case study of carbonated metaperidotite, Val d'Efra, Central Alps, Switzerland. Journal of Petrology 46 (8):1725-1746. doi:10.1093/petrology/egi034

Frank TD, Fielding CR (2003) Marine origin for Precambrian, carbonate-hosted magnesite? Geology 31:1101-1104

Ghosh P, Adkins J, Affek H, Balta B, Guo W, Schauble EA, Schrag D, Eiler JM (2006) 13C–18O bonds in carbonate minerals: A new kind of paleothermometer. Geochim Cosmochim Acta 70:1439-1456

Ghosh P, Eiler J, Campana SE, Feeney RF (2007) Calibration of the carbonate 'clumped isotope' paleothermometer for otoliths. Geochim Cosmochim Acta 71 (11):2736-2744. doi:10.1016/j.gca.2007.03.015

Grauel A-L, Schmid TW, Hu B, Bergami C, Capotondi L, Zhou L, Bernasconi SM (2013) Calibration and application of the 'clumped isotope' thermometer to foraminifera for high-resolution climate reconstructions. Geochim Cosmochim Acta 108:125-140. doi:10.1016/j.gca.2012.12.049

Guo W (2008) Carbonate clumped isotope thermometry : application to carbonaceous chondrites and effects of kinetic isotope fractionation., California Institute of Technology, Pasadena

Guo WF, Mosenfelder JL, Goddard WA, Eiler JM (2009) Isotopic fractionations associated with phosphoric acid digestion of carbonate minerals: Insights from first-principles theoretical modeling and clumped isotope measurements. Geochim Cosmochim Acta 73 (24):7203-7225. doi:10.1016/j.gca.2009.05.071

Halevy I, Fischer WW, Eiler JM (2011) Carbonates in the Martian meteorite Allan Hills 84001 formed at 18 +/- 4 degrees C in a near-surface aqueous environment. Proc Natl Acad Sci U S A 108 (41):16895-16899. doi:10.1073/pnas.1109444108

Hänchen M, Prigiobbe V, Baciocchi R, Mazzotti M (2008) Precipitation in the Mg-carbonate system: Effects of temperature and CO2 pressure. Chem Eng Sci 63:1012-1028

Henkes GA, Passey BH, Wanamaker AD, Jr., Grossman EL, Ambrose WG, Jr., Carroll ML (2013) Carbonate clumped isotope compositions of modern marine mollusk and brachiopod shells. Geochim Cosmochim Acta 106:307-325. doi:10.1016/j.gca.2012.12.020

Huntington KW, Eiler JM, Affek HP, Guo W, Bonifacie M, Yeung LY, Thiagarajan N, Passey B, Tripati A, Daëron M, Came R (2009) Methods and limitations of 'clumped' CO2 isotope (Δ47) analysis by gas-source isotope ratio mass spectrometry. Journal of Mass Spectrometry 44 (9):1318-1329. doi:10.1002/jms.1614

Lee MR, Lindgren P, Sofe MR, Alexander CMOD, Wang J (2012) Extended chronologies of aqueous alteration in the CM2 carbonaceous chondrites: Evidence from carbonates in Queen Alexandra Range 93005. Geochim Cosmochim Acta 92:148-169. doi:10.1016/j.gca.2012.06.005

O'Neil JR (1968) Hydrogen and oxygen isotope fractionation between ice and water. Journal of Physical Chemistry 72 (10):3683-&. doi:10.1021/j100856a060

Passey BH, Henkes GA (2012) Carbonate clumped isotope bond reordering and geospeedometry. Earth and Planetary Science Letters 351:223-236. doi:10.1016/j.epsl.2012.07.021

Passey BH, Levin NE, Cerling TE, Brown FH, Eiler JM (2010) High-temperature environments of human evolution in East Africa based on bond ordering in paleosol carbonates. Proc Natl Acad Sci U S A 107 (25):11245-11249. doi:10.1073/pnas.1001824107

Pohl W, Siegl W (1986) Sediment-hosted magnesite deposits. In: Wolf KH (ed) Handbook of Strata-bound and Stratiform Ore Deposits, vol 14. Elsevier, Amsterdam, pp 223-310

Power IM, Wilson SA, Thom JM, Dipple GM, Gabites JE, Southam G (2009) The hydromagnesite playas of Atlin, British Columbia, Canada: A biogeochemical model for CO2 sequestration. Chemical Geology 260 (3-4):286-300. doi:10.1016/j.chemgeo.2009.01.012

Saenger C, Affek HP, Felis T, Thiagarajan N, Lough JM, Holcomb M (2012) Carbonate clumped isotope variability in shallow water corals: Temperature dependence and

growth-related vital effects. Geochim Cosmochim Acta 99:224-242. doi:10.1016/j.gca.2012.09.035

Saldi GD, Schott J, Pokrovsky OS, Gautier Q, Oelkers EH (2012) An experimental study of magnesite precipitation rates at neutral to alkaline conditions and 100-200 degrees C as a function of pH, aqueous solution composition and chemical affinity. Geochim Cosmochim Acta 83:93-109. doi:10.1016/j.gca.2011.12.005

Saldi GD, Schott J, Pokrovsky OS, Oelkers EH (2010) An experimental study of magnesite dissolution rates at neutral to alkaline conditions and 150 and 200 degrees C as a function of pH, total dissolved carbonate concentration, and chemical affinity. Geochim Cosmochim Acta 74 (22):6344-6356. doi:10.1016/j.gca.2010.07.012

Schauble EA, Ghosh P, Eiler JM (2006) Preferential formation of C-13-O-18 bonds in carbonate minerals, estimated using first-principles lattice dynamics. Geochim Cosmochim Acta 70 (10):2510-2529. doi:10.1016/j.gca.2006.02.011

Streit E, Kelemen P, Eiler J (2012) Coexisting serpentine and quartz from carbonate-bearing serpentinized peridotite in the Samail Ophiolite, Oman. Contributions to Mineralogy and Petrology 164 (5):821-837. doi:10.1007/s00410-012-0775-z

Thiagarajan N, Adkins J, Eiler J (2011) Carbonate clumped isotope thermometry of deep-sea corals and implications for vital effects. Geochim Cosmochim Acta 75 (16):4416-4425. doi:10.1016/j.gca.2011.05.004

Tripati AK, Eagle RA, Thiagarajan N, Gagnon AC, Bauch H, Halloran PR, Eiler JM (2010) C-13-O-18 isotope signatures and 'clumped isotope' thermometry in foraminifera and coccoliths. Geochim Cosmochim Acta 74 (20):5697-5717. doi:10.1016/j.gca.2010.07.006

Wang ZG, Schauble EA, Eiler JM (2004) Equilibrium thermodynamics of multiply substituted isotopologues of molecular gases. Geochim Cosmochim Acta 68 (23):4779-4797. doi:10.1016/j.gca.2004.05.039

Table 1. Clumped isotope data for calcite standards. Δ47 following heated gas and hot acid fractionation corrections. Analytical errors are reported as the standard error of the mean of all acquisitions (8) of an extraction, propagated through heated gas corrections for Δ47.

Sample	Accepted Δ47 (‰)	Year	Method	Rxn#	$\delta^{13}C_{PDB}$ (‰)	$\delta^{18}O_{SMOW}$ (‰)	Δ47 (‰)	Δ47 Residual
Carrara	0.352	2011	online		2.341 ± 0.001	37.302 ± 0.001	0.408 ± 0.016	0.056
			online		2.340 ± 0.001	37.288 ± 0.001	0.363 ± 0.008	0.011
			offline	C1	2.260 ± 0.001	36.759 ± 0.001	0.398 ± 0.009	0.046
			offline	C2	2.211 ± 0.001	36.946 ± 0.001	0.450 ± 0.007	0.098
			offline	C3	2.427 ± 0.001	36.754 ± 0.002	0.414 ± 0.011	0.062
		2012	online		2.268 ± 0.003	36.916 ± 0.006	0.335 ± 0.013	-0.017
			online		2.222 ± 0.002	36.950 ± 0.004	0.323 ± 0.022	-0.029
			online		2.188 ± 0.000	36.798 ± 0.002	0.323 ± 0.025	-0.029
			online		2.196 ± 0.001	36.783 ± 0.005	0.354 ± 0.018	0.002
			offline	Rxn #1	2.380 ± 0.003	36.745 ± 0.005	0.401 ± 0.023	0.049
			offline	Rxn #12*	2.858 ± 0.003	36.035 ± 0.006	0.364 ± 0.016	0.012
			offline	Rxn #3**	2.441 ± 0.002	35.736 ± 0.004	0.457 ± 0.017	0.105
TV01	0.662	2011	online		2.555 ± 0.001	30.466 ± 0.002	0.683 ± 0.011	0.021
			online		2.544 ± 0.001	30.506 ± 0.001	0.625 ± 0.010	-0.037
			offline	T1	2.564 ± 0.001	29.993 ± 0.002	0.693 ± 0.010	0.031
			offline	T3	2.589 ± 0.001	30.104 ± 0.001	0.663 ± 0.009	0.001
		2012	online		2.514 ± 0.003	30.074 ± 0.005	0.663 ± 0.017	0.001
			online		2.401 ± 0.002	30.101 ± 0.006	0.654 ± 0.016	-0.008
			online		2.458 ± 0.002	29.948 ± 0.005	0.634 ± 0.027	-0.028
			offline	Rxn #4	2.694 ± 0.002	29.398 ± 0.004	0.720 ± 0.019	0.058
			offline	Rxn #23	2.546 ± 0.002	29.648 ± 0.004	0.701 ± 0.012	0.039
			offline	Rxn #22	2.714 ± 0.003	29.322 ± 0.006	0.750 ± 0.019	0.088

*This extraction is excluded from considerations of average offsets because of its anomalously high $\delta^{13}C$ value.

**This sample developed a leak on the backspace of the reaction vessel during phosphoric acid digestion, but it did not seem to affect the reaction space.

Table 2. Clumped isotope data for magnesite samples formed at known *T*

Sample	Type	Provided by	Year	T (°C)	$\delta^{13}C_{PDB}$ (‰)	$\delta^{18}O_{PDB}$ (‰)	Δ47 (‰), HG-, hot acid-, "online" std-corrected
Mgs III r1	Synthetic	Oelkers	2011	250 ± 0.5	-19.437	-31.787	0.312 ± 0.016
Mgs III r2			2011	250 ± 0.5	-19.111	-32.007	0.343 ± 0.011
Mgs III r3			2012	250 ± 0.5	-19.140	-32.247	0.349 ± 0.020
Mgs III r4			2012	250 ± 0.5	-19.388	-32.108	0.379 ± 0.016
				Average	-19.269	-32.037	0.346
				Stdev	0.167	0.194	0.027
Dclq200 r1	Synthetic	Oelkers	2012	200 ± 0.5	-17.643	-31.746	0.382 ± 0.018
Dclq200 r2			2012	200 ± 0.5	-17.929	-31.390	0.384 ± 0.022
				Average	-17.786	-31.568	0.383
				Stdev	0.202	0.252	0.001
M2-150 r1	Synthetic	Oelkers	2011	150 ± 0.5	-21.012	-28.801	0.382 ± 0.016
M2-150 r2			2011	150 ± 0.5	-20.590	-28.504	0.353 ± 0.012
Dclq150 r1			2012	150 ± 0.5	-24.267	-26.780	0.406 ± 0.016
Dclq150 r2			2012	150 ± 0.5	-24.173	-26.958	0.461 ± 0.024
				Average	-22.510	-27.761	0.401
				Stdev	1.982	1.039	0.046
ht-5 r1*	Synthetic	Mazzotti	2011	120 ± 1	-25.685	-24.051	0.584 ± 0.012
ht-5 r2			2011	120 ± 1	-25.177	-24.672	0.455 ± 0.011
ht-5 r3			2012	120 ± 1	-25.623	-24.383	0.423 ± 0.014
ht-5 r4**			2012	120 ± 1	-25.568	-24.391	0.435 ± 0.016
				Average	-25.513	-24.374	0.438
				Stdev	0.229	0.254	0.016
M223	Synthetic	Deelman	2012	40	-14.846	-9.359	0.529 ± 0.016
16I2	Metaperidotite	Ferry	2011	645 ± 10	-6.682	-21.076	0.310 ± 0.007
AT03-44-7 r1	Listvenite	Dipple	2011	245 ± 35	-3.912	-10.825	0.398 ± 0.015
AT03-44-7 r2			2011	245 ± 35	-3.684	-11.200	0.397 ± 0.017
				Average	-3.798	-11.013	0.398
				Stdev	0.161	0.273	0.001
playa_1 r1	Playa	Dipple	2011	6 ± 6	4.282	-14.837	0.757 ± 0.016
playa_1 r2	magnesite		2011	6 ± 6	4.236	-14.902	0.750 ± 0.012
playa_2 r1			2012	6 ± 6	2.393	-14.688	0.770 ± 0.011
playa_2 r2**			2012	6 ± 6	2.449	-14.880	0.794 ± 0.016
				Average	3.340	-14.827	0.768
				Stdev	1.062	0.096	0.019

*The LN tank ran empty during GC transit, and Δ47 value is much higher than that of replicate extractions of ht-5, so this extraction is excluded from averages.

**Developed backspace leaks, but it did not seem to affect the reaction space.

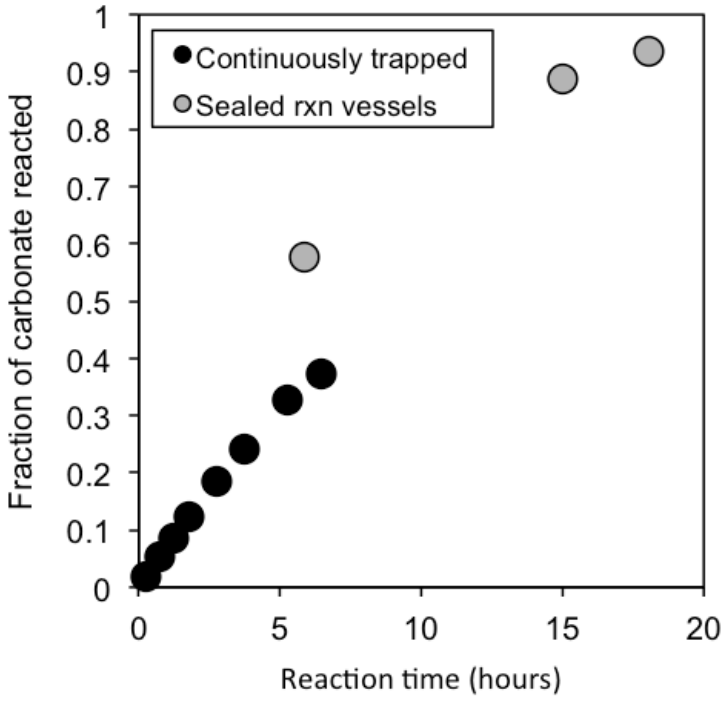

Figure 1. Reaction progress versus time for phosphoric dissolution of magnesite at 90°C in sealed reaction vessels (black circles) and in a stirred reaction apparatus with continuous cryogenic trapping of CO_2. Fraction of carbonate reacted was calculated from the pressure of evolved CO_2 over a calibrated volume relative to the mass of carbonate reacted.

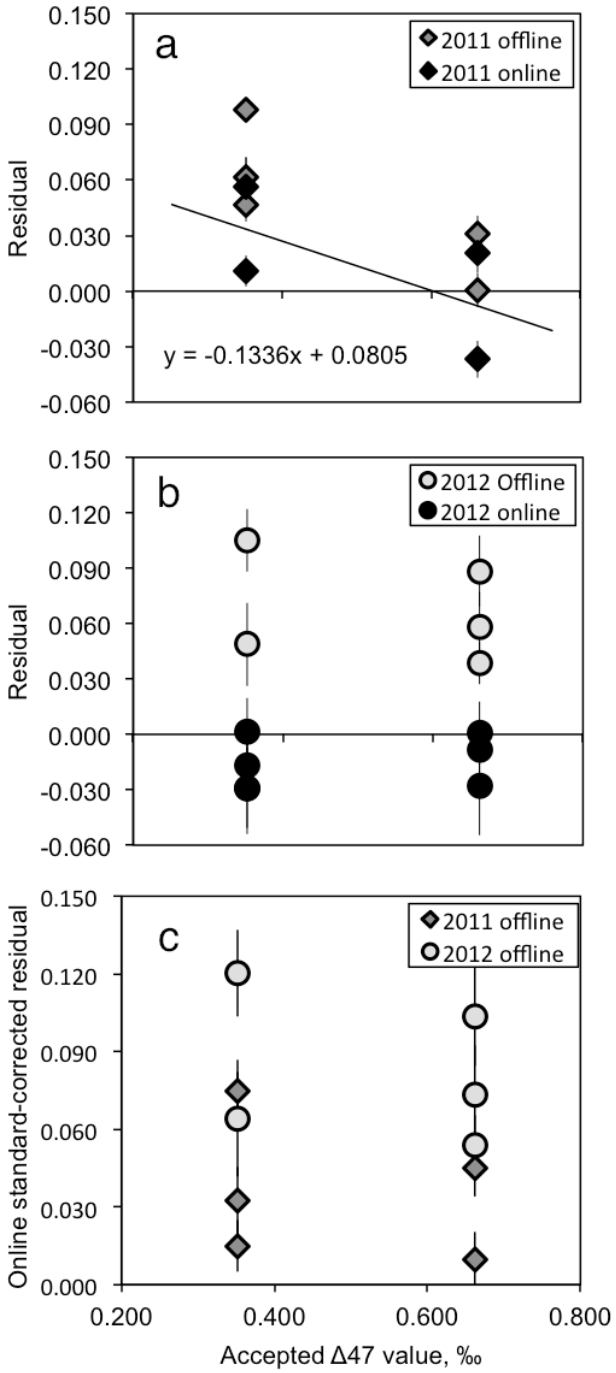

Figure 2. Residual Δ47 values from calcite standards compared with expected values. (a) Calcite standards measured in 2011, (b) Calcite standards measured in 2011, (c) Offline calcite standards measured in 2011 and 2012 after correcting for offsets observed in online standards.

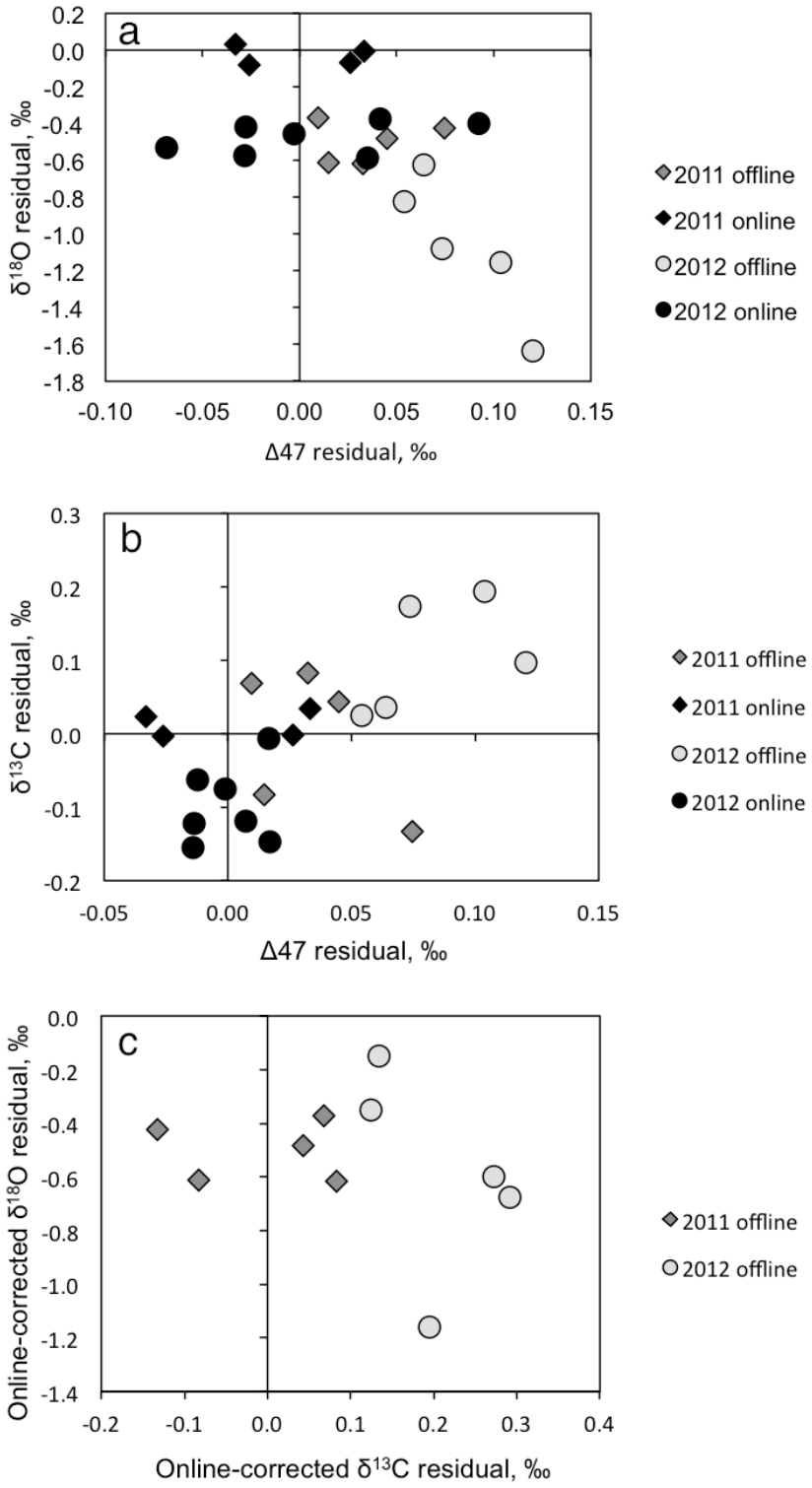
a
δ18O residual, ‰
Δ47 residual, ‰
2011 offline
2011 online
2012 offline
2012 online
b
δ13C residual, ‰
Δ47 residual, ‰
2011 offline
2011 online
2012 offline
2012 online
c
Online-corrected δ18O residual, ‰
Online-corrected δ13C residual, ‰
2011 offline
2012 offline

Figure 3. Residual $\delta^{18}O$ and $\delta^{13}C$ of calcite standards. (a) Raw $\delta^{18}O$ residuals versus online-corrected $\Delta47$ residuals for all extractions of Carrara and TV01 standards, (b) Raw $\delta^{13}C$ residuals versus online-corrected $\Delta47$ residuals for all extractions of Carrara and TV01 standards, (c) $\delta^{13}C$ residuals versus $\delta^{18}O$ residuals for offline calcite standards following correction for online offsets observed in (a) and (b).

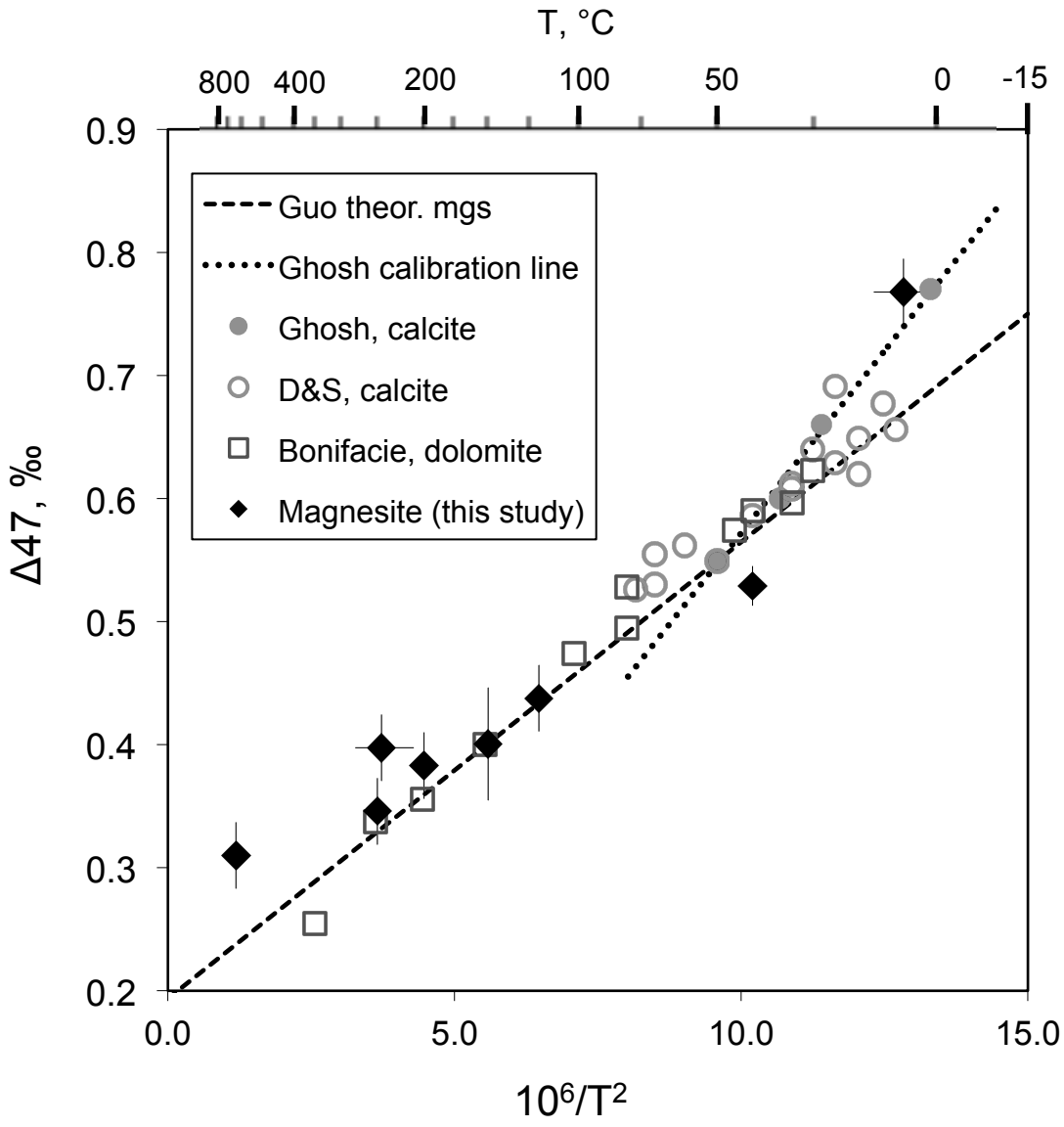

Figure 4. Sample-averaged Δ47 values in magnesite versus $10^6/T^2$, compared with the calibration data of Ghosh et al. (2006), Dennis and Schrag (2010), and Bonifacie (in prep.) and the theoretical magnesite calibration of Guo et al. (2009). Error bars represent the greater of one standard deviation of replicate measurements of the magnesite sample and one standard deviation of the offline calcite standards for each year.

Chapter 4: Geochemistry and petrology of listvenite in the Oman Ophiolite

Abstract

Extensive outcrops of listvenite—fully carbonated peridotite, with all Mg in carbonate minerals and all Si in quartz—occur along the basal thrust of the Samail Ophiolite in Oman. Here we examine mineralogical, chemical and isotopic evidence for the temperatures, timing, and fluid compositions involved in the formation of this listvenite. The listvenites are composed primarily of magnesite (and/or dolomite) + quartz + relict Cr-spinel. In some instances the conversion of peridotite to listvenite is nearly isochemical except for the addition of CO_2, while other samples have seen significant calcium addition and/or variable minor addition of Al, Ti, K, and Mn. Along margins where listvenite bodies are in contact with serpentinized peridotite, talc and antigorite are also present in addition to carbonate and quartz. Thermodynamically stable coexistence of antigorite, talc, and quartz in serpentinite along the margins of the listvenite would require reaction temperatures around 80-110°C. This is consistent with carbonate clumped isotope thermometry in listvenite, and with conventional stable isotope exchange thermometry (assuming fluid compositions with $\delta^{18}O$ near zero), which yield peak temperatures around 100°C. Depending on the reaction pressure, thermodynamic stability of the dominant magnesite + quartz assemblage (relative to talc + magnesite) at these temperatures may require that these minerals formed at relatively high P_{CO2}. CO_2-enriched fluids were likely derived from underlying calcite-bearing sediment during emplacement of the ophiolite. Initial $^{87}Sr/^{86}Sr$ values in the listvenite vary from 0.7085 to 0.7135. Most are significantly higher than seawater values and consistent with values

measured in the underlying metasediments. An internal Rb-Sr isochron from one listvenite sample yields an age of 97 ± 29 Ma, consistent with the timing of emplacement of the ophiolite over allochthonous sediments of the Hawasina group, and autochthonous sediments of the Arabian continental margin. While constraints on the pressure of listvenite formation are lacking, these moderate temperatures suggest that listvenites formed at relatively shallow depths, making release of carbonate-saturated pore-water due to compaction of subducted sediment or low-pressure phase transitions of hydrous minerals, the probable sources of the CO_2-bearing fluid. Alternatively, there might have been substantial transport of fluids along the slab interface from regions with higher pressures and temperatures, but this seems unlikely as decompression and cooling of such transported fluids would have lowered the carbon content. Carbonate dissolution from subducted sediments and transfer of CO_2 to the mantle wedge via listvenitization may be an important process in forearc hydrothermal systems. The presence of fully carbonated peridotite deposits demonstrate that peridotite carbonation reactions can proceed to completion on large scales, suggesting that in situ mineral carbonation of peridotite may offer a viable solution for carbon storage.

Introduction

Listvenite (*sensu stricto*) is a fuchsite-quartz-carbonate assemblage produced by alteration of ultramafic rocks, but the term has been broadly applied to include many other carbonate-rich alteration products of ultramafic rocks (Halls and Zhao 1995). In this paper, we use the term to refer to rocks composed almost entirely of quartz plus magnesite and/or dolomite, formed by replacement of peridotite. Listvenite deposits

initially attracted attention for their association with gold mineralization and other economically-valuable hydrothermal deposits (Rose 1837), but more recently have been highlighted as a natural analog to mineral carbon storage (Hansen et al. 2005; Kelemen et al. 2011; Beinlich et al. 2012) and as a window into peridotite carbonation processes in the hanging wall of subduction zones (Kelemen et al., 2011).

The presence of listvenite near the base of the Oman ophiolite has been noted by several researchers (Glennie et al. 1974; Stanger 1985; Villey et al. 1986; Wilde et al. 2002; Nasir et al. 2007; Kelemen et al. 2011), but there has been no consensus on a model for the formation of listvenite in Oman. Referred to as alternatively as "Amqat," birbirite, silicified serpentinite, listwaenite, or listwanite, listvenite in Oman has been proposed to form by leaching of magnesium under tropical weathering conditions in the late Tertiary (Glennie et al. 1974), reaction with warm groundwater during Paleogene faulting (Stanger 1985; Wilde et al. 2002), and reaction with sediment-derived fluids during emplacement of the ophiolite (Kelemen et al. 2011). We present geochemical data from Oman listvenites (both *sensu stricto* and *sensu lato*) to provide constraints on the timing, temperature, and fluid composition and sources or listvenitization.

We collected listvenite, other highly-carbonated peridotite lithologies, and nearby metasediments and serpentinized peridotite samples in January of 2009, 2010, and 2011 from six localities: (1) a large antiform comprising a mountain along Wadi Mansah, (2) the highway roadcut at Fanjah, (3) Amqat, (4) an outcrop near the Tawah locality of Nasir et al., 2007, (5) Tuf and (6) Wadi Abyad. These locations are shown on the map in Figure 1, and a list of sample locations and descriptions can be found in Appendix 1.

At Tuf and Wadi Abyad, we find highly carbonated peridotites composed primarily

of magnesite + talc ± serpentine, in localized, centimeter- to meter-scale zones within serpentinized peridotite (Figure 2). Without quartz, and with some Mg remaining in silicate phases rather than in carbonates, these "soapstones" are not listvenites following the definition of Halls and Zhao (1995), but such rocks do not have equivalents in the active carbonation systems observed in Oman today (Streit et al., 2012; Kelemen et al., 2011). Instead, they fall within a spectrum of carbonated alteration products of peridotite that formed at depth that includes true listvenites.

The Wadi Mansah, Fanjah, Amqat, and Tawah occurrences fall within the region of detailed mapping of Amqat occurrence presented in Stanger (1985), but not all listvenite found at these localities is consistent with previous descriptions of listvenite from this region. Listvenites at the Fanjah roadcut, Amqat, and Tawah have been described in previous studies (Glennie et al. 1974; Stanger 1985; Wilde et al. 2002; Nasir et al. 2007) to include highly silicified serpentinite containing only minor dolomite and/or calcite (referred to as "Amqat" by Glennie et al. (1974) and Stanger (1985); as "silica-iron hydroxide," "SIH," or simply "listwaenite" by Wilde et al. (2002); and as "Type II listwaenite" by Nasir et al. (2007)), and carbonate-dominated listvenite composed of dolomite and/or calcite with accessory fuchsite and oxides (the "Type I listwaenite" of Nasir et al. (2007)). The listvenite in Wadi Mansah differs from samples described by previous studies of Oman listvenites in the predominance of magnesite, present in ~10m thick magnesite-quartz listvenite bands occurring within partially serpentinized peridotite and in an overlying ~100m thick body of dolomite-quartz and magnesite-quartz listvenite that makes up the crest of the antiform. The magnesite + quartz assemblage that typifies listvenite at the Wadi Mansah locality reflects carbonation of peridotite with relatively

little change to the bulk composition beyond the addition of CO_2, whereas other listvenite bodies in Oman are dominated by calcium carbonates (e.g., Stanger 1985; Wilde et al. 2002; Nasir et al. 2007).

A geologic map of the Wadi Mansah locality is presented in Figure 3. In Wadi Mansah, listvenite forms 10 to ~ 200 meter bands roughly parallel to banding in the host peridotite (pictured in Figure 4). The listvenite bands probably are also parallel to the basal thrust juxtaposing hanging wall peridotite with metasediments in the footwall. The bands may have been localized along imbricate faults associated with the basal thrust. Beneath the fault are minor amphibolites and greenschist facies metabasalts (some pillows) and chert, plus a much more extensive mass of metasedimentary phyllites with quartz, calcite, clinochlore, illite and muscovite. These lithologies were grouped and mapped as part of the metamorphic sole of the ophiolite by Villey et al. (1986). In turn, beneath the metamorphic sole are diagenetically modified sediments of the Hawasina group (Villey et al. 1986). Our samples from Wadi Mansah include transects across the transitional margins between magnesite + quartz listvenite bands and partially serpentinized peridotite. While we report data from a limited number of samples from other localities, we focus primarily on listvenite from the site near Wadi Mansah, where listvenite is surrounded in three dimensions by partially serpentinized peridotite.

Methods

Sample processing and compositional analyses

Hand samples of listvenites, metasediments, and less altered peridotites were collected from listvenite localities in 2009, 2010, and 2011. Sub-samples (~20-50 grams)

were chipped using a jaw crusher and powdered using ceramic puck mill. Splits of these powders were used for X-ray diffraction, X-ray fluorescence, and Sr isotopic studies. Cut thin-section blanks were sent to Burnham Petrographics for preparation of polished thin sections.

The mineralogical and elemental compositions of samples were studied by petrographic microscope, powder X-ray diffraction (XRD), X-ray fluorescence (XRF), and electron microprobe. Powdered samples were analyzed by XRD using a Panalytical X'Pert powder X-ray diffractometer at Lamont-Doherty Earth Observatory and peaks for constituent minerals were identified using MacDiff and Match! software, with semi-quantitative estimates of mineral proportions calculated in Match!. Whole rock major and trace element com- position were determined by XRF at the Washington State University GeoAnalytical Lab, where loss on ignition (LOI), primarily due to volatilization of H_2O + CO_2, was also measured (http://www.sees. wsu.edu/Geolab/equipment/xrf.html). Polished thin sections were quantitatively analyzed with a 5-spectrometer Cameca SX-100 electron microprobe located at the American Museum of Natural History in New York, using a 10 lm beam diameter, with 15 kV accelerating voltage, 10nA current, and 20–30 s peak time, to analyze the major element composition of phases in thin using natural and synthetic standards.

Sr Isotopes and isotopic dating

Sr isotopic analyses were completed at Lamont-Doherty Earth Observatory. Sample dissolution and element purifications of bulk powders were performed in the clean lab (see Appendix 2 for detailed procedures), and Sr isotope ratios were measured on the VG Sector 54 multi-collector thermal ionization mass spectrometer (TIMS). Mineral

separation for determination of an Rb-Sr mineral isochron in sample OM10-26 was partially achieved by magnetic separation of sieved grains liberated by self-fragmentation under high voltage (Selfrag). Although the very fine-grained nature of these rocks and variable mineral compositions prevented complete separation of minerals, eight fractions with variable proportions of quartz, magnesite, and fuchsite were obtained and analyzed for Sr isotopic ratios. Rb:Sr ratios for Rb-Sr dating were analyzed by inductively coupled plasma mass spectrometry (ICP-MS) measured on the VG PlasmaQuad Excell ICPMS. Preliminary Ar-Ar dating was performed on picked fuchsite-rich grains in the Argon Geochronology For The Earth Sciences (AGES) Lab at LDEO.

Carbonate clumped isotopes

Clumped isotopic data were obtained for eight dolomite-bearing and nine magnesite-bearing listvenite samples from the Wadi Mansah and Tawah localities, one dolomite-bearing and three calcite-bearing metasediment samples from the Wadi Mansah locality, and two soapstone samples from Tuf and Abyad. All samples were analyzed at the California Institute of Technology, over the same three sessions in 2009, 2011 and 2012 in which the low-temperature carbonate samples from Chapter 2 and magnesite samples from Chapter 3 were analyzed. Chipped samples were crushed using a mortar and pestle and sieved to separate a 150-250 μm grain-size fraction. Listvenite sample OM09-19 contains fine-grained dolomite intergrown with quartz cut by magnesite veins and abundant quartz veins, so mm-scale subsamples were cut from a stained, sawed slab to isolate dolomite and magnesite. Soapstone sample OM11-94 is zoned, containing magnesite-talc, serpentine-talc, and serpentine-olivine regions. Only the magnesite-talc region was subsampled for clumped isotope analysis. Magnesite samples were rinsed

with ethyl alcohol and dried overnight in an oven at 40°C to remove water, prior to offline phosphoric acid digestion at 90°C in sealed reaction vessels for 17 hours, as described in Chapter 3. To avoid contamination from coexisting dolomite, CO_2 evolved from magnesite in the first 20 minutes of phosphoric acid digestion was discarded. Dolomite and calcite samples analyzed in 2011 and 2012 were reacted using the automated online extraction system described in Passey et al. (2010), wherein samples are reacted for 20 minutes in a common acid bath maintained at 90°C with continuous cryogenic trapping of evolved CO_2 followed by further cryogenic and GC purification. Two dolomite samples analyzed in 2009 were reacted with phosphoric acid at 90°C for 20min in sealed reaction vessels.

$\delta^{13}C$, $\delta^{18}O$ and clumped isotope ratios, reported as $\Delta 47$, were measured on a Thermo Finnigan MAT 253 gas source mass spectrometer at Caltech, employing standard published configurations and methods (Huntington et al. 2009; Passey et al. 2010). Heated gas samples were analyzed daily to correct for instrument nonlinearity and "scale compression," allowing data to be normalized to the stochastic reference frame used for the original calibration of the clumped isotope thermometer reported in Ghosh et al. (2006). Following heated gas normalization, the empirically derived acid fractionation correction of +0.081‰ was added to $\Delta 47$ data to account for the difference between the phosphoric acid temperature of 90°C used in this study and the phosphoric acid temperature of 25°C used by Ghosh et al. (2006) in the original calibration (Passey et al. 2010). $\Delta 47$, $\delta^{13}C$, and $\delta^{18}O$ values were standardized to Carrara and TV01 calcite standards by subtracting observed offsets for online standards, with an additional minor correction to account for offsets observed in magnesite samples reacted offline (see

Chapter 3 for observed offsets in standards and magnesite samples measured in 2011 and 2012). Clumped isotope temperatures were calculated using the empirical calibration of Ghosh et al. (2006) for T<50°C and the theoretical calibration of Guo et al. (2009) for T>50°C. $\delta^{18}O$ in carbonate was calculated using the CO_2-carbonate $\delta^{18}O$ fractionation factors for phosphoric digestion from Das Sharma et al. (2002).

Oxygen isotopes in quartz

$\delta^{18}O$ was measured in quartz separates from nine listvenite samples in which clumped isotope compositions were also analyzed. Where sufficient material was available, the same crushed and sieved subsamples used for clumped isotope analysis were also used. Where more material was required, the samples were crushed and sieved to 150-250μm and Frantzed to separate the non-magnetic fraction at 0.4A, 20° side-slope. For sample OM09-11, in addition to quartz from the subsample of the fine-grained quartz-magnesite matrix that was used for clumped isotope analysis, a coarser quartz vein was also sampled (OM09-11-V). In addition to the bulk sample that was used for clumped isotope analysis, a nearly pure quartz separate from the non-magnetic fraction (Frantzed at 1.2A, 5° side-slope) of the Selfragged OM10-26 subsample was also analyzed. 30-80mg of each sample was reacted with 3-7ml of 1M HCl at room temperature for three days to remove carbonate, then with ~3ml of 10% oxalic acid at room temperature for three days to remove iron oxide. Samples were then triple-rinsed with DI water and dried overnight in an oven. Many of the samples still contained quartz grains that were stained or intergrown with fine-grained oxides, so cleaned samples were picked under a microscope to remove the most contaminated grains. $\delta^{18}O$ measurements were performed at the Earth Systems Center for Stable Isotopic Studies (ESCSIS) at Yale

University, using CO_2 laser fluorination techniques. Measured sample $\delta^{18}O$ values were standardized to a Gore Mountain Garnet ($\delta^{18}O$ = 5.8‰ SMOW) standard and an NBS28 quartz standard ($\delta^{18}O$ = 9.6‰ SMOW).

Results

Bulk and mineral compositions

Listvenite bulk compositions, at the cubic meter scale, generally approximate that of average Oman harzburgite (Hanghoj et al. 2010) with the addition of CO_2 and in many cases Ca. While other studies have noted a high degree of silicification in listvenites (e.g., Stanger 1985; Wilde et al. 2002), we find similar numbers of samples showing silica gains and losses, with silica content least variable and most similar to harzburgite in the magnesite + quartz assemblage (Figure 4). The abundance of quartz veins makes it clear that silica was mobilized in the system, and the relatively high Mg-numbers of quartz-rich samples demonstrate that the high proportion of silica in those samples is due to addition of Si, not leaching of Mg as Glennie et al. (1974) originally proposed for Amqat. However, it is likely silica has been re-distributed within the outcrop rather than introduced from an external source. Dolomite-quartz listvenites exhibit greater compositional variability than their magnesite counterparts, and appear to have lost Mg and gained Ca.

Minor and trace elements in listvenites are also broadly similar to average Oman harzburgite, with the most notable exceptions being the addition of potassium, a hallmark of listvenitization (s.s.) (Halls and Zhao 1995), and addition of manganese in most dolomite-bearing listvenites (Figure 6). Components commonly considered to be

immobile during hydrothermal alteration, such as Ti, Al, and Cr, can vary in concentration by up to more than an order of magnitude in Oman listvenites, and while they remain positively correlated, enrichments in Ti and Al, for example, are not proportional in a way that can be explained by losses in other components and therefore suggest either mobility during hydrothermal alteration or greater local variability in protolith than that documented by Hanghoj et al. (2010).

Volatile-free major and trace element bulk compositions of magnesite-quartz listvenites from the Wadi Mansah locality are frequently the same, within error, as average Oman harzburgite for all elements for which our XRF data can be compared with the data from Hanghoj et al. (2010), as shown in several selected isocon plots in Figure 7. By contrast, dolomite-quartz listvenite bulk compositions are not only highly enriched in calcium and depleted in magnesium, but show variable addition or loss of other major and trace elements, such that no samples are the same, within error, as the bulk composition of average harzburgite even when projected from Ca and CO_2.

Optical microscopy, XRD analysis, and electron microprobe reveal that our listvenite samples are predominantly composed of magnesite and/or dolomite + quartz, with antigorite ± talc ± chlorite present instead of quartz in samples collected from transitional zones between listvenite and partially serpentinized peridotite. Table 1 lists mineral parageneses observed in listvenites and associated rocks, with semi-quantitative estimates of mineral proportions calculated in from XRD spectra where available. Carbonate and quartz are finely intergrown, frequently down to micron scale and also form hierarchical fracture networks, in which cross-cutting relationships suggest quartz and carbonate veins are coeval, though dolomite and calcite veins sometimes post-date

the magnesite + quartz as cross-cutting veins and vugs (Figure 8a: intergrown magnesite + quartz and vein networks; Figure 9: carbonate cross-cutting relationships). Unlike serpentinitized peridotite far from listvenites in Oman (e.g., Boudier et al. 2010; Streit et al. 2012), serpentine near the margins of listvenite bodies is primarily antigorite rather than lizardite, though XRD suggests both polytypes maybe present. In these samples, antigorite may coexist with chlorite, talc, and in one sample, quartz (8c-e). Antigorite, which is the more Si-rich serpentine polytype, may be stabilized relative to lizardite near the listvenite zones because precipitation of magnesium carbonates increases silica activity in the fluid (Frost, 1985).

Mineral compositions from electron microprobe analyses of carbonates, Mg-phyllosilicates, olivine, spinels, and other minor phases are given in Tables 2-6. While carbonates from the active, low-temperature carbonation system in Oman have <0.5 wt% FeO (Streit et al., 2012), magnesite and dolomite from Oman listvenites have an Mg# of ~95 on average (~5 wt% FeO in magnesite, ~2 wt% in dolomite). Serpentine from serpentinized peridotite occurring within meters of the margins of listvenite has an average Mg# of ~95, which is the value expected for antigorite in Fe/Mg exchange equilibrium with typical mantle olivine from the Oman ophiolite with an Mg# of 91 (Trommsdorff and Evans 1972). However, in some partially serpentinized peridotite near listvenite or other highly-carbonated peridotite, more Fe-rich serpentine (e.g., Mg# ~85) surrounds or completely replaces relict olivine in mesh cores surrounded by serpentine with Mg# ~95, as pictured in Figure 10. In OM10-06, some of these mesh cores also contain low-Fe magnesite and dolomite. The distribution of iron in Mg-rich phases for

low-temperature carbonate-veined serpentinites, listvenites, and “talc-listvenites” is shown in Figure 11.

Most of the remaining iron, ~2-3wt% in magnesite-quartz listvenite, takes the form of iron oxides and hydroxides. In partially serpentinized peridotite adjacent to the listvenite bodies, in transitional carbonated peridotite on the margin of listvenite bands, and in highly carbonated, calcite-rich serpentinites from the Fanjah roadcut, magnetic minerals occur in high enough abundance that a strong hand magnet has a notable attraction to the thin section billet. In partially serpentinized peridotite, this is assumed to be due to the presence of magnetite, identified in thin section on the basis of electron microprobe totals ~92-94 wt%, while XRD suggests the presence of maghemite in samples from the Fanjah roadcut. Much of the magnetite identified in these partially serpentinized peridotites is extremely fine-grained and occurs in disseminated patches or irregular veins, but larger aggregates, up to 30 μm in thickness, can be found rimming Cr-spinels. Fully carbonated listvenites are unaffected by a hand magnet, and the coarsest grained Fe-oxides (typically <10-20 μm), which occur as isolated needles, veinlets and reactive rims on Cr-spinels, yield probe totals around 85-89 wt% consistent with hematite. Other Fe-oxide veins in listvenite yield lower probe totals, in the high 70s, which could represent goethite or other iron hydroxides. However, much of the iron in listvenite is present as extremely fine-grained iron oxide/hydroxide that takes the form of fine strands or small patchy areas with a bright, mottled appearance in back-scattered electron images. Although even 1μm point analyses of these phases most likely represent mixed analyses, electron microprobe analyses typically yield totals in the high 70s and indicate ~5wt% SiO_2 even when the iron phase occurs within carbonate veins. Fe

XANES spectra collected by collaborators at UC Boulder are unique among their large library of model compound, but are best approximated in some areas by amorphous Fe(III)-oxide microbial mat models acquired from low-temperature submarine hydrothermal vents (A. Templeton and L. Mayhew, pers.comm., 2011). The identity of host phase for much of the iron in listvenite remains unclear.

Relict chromian spinels are ubiquitous in listvenites from all localities in the Samail massif, and in many cases serve as the clearest indication of a peridotite protolith. While Cr-spinel is typically the only relict phase remaining from the protolith, even these have experienced significant alteration, with $MgAl_2O_4$-rich end-members typical of Oman harzburgite present only in partially serpentinized peridotites and the less-altered cores of spinels in some listvenite samples (Table 5). Most spinel analyses have much lower Mg# and higher Cr# than spinel from fresh Oman peridotite (average Mg# of ~30 in listvenites and associated carbonated peridotite compared to ~60 in harzburgite and ~50 in dunite from Oman, average Cr# of ~80 compared to ~50 in harzburgite and ~60 in dunite) (Hanghoj et al. 2010). These data probably reflect addition of iron to spinel – as well as formation of fine-grained oxides – during replacement of olivine and serpentine with high Mg# carbonate, and loss of Al from spinel to form chromian chlorite.

Although the bulk compositions of almost all our listvenite samples are at least slightly enriched in potassium, fuchsite (Cr-rich muscovite) is rarely present in our samples, occurring in trace quantities in a few samples and in minor quantities in only one sample (OM10-26). Fuchsite occurs in mm-scale bright bluish-green spots composed primarily of quartz intergrown with minor amounts of very-fine-grained fuchsite. Fuchsite in OM10-26 pseudomorphically replaces Cr-spinel (Figure 12), which is not

present as relicts in this sample unlike most other samples, and fuchsite compositions trend to Cr-rich spinel compositions (Figure 13).

Sr isotopic compositions

Bulk strontium isotopic ratios for listvenites and underlying metasediments and metavolcanics from Wadi Mansah and a soapstone from Tuf (Table 7) range from $^{87}Sr/^{86}Sr$ values of 0.7085 to $^{87}Sr/^{86}Sr$ values in the listvenite vary from 0.7085 to 0.7135. Most of these ratios are significantly higher than in Cretaceous to modern seawater, and are consistent with values within the underlying allochthonous metasediments, which range from 0.7044 to 0.7189 (Figure 14). Even more radiogenic strontium isotope ratios have been reported in autochthonous clastic sediments, with $^{87}Sr/^{86}Sr$ values up to 0.77 (Weyhenmeyer 2000).

The presence of K-bearing fuchsite in OM10-26 provides a host for Rb, allowing for differential in-growth of ^{87}Sr and construction of an internal isochron (Figure 15). Due to the very fine-grained nature of this sample, we analyzed Sr isotopic ratios and Rb and Sr concentration on eight magnetically separated fractions representing variable proportions of magnesite, quartz, and fuchsite (Table 8). This yields an isochron age of 97 ± 29 Ma, calculated using ISOPLOT (model 3) (Ludwig, 2003). The scatter in these data exceed the expected scatter due to analytical errors, suggesting "geologic" scatter may result from non-uniform initial strontium isotope ratios or later alteration resulting in addition or loss of Rb and/or Sr from some phases[1].

[1] The nominal analytical errors may underestimate the uncertainty of the entire procedure, given that two separate dissolutions of bulk powder of OM10-26 differ in

^{40}Ar-^{39}Ar analyses of picked fuchsite-rich grains did not produce a reliable age (Figure 16). Although the integrated age of 96 Ma is in agreement with the Rb-Sr age, most Ar was released in the first heating step, which yielded an unreasonable age of ~123 Ma, older than the igneous age of the ophiolite (Tilton et al. 1981; Rioux et al. 2012). Given the weathered appearance of the fuchsite, its fine-grained nature, and its intimate association with quartz that could contain micron-scale fluid inclusions, it is not surprising that the Ar isotope system may have been disturbed.

Stable isotopes

Measured Δ47, $\delta^{13}C$, and $\delta^{18}O$ in carbonate from listvenite, soapstone, and underlying metasediments are reported in Table 9, and illustrated in Figure 17. A table of all clumped isotope measurements, including standards and heated gases is presented in Appendix 3. Clumped isotope temperatures were calculated using the theoretical Δ47-T relationships derived by Guo et al. (2009) for T>50°C and using the calibration of Ghosh et al. (2006) for T<50°C. Measured Δ47 values correspond to temperatures of 32-119°C for listvenite and 54-149°C for underlying metasediment. $\delta^{13}C$ values range from -5.7 to +1.1‰, and listvenite and metasediment values overlap. Carbonate $\delta^{18}O$ values are 21.9-24.6‰ (SMOW) in magnesite-quartz listvenite, 19.8-26.3‰ in dolomite-quartz listvenite, 21.1-22.2‰ in calcite from underlying metasediment and 21.7‰ in dolomite metasediment. The two soapstone samples analyzed yielded the highest and lowest values of all highly carbonated peridotites analyzed, for both Δ47 and $\delta^{18}O$, with OM11-17 the

---

$^{87}Sr/^{86}Sr$ by ~0.003, more than two orders of magnitude higher than the standard deviation of filament duplicates prepared from the same dissolution/purification.

highest Δ47 and $\delta^{18}O$ carbonate values (0.637‰ and 28.1‰, SMOW, respectively) and OM11-94 yielding the lowest Δ47 and $\delta^{18}O$ values (0.307‰ and 12.7‰, SMOW, respectively). $\delta^{18}O$ values in quartz (Table 10) range from 21.5‰ to 23.8‰ in magnesite-quartz listvenite and from 16.5‰ to 25.7‰ in dolomite-quartz listvenite and are correlated with $\delta^{18}O$ in carbonate (Figure 18).

Discussion

Timing of listvenitization

The Rb-Sr age derived from one magnesite-quartz listvenite sample (OM10-26) suggests that listvenite formation occurred during emplacement of the ophiolite, which was initiated ~94 Ma and continued until ~78 Ma (Hacker et al. 1996), rather than during a period of increased heat flow in the early Tertiary (~36-40 Ma) as proposed by Wilde et al. (2002). This age is also consistent with age constraints from late Paleocene to Eocene conglomerates that are mapped as unconformably overlying the listvenite (Villey et al. 1986). Given that the Rb-Sr age comes from a single magnesite-quartz listvenite sample, it is possible that dolomite-quartz listvenites could have formed in a different environment than the magnesite-quartz listvenites, but the spatial association of dolomite-quartz listvenites with the magnesite-quartz listvenites makes it seem unlikely that the two types are unrelated in their formation. Clear differences exist between dolomite listvenite and magnesite listvenite—dolomite listvenite samples are highly enriched in Ca, show far more variation in other major elements than magnesite-quartz listvenites. In samples that contain both magnesite and dolomite veins, dolomite typically post-dates magnesite. However, isotopic data ($^{87}Sr/^{86}Sr$, Δ47, $\delta^{13}C$, and $\delta^{18}O$) are generally similar

for dolomite and magnesite listvenites, and we infer that both listvenite types formed during the same time interval.

Temperature constraints: mineral parageneses

The similarity of the volatile-free bulk compositions of magnesite-quartz listvenites to those of relatively unaltered Oman harzburgites suggests a relatively simple alteration history, allowing us to make inferences about the conditions of peridotite carbonation. In Figure 19, we present a temperature-X_{CO2} phase diagram for the MgO-SiO_2-H_2O-CO_2 system to examine the regions of stability for the assemblages observed in listvenite (magnesite + quartz), and in transitional samples along the margins between listvenite and partially serpentinized peridotite (magnesite + talc + antigorite, quartz + talc + antigorite). This diagram was calculated using THERMOCALC (Holland and Powell 1998; Holland and Powell 2011). Reduction of activities of the Mg-end-members for antigorite and talc, based on electron probe analyses, makes no discernable difference in this result. Assuming that the thermodynamic data for the phases are correct, stable coexistence of antigorite, quartz and talc requires temperatures of ~80 ± 5°C (1σ) and is relatively insensitive to pressure. Recalculating this phase diagram at pressures between 10bar and 10kbar, results in less than 10°C difference in temperature of the antigorite + quartz = talc + H_2O; the primary effect of increasing pressure is to shift phase boundaries involving magnesite to lower X_{CO2} (Figure 20). As in the case of chrysotile + quartz = talc + H_2O (Streit et al. 2012), the calculated temperature of the antigorite + quartz = talc + H_2O reaction is higher (106°C) if the thermodynamic database of Gottschalk (1997) is used rather than Holland and Powell (2011).

Thus, the apparent coexistence of antigorite, quartz and talc (see Figure 8, panels c and e) provides a temperature estimate for the margin of the listvenite bands. This also provides constraints for the temperature of listvenite formation, as it is unlikely that a strong thermal contrast could be maintained over the <2 m wide transition zone between listvenite and partially serpentinized peridotite. The change in parageneses, from magnesite + quartz to antigorite + quartz (± talc, ± carbonate minerals) to chrysotile + lizardite + magnetite (+ relict olivine and orthopyroxene) is probably due to a decrease in X_{CO2}, with little or no temperature variation. If temperature was restricted to a relatively small range near the invariant point during alteration, the region in which talc + magnesite is stable without serpentine is very small, which could explain why this assemblage is not observed in association with the listvenite bodies studied here. Similarly, the presence of serpentine-free magnesite + talc assemblages at centimeter- to meter-scale at Abyad may indicate higher alteration temperatures at that locality, since the stability field of magnesite + talc expands in X_{CO2} space at higher temperature.

Temperature constraints: Clumped isotope thermometry and oxygen isotopes

Temperature estimates derived from stable isotope data are broadly consistent with the coexisting mineral equilibria described in the previous section. The average carbonate clumped isotope temperature in listvenite is 75°C in magnesite-quartz listvenite and 101°C in dolomite-quartz listvenite, in good agreement with antigorite + quartz = talc phase boundary at ~80-106°C. Magnesite from a soapstone sample from Abyad yielded Δ47 values of 0.307 ± 0.021‰ corresponding to a metamorphic temperature, or a closure temperature, of ~300°C (see Chapter 3). This higher

temperature for magnesite coexisting with talc without serpentine is consistent with the fact that magnesite + talc is stable over a wider range of fluid compositions at higher temperature. $\delta^{18}O$ values in magnesite from this sample, 12.7 ± 0.1‰ (SMOW), are also much lower than those measured in listvenite, consistent with a high-temperature origin. Magnesite in soapstone from Tuf, which contains both serpentine and talc, has higher Δ47 and $\delta^{18}O$ values, 0.637 ± 0.029‰ and 28.1 ± 0.2‰ (SMOW), respectively, than carbonates from listvenite and yields a clumped isotope temperature of 27 ± 8°C.

Although average clumped isotope temperatures in listvenite agree well with the petrologic temperature estimates, the broad range of Δ47 values across listvenite samples, compared with the much narrower range of $\delta^{18}O$ values in both carbonate in quartz, suggests that Δ47 values may have been subject to bond re-ordering after the initial precipitation of the carbonate. For example, the relative standard deviation of clumped isotope temperatures in magnesite listvenites is 27%, while the relative standard deviation of conventional oxygen isotopes temperatures in those sample samples is only 6-9% for magnesite and 4-6% for quartz[2]

Quartz and magnesite $\delta^{18}O$ values are positively correlated, but quartz-carbonate fractionation factors cannot be reliably used to independently estimate temperatures and oxygen isotopic compositions of the fluid in our samples. Quartz appears to be in isotopic equilibrium with magnesite, but the temperature dependence of magnesite-quartz fractionation factors is weak and non-monotonic when calculated using the reduced

[2] for assumed $\delta^{18}O$ of water between -5 and +10‰, and using the magnesite-water fractionation factors of Chacko and Deines (2008), Schauble et al. (2006), or Aharon (1988) and quartz-water fractionation factors of Friedman and O'Neil (1977) or Sharp and Kirschner (1994)

partition function ratios for magnesite of Chacko and Deines (2008) or Schauble et al. (2006). Although we cannot use quartz-magnesite $\delta^{18}O$ fractionation to derive precipitation temperatures, the fact that the two phases appear to be in isotopic equilibrium is another indication, in addition to textural and compositional evidence, that magnesite and quartz co-precipitated.

Quartz and dolomite $\delta^{18}O$ values are also positively correlated, but at least some samples appear to be out of equilibrium. Dolomite has higher $\delta^{18}O$ than quartz in all four dolomite-quartz samples in which we analyzed quartz, in contrast to uniformly positive quartz-dolomite fractionation factors calculated using dolomite fractionation factors from Chacko and Deines (2008), Schauble et al. (2006), or Sheppard and Schwarcz (1970) and quartz fractionation factors from Friedman and O'Neil (1977) or Sharp and Kirschner (1994). Two samples had only slight negative quart-dolomite fractionations of -0.2‰ and -0.4‰, which correspond to isotopic equilibration at temperatures of ~90°C using fractionation factors from Schmidt et al. (2005) and Friedman and O'Neil (1977), but would require temperatures of ~150°C if quartz fractionation factors are taken from Sharp and Kirschner (1994), ~200°C if dolomite fractionation factors are taken from Vasconcelos et al. (2005), and ~250-300°C if dolomite fractionation factors are taken from Northrop and Clayton (1966). Two samples had quartz-carbonate fractionations of -3.3‰, which is unattainable for most combinations of available dolomite and quartz fractionation factors, only being reached at temperatures in excess of 250°C for quartz-dolomite fractionation factors derived from Schmidt et al. (2005) and Friedman and O'Neil (1977). Vein dolomite in one of these samples, OM09-19, is also out of oxygen isotopic equilibrium with groundmass magnesite, as dolomite has higher $\delta^{18}O$ than

magnesite in this sample, whereas theory predicts that magnesite should be heavier in $\delta^{18}O$ than dolomite in all cases (Schauble et al. 2006; Chacko and Deines 2008).

We interpret the scatter the clumped isotope data to be due to post-precipitation modification of the carbonate. During obduction of the ophiolite, cooling rates in the basal peridotite would be expected to be slow, perhaps allowing continued re-ordering of C-O bonds extending to temperatures lower than the apparent equilibrium temperatures of 150-300°C observed in other slowly-cooled metamorphic carbonates and carbonatites (Ghosh et al. 2006; Dennis and Schrag 2010; Ferry et al. 2011; Passey and Henkes 2012; Falk et al. in prep (Chapter 3 of this thesis)). According to the relationship between closure temperature and cooling rate from calcite samples in the re-ordering experiments of Passey and Henkes (2012), a closure temperature <100°C would correspond to a cooling rate of less than 10^{-4} °C/Myr – in other words, to constant temperature < 100°C for millions of years. Passey and Henkes (2012) found that inferred cooling rates derived from the two different calcite samples they studied spanned over two orders of magnitude for any particular apparent equilibrium temperature. It is unknown to what extent reordering rates might differ for carbonates other than calcite or vary as a function of lattice defects or trace and minor element concentrations. Thus it is possible that re-ordering rates could be more rapid in our samples, and might vary significantly between samples.

The clumped isotope signal could also have been partially re-equilibrated during post-emplacement interaction with groundwater. Another result of post-emplacement water-rock interactions could be late precipitation of additional carbonate within pore space of the listvenite. Mixing of CO_2 derived from this younger, low temperature

component with CO_2 derived from carbonate precipitated during listvenite formation could lead to anomalous Δ47 values. Mixing of two carbonates with different $\delta^{13}C$ and/or $\delta^{18}O$ may result in a Δ47 value of the mixture that is not only non-linear with respect to the weighted proportions of the endmembers, but that outside the range of Δ47 values of the two endmembers (Eiler and Schauble 2004). The highest Δ47 values we observe in listvenite correspond to the lowest $\delta^{13}C$ values, so it is possible that these high Δ47 values are artificially high as the result of non-linear mixing with a carbonate precipitated from a source with low $\delta^{13}C$, such as meteoric water for example.

Regardless of the exact mechanism generating high Δ47 values in some listvenite samples, most of the clumped isotope data cluster around peak temperatures of ~100°C and are consistent with $\delta^{18}O$ values in carbonate and quartz where it appears that stable isotope equilibrium has been achieved. These temperatures are similar to those estimated from mineral parageneses at the boundary of the listvenite. Although these temperatures are significantly lower than the ~150°C clumped isotope temperatures recorded by calcite-bearing metasediments within ~100m of the basal thrust beneath the listvenite, it may be that these metasediments are part of the metamorphic sole, which experienced peak temperatures around 800°C in the early stages of detachment of the ophiolite (Ghent and Stout 1981), and that the fluids responsible for listvenitization were derived from unmetamorphosed sedimentary rocks beneath the sole.

The temperatures recorded by our listvenite samples are warmer than the inferred maximum temperatures of ~65°C for listvenite formation proposed by Wilde et al. (2002), and significantly cooler than temperature estimates from other listvenite bodies worldwide: about 210-250°C in Canada (Madu et al. 1990; Schandl and Wicks 1991;

Andrew 1985), 280-340°C in Armenia (Spiridonov 1991), 200-300°C in eastern Australia (Oskierski et al. 2013), 250-350°C in California (Weir and Kerrick 1987), and 150-250°C in Morocco (Buisson and Leblanc 1987).

Fluid sources for listvenite formation

Sr isotopic data can be viewed as a proxy for the source of Ca, and by association other elements enriched during formation of listvenites. In low-temperature carbonate veins in serpentinite and travertine from the Oman ophiolite, $^{87}Sr/^{86}Sr$ is higher than mantle values but bounded by modern seawater values, suggesting that Sr in those rocks could be derived from seawater via evaporation and rainfall and mantle Sr (Kelemen et al., 2011, Supplementary Figure 3). By contrast, Sr in listvenites must include a substantial component derived from more radiogenic sources. Metasediments underlying the listvenite at the Wadi Mansah locality include several suitably radiogenic sources. The fact that some listvenites have minimum initial $^{87}Sr/^{86}Sr$ in excess of minimum initial values in these metasediments suggests that our sampling may not encompass the full compositional range of the metasediments, or that other sources are involved, such as underlying allochthonous and autochthonous sediments, such as the more radiogenic (~0.72-0.77) clastic sediments measured by Weyhenmeyer et al. (2000).

$\delta^{13}C$ values range from -5.7 to +1.1‰, with overlapping values for listvenites and metasediments, which is also consistent with a sediment-derived source of carbon in the listvenite. Most listvenite and metasediment samples have $\delta^{13}C$ values between -2.5 and +1‰, with the exception of just a few samples. Listvenite and metasediment samples with lower $\delta^{13}C$ values also have higher $\Delta47$ values, which may indicate that these

samples have undergone lower temperature surface weathering, resulting in additional carbonate precipitation and/or isotopic re-equilibration. These lower $\delta^{13}C$ values are consistent with some of the low-temperature carbonate veins in serpentinized peridotite in Oman, which typically have $\delta^{13}C$ values of 0 to -10‰ (Kelemen et al., 2011), suggesting exchange with meteoric source of carbon. Accordingly, we focus primarily on the majority of listvenite and metasediment samples that have higher $\delta^{13}C$ and lower $\Delta 47$ values.

The fluid mediating this transfer could be derived from sediment-equilibrated seawater released upon compaction of pore space or from devolatilization of hydrous minerals in sediments. This would also be consistent with stable isotope data. Assuming the temperatures indicated by mineral paragenesis and the highest recorded clumped isotope temperatures are most representative of the temperature of listvenite formation, at 80-110°C, $\delta^{18}O$ compositions of carbonate and quartz in listvenite would typically be in equilibrium with fluid $\delta^{18}O$ values ranging from about -5 to 7‰, depending on the choice of fractionation factors (Figure 21). The $\delta^{18}O$ of Cretaceous seawater in sedimentary pore space would evolve to about 5 to 7‰ if it were fully equilibrated with authigenic calcite and to about -6 to -9‰ if it were fully equilibrated with clastic quartz[3]. Thus, the listvenite $\delta^{18}O$ values are within the range for fluid derived from subducting sediments. The fact that most dolomite listvenite samples record slightly higher $\delta^{18}O$ could be due to a higher proportion of calcite in the source sediment, consistent with their extreme

[3] assuming an initial temperature of 10°C; initial $\delta^{18}O$ of -1‰ for seawater, 31‰ for calcite, 6‰ for quartz; initial porosity of 0.70; final temperature of 80-110°C; final porosity of 0.56-0.50; and mineral-water fractionation factors from Friedman and O'Neil (1977)

calcium enrichment, or could result from precipitation of dolomite at lower temperatures than magnesite, consistent with the tendency of dolomite to become more stable relative to magnesite at a given fluid Mg/Ca ratio with decreasing temperature (Rosenberg and Mills 1966).

Listvenite formed during the emplacement of the Oman ophiolite provides a window into CO_2 metasomatism in the shallow hanging wall of subduction zones. Along typical subduction zone geotherms, slab-top temperatures around 80-110°C are reached at depths of ~10-30 km (Rupke et al. 2004). Listvenite a few hundred meters above the basal thrust would experience higher temperatures. It is unlikely that listvenitization occurred at pressures greater than 10 kbar or less 2 kb, considering the temperature constraints described above. Geological data also provide constraints on pressure. The crustal section of the Samail ophiolite, overlying mantle peridotites, is 5-7km thick (Nicolas et al. 2000). The mantle section of the ophiolite, overlying the basal thrust, probably had a variable thickness. It is up to 15 km thick in present day sections (e.g., Boudier & Coleman, 1981). This yields a combined thickness of 5 to 22 km for the section overlying the Wadi Mansah listvenites at the time of their formation. At these pressures, high concentrations of CO_2 in the fluid are not required to stabilize magnesite-quartz listvenites. The CO_2 concentration necessary for the stability of magnesite + quartz at these temperatures varies with pressure, from X_{CO2} of at least ~10^{-7} at a pressure of 10kb to at least ~10^{-2} at 10 bar (see Figure 20).

If listvenite formation occurred during emplacement of the ophiolite and the antigorite-quartz-talc assemblage observed at the margins of the listvenite body is indicative of peak temperatures, then seawater CO_2 concentrations would be sufficient to

stabilize magnesite + quartz. In contrast, low pressure alteration involving shallow groundwater at similar temperatures, as in the models of Stanger (1985) and Wilde et al. (Wilde et al. 2002), would require a more CO_2-rich fluid (e.g., X_{CO2} of at least ~10^{-2}).

An alternative method of estimating the required CO_2 concentration for magnesite + quartz stability is through water-rock reaction path models using EQ3/6 v.8.0 (Wolery and Jarek 2003). In these models, water was saturated in CO_2 at 2kb and 100°C or 1bar and 90°C to yield carbon concentrations (X_{CO2}) of $10^{-1.40}$ and $10^{-3.67}$, respectively. These fluids were titrated with the compositional equivalent of average Oman harzburgite resulting in precipitation of magnesite + quartz at high water-rock ratios, with quartz replaced by talc and then antigorite as the water-rock ratio decreased. In these models, talc joined the equilibrium assemblage at X_{CO2} ~$10^{-3.8}$ (~110 ppm C) at 2kb and 100°C, more than order of magnitude higher than phase boundary calculated in THERMOCALC (X_{CO2} ~10^{-5} at 2kb and 100°C), but still only slightly more CO_2-rich than seawater (X_{CO2} ~$10^{-4.4}$ (Turekian 1968)). When the reaction between pore water and peridotite is modeled at 5kb and 100°C, talc joins the equilibrium assemblage at X_{CO2} ~$10^{-3.5}$ (~200 ppm C), a slight increase in X_{CO2} with pressure, whereas talc is not stable relative to magnesite + quartz in THERMOCALC calculations at the same PT above X_{CO2} ~10^{-6}, a significant decrease in X_{CO2} with pressure.

When we look at the listvenite boundary with the eyes of a metamorphic petrologist (THERMOCALC), we see reactions between minerals, CO_2, and H_2O and observe that by Le Chatelier's principle, the reaction 3 magnesite + 4 quartz + H2O = talc + 3 CO2 will have a negative slope in P-X_{CO2} space. The aqueous geochemist (EQ3/6) sees this boundary as a function of the saturation states of magnesite, quartz, and

talc in the fluid, and the role of aqueous species cannot be ignored; indeed they are the basis of the model calculations. Given that the volatile-free bulk composition of the protolith remains practically unchanged in magnesite-quartz listvenite, the phase boundary approach of the metamorphic petrologist may be more appropriate in that case, while the dolomite-quartz listvenite, which has experienced more chemical exchange with the fluid, may require the aqueous geochemist's touch. Although neither model perfectly captures the system—calculation of reactions between mineral end-members in THERMOCALC neglects aqueous species, while EQ3/6 calculations rely on data extrapolated from low *PT* conditions—applying both approaches gives a broader view of the nature of the listvenite-forming reactions.

Metamorphic decarbonation of sediments is not expected to occur in the forearc (e.g., Kerrick and Connolly 2001; Gorman et al. 2006), but carbonate dissolution has been shown to be a source of CO_2 in metasomatic processes in subduction zones (e.g., Mottl et al. 2004; Frezzotti et al. 2011). Carbonate dissolution and release of CO_2-enriched fluids could occur gradually as pore-water in equilibrium with sediments is compacted, or more suddenly as freshwater is released from dehydration of minerals in the sediments, such as clays, and reacts with carbonate-bearing sediments. The resulting fluid, saturated in the minerals in the sedimentary host rock, would rise into the overlying mantle, perhaps migrating first along the slab interface or subparallel faults.

We model the sediment-equilibration process in EQ3/6 as a closed reaction between Cretaceous seawater (Wallmann 2001; Timofeeff et al. 2006) and an excess of calcite, quartz, clinochlore, and kaolinite, at pressures of 1, 2, and 5 kb and temperatures

of 30-250°C. In this model step, calcite dissolution during subduction can result in large increases in the carbon concentration in the fluid, as shown in Figure 22.

Although the carbon concentration of fluids generated at 5kb are in excess of what is necessary to stabilize the carbonate + quartz assemblage that characterizes listvenite, EQ3/6 models of the reaction between this fluid and peridotite at pressures of 2 or 5kb were unsuccessful in producing carbonate, quartz, and talc in ratios consistent with those observed in Oman listvenite.

A rough mass balance calculation shows that the flux of CO_2-bearing fluid from the subducted sediments is sufficient for the formation of the extensive listvenites observed in Oman. A 100-meter thick column of listvenite containing 30 wt% CO_2 contains ~25,000 kg C/m^2. If we assume the fluid carbon concentration was ~250-450ppm C (equilibration of pore water with sediments at 5kb, at temperatures of 50-100°C), then the mass of fluid reacted to form this listvenite would be ~5.5×10^7 to 9.8×10^7 kg/m^2, or ~3-5 kg/yr/m^2 if averaged over ~20Ma of obduction. In the case of pore water release, sediments start with a pore volume fraction of ~0.4-0.7, and after rapid compaction to ~0.2 porosity in the first couple kilometers of burial (or subduction), porosity decreases by ~0.04/km, or ~1.4 wt% water / km (Bond and Kominz 1984) over a depth interval of 2-7km. Thus, for a hypothetical 1500 m column of sediment being subducted at a rate of 6 cm/yr, ~3 kg of pore water/m^2/yr would be released by compaction beneath the hanging wall mantle. This is on the order of the amount of fluid required to form the listvenite. Obviously, these are very approximate calculations. If package of subducting sediment were thinner, it would provide less fluid via compaction; if it were thicker, more fluid. Furthermore, focusing of fluid flow could yield localized,

high fluid fluxes. Seafloor fluid expulsion in forearcs demonstrates that water released by dehydration of subducted sediments is transported both vertically and trench-ward by deep-seated thrust faults (Hensen et al. 2004). In Oman, listvenite follows major fault zones, and the antiformal structure of the Wadi Mansah locality, if present during carbonation, could also have localized fluid flow.

Mineral dehydration could also contribute fluid. Average global subducting sediment (GLOSS) (Plank and Langmuir 1998) contains ~7% mineral-bound water. Thermodynamic models used by, e.g., Gorman et al. (2006) do not include critical reactions involving the transformation of clay minerals to micas and chlorite. These can involve considerable quantities of dehydration. For example, reactions involving clay minerals feldspar and quartz, at depths of 2-5km and temperatures of 80 to 175°C, may evolve up to ~ 30 wt% H_2O (Lynch 1997). For a 1500 m thick sediment section including 50% clay rich lithologies, subducting at 6 cm/yr, this would produce 1800 kg of water/m^2/yr. Thus, shallow dehydration reactions involving clays could be a much larger source of aqueous fluid saturated in sedimentary carbonate minerals, compared to the expulsion of pore waters during compaction. Such transformations of hydrated minerals, including expulsion of interlayer water and conversion of opal-A to opal-CT at 30° to 80°C and expulsion of interlayer water and conversion of smectite to illite at 50° to 150°C have been proposed as the source of low-chlorinity waters upwelling at serpentine mud volcanoes in the Mariana forearc (Mottl et al. 2004) and at seafloor sites in accretionary prisms (Bebout 2013).

At higher temperature, modeling by Rupke et al. (2004) and Gorman et al. (2006) – which does not account for all of the shallower dehydration reactions described in the

previous paragraph, indicates that ~50% of the mineral-bound water in sediments should be released by dehydration in a pulse between ~30 and 50 km depth. A 1500 m column of sediment being subducted at a rate of 6 cm/yr would be expected to release ~6000 kg H_2O/yr in this dehydration front. These are huge fluxes compared to those estimated for compaction, above. If some of this fluid migrated up the subduction zone within a subducting sediment layer, maintaining equilibrium carbon concentrations, and then reacted with peridotite at shallower depth, this would be sufficient to account for the observed mass of carbonates in Oman listvenite.

Implications for carbon capture and storage (CCS)

Carbonation of peridotite has been proposed as a method for permanent CO_2 storage (e.g., Seifritz 1990; Lackner et al. 1995) as well as distributed, geological capture of CO2 (Kelemen and Matter 2008; Kelemen et al. 2011). Natural analogs to *in situ* mineral carbon sequestration in ultramafic bodies present potential alternatives to ex situ mineral carbonation, avoiding the costs of mining, transporting, and treating ultramafic material (e.g., Cipolli et al. 2004; Hansen et al. 2005; Kelemen and Matter 2008; Kelemen et al. 2011; Beinlich et al. 2012). However, a major concern regarding *in situ* carbonation is that the solid volume increases expected during peridotite carbonation would result in loss of porosity and permeability, and armoring of reactive mineral surfaces, thereby limiting reaction progress (e.g., Xu et al. 2004; Hansen et al. 2005).

The presence of listvenite bodies demonstrates that geological carbonation of peridotite can progress to completion under natural conditions.

Hansen et al. (2005) and Beinlich et al. (2012) suggest that smaller solid volume increases associated with carbonation of serpentine rather than olivine reduce the risk of pore space clogging. In Oman, Stanger (1985) proposes that total serpentinization of the basal peridotite preceded formation of the "Amqat" lithology (listvenite). However, we find tens of percent of relict olivine in samples taken within meters of magnesite-quartz listvenites. These relicts are surrounded by high-Fe serpentine that likely formed much later than listvenites, at lower temperatures (Streit et al. 2012), indicating that relict olivine was probably abundant at the initiation of listvenite formation. In spite of the larger volume increases associated with carbonation of olivine, complete carbonation was attained within the listvenite zones.

This solid volume increase may even contribute to reaction progress by maintaining permeability through reaction-driven cracking (e.g., MacDonald and Fyfe 1985; Kelemen et al. 2011; Kelemen and Hirth 2012). Although listvenite bodies in Oman probably follow pre-existing fault zones, and fluid flow may have been localized along such faults, vein orientations in most of our listvenite samples are random or mutually orthogonal, and thus do not appear to be tectonically controlled. Quartz and carbonate veins occur as hierarchical networks extending down to micron scales, forming perpendicular vein sets suggestive of isotropic stresses (e.g., see Figures 4b and 8a). Reaction-driven cracking will be favored when reaction rates are high and stress increases due to volume changes during reaction can outpace viscous relaxation. At ~80-106°C and P_{CO2} on the order of ~1 to 5 bars (surface water at 2 to 10 kb), our fit (Kelemen and Matter 2008) to experimental data on olivine carbonation at pH ~6-8 (O'Connor et al. 2005; Chizmeshya et al. 2007) yields rates ~ 10^4 to 10^5 higher than the

rate of surficial weathering, It appears these conditions were sufficient to promote self-fracturing during peridotite carbonation.

Conclusions

Mineralogical and isotopic data support the hypothesis that magnesite-quartz listvenites formed during obduction of the Oman ophiolite, as CO_2-enriched fluids derived from underlying sediments metasomatized hanging wall peridotite. Globally, extensive carbonation of mantle wedge peridotite may be more common in above subduction zones than has been previously recognized. Even without extremely high CO_2 concentrations and at temperatures below those corresponding to peak reaction rates in olivine carbonation experiments, complete carbonation of peridotite is attainable in nature.

References

Aharon P (1988) A stable-isotope study of magnesites from the Rum Jungle Uranium Field, Australia - Implications for the origin of strata-bound massive magnesites. Chemical Geology 69 (1-2):127-145. doi:10.1016/0009-2541(88)90164-7

Andrew K (1985) Fluid inclusion and chemical studies of gold--quartz veins in the Atlin Camp, Northwestern British Columbia. University of British Columbia, Vancouver, B.C.

Bebout GE (2013) Metasomatism in Subduction Zones of Subducted Oceanic Slabs, Mantle Wedges, and the Slab-Mantle Interface. In: Harlov DE, Austrheim H (eds) Metasomatism and the Chemical Transformation of Rock: The Role of Fluids in Terrestrial and Extraterrestrial Processes. Lecture Notes in Earth System Sciences. Springer, pp 289-349

Beinlich A, Plumper O, Hovelmann J, Austrheim H, Jamtveit B (2012) Massive serpentinite carbonation at Linnajavri, N-Norway. Terra Nova 24 (6):446-455. doi:10.1111/j.1365-3121.2012.01083.x

Bond GC, Kominz MA (1984) Construction of tectonic subsidence curves for the early Paleozoic miogeocline, southern Canadian Rocky Mountains - implications for subsidence mechanisms, age of breakup, and crustal thinning. Geol Soc Am Bull 95 (2):155-173. doi:10.1130/0016-7606(1984)95<155:cotscf>2.0.co;2

Boudier F, Baronnet A, Mainprice D (2010) Serpentine mineral replacements of natural olivine and their seismic implications: Oceanic lizardite versus subduction-related antigorite. J Petrol 51:495-512

Buisson G, Leblanc M (1987) gold in mantle peridotites from upper proterozoic ophiolites in Arabia, Mali, and Morocco. Economic Geology 82 (8):2091-2097

Chacko T, Deines P (2008) Theoretical calculation of oxygen isotope fractionation factors in carbonate systems. Geochim Cosmochim Acta 72:3642-3660

Chizmeshya AVG, McKelvy MJ, Squires K, Carpenter RW, Béarat H (2007) DOE Final Report 924162: A novel approach to mineral carbonation: Enhancing carbonation while avoiding mineral pretreatment process cost 29 pages plus appendices. Arizona State University, Tempe, AZ

Cipolli F, Gambardella B, Marini L, Ottonello G, Zuccolini MV (2004) Geochemistry of high-pH waters from serpentinites of the Gruppo di Voltri (Genova, Italy) and reaction path modeling of CO2 sequestration in serpentinite aquifers. Applied Geochem 19 (5):787-802

Das Sharma S, Patil DJ, Gopalan K (2002) Temperature dependence of oxygen isotope fractionation of CO2 from magnesite-phosphoric acid reaction. Geochim Cosmochim Acta 66:589-593

Dennis KJ, Schrag DP (2010) Clumped isotope thermometry of carbonatites as an indicator of diagenetic alteration. Geochim Cosmochim Acta 74 (14):4110-4122. doi:10.1016/j.gca.2010.04.005

Eiler JM, Schauble E (2004) (OCO)-O-18-C-13-O-16 in Earth's atmosphere. Geochim Cosmochim Acta 68 (23):4767-4777. doi:10.1016/j.gca.2004.05.035

Ferry JM, Passey BH, Vasconcelos C, Eiler JM (2011) Formation of dolomite at 40-80 degrees C in the Latemar carbonate buildup, Dolomites, Italy, from clumped isotope thermometry. Geology 39 (6):571-574. doi:10.1130/g31845.1

Frezzotti ML, Selverstone J, Sharp ZD, Compagnoni R (2011) Carbonate dissolution during subduction revealed by diamond-bearing rocks from the Alps. Nature Geoscience 4 (10):703-706. doi:10.1038/ngeo1246

Friedman I, O'Neil JR (1977) Compilation of stable isotope fractionation factors of geochemical interest. In: Fleischer M (ed) USGS Prof. Paper 440-KK, Data of Geochemistry, 6th Edition. USGS, Reston, VA, p 12

Ghent ED, Stout MZ (1981) Metamorphism at the base of the samail ophiolite, southeastern oman mountains. Journal of Geophysical Research 86 (NB4):2557-2571. doi:10.1029/JB086iB04p02557

Ghosh P, Adkins J, Affek H, Balta B, Guo W, Schauble EA, Schrag D, Eiler JM (2006) 13C–18O bonds in carbonate minerals: A new kind of paleothermometer. Geochim Cosmochim Acta 70:1439-1456

Glennie KW, Bouef MGA, Hughes-Clarke MW, Moody-Stuart M, Pilaar WFH, Reinhardt BM (1974) Geology of the Oman Mountains, vol 31. Verhundelingen van het koninklijk Nederlnnds Geologisch-Mijnbouwkundig Genootschap.

Gorman PJ, Kerrick DM, Connolly JAD (2006) Modeling open system metamorphic decarbonation of subducting slabs. Geochemistry Geophysics Geosystems 7. doi:10.1029/2005gc001125

Gottschalk M (1997) Internally consistent thermodynamic data for rock-forming minerals in the system SiO2-TiO2-Al2O3-Fe2O3-CaO-MgO-FeO-K2O-Na2O-H2O-CO2. European Journal of Mineralogy 9:175-223

Guo WF, Mosenfelder JL, Goddard WA, Eiler JM (2009) Isotopic fractionations associated with phosphoric acid digestion of carbonate minerals: Insights from first-principles theoretical modeling and clumped isotope measurements. Geochim Cosmochim Acta 73 (24):7203-7225. doi:10.1016/j.gca.2009.05.071

Hacker BR, Mosenfelder JL, Gnos E (1996) Rapid emplacement of the Oman ophiolite: Thermal and geochronologic constraints. Tectonics 15 (6):1230-1247. doi:10.1029/96tc01973

Halls C, Zhao R (1995) Listvenite and related rocks: Perspectives on terminology and mineralogy with reference to an occurrence at Cregganbaun, Co. Mayo, Republic of Ireland. Mineral Deposita 30:303-313

Hanghoj K, Kelemen PB, Hassler D, Godard M (2010) Composition and Genesis of Depleted Mantle Peridotites from the Wadi Tayin Massif, Oman Ophiolite; Major and Trace Element Geochemistry, and Os Isotope and PGE Systematics. Journal of Petrology 51 (1-2):201-227. doi:10.1093/petrology/egp077

Hansen LD, Dipple GM, Gordon TM, Kellett DA (2005) Carbonated serpentinite (listwanite) at Atlin, British Columbia: A geological analogue to carbon dioxide sequestration. Can Mineral 43:225-239

Hensen C, Wallmann K, Schmidt M, Ranero CR, Suess E (2004) Fluid expulsion related to mud extrusion off Costa Rica - A window to the subducting slab. Geology 32 (3):201-204. doi:10.1130/g20119.1

Holland TJB, Powell R (1998) An internally consistent thermodynamic data set for phases of petrological interest. J Metamorphic Geol 16:309-343

Holland TJB, Powell R (2011) An improved and extended internally consistent thermodynamic dataset for phases of petrological interest, involving a new equation of state for solids. Journal of Metamorphic Geology 29 (3):333-383. doi:10.1111/j.1525-1314.2010.00923.x

Huntington KW, Eiler JM, Affek HP, Guo W, Bonifacie M, Yeung LY, Thiagarajan N, Passey B, Tripati A, Daëron M, Came R (2009) Methods and limitations of 'clumped' CO2 isotope (Δ47) analysis by gas-source isotope ratio mass spectrometry. Journal of Mass Spectrometry 44 (9):1318-1329. doi:10.1002/jms.1614

Kelemen PB, Hirth G (2012) Reaction-driven cracking during retrograde metamorphism: Olivine hydration and carbonation. Earth and Planetary Science Letters 345:81-89. doi:10.1016/j.epsl.2012.06.018

Kelemen PB, Matter J, Streit EE, Rudge JF, Curry WB, Bluztajn J (2011) Rates and mechanisms of mineral carbonation in peridotite: Natural processes and recipes for enhanced, in situ CO2 capture and storage. Ann Rev Earth Planet Sci 39:545-576

Kelemen PB, Matter JM (2008) In situ carbonation of peridotite for CO2 storage. Proc Nat Acad Sci USA 105:17,295-217,300

Kerrick DM, Connolly JAD (2001) Metamorphic devolatilization of subducted marine sediments and the transport of volatiles into the Earth's mantle. Nature 411 (6835):293-296. doi:10.1038/35077056

Lackner KS, Wendt CH, Butt DP, Joyce EL, Sharp DH (1995) Carbon-dioxide disposal in carbonate minerals. Energy 20 (11):1153-1170

Lynch FL (1997) Frio shale mineralogy and the stoichiometry of the smectite-to-illite reaction: The most important reaction in clastic sedimentary diagenesis. Clays and Clay Minerals 45 (5):618-631. doi:10.1346/ccmn.1997.0450502

MacDonald AH, Fyfe WS (1985) Rate of serpentinization in seafloor environments. Tectonophys 116 (1-2):123-135

Madu BE, Nesbitt BE, Muehlenbachs K (1990) A mesothermal gold-stibnite-quartz vein occurrence in the Canadian Cordillera. Econ Geol 85:1260-1268

Mottl MJ, Wheat G, Fryer P, Gharib J, Martin JB (2004) Chemistry of springs across the Mariana forearc shows progressive devolatilization of the subducting plate. Geochim Cosmochim Acta 68:4915-4933

Nasir S, Al Sayigh AR, Al Harthy A, Al-Khirbash S, Al-Jaaidi O, Musllam A, Al-Mishwat A, Al-Bu'saidi S (2007) Mineralogical and geochemical characterization of listwaenite from the Semail ophiolite, Oman. Chemie Der Erde 67:213-228

Nicolas A, Boudier E, Ildefonse B, Ball E (2000) Accretion of Oman and United Arab Emirates ophiolite: Discussion of a new structural map. Marine Geophys Res 21 (3-4):147-179

Northrop DA, Clayton RN (1966) Oxygen-isotope fractionations in systems containing dolomite. Journal of Geology 74 (2):174-&

O'Connor WK, Dahlin DC, Rush GE, Gerdemann SJ, Nilsen DN (2005) Final report: Aqueous mineral carbonation, DOE/ARC-TR-04-002. Office of Process Development, Albany Research Center, Office of Fossil Energy, US DOE, Albany, OR

Oskierski HC, Bailey JG, Kennedy EM, Jacobsen G, Ashley PM, Dlugogorski BZ (2013) Formation of weathering-derived magnesite deposits in the New England Orogen, New South Wales, Australia: Implications from mineralogy, geochemistry and genesis of the Attunga magnesite deposit. Mineralium Deposita 48 (4):525-541. doi:10.1007/s00126-012-0440-5

Passey BH, Henkes GA (2012) Carbonate clumped isotope bond reordering and geospeedometry. Earth and Planetary Science Letters 351:223-236. doi:10.1016/j.epsl.2012.07.021

Passey BH, Levin NE, Cerling TE, Brown FH, Eiler JM (2010) High-temperature environments of human evolution in East Africa based on bond ordering in paleosol carbonates. Proc Natl Acad Sci U S A 107 (25):11245-11249. doi:10.1073/pnas.1001824107

Plank T, Langmuir CH (1998) The chemical composition of subducting sediment and its consequences for the crust and mantle. Chemical Geology 145 (3-4):325-394. doi:10.1016/s0009-2541(97)00150-2

Rioux M, Bowring S, Kelemen P, Gordon S, Dudas F, Miller R (2012) Rapid crustal accretion and magma assimilation in the Oman-UAE ophiolite: High precision U-Pb zircon geochronology of the gabbroic crust. Journal of Geophysical Research-Solid Earth 117. doi:10.1029/2012jb009273

Rose G (1837) Mineralogisch-geognostiche Reise nach dem Ural, dem Altai und dem Kaspischen Meere. Volume 1: Reise nach dem nördlichen Ural und dem Altai. G.E. Reimer (Verlag der Sanderschen Buchhandlung), Berlin

Rosenberg PE, Mills JW (1966) A mechanism for emplacement of magnesite in dolomite. Economic Geology 61 (3):582-&

Rupke LH, Morgan JP, Hort M, Connolly JAD (2004) Serpentine and the subduction zone water cycle. Earth and Planetary Science Letters 223 (1-2):17-34. doi:10.1016/j.epsl.2004.04.018

Schandl ES, Wicks FJ (1991) Carbonate and associated alteration of ultramafic and rhyolitic rocks at the Hemingway Property, Kidd Creek Volcanic Complex, Timmins, Ontario. Econ Geol 88:1615-1635

Schauble EA, Ghosh P, Eiler JM (2006) Preferential formation of C-13-O-18 bonds in carbonate minerals, estimated using first-principles lattice dynamics. Geochim Cosmochim Acta 70 (10):2510-2529. doi:10.1016/j.gca.2006.02.011

Schmidt M, Xeflide S, Botz R, Mann S (2005) Oxygen isotope fractionation during synthesis of CaMg carbonate and implications for sedimentary dolomite formation. Geochim Cosmochim Acta 69:4665-4674

Seifritz W (1990) CO2 disposal by means of silicates. Nature 345:486

Sharp ZD, Kirschner DL (1994) Quartz-calcite oxygen-isotope thermometry - A calibration based on natural isotopic variations. Geochim Cosmochim Acta 58 (20):4491-4501. doi:10.1016/0016-7037(94)90350-6

Sheppard SM, Schwarcz HP (1970) Fractionation of carbon and oxygen isotopes and magnesium between coexisting metamorphic calcite and dolomite. Contributions to Mineralogy and Petrology 26 (3):161-&. doi:10.1007/bf00373200

Spiridonov EM (1991) Listvenites and zodites. Int Geol Rev 33:397-407

Stanger G (1985) Silicified serpentinite in the Semail nappe of Oman. Lithos 18 (1):13-22

Streit E, Kelemen P, Eiler J (2012) Coexisting serpentine and quartz from carbonate-bearing serpentinized peridotite in the Samail Ophiolite, Oman. Contributions to Mineralogy and Petrology 164 (5):821-837. doi:10.1007/s00410-012-0775-z

Tilton GR, Hopson CA, Wright JE (1981) Uranium-lead isotopic ages of the Samail Ophiolite, Oman, with applications to Tethyan ocean ridge tectonics. J Geophys Res 86:2763-2775

Timofeeff MN, Lowenstein TK, da Silva MA, Harris NB (2006) Secular variation in the major-ion chemistry of seawater: Evidence from fluid inclusions in Cretaceous halites. Geochim Cosmochim Acta 70 (8):1977-1994. doi:10.1016/j.gca.2006.01.020

Trommsdorff V, Evans BW (1972) Progressive metamorphism of antigorite schists in the Bergell tonalite aureole (Italy). Am J Sci 272 (5):423-437

Turekian KK (1968) Oceans. Prentice-Hall, Englewood, Cliffs, N.J.

Vasconcelos C, McKenzie JA, Warthmann R, Bernasconi SM (2005) Calibration of the d18O paleothermometer for dolomite precipitated in microbial cultures and natural environments. Geology 33:317-320

Villey M, Le Metour J, De Gramont X (1986) Geological Map of Fanjah.

Wallmann K (2001) Controls on the Cretaceous and Cenozoic evolution of seawater composition, atmospheric CO2 and climate. Geochim Cosmochim Acta 65 (18):3005-3025. doi:10.1016/s0016-7037(01)00638-x

Weir RH, Kerrick DM (1987) Mineralogic, fluid inclusion, and stable isotope studies of several gold-mines in the Mother Lode, Tuolumne and Mariposa Counties, California. Economic Geology 82 (2):328-344

Weyhenmeyer CE (2000) Origin and evolution of groundwater in the alluvial aquifer of the eastern Batinah coastal plain, Sultanate of Oman: A hydrogeochemical approach. Universität Bern, Bern, Switzerland

Wilde A, Simpson L, Hanna S (2002) Preliminary study of Cenozoic alteration and platinum deposition in the Oman ophiolite. J Virtual Explorer 6:7-13

Wolery TW, Jarek RL (2003) Software User's Manual EQ3/6, Version 8.0. US Department of Energy, Office of Civilian Radioactive Waste Management, Office of Repository Development, Software Document Number 10813-UM-8.0-00,376.

Xu WY, Apps JA, Pruess K (2004) Numerical simulation of CO2 disposal by mineral trapping in deep aquifers. Applied Geochem 19:917-936

Table 1. Mineral parageneses

Sample	type	Mgs	Dol	Cc	Qtz	Tlc	Serp:	Liz	Atg	Chl	Ol	Kao	Sp	Fe-ox	Mag?	Di	En	un-ID, %I	Other phases
OM09-11	listv.	77			23														fuchs (tr)
OM09-15	listv.	10			90														
OM09-16	listv.	78			22	x													
OM09-18	listv.	79	tr		21								x	x					
OM09-19	listv.	X	X		X									x					
OM09-20	listv.		86		14														
OM09-27	listv.		X		X								x	x					Anhy (tr), celest (tr), hal(tr)
OM09-28	listv.	79	1		20														
OM09-29	listv.	X	X		X								x						
OM09-30	listv.	80	18		2														
OM10-03	listv.	64	36										x						
OM10-25	listv.	76	9	2	13														
OM10-26	listv.	75			25													44.6, 20%	fuchs (min), pheng (tr), bar (tr), psi (tr), hpr (tr)
OM09-65	listv.		35	64	1														
OM09-66	listv.		62		45							3							
OM09-67	listv.		44		56														
OM09-69	listv.		73		27														
OM09-71	listv.	X	X	X	X								x	x					Barite (tr)
OM09-73	listv.		97		3														
OM09-74	listv.	X	x	tr	X								x	x					

Numbers indicate semi-quantitative estimates of abundances from Match! XRD software.
X = major phase, x =minor phase, tr = trace phase
Mag? = thin section billet attracted to hand magnet? X=strongly, x=weakly
Abbreviations: listv.= listvenite, trans. = transitional zone between listvenite and serpentinized peridotite, s.p.=serpentinized peridotite; mgs=magnesite, dol=dolomite, cc=calcite, qtz=quartz, serp=serpentine, atg=antigorite, chl=chlorite, kaol=kaolinite (represents clay), fe-ox=iron oxides, di=diopside, en=enstatite, anhy=anhydrite, celest=celestine, hal=halite fuchs=fuchsite, pheng=phengite, bar=barite, psi=psilomelane, hpr=hydrous pseudorutile; un-ID=2-theta of peaks which were not well matched with any minerals with relative intensity noted.

Table 1. Mineral Parageneses (continued)

Sample	type	Mgs	Dol	Cc	Qtz	Tlc	Serp:	Liz	Atg	Chl	Ol	Kao	Sp	Fe-ox	Mag?	Di	En	un-ID, %I	Other phases
OM09-75	listv.		83	3	9							5							
OM10-09	listv.		X										x					27.9, 1%	psi (minor)
OM10-10	listv.		38	5	57														
OM10-11	listv.		99		1														
OM10-13	listv.																		
OM10-14	listv.		90	5	5														
OM10-15	listv.		77	8	15													27.8, 2%	
OM10-19	listv.		69	5	26													27.8, 2%	
OM10-20	listv.		78	4	18													27.8, 2%	
OM10-24	listv.		76	30	4													27.8, 2%	
OM09-12	trans.	8	4		3	tr	76	34	42	9			x	x					
OM10-02	trans.	53	5			9	33	19	14		tr		x						Ni-sulfide, Ni-serp
OM10-04	trans.	38	3				59	31	28				x						
OM10-05	trans.		14				86	40	46				x		x				
OM09-13	s.p.						71	32	39	29			x	x	X				
OM09-14	s.p.						27				57						16		
OM10-01	s.p.						50	9	41		27						23		Cu-Fe-sulfide (tr)
OM10-08	s.p.						100	67	33										
OM10-06	s.p.						59	26	33		41			x	X				
OM10-07	s.p.						73	25	48		27			x	X	x			

Table 2: Averaged electron micro-probe analyses of carbonate minerals (sample numbers prefixed "OM")

Sample:	09-15	09-27	09-71	09-74	10-10	09-16	09-18	09-19	09-27	09-28	09-71	09-74	10-04	10-10	10-26	09-12	10-05
Lithology:	listv.	listv.	listv.	listv.	listv.	listv.	listv.	listv.	listv.	listv.	listv.	listv.	listv.	listv.	listv.	s.p.	s.p.
Mineral:	cc	cc	cc	cc	cc	dol	dol	dol	dol	dol	dol	dol	dol	dol	dol	dol	dol
wt%																	
stdev																	
CaO	49.7	54.0	44.7	54.8	56.4	29.5	28.4	28.7	28.5	28.6	27.4	29.3	29.8	30.1	29.9	29.5	28.8
	1.0	*0.5*	*3.8*	*1.4*	*2.4*	*0.9*	*0.2*	*0.5*	*0.7*	*1.5*	*1.8*	*2.2*	*0.6*	*0.4*	*0.2*	*0.6*	*0.4*
MgO	3.1	1.6	2.9	1.2	1.5	18.7	20.2	18.1	19.2	21.3	16.6	18.2	21.9	21.8	22.1	20.8	20.8
	1.2	*0.1*	*0.8*	*1.0*	*0.4*	*1.1*	*0.1*	*0.7*	*1.0*	*1.2*	*1.2*	*1.2*	*0.5*	*0.2*	*0.2*	*0.8*	*0.4*
FeO	1.7	0.3	5.2	0.1	0.0	4.1	1.9	4.0	3.7	1.7	2.3	3.0	1.2	0.0	0.3	2.0	0.4
	1.3	*0.2*	*1.9*	*0.1*	*0.0*	*2.5*	*0.1*	*0.5*	*1.0*	*1.1*	*1.1*	*1.5*	*0.7*	*0.0*	*0.2*	*0.9*	*0.1*
MnO	0.01	0.01	0.02	0.19	0.03	0.02	-	-	0.09	0.05	0.10	0.10	0.02	0.04	0.01	-	1.07
	0.02	*0.01*	*0.02*	*0.11*	*0.03*	*0.03*			*0.03*	*0.04*	*0.13*	*0.11*	*0.02*	*0.04*	*0.01*		*0.31*
Total	54.5	55.9	52.8	56.3	58.7	52.3	50.5	50.8	51.5	51.7	46.6	50.7	53.2	52.0	52.5	52.3	51.2
	0.8	*0.5*	*2.8*	*0.8*	*2.7*	*0.7*	*0.2*	*0.3*	*1.2*	*0.9*	*1.2*	*1.8*	*0.4*	*0.3*	*0.2*	*0.7*	*0.4*
Mole %																	
cc	89.9	95.6	84.6	97.0	96.5	50.3	49.0	50.3	49.1	48.0	52.4	51.4	48.8	49.9	49.1	49.1	49.6
mgs	7.7	4.0	7.7	3.0	3.5	44.2	48.4	44.1	45.9	49.8	44.2	44.4	49.7	50.1	50.5	48.3	49.9
sid	2.4	0.4	7.7	0.1	0.0	5.5	2.6	5.5	5.0	2.2	3.4	4.1	1.5	0.0	0.4	2.6	0.5
n	5	3	10	16	6	14	4	16	12	13	12	118	8	7	2	5	3

Table 2 (Continued): Electron micro-probe analyses of carbonate minerals

Sample:	09-11	09-16	09-18	09-19	09-28	09-29	09-71	09-74	10-03	10-04	10-26	10-02	10-05	10-06	Calcite	Dolomite	Siderite
Lithology:	listv.	listv.	listv.	listv.	listv.	listv.	listv.	listv.	listv.	lsv-tr.	listv.	lsv-tr.	s.p.	s.p.	std	std	std
Mineral	mgs	mgs	mgs	mgs	mgs	mgs	mgs	mgs	mgs	mgs	mgs	mgs	mgs	mgs	cc	dol	sid
wt%																	
stdev																	
CaO	0.3	0.1	0.2	0.5	0.3	0.4	0.5	0.2	0.1	0.2	0.4	0.1	0.2	1.1	56.2	30.2	0.0
	0.2	*0.1*	*0.2*	*0.3*	*0.2*	*0.4*	*0.3*	*0.1*	*0.0*	*0.3*	*0.2*	*0.1*	*0.2*	*0.6*	*0.3*	*0.6*	*0.0*
MgO	53.3	46.2	52.8	51.7	46.4	43.7	43.3	45.6	47.4	46.4	45.5	46.6	54.6	49.3	0.1	22.0	0.2
	4.2	*0.8*	*3.4*	*3.4*	*0.7*	*3.4*	*3.5*	*1.1*	*0.7*	*0.6*	*1.4*	*1.6*	*1.0*	*2.6*	*0.1*	*0.3*	*0.1*
FeO	3.4	3.8	3.8	4.0	3.8	6.5	4.3	4.3	3.5	5.4	5.0	4.6	3.0	0.5	0.0	0.1	57.9
	2.8	*0.9*	*1.4*	*1.5*	*1.0*	*5.0*	*0.9*	*1.8*	*0.5*	*1.0*	*2.2*	*2.1*	*0.6*	*0.4*	*0.0*	*0.1*	*0.6*
MnO	-	0.07	-	-	0.04	0.32	0.04	0.11	0.09	0.72	0.09	0.19	0.60	0.89	0.12	0.02	2.68
		0.05			*0.02*	*0.28*	*0.02*	*0.03*	*0.08*	*0.51*	*0.06*	*0.11*	*0.08*	*0.11*	*0.04*	*0.02*	*0.09*
Total	57.0	50.1	57.1	56.2	50.6	51.0	48.2	50.3	51.4	53.6	51.0	53.8	58.8	52.8	56.5	52.4	61.0
	1.6	*0.7*	*2.3*	*2.9*	*0.6*	*2.1*	*3.1*	*1.4*	*0.5*	*0.8*	*1.2*	*1.8*	*1.2*	*1.6*	*0.3*	*0.4*	*0.6*
Mole %																	
cc	0.4	0.2	0.3	0.7	0.4	0.6	0.9	0.3	0.2	0.3	0.5	0.1	0.2	1.6			
mgs	96.1	95.4	95.7	95.1	95.2	91.6	93.9	94.7	95.8	93.6	93.6	94.0	96.8	97.8			
sid	3.6	4.4	4.0	4.2	4.4	7.7	5.2	5.0	4.0	6.1	5.8	5.9	3.0	0.6			
n	16	14	9	31	20	7	5	12	8	8	16	24	2	5	6	9	6

Abbreviations: listv. = listvenite, lsv-tr. = transitional listvenite, s.p. = serpentinized peridotite; cc = calcite, mgs = magnesite, sid = siderite

Table 3: Electron micro-probe analyses of chlorite, serpentine, and talc (sample numbers prefixed "OM")

Sample:	10-04	10-26	10-07	09-12	10-04	09-13	10-01	10-02	10-02	10-05	10-06	10-06	10-07	09-16	10-02
Lithology:	lsv-tr.	listv.	s.p.	s.p.	lsv-tr.	s.p.	s.p.	lsv-tr.	lsv-tr.	s.p.	s.p.	s.p.	s.p.	listv.	lsv-tr.
Mineral:	chl	chl	chl	atg	serp	serp	serp	serp	Ni-serp	serp	serp1	serp2	serp	talc	talc
wt%															
stdev															
SiO2	33.3	48.5	34.5	44.3	43.2	41.4	41.7	42.8	34.0	42.6	40.5	35.7	42.4	59.9	58.2
	0.7	*1.5*	*0.2*	*2.0*	*0.7*	*2.0*	*1.5*	*0.6*	*1.2*	*1.8*	*3.2*	*2.6*	*1.6*	*0.7*	*1.9*
Al2O3	13.80	22.88	11.67	0.78	0.11	1.22	0.21	0.08	0.01	0.16	0.04	0.03	1.55	0.23	0.02
	0.27	*12.03*	*0.93*	*0.53*	*0.22*	*1.40*	*0.68*	*0.08*	*0.01*	*0.25*	*0.10*	*0.14*	*0.79*	*0.05*	*0.02*
FeO	3.6	0.7	3.9	3.1	2.5	3.9	5.0	2.7	3.2	4.0	4.2	11.5	3.6	1.1	2.3
	0.2	*0.4*	*0.2*	*0.5*	*0.5*	*1.0*	*2.8*	*0.4*	*0.2*	*2.9*	*1.6*	*2.8*	*0.5*	*0.1*	*0.4*
MgO	34.8	10.7	36.1	36.5	40.5	37.2	41.1	40.2	15.6	38.7	40.6	37.3	39.9	27.8	31.4
	0.2	*7.6*	*0.1*	*2.9*	*1.1*	*1.3*	*3.8*	*1.1*	*2.7*	*3.4*	*1.7*	*2.1*	*0.4*	*0.3*	*0.8*
Cr2O3	1.82	1.61	0.29	0.08	0.03	0.22	0.03	0.02	0.39	0.08	0.02	0.01	0.15	0.01	0.01
	0.50	*1.38*	*0.16*	*0.19*	*0.05*	*0.35*	*0.07*	*0.04*	*0.20*	*0.20*	*0.02*	*0.02*	*0.13*	*0.01*	*0.02*
NiO	0.15	0.13	0.19	0.27	0.34	0.23	0.36	0.36	33.60	0.43	0.32	0.46	0.18	1.23	0.32
	0.04	*0.09*	*0.06*	*0.21*	*0.13*	*0.08*	*0.10*	*0.12*	*5.11*	*0.31*	*0.09*	*0.09*	*0.11*	*0.17*	*0.18*
Total	87.6	87.0	87.0	85.1	86.7	84.4	88.6	86.0	87.0	86.1	85.7	85.1	87.9	90.8	92.3
	0.4	*2.4*	*0.9*	*3.5*	*1.0*	*2.8*	*1.0*	*1.5*	*4.8*	*3.0*	*2.3*	*1.6*	*0.9*	*1.1*	*1.0*
Mg#	94.5	95.0	96.2	95.5	96.6	94.4	93.5	96.4	89.5	94.3	94.6	85.3	95.2	97.8	96.1
n	4	5	3	45	39	5	13	56	6	17	39	27	8	6	6

Abbreviations: listv.= listvenite, lsv-tr. = transitional listvenite, s.p. = serpentinized peridotite; chl = chlorite, atg = antigorite, serp = serpentine

Table 4: Electron micro-probe analyses of olivine

Sample:	OM10-02	OM10-01	OM10-06	OM10-07
Lithology:	s.p.	s.p.	s.p.	s.p.
wt%				
stdev				
SiO2	43.6	40.9	40.5	40.5
	0.4	*0.5*	*0.4*	*0.2*
FeO	2.2	9.1	8.5	10.6
	0.7	*0.2*	*0.1*	*0.9*
MgO	55.0	50.0	51.6	50.4
	2.2	*0.2*	*0.6*	*1.9*
NiO	0.25	0.40	0.40	0.43
	0.08	*0.02*	*0.03*	*0.03*
Total	101.2	100.6	101.2	102.2
	1.8	*0.3*	*0.7*	*0.7*
Mg#	97.8	90.7	91.5	89.5
n	2	4	9	2

Abbreviation: s.p. = (partially) serpentinized peridotite

Table 5: Electron micro-probe analyses of spinels (sample numbers prefixed "OM")

Sample:	09-18	09-74	10-03	10-04	10-04	10-09a	09-12	10-02	10-02	10-05	10-05	10-08	09-13	10-01	10-06	10-06
Lithology:	listv.	listv.	listv.	listv.	listv.	listv.	s.p.	s.p.	s.p.	s.p.	s.p.	s.p.	s.p.	s.p.	s.p.	s.p.
wt%																
stdev																
Al2O3	7.5	33.5	14.6	0.7	15.1	32.4	0.4	3.2	4.7	2.5	13.8	8.8	6.6	46.9	3.3	16.6
	0.2		*4.9*	*0.7*	*1.3*	*0.8*	*0.2*	*0.6*	*0.8*	*1.4*	*0.7*	*0.4*	*3.5*	*1.2*	*3.0*	*0.4*
FeO*	26.0	17.7	25.5	49.2	24.6	17.2	61.3	40.8	28.0	47.6	24.4	24.5	56.9	14.8	53.2	26.4
	0.3		*6.4*	*3.5*	*1.3*	*1.0*	*1.6*	*2.7*	*1.8*	*5.0*	*1.2*	*1.1*	*10.5*	*0.7*	*10.3*	*3.1*
FeO	23.0	17.2	22.3	25.8	22.5	16.7	28.5	23.2	22.1	25.9	22.8	22.1	25.5	12.3	26.5	22.3
	0.4		*2.6*	*0.6*	*1.6*	*0.4*	*0.5*	*0.7*	*0.9*	*0.8*	*1.4*	*0.7*	*1.0*	*0.5*	*0.3*	*1.0*
Fe2O3	3.3	0.6	3.6	26.0	2.3	0.5	36.4	19.6	6.6	24.1	1.7	2.7	35.0	2.8	29.7	4.6
	0.1		*4.6*	*4.4*	*1.1*	*1.2*	*1.9*	*2.3*	*1.3*	*5.4*	*0.6*	*0.7*	*11.4*	*0.4*	*11.1*	*2.5*
MgO	6.2	12.5	6.8	2.0	7.1	11.7	0.3	4.2	6.2	2.1	6.8	7.1	4.1	17.4	2.2	7.5
	0.1		*2.4*	*0.3*	*1.3*	*0.9*	*0.2*	*0.4*	*0.7*	*0.2*	*1.2*	*0.5*	*0.8*	*0.4*	*1.0*	*0.9*
MnO	0.46	0.16	0.44	0.65	0.44	0.20	1.31	0.59	0.94	0.53	0.43	0.42	0.66	0.15	0.78	0.41
	0.04		*0.22*	*0.07*	*0.16*	*0.04*	*0.08*	*0.03*	*0.35*	*0.12*	*0.04*	*0.05*	*0.19*	*0.02*	*0.23*	*0.03*
Cr2O3	58.6	33.7	48.9	38.5	50.8	36.4	29.2	43.5	59.0	37.6	52.7	59.1	27.8	20.0	33.6	47.3
	0.2		*6.4*	*3.7*	*1.8*	*0.7*	*1.7*	*1.8*	*1.3*	*2.8*	*1.7*	*1.1*	*7.7*	*1.1*	*8.5*	*3.2*
Total	99.2	98.3	97.4	95.2	98.9	98.4	93.7	95.4	100.1	94.3	98.9	100.7	100.5	100.2	97.9	99.4
	0.5		*2.0*	*1.2*	*1.6*	*1.1*	*1.4*	*0.6*	*1.1*	*1.8*	*1.2*	*0.4*	*0.6*	*0.4*	*1.3*	*0.8*
Mole %																
MgAl2O4	16	57	30	3	30	55	3	8	11	7	28	18	15	73	9	33
Fe3O4	4	1	5	39	3	1	53	28	9	36	2	3	47	3	42	6
FeCr2O4	62	41	59	46	60	42	39	46	55	49	62	59	29	22	42	56
MgCr2O4	18	0	6	12	7	0	5	19	25	8	8	20	10	0	8	6
Mg#	29.7	55.6	32.7	6.8	33.9	54.8	0.8	15.6	28.4	7.3	33.1	34.2	11.9	68.1	7.4	33.6
Cr#	84.0	40.3	69.6	97.5	69.2	43.0	98.0	90.2	89.4	91.2	72.0	81.8	74.6	22.6	89.5	65.6
n	2	1	13	8	10	6	6	4	27	3	5	13	5	13	6	3

FeO:Fe_2O_3 ratio calculated assuming spinel group formula of $A^{2+}B^{3+}{}_2O_4$, where A is Mg^{2+}, Mn^{2+}, or Fe^{2+}, and B is Al^{3+}, Cr^{3+}, or Fe^{3+}

Table 6: EMPA of minerals found in a limited number of samples (sample numbers prefixed "OM")

Sample:	10-26	10-26	10-26	09-27	09-27	10-01	10-07		10-02
Lithology	listv.	listv.	listv.	listv.	listv.	s.p.	s.p.		s.p.
Mineral	Fuchs.	Pheng.	HPR	Anhydr.	Celest.	En	Di		Ni-sulfide
wt%								wt%	
stdev								*stdev*	
SiO2	28.8	53.1	1.8	0.6	0.5	54.4	54.8	Si	1.5
	9.3		*1.7*	*0.4*					*1.3*
TiO2	0.4	0.0	84.9	0.0	0.0	0.1	0.0	Ti	0.0
	0.6		*4.9*	*0.0*					*0.0*
Al2O3	14.3	25.9	0.2	0.0	0.0	4.2	0.2	Al	0.0
	3.2		*0.2*	*0.0*					*0.0*
FeO*	6.8	2.7	6.1	3.4	2.4	5.4	1.3	Fe	0.4
	2.4		*1.1*	*3.3*					*0.6*
MgO	3.5	3.0	0.1	2.0	0.6	31.2	19.2	Mg	0.0
	1.6		*0.1*	*1.0*					*0.0*
CaO	0.4	0.2	0.0	36.8	1.9	3.8	25.0	Ca	0.0
	0.1		*0.0*	*2.9*					*0.0*
K2O	3.4	7.9		0.0	0.0	0.0	0.0	K	
	1.2			*0.0*					
SO3			0.0	50.6	36.0			S	27.7
			0.0	*6.9*					*7.9*
SrO					45.5			Sr	
Cr2O3	19.8	2.1	1.0	0.1	0.1	0.7	0.0	Cr	0.0
	8.4		*1.4*	*0.0*					*0.0*
NiO	0.90	0.10	0.03	0.02	0.00	0.10	0.04	Ni	58.4
	0.40		*0.03*	*0.02*					*13.1*
Total	78.7		94.2	93.7	89.9	100.1	100.8	Total	88.0
	5.6		*2.1*	*3.6*					*14.9*
n	36	1	7	2	1	1		*n*	5

Abbreviations: listv. = listvenite, s.p. = serpentinized peridotite; Fuchs. = fuchsite, Pheng. = phengite, HPR = hydrated pseudorutile, Anhydr. = anhydrite, Celest. = celestine, En = enstatite Di = diopside

Additional notes: The average composition of magnesite in OM10-02 has been subtracted from contaminated analyses of Ni-sulfide

Table 7. Bulk Sr isotopic data

Sample No,	Type	Sr, ppm	Rb, ppm	87Sr/86Sr, meas.	87Sr/86Sr, 94Ma
OM10-11	dol-qtz listv.	297	0.4	0.709548	0.709543
OM10-14	dol-qtz listv.	258	0.4	0.709600	0.709594
OM10-15	dol-qtz listv.	190	0.8	0.712724	0.712708
OM10-20	dol-qtz listv.	326	0.7	0.711183	0.711175
OM09-20	dol-qtz listv.	339	0.6	0.713542	0.713536
OM09-15	mgs-qtz listv.	48	0.7	0.709531	0.709476
OM10-03	mgs-qtz listv.	23	0.3	0.711304	0.711259
OM10-26	mgs-qtz listv.	42	22.8	0.711393	0.709331
OM10-02	talc listv.	41	0.0	0.710738	0.710738
OM11-17	talc listv. (Tuf)	128	0.0	0.708475	0.708475
OM10-18	metased.	1736	3.5	0.711211	0.711204
OM11-39	metased.	58	79.0	0.715810	0.710699
OM11-42	metased.	40	68.0	0.718880	0.712516
OM11-43	metased.	682	12.5	0.709080	0.709011
OM11-45	metased.	225	0.7	0.708348	0.708336
OM11-47	metased.	59	0.8	0.709190	0.709139
OM11-48	metased.	500	79.4	0.708950	0.708351
OM11-50	metased.	172	0.0	0.706125	0.706125
OM10-21	metavolc.	357	6.7	0.705433	0.705362
OM11-41	metavolc.	421	7.4	0.704419	0.704353
2-σ analytical uncertainty:		4.6	1.7	0.000003	

Table 8: OM10-26 Rb-Sr data for isochron, Rb and Sr concentrations by ICPMS

Subset	Side slope	Current	Rb	± 2σ	Sr	± 2σ	Rb/Sr	± 2σ	87Sr/86Sr
2	Hand-magnet		6.5	0.3	42.4	0.8	0.153	0.007	0.709922
3	20°	0.25 A	4.4	0.3	76.6	1.1	0.057	0.004	0.709405
4	20°	0.5 A	9.4	0.3	36.3	0.9	0.258	0.011	0.710919
5	20°	0.7 A	49.7	0.8	77.9	1.5	0.638	0.016	0.713141
6	20°	0.9 A	62.3	0.9	55.9	1.4	1.115	0.032	0.713900
7	20°	1.2 A	54.8	0.7	43.9	0.9	1.249	0.031	0.714000
8	5°	1.2 A	36.3	0.5	50.9	0.8	0.712	0.015	0.712755
Bulk			23.6	0.8	40.6	1.6	0.580	0.029	0.711393

Table 9. Sample-averaged clumped isotope data for listvenites and associated rock

Year	Type	Sample	Min.	n	$\delta^{13}C$, ‰	$\delta^{18}O$ carb. ‰ (VSMOW)	Δ47	T, °C
2011	listv.	OM09-19 dol	Dol	1	0.71 ± 0.25	25.00 ± 0.05	0.456 ± 0.036	107 + 28 /- 23
2012	listv.	OM09-20-c	Dol	2	1.09 ± 0.05	25.17 ± 0.07	0.475 ± 0.020	94 + 13 /- 12
2012	listv.	OM09-20-f	Dol	2	0.83 ± 0.03	25.90 ± 0.04	0.454 ± 0.016	108 + 12 /- 11
2009	listv.	OM09-27	Dol	1	0.80 ± 0.00	24.74 ± 0.01	0.533 ± 0.047	63 + 25 /- 20
2009	listv.	OM09-75	Dol	1	0.19 ± 0.00	23.09 ± 0.00	0.450 ± 0.047	111 + 38 /- 29
2012	listv.	OM10-14	Dol	2	-1.65 ± 0.03	19.75 ± 0.04	0.522 ± 0.017	68 + 9 /- 8
2011	listv.	OM10-15	Dol	2	-0.30 ± 0.02	24.23 ± 0.08	0.440 ± 0.035	119 + 30 /- 24
2012	listv.	OM10-20	Dol	2	-0.36 ± 0.05	26.34 ± 0.01	0.516 ± 0.019	72 + 10 /- 9
2011	listv.	OM10-11	Dol	2	-5.66 ± 0.08	21.85 ± 0.06	0.604 ± 0.035	*35 + 9 /- 8*
2012	listv.	OM09-11	Mgs	2	0.67 ± 1.03	23.85 ± 1.11	0.468 ± 0.036	94 + 27 /- 22
2012	listv.	OM09-15	Mgs	2	-2.34 ± 0.34	22.25 ± 0.50	0.506 ± 0.025	72 + 15 /- 13
2012	listv.	OM09-16	Mgs	2	-0.91 ± 0.15	21.90 ± 1.15	0.467 ± 0.030	95 + 22 /- 19
2012	listv.	OM09-18	Mgs	2	-1.56 ± 0.04	22.42 ± 0.11	0.464 ± 0.020	97 + 14 /- 13
2011	listv.	OM09-19 mgs	Mgs	2	0.16 ± 0.12	24.28 ± 0.32	0.494 ± 0.035	79 + 23 /- 19
2012	lsv.-tr	OM10-02	Mgs	1	-0.62 ± 0.06	22.82 ± 0.12	0.517 ± 0.024	65 + 13 /- 12
2011	listv.	OM10-03	Mgs	2	-2.42 ± 0.13	22.43 ± 0.35	0.534 ± 0.035	57 + 18 /- 16
2012	listv.	OM10-03-s	Mgs	1	-2.57 ± 0.06	22.91 ± 0.12	0.541 ± 0.021	53 + 11 /- 10
2012	lsv.-tr	OM10-04	Mgs	2	-3.56 ± 0.33	23.34 ± 0.36	0.616 ± 0.017	*32 + 4 /- 4*
2011	listv.	OM10-26	Mgs	2	0.09 ± 0.02	24.56 ± 0.10	0.461 ± 0.035	100 + 27 /- 22
2012	tlc-listv.	OM11-17	Mgs	2	-5.04 ± 0.17	28.05 ± 0.22	0.637 ± 0.029	*27 + 7 /- 6*
2012	tlc-listv.	OM11-94	Mgs	2	1.86 ± 0.08	12.75 ± 0.10	0.307 ± 0.021	299 + 63 /- 47
2012	metased.	OM11-43	Cc	1	-2.40 ± 0.05	21.35 ± 0.09	0.408 ± 0.026	149 + 27 /- 23
2012	metased.	OM11-45	Cc	1	-0.07 ± 0.05	22.20 ± 0.09	0.411 ± 0.022	146 + 22 /- 19
2012	metased.	OM11-48	Cc	1	-0.47 ± 0.05	21.11 ± 0.09	0.392 ± 0.026	165 + 30 /- 25
2012	metased.	OM11-47	Dol	1	-4.44 ± 0.05	21.68 ± 0.09	0.554 ± 0.025	54 + 11 /- 10

δ13C, δ18O, and Δ47 corrected (heated gas correction, hot acid correction, and "offline" correction where necessary) as described in text.

Temperature calculated using calibration of Ghosh et al. (2007) for T<50°C, Guo et al. (2009) for T>50°C

Reported uncertainty is greatest of sample stdev (for n=2), stdev of all acquiisitions for a single extraction, and stdev of calcite standards

Table 10. δ18O in quartz from listvenites

Sample	δ18O, ‰ (SMOW)	Std. dev.
OM09-19 DOL	21.7	1.2
OM09-20-0.4	25.7	0.5
OM10-14-0.4	16.5	0.1
OM10-15 0.4	23.9	0.1
OM09-11	21.7	0.1
OM09-11-QV	22.7	0.2
OM09-18	21.5	0.6
OM09-19 MGS	22.6	0.1
OM10-03-s	22.3	0.3
OM10-26 bulk	23.8	0.8
OM10-26Q	22.7	0.9

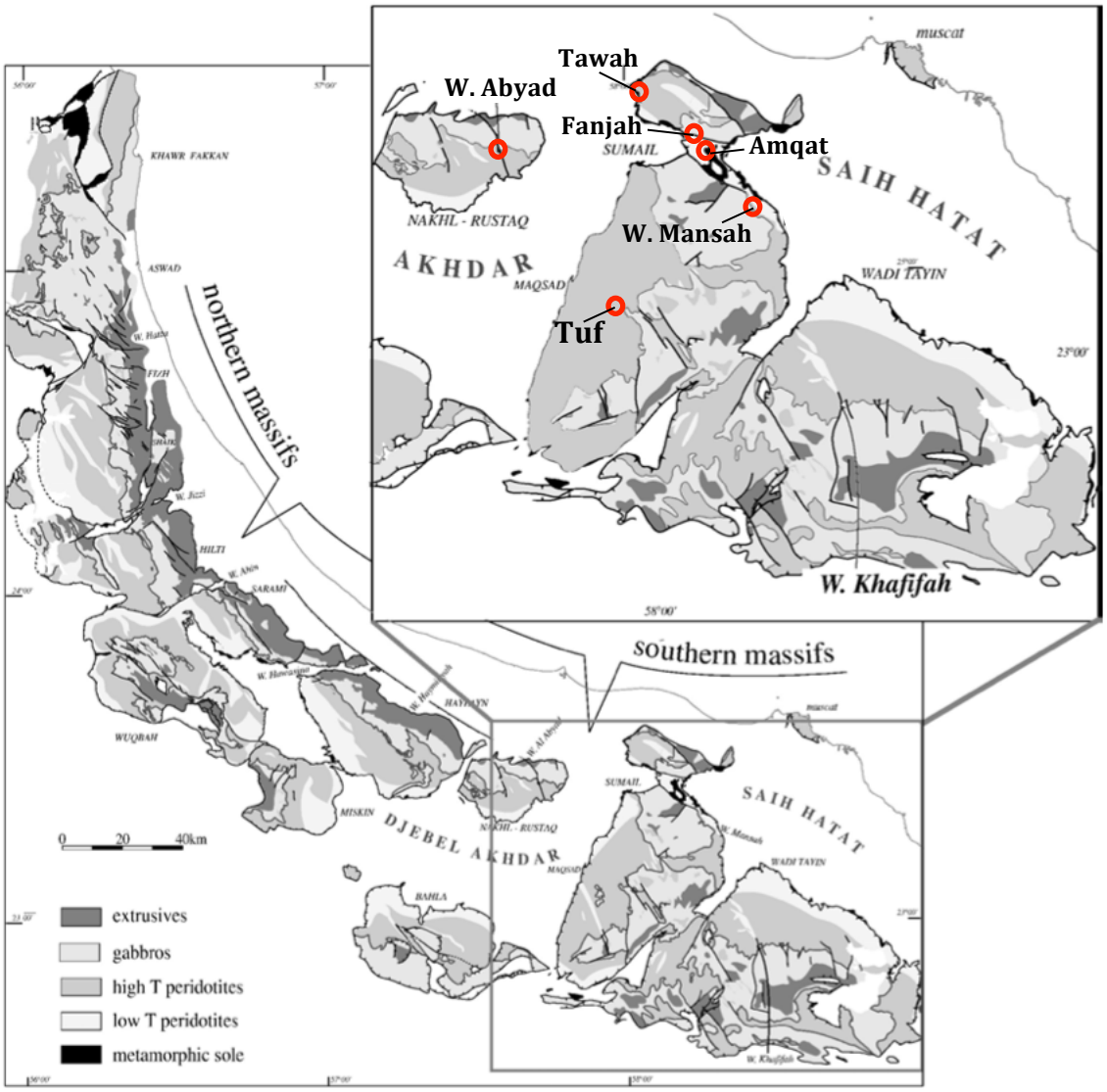

Figure 1. Map of listvenite localities (map modified from Nicolas et al. 2000)

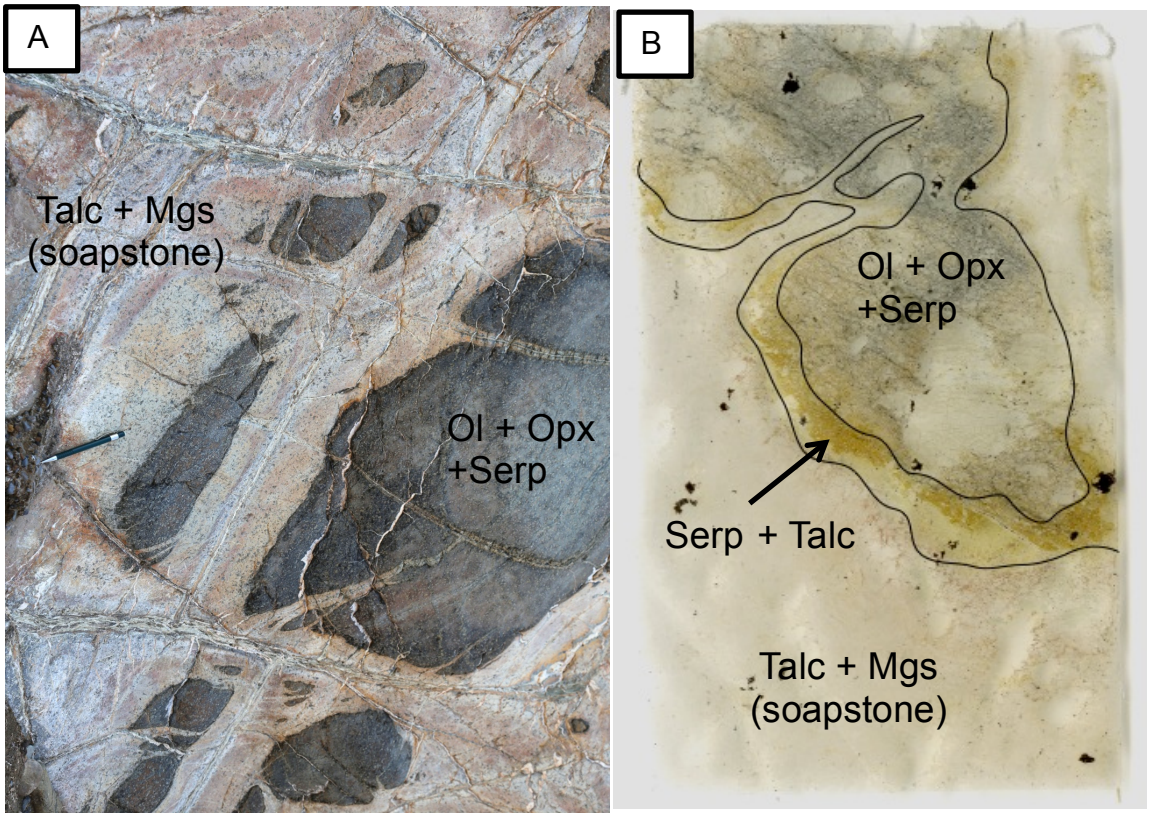

Figure 2. Zoned soapstone reaction fronts in Wadi Abyad, (a) in outcrop (pen for scale) and (b) in thin section.

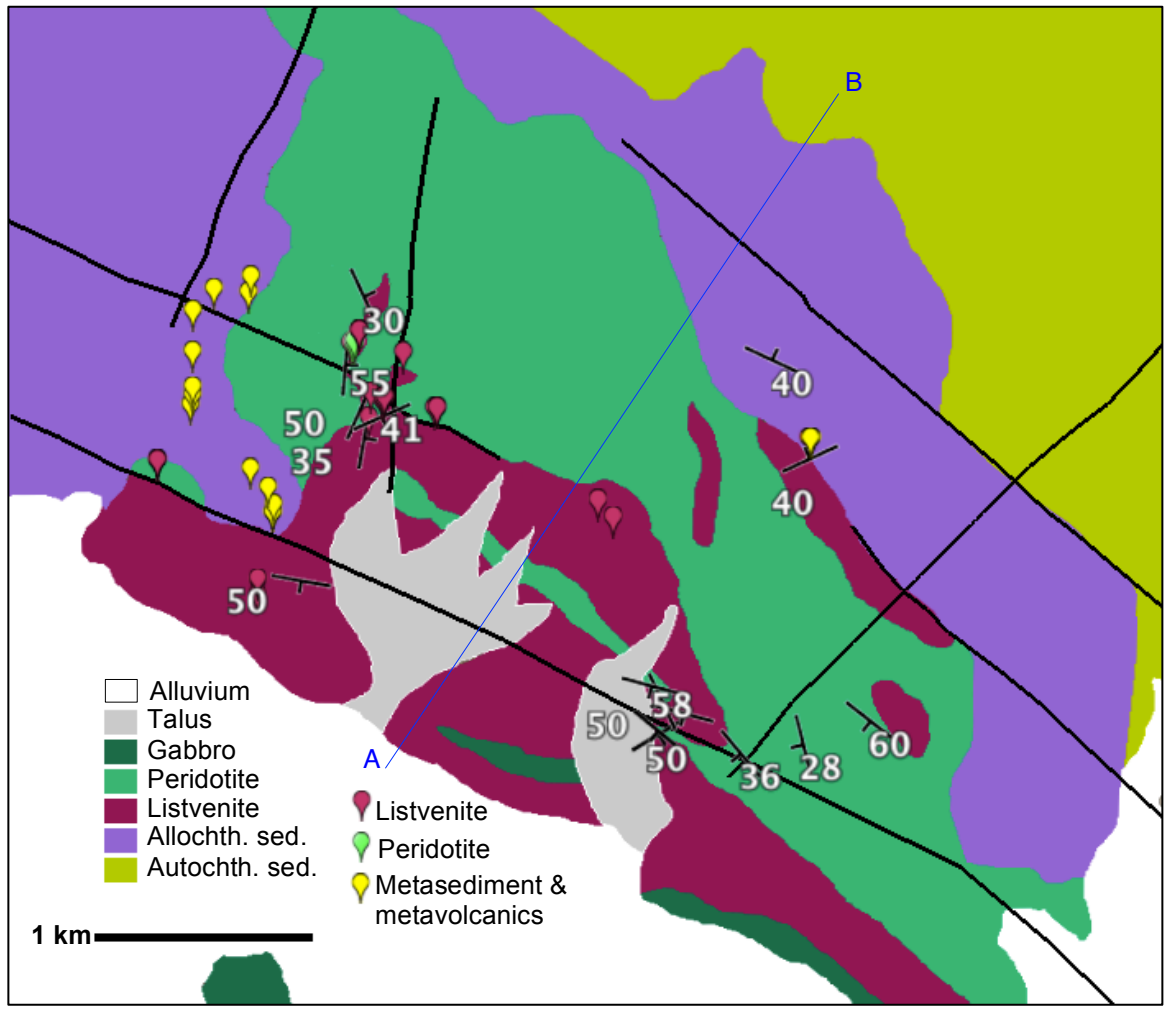
B
A
30
55
50
41
35
50
40
40
50
58
50
50
36
28
60
Alluvium
Talus
Gabbro
Peridotite
Listvenite
Allochth. sed.
Autochth. sed.
Listvenite
Peridotite
Metasediment &
metavolcanics
1 km

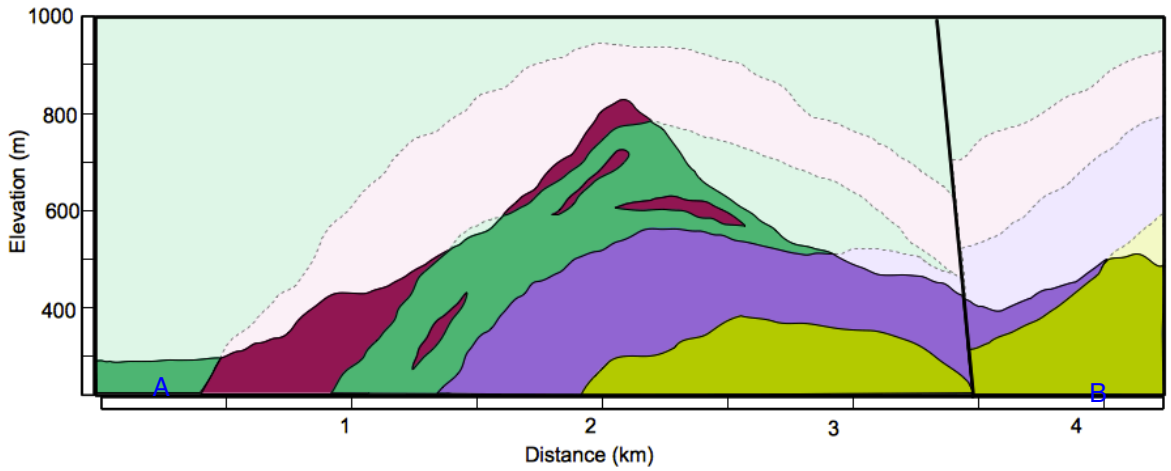
1000
800
600
400
Elevation (m)
A
B
1
2
3
4
Distance (km)

Figure 3. Geologic map and representative cross-section of the Wadi Mansah listvenite locality, including individual sample locations (place-markers). Adapted from Villey et al. (1986), Google Earth data, and field observations (including hand-held GPS measurements and attitudes of composition banding, contacts, and fault surfaces). Map area between 2582600 m and 2587150 m N and 619900 m and 625400 m E in UTM zone 40 Q.

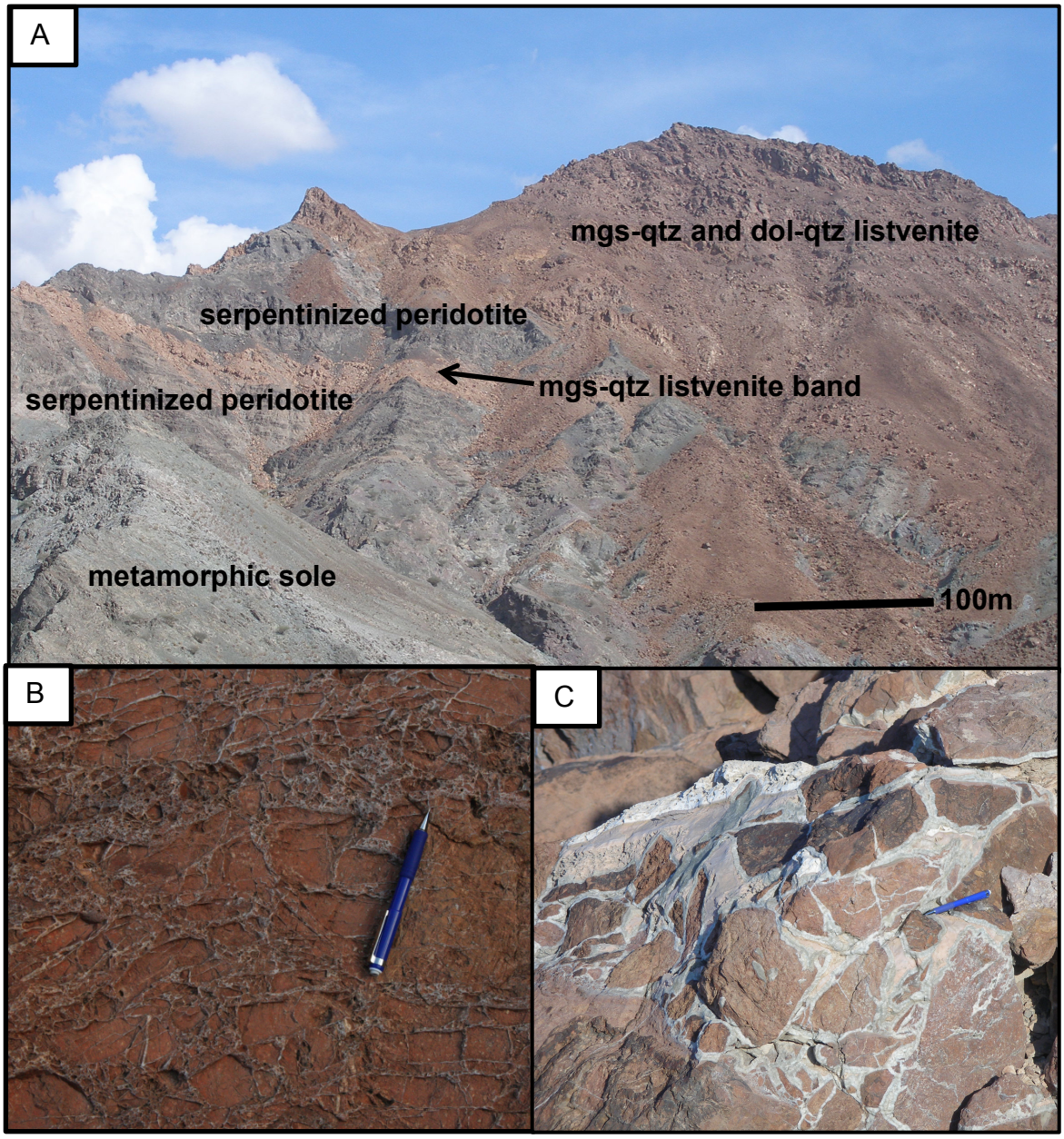

Figure 4. Listvenite outcrops at Wadi Mansah. (a) listvenite bands enclosed in serpentinized peridotite; (b) hierarchical quartz and carbonate veins (photo by P. Kelemen); (c) coarse, fracture-filling dolomite from the ridge crest.

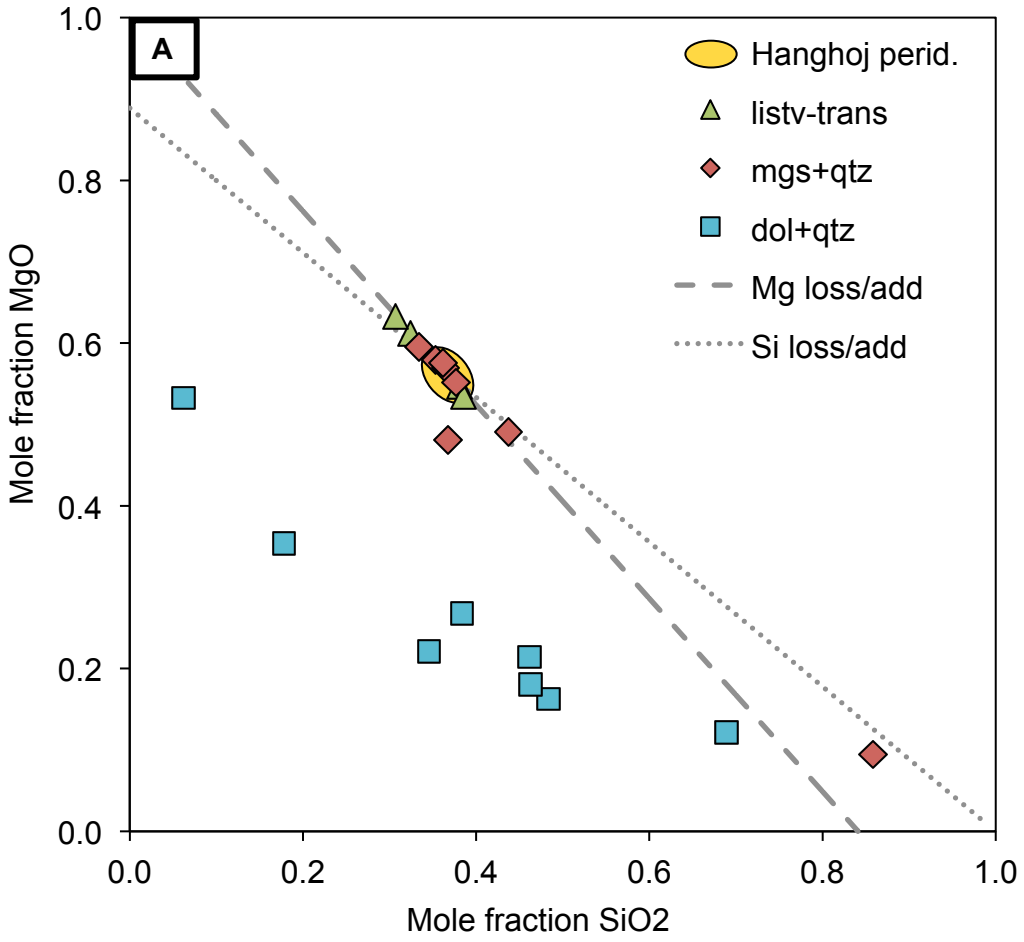

Figure 5. (a) Volatile-free molar MgO versus molar SiO_2. (b) Volatile-free molar MgO + CaO versus molar SiO_2. (c) Mg# versus molar SiO_2. Dashed and dotted grey lines show expected composition an average peridotite composition is perturbed only by loss or addition of Mg or Si, respectively. Quartz + magnesite listvenites compositions (red diamonds) and serpentine-bearing transitional rocks from the margin of the listvenite body (green triagnles) mostly fall within the range of fresh peridotite observed in Oman by Hanghoj et al. (2010) (yellow oval). Dolomite + quartz listvenite compositions (blue squares) span a broader range of Si concentrations and are deficient in Mg, primarily due to variable Ca addition. Low Mg numbers in the dolomite + quartz listvenites could be explained by Mg loss accompanied by Ca addition or by Fe addition.

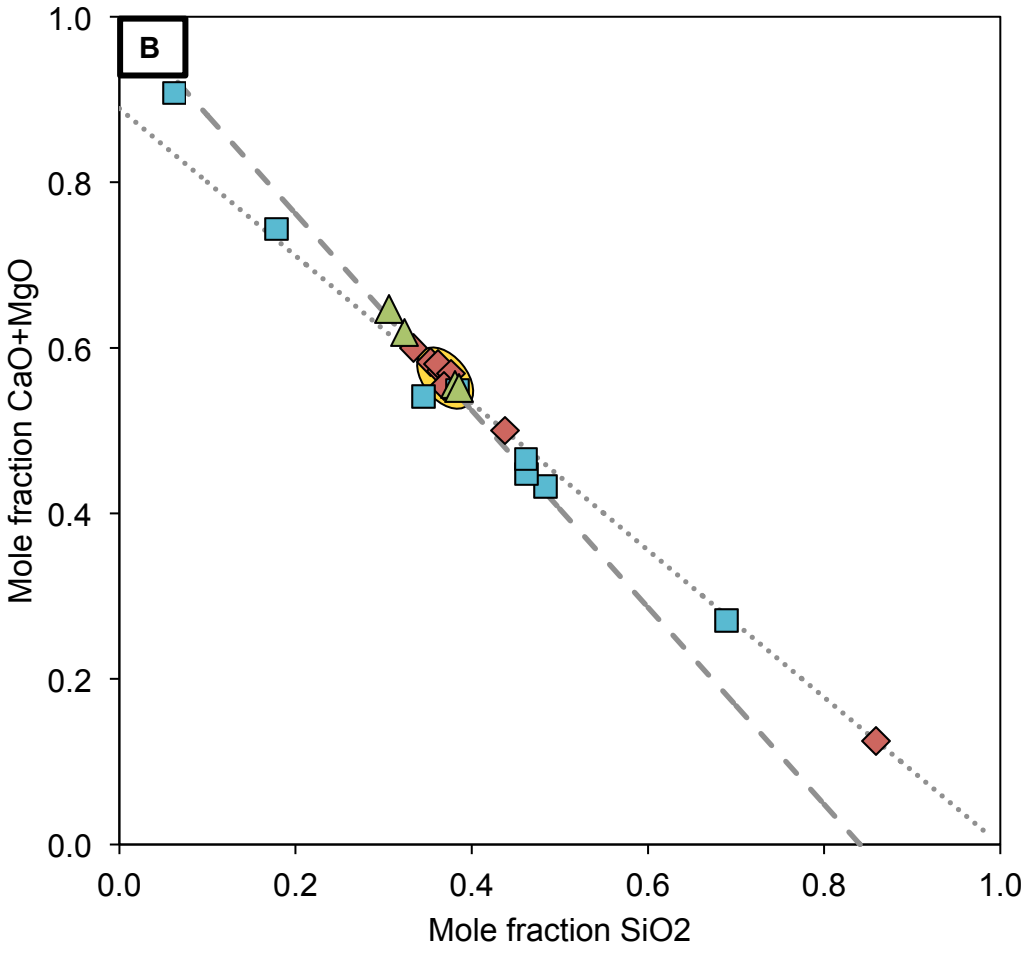

Figure 5. (a) Volatile-free molar MgO versus molar SiO_2. (b) Volatile-free molar MgO + CaO versus molar SiO_2. (c) Mg# versus molar SiO_2. Dashed and dotted grey lines show expected composition an average peridotite composition is perturbed only by loss or addition of Mg or Si, respectively. Quartz + magnesite listvenites compositions (red diamonds) and serpentine-bearing transitional rocks from the margin of the listvenite body (green triagnles) mostly fall within the range of fresh peridotite observed in Oman by Hanghoj et al. (2010) (yellow oval). Dolomite + quartz listvenite compositions (blue squares) span a broader range of Si concentrations and are deficient in Mg, primarily due to variable Ca addition. Low Mg numbers in the dolomite + quartz listvenites could be explained by Mg loss accompanied by Ca addition or by Fe addition.

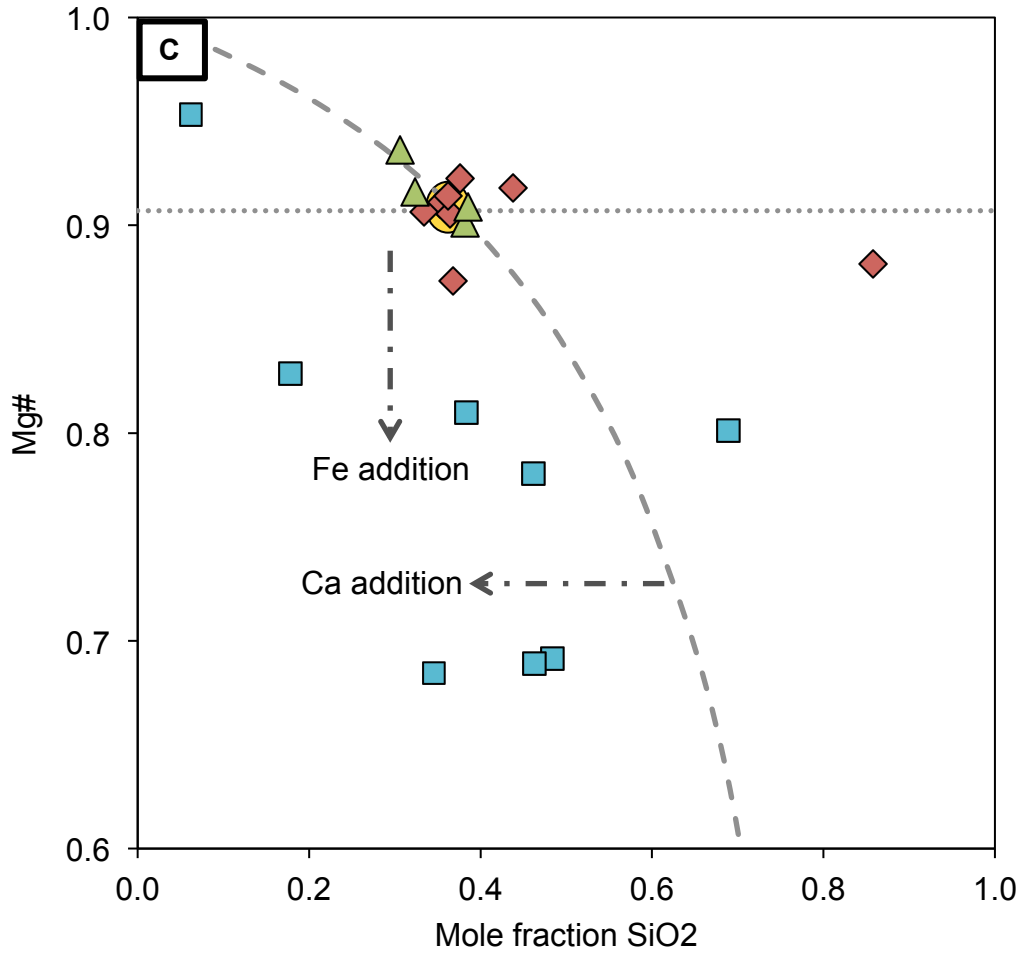

Figure 5. (a) Volatile-free molar MgO versus molar SiO_2. (b) Volatile-free molar MgO + CaO versus molar SiO_2. (c) Mg# versus molar SiO_2. Dashed and dotted grey lines show expected composition an average peridotite composition is perturbed only by loss or addition of Mg or Si, respectively. Quartz + magnesite listvenites compositions (red diamonds) and serpentine-bearing transitional rocks from the margin of the listvenite body (green triagnles) mostly fall within the range of fresh peridotite observed in Oman by Hanghoj et al. (2010) (yellow oval). Dolomite + quartz listvenite compositions (blue squares) span a broader range of Si concentrations and are deficient in Mg, primarily due to variable Ca addition. Low Mg numbers in the dolomite + quartz listvenites could be explained by Mg loss accompanied by Ca addition or by Fe addition.

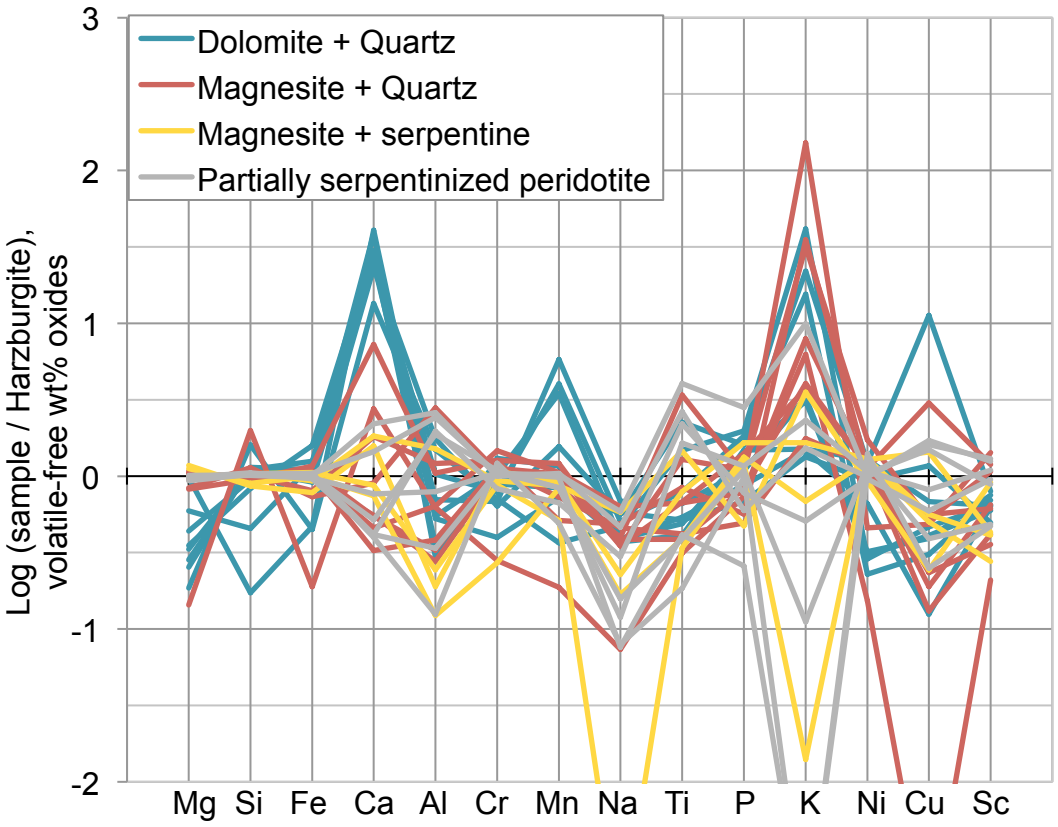

Figure 6. XRF data from listvenites and associated rocks compared to average Oman harzburgite (Hanghoj et al, 2010). XRF data are projected from loss-on-ignition (LOI), and the volatile-free composition is ratioed to average Oman harzburgite. The logarithm of these ratios are plotted here, such that a value of zero is identical in composition of average Oman harzburgite, positive values indicate enrichments relative to the protolith, and negative values indicate depletions relative to the protolith. Magnesite + quartz listvenite (red), dolomite + quartz listvenite (blue), transitional serpentine-bearing samples from the margin of the listvenite body (yellow), and partially serpentinized peridotite (grey) are similar in composition to average Oman harzburgite, but all listvenite samples have some enrichment in K, and dolomite + quartz listvenite samples are highly enriched in Ca and moderately enriched in Mn.

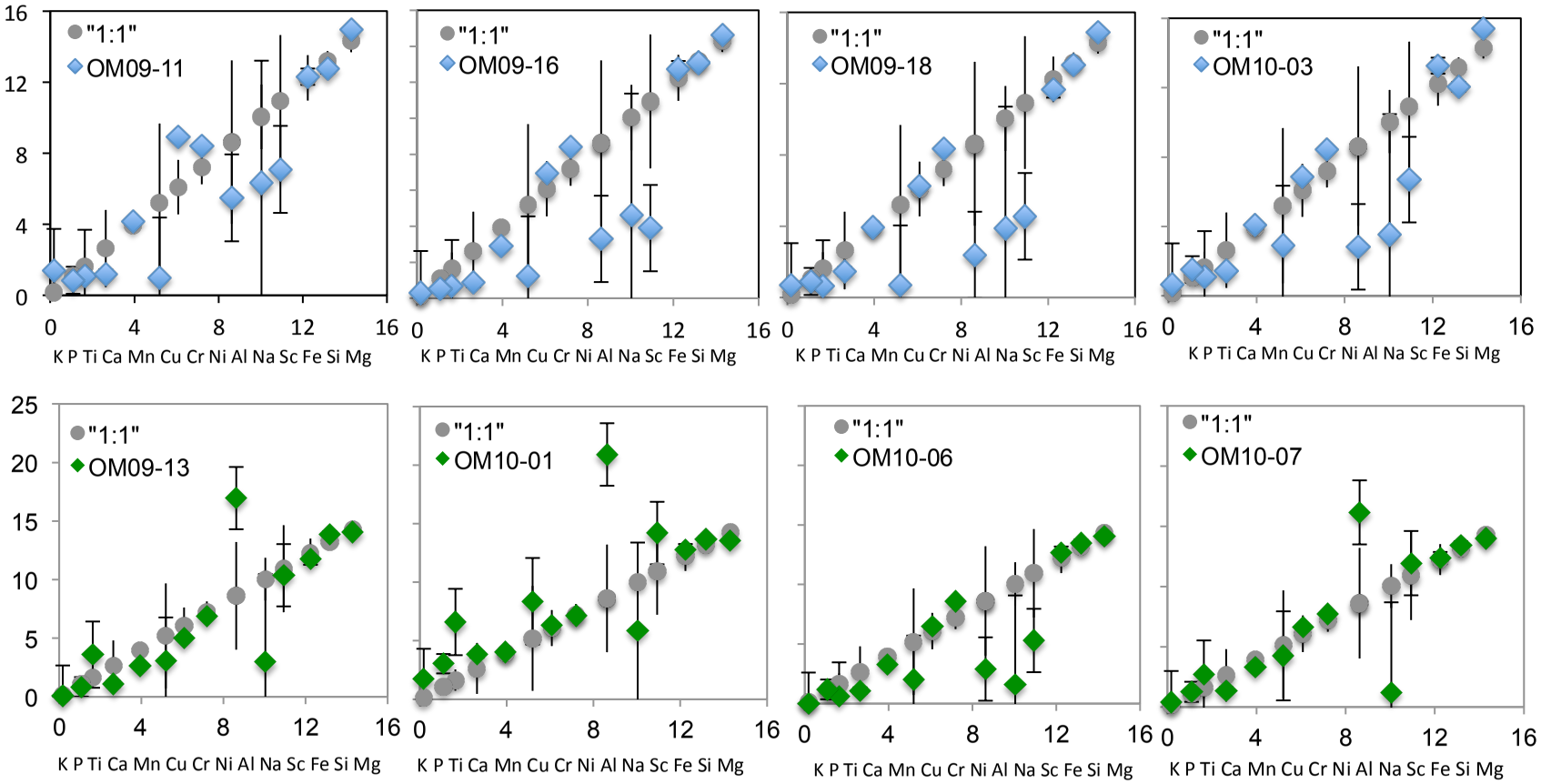
"1:1"
OM09-11
OM09-16
OM09-18
OM10-03
OM09-13
OM10-01
OM10-06
OM10-07
K P Ti Ca Mn Cu Cr Ni Al Na Sc Fe Si Mg

Figure 7. Isocon diagrams for some magnesite + quartz listvenites (top, blue) and ambient serpentinized peridotite (bottom, green) with compositions near average Oman harzburgite. X axes are volatile-free element concentrations in the protolith (average Oman harzburgite (Hanghoj et al. 2010)); error bars on grey 1:1 line represent 2-σ natural compositional variability in Oman harzburgite. Y axes are volatile-free element concentrations in altered rocks; error bars represent 2-σ analytical uncertainty. Element concentrations are scaled as 50 × wt% K_2O, 100 × wt% P_2O_5, 100 × wt% TiO_2, 2.5 × wt% CaO, 30 × wt% MnO, 0.3 × ppm Cu, 15 × wt% Cr_2O_3, 0.003 × ppm Ni, 10 × wt% Al_2O_3, 100 × wt% Na_2O, 1 × ppm Sc, 1.5 × wt% FeO*, 0.3 × wt% SiO_2, 0.32 × wt% MgO.

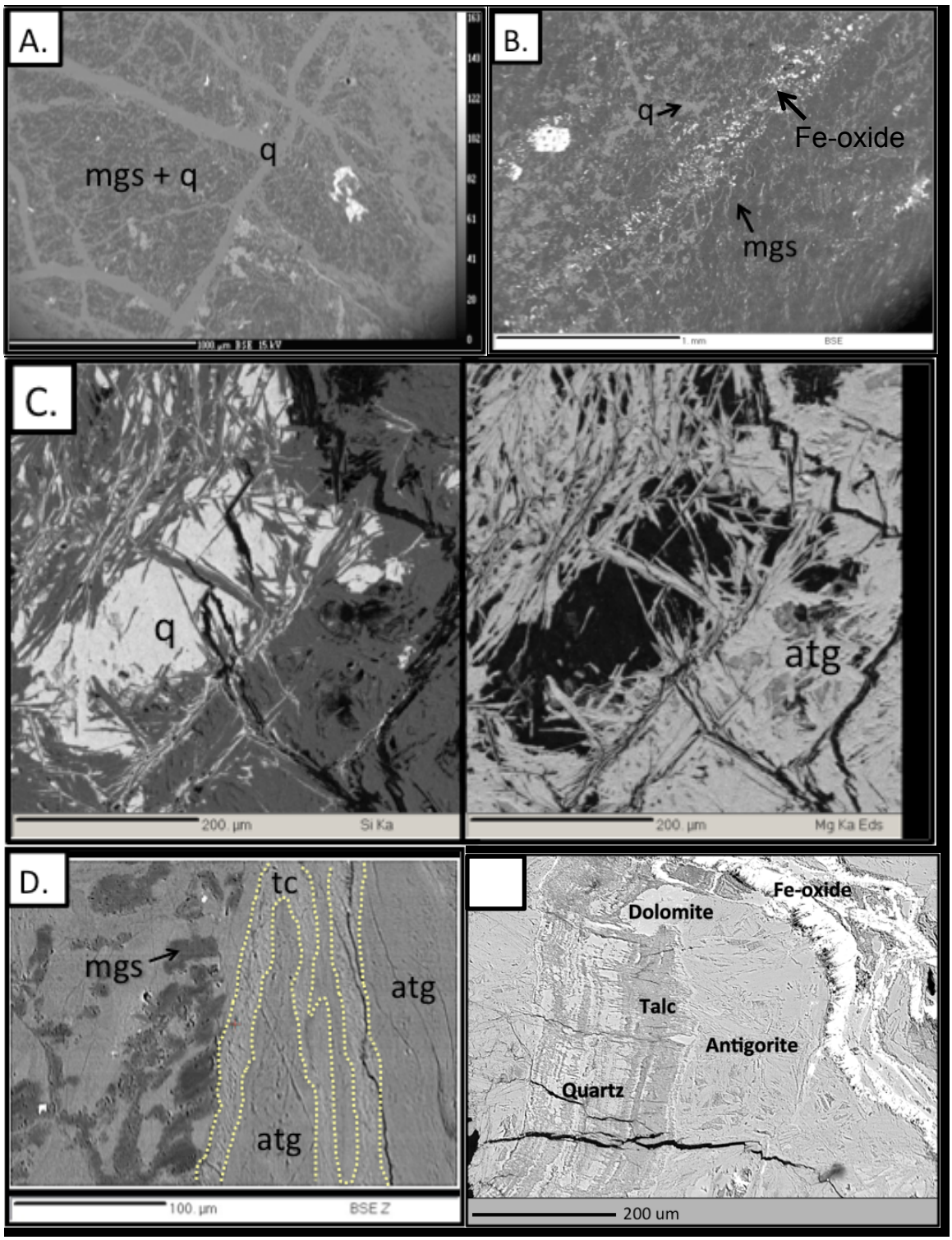
A.
mgs + q
q
B.
q
Fe-oxide
mgs
1. mm
BSE
C.
q
200. µm
Si Ka
atg
200. µm
Mg Ka Eds
D.
tc
mgs
atg
atg
100. µm
BSE Z
Fe-oxide
Dolomite
Talc
Antigorite
Quartz
200 um

Figure 8. Micro-textures in listvenite and transitional zones at Wadi Mansah, back-scattered electron (BSE) images and elemental maps. (a) A representative BSE image of listvenite sample OM09-15 shows fine, intergrown magnesite and quartz cut by dense networks of quartz veins fine, bright Fe-oxides are scattered through the matrix and larger, bright relict Cr-spinel attests to the peridotite protolith. (b) BSE image of magnesite and quartz, lacking sharply defined monomineralic vein networks, and intergrown with abundant fine-grained Fe-oxide in sample OM10-03. (c) Bladed antigorite intergrown with quartz in sample OM09-12, a serpentinized peridotite from collected near the listvenite margin, shown in an WDS elemental map of Si content (left) and an EDS elemental map of Mg content (right). (d) Talc-serpentine (antigorite) vein adjacent to magnesite intergrown with serpentine in sample OM10-02, a serpentinized peridotite sample collected at the margin of the listvenite. Yellow dotted lines added to emphasize boundary between talc and antigorite. Although not pictured here, magnesite is also present in these small, mixed veins. (e) Mixed veins of quartz, talc, and Fe-oxide in antigorite in sample OM09-12.

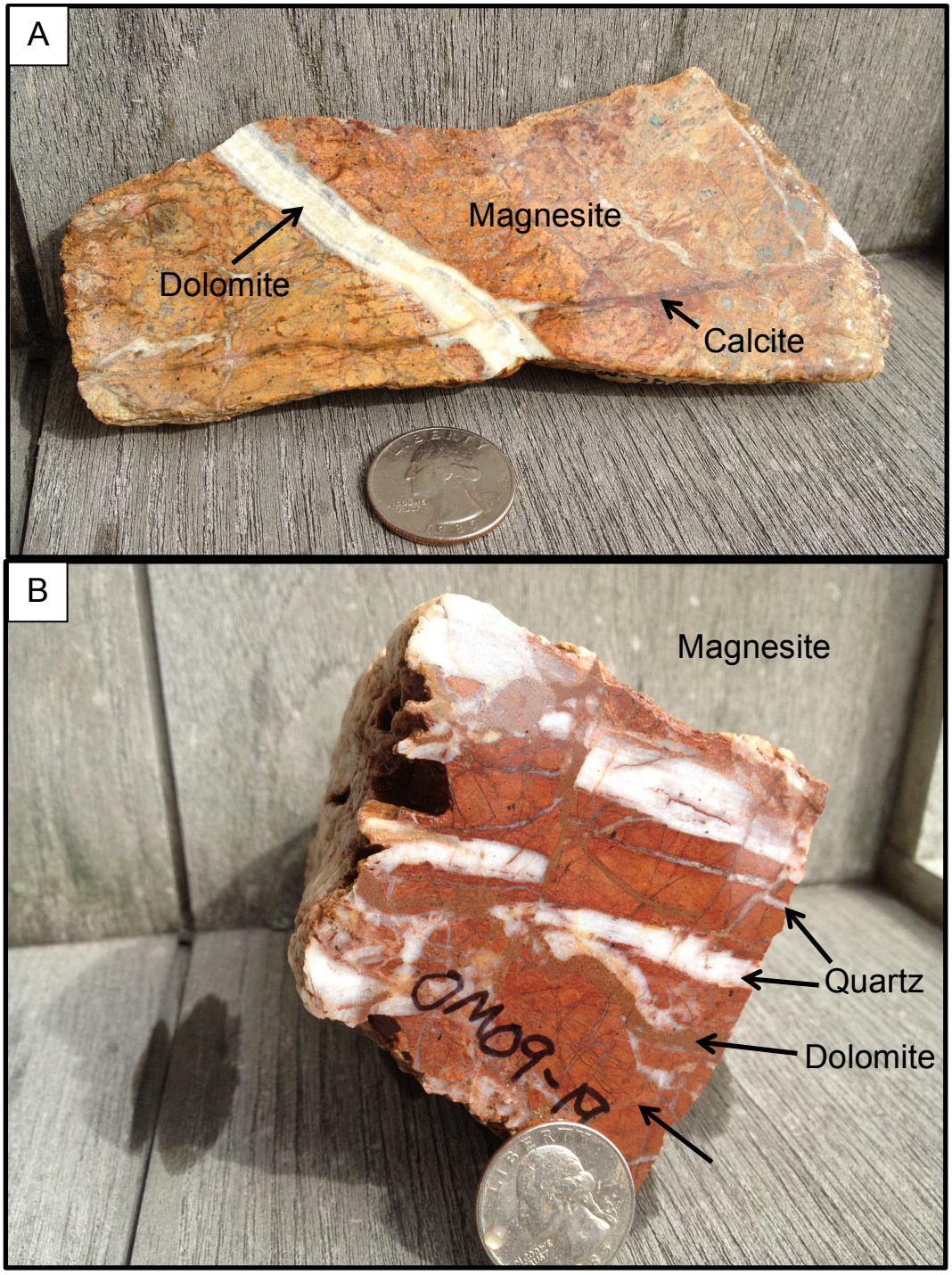

Figure 9. Cross-cutting relationships between carbonate minerals. (a) Coarse dolomite and calcite veins cut magnesite + quartz listvenite, OM09-74; (b) Brown dolomite-quartz and grey quartz veins cut red magnesite + quartz and white quartz veins, OM09-19.

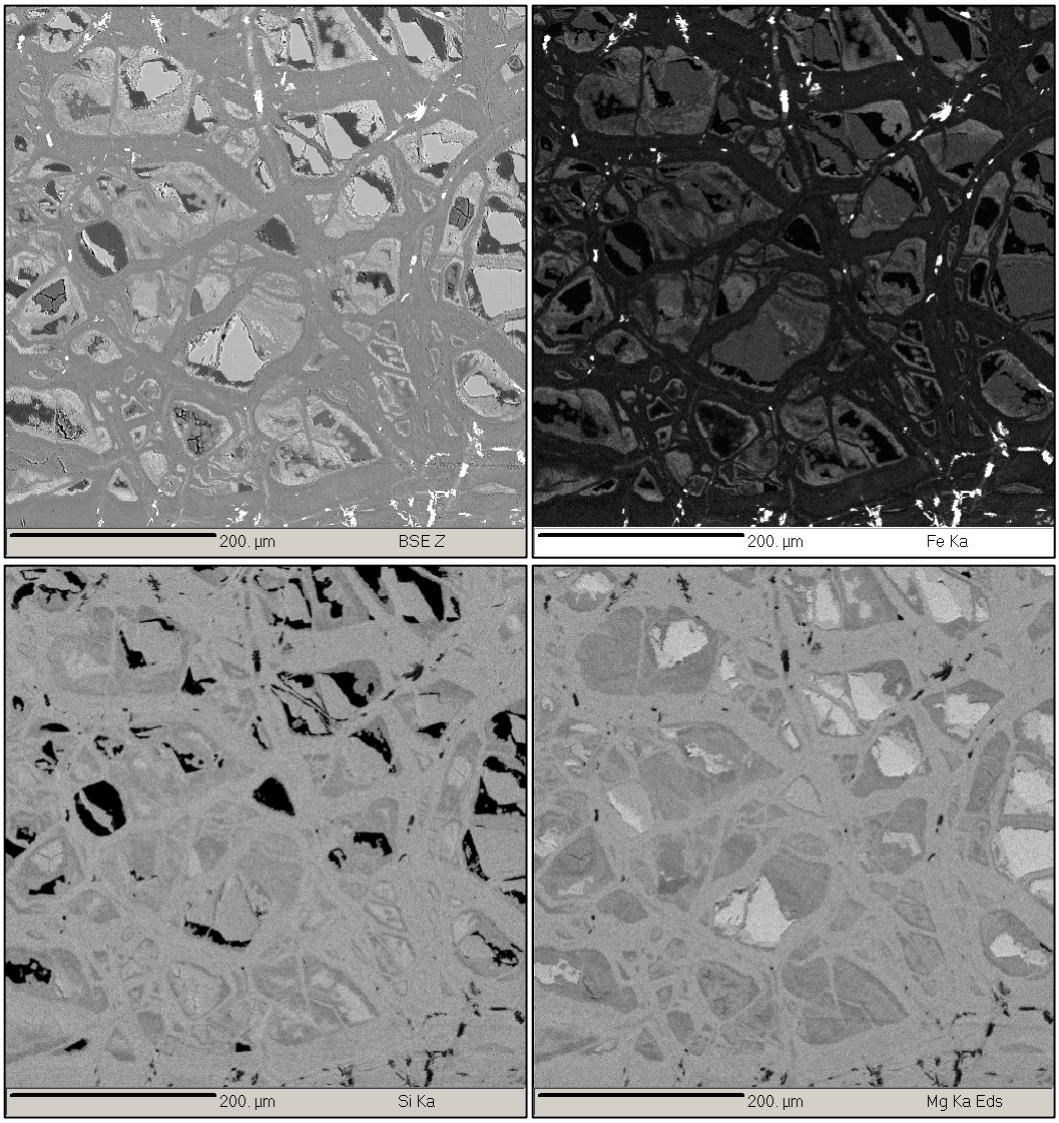

Figure 10. Partially serpentinized peridotite with high-Fe serpentine around olivine relicts in sample OM10-06, a partially serpentinized peridotite sample from near the margin of the listvenite at Wadi Mansah, shown in (a) back-scattered electron image, WDS elemental maps of (b) Fe and (c) Si, and (d) EDS elemental map of Si. Fe-rich serpentine is interpreted to post-date mesh texture veinlets and to have formed as a product of low-temperature serpentinization.

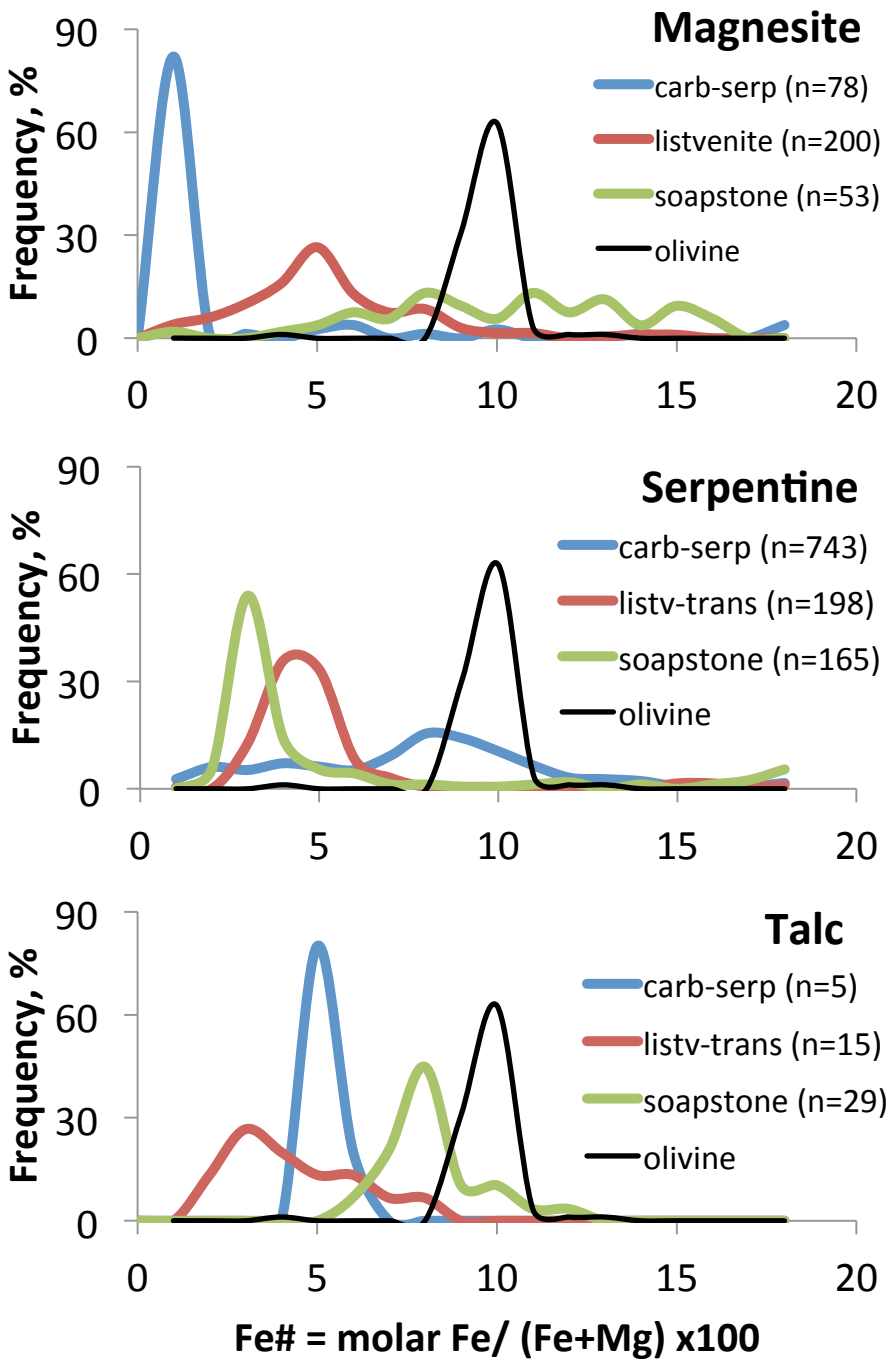

Figure 11. Fe# (molar Fe/(molar Fe + Mg)) histograms for magnesite, serpentine, and talc in carbonate-veined serpentinite, listvenite, and soapstone.

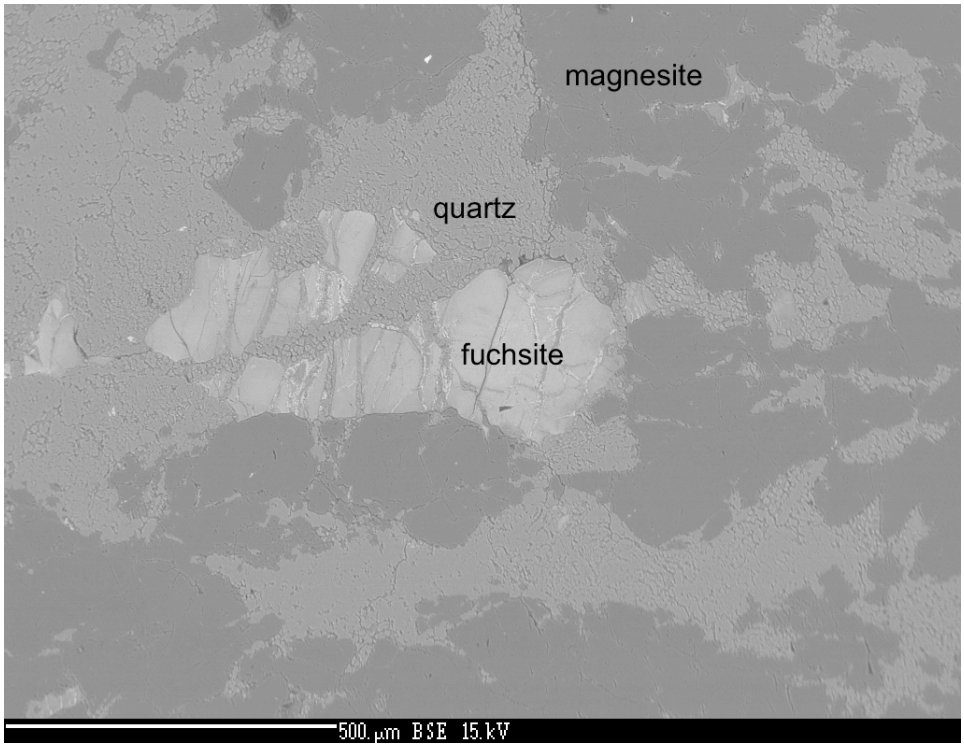

Figure 12. Fuchsite after Cr-spinel in OM10-26, back-scattered electron image (BSE)

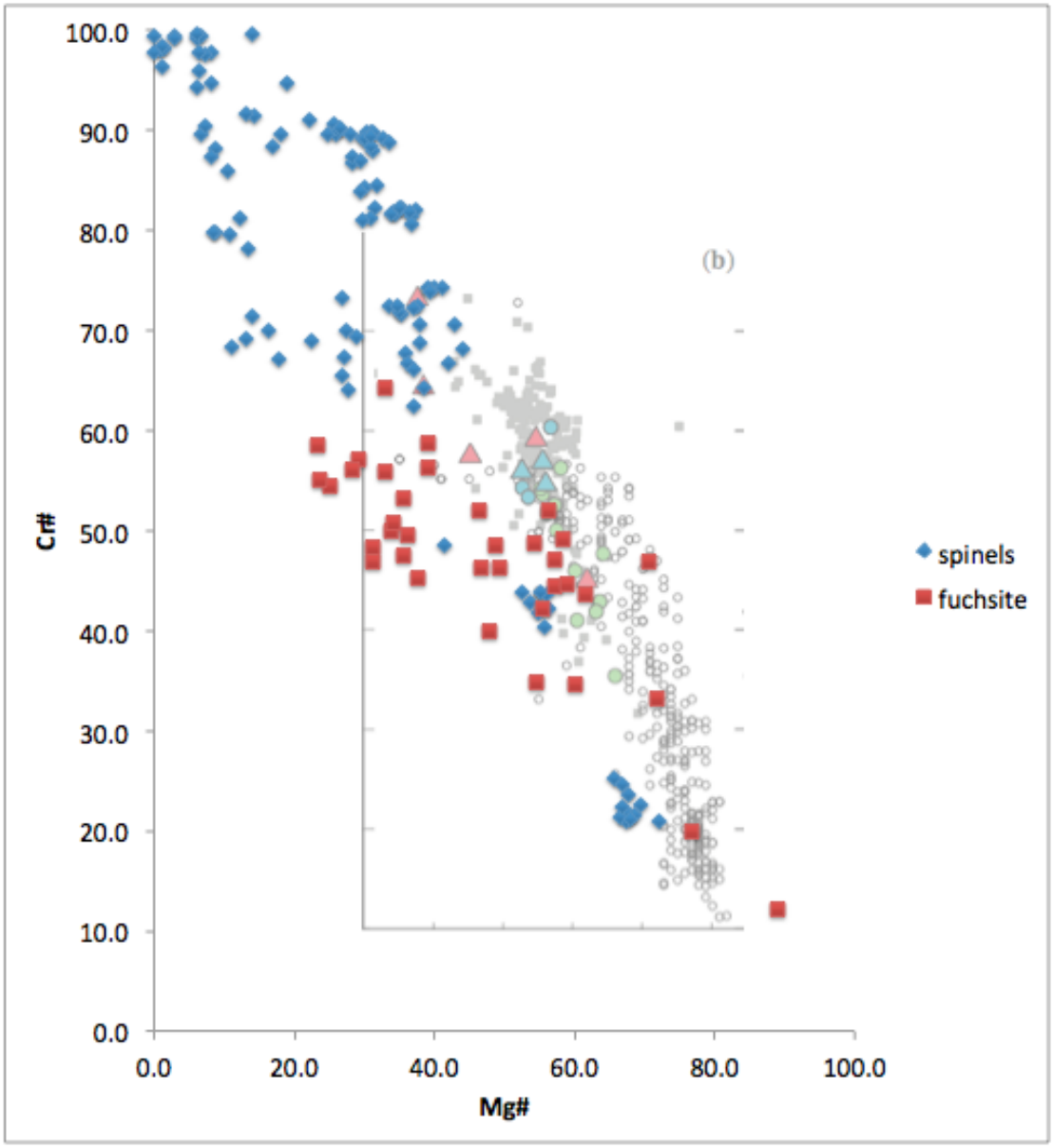

Figure 13. Fuchsite & spinel Cr# vs. Mg# for listvenites and partially serpentinized peridotite enclosing listvenite bodies, compared to values in fresh Oman peridotite and abyssal peridotites (fig 5b from Hanghoj et al. 2010, greyed)

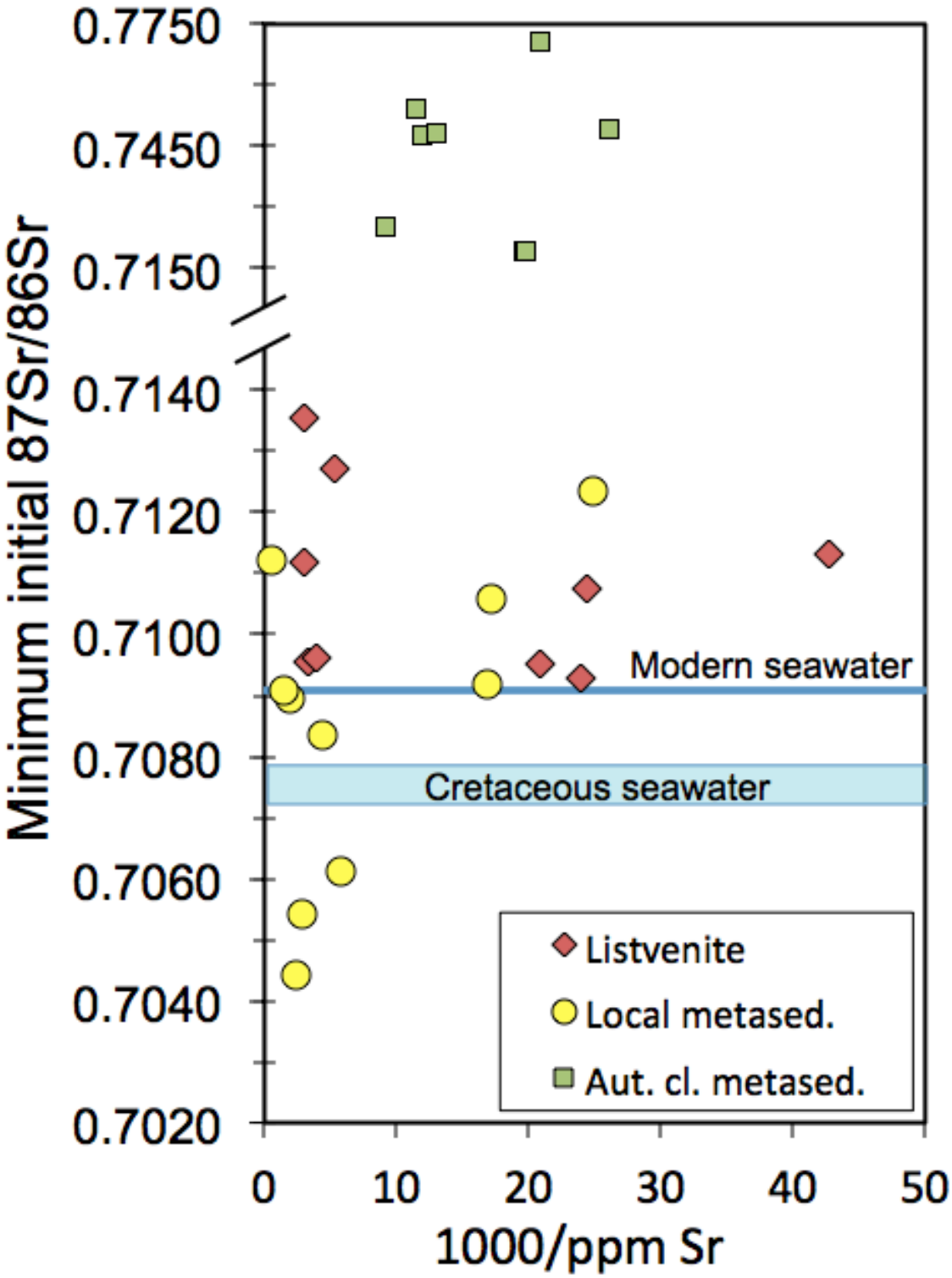
0.7750
0.7450
0.7150
0.7140
0.7120
0.7100
0.7080
0.7060
0.7040
0.7020
Minimum initial 87Sr/86Sr
Modern seawater
Cretaceous seawater
Listvenite
Local metased.
Aut. cl. metased.
0
10
20
30
40
50
1000/ppm Sr

Figure 14. Minimum initial Sr isotope ratios for listvenites (red diamonds), local underlying allochthonous metasediments and metavolcanics from the metamorphic sole (yellow circles), and autochthonous clastic metasediments from Weyhenmeyer (2000) (green squares). Minimum initial Sr isotope ratio assumes a maximum age of 96 Ma and calculates the initial 87Sr/86Sr based on the measured present 87Sr/86Sr and measured Rb:Sr ratio for the listvenite and local metasediment measured in this study. Rb concentrations were not available for the autochthonous clastic metasediments from Weyhenmeyer (2000), so an estimated Rb concentration of 100ppm was used to calculate an approximate minimum initial Sr isotope ratio at 96 Ma.

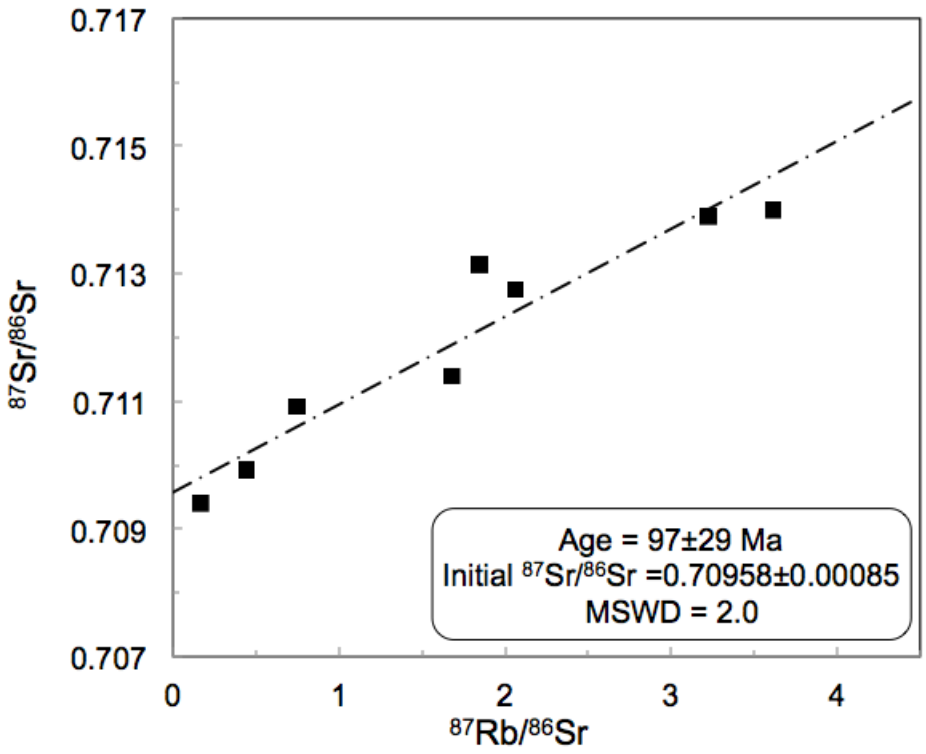

Figure 15. Internal Rb-Sr isochron for OM10-26 yields an age of 97 ± 29 Ma, consistent with the timing of emplacement of the Oman Ophiolite. Age calculated using ISOPLOT (model 3).

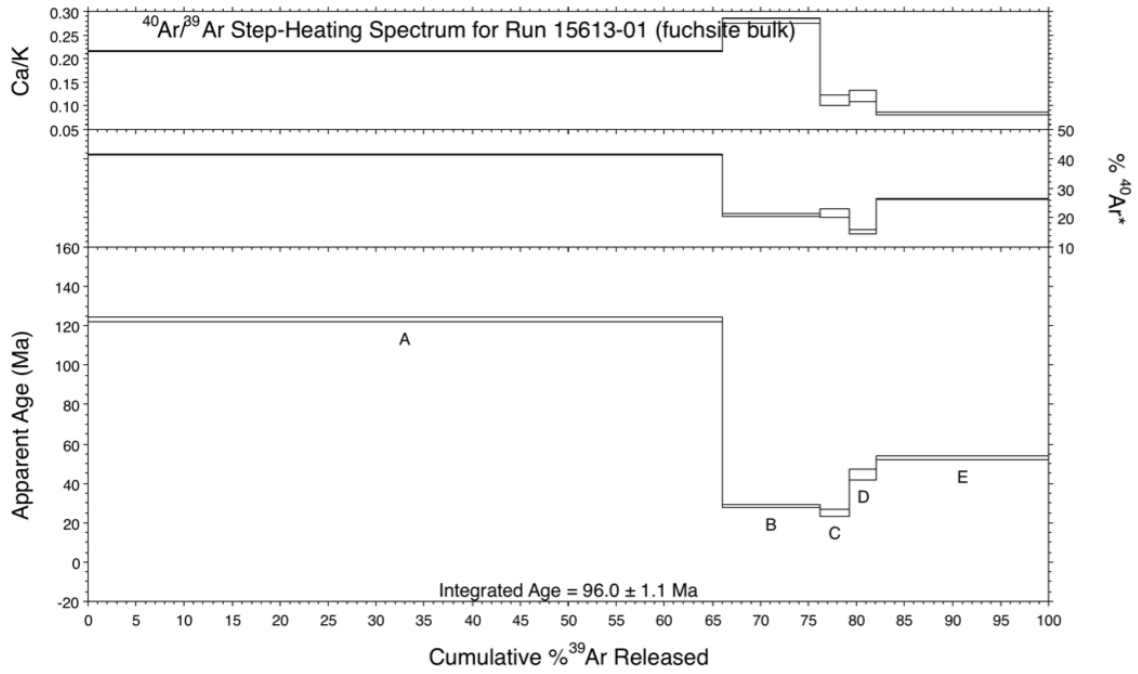

Figure 16. Ar-Ar geochronology in OM10-26. Step heating of fuchsite-rich grains yields unrealistically high ages in the first heating step, and scattered ages of heating steps may suggest mixing of several components. Although fuchsite likely formed during listvenite formation, these weathered aggregates of fuchsite do not appear to retain an Ar-Ar age signal from the initial formation of fuchsite.

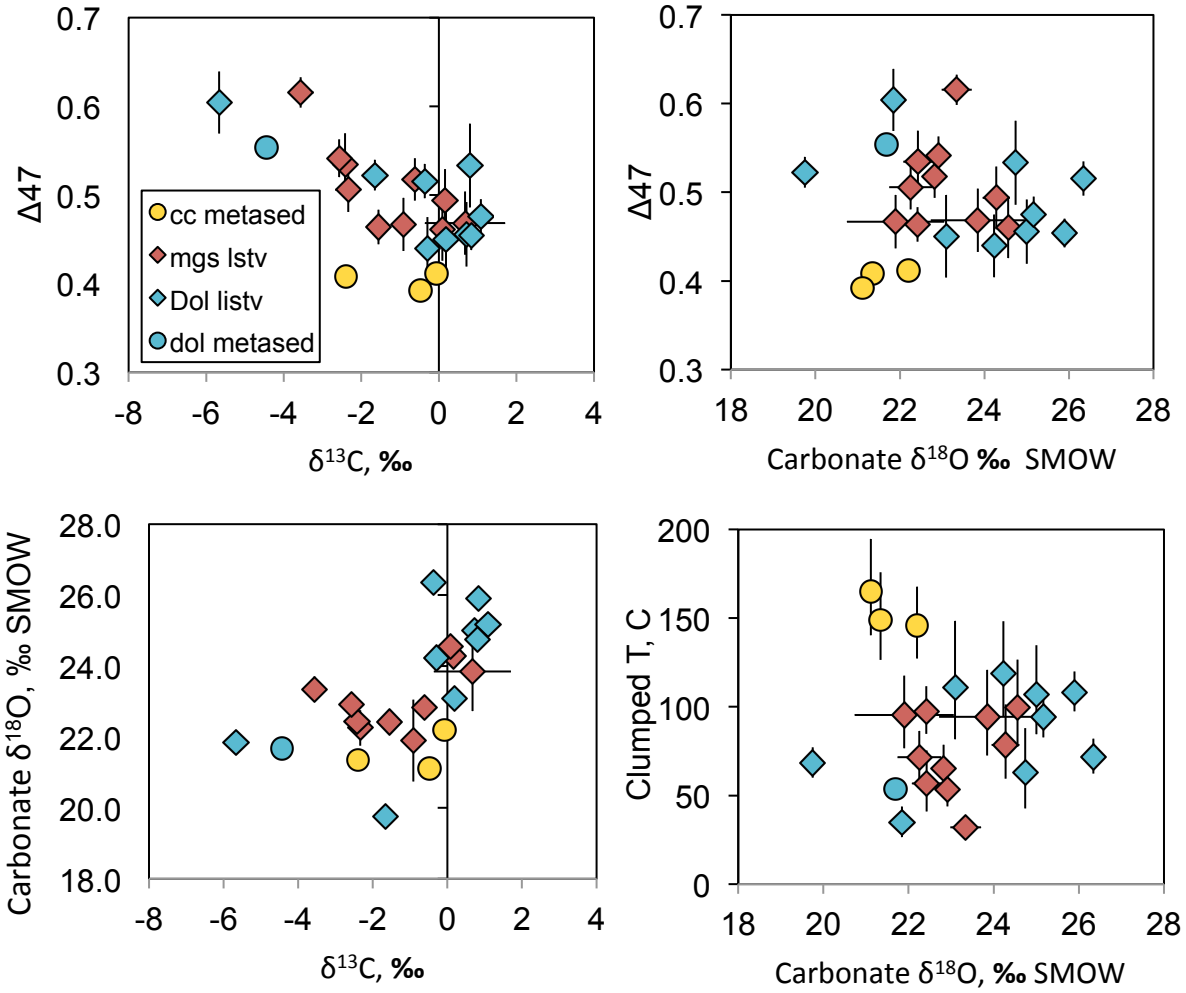

Figure 17. Cross-plots of Δ47, $\delta^{13}C$, $\delta^{18}O$, and clumped T (Ghosh et al., 2007; Guo et al. 2009) in listvenite and associated lithologies: magnesite + quartz listvenite (red diamonds), dolomite + quartz listvenite (blue diamonds), calcite-bearing metasediment (yellow circles), dolomite-bearing metasediment (blue circle). $\delta^{13}C$ values cluster around -3 to +1‰, with overlapping values for listvenites and metasediments. Carbonate $\delta^{18}O$ values in listvenite mostly fall within a range of 22 to 26‰ (SMOW). If all listvenite samples formed from fluids of similar isotopic composition, these $\delta^{18}O$ values imply a much narrower range of temperatures than the ~30 to 120°C recorded by clumped isotopes.

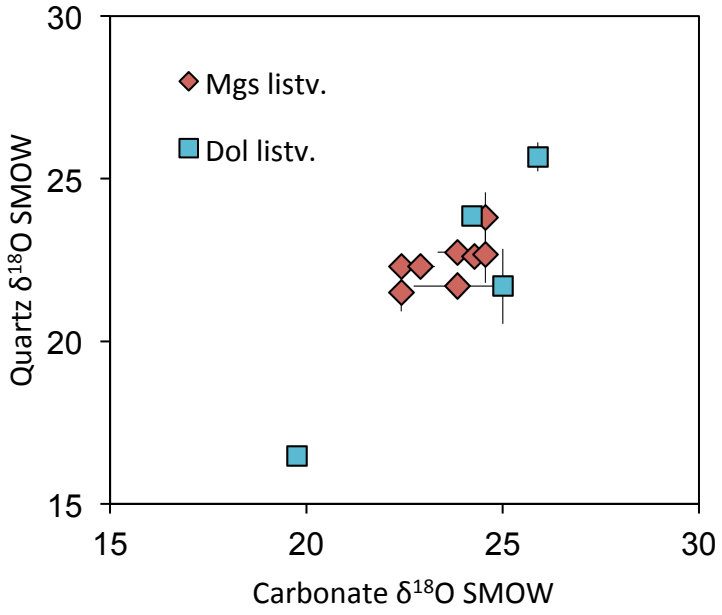

Figure 18. $\delta^{18}O$ values in quartz are correlated with $\delta^{18}O$ in carbonate (red diamonds = magnesite + quartz listvenite, blue squares = dolomite + quartz listvenite)

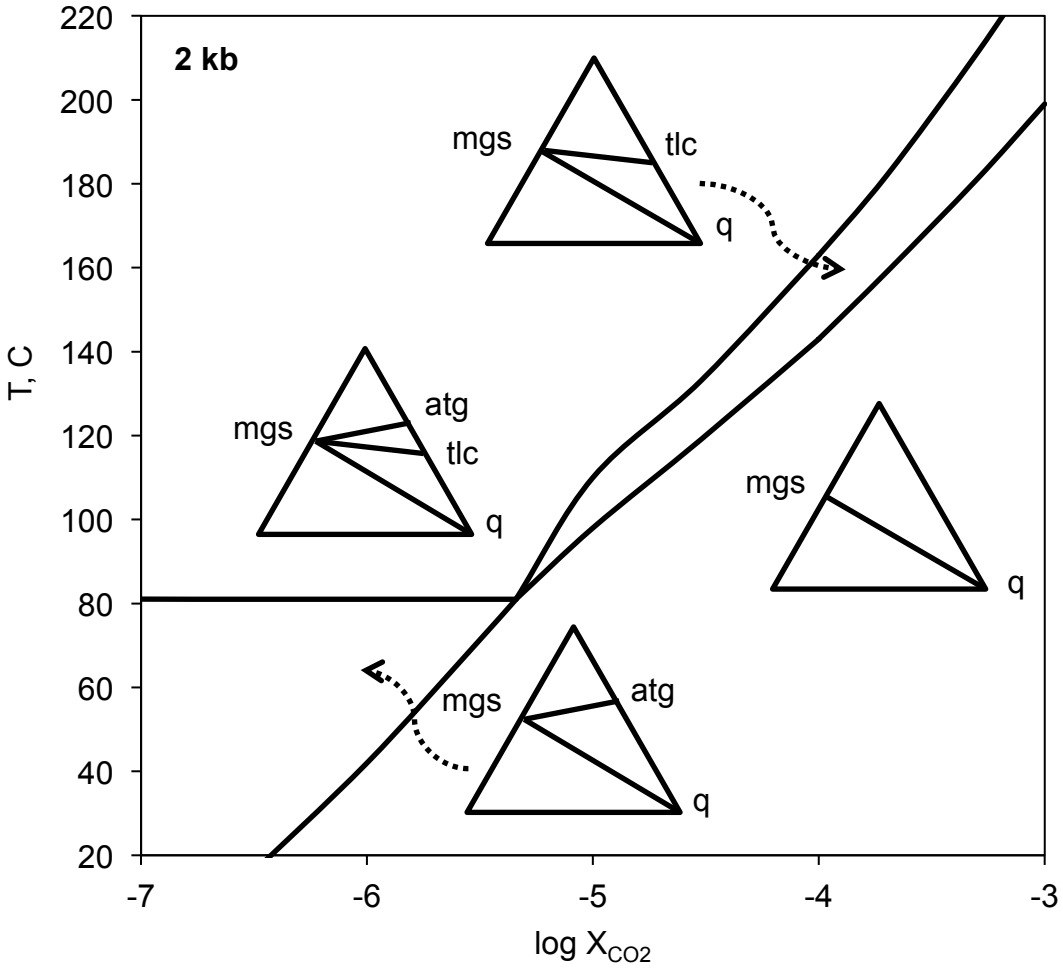

Figure 19. T-XCO2 phase diagram for magnesite, antigorite, talc, and quartz at 2kb, calculated using THERMOCALC.

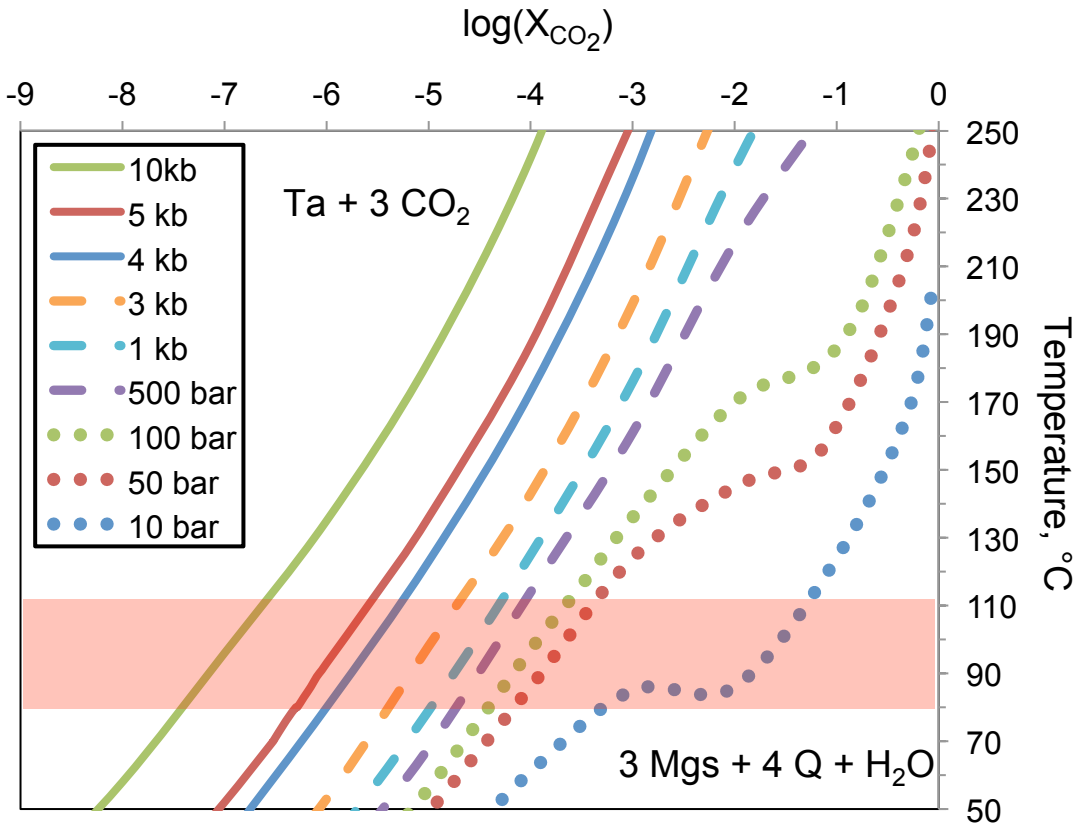

Figure 20. T-X phase boundaries for the reaction 3 magnesite + 4 quartz + H_2O = talc + 3 CO_2, calculated in THERMOCALC for pressures from 10 bar to 10 kbar.

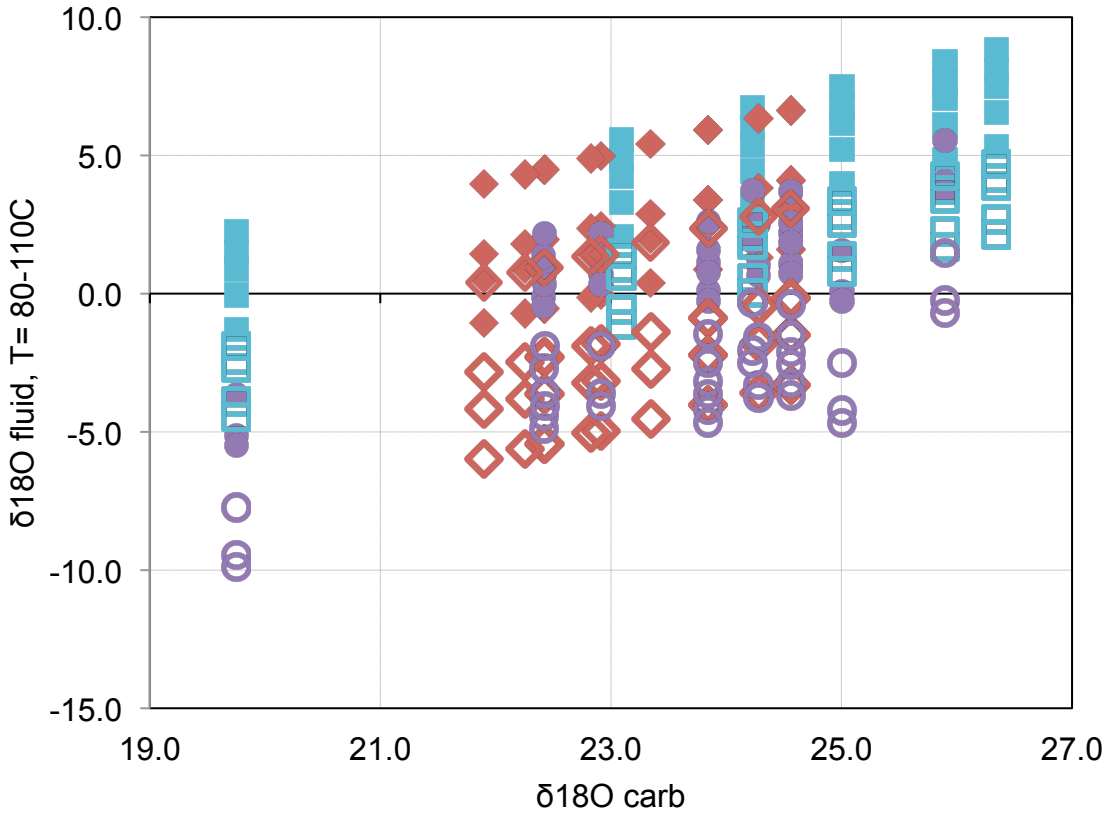

Figure 21. Fluid $\delta^{18}O$ from carbonate and quartz versus carbonate $\delta^{18}O$ at temperatures of 80-110°C. Blue squares = dolomite, red diamonds = magnesite, purple circles = quartz. Open symbols represent $\delta^{18}O$ of the fluid calculated from mineral-water $\delta^{18}O$ fractionation factors at a temperature of 80°C, filled symbols at 110°C. The range of fluid $\delta^{18}O$ shown for a single sample and temperature represents the variability in available fractionation factors (top to bottom): Dol - Schauble et al. (2006); Vasconcelos et al. (2005); Chacko and Deines (2008); Northrop and Clayton (1966); Schmidt et al. (2005), Mgs - Aharon (1988) magnesite (1), Aharon (1988) magnesite (2), Schauble et al. (2006), Chacko and Deines (2008); Qtz - Friedman and O'Neil (1977), Sharp and Kirschner (1994). Oxygen isotopes in magnesite and quartz are in fairly good agreement for most choices of fractionation factors, while dolomite oxygen isotope values tend to be slightly low relative to quartz, for available fractionation factors.

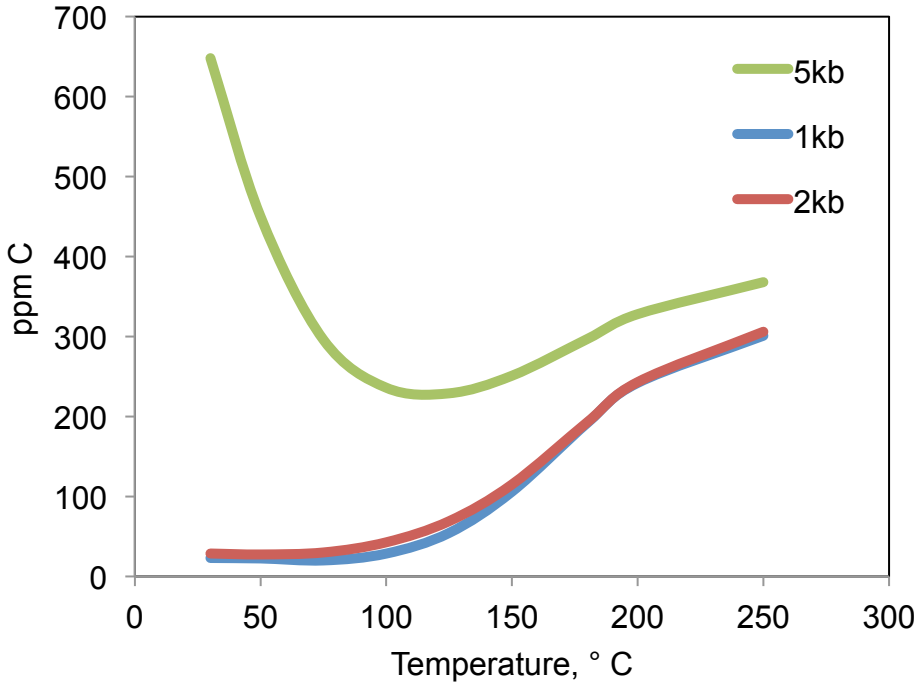

Figure 22. Carbon concentration in pore-water saturated in sediment at pressures of 1, 2, 5kb and temperatures between 25 and 300°C, calculated in EQ3/6

Appendix 1. All sample locations and descriptions. UTM locations in zone 40Q

Sample #	Type	Description in field notes	location	E	N	elev	Minerals identified by XRD
OM07-01	vein	carbonate vein on fault	Muscat				
OM07-02	vein	carbonate vein on fault	Muscat				
OM07-03	vein	carbonate vein on fault, brecciatd fault w several 5-10 cm carb veins, slicks (Hacker notes)	Bani Karous/Al Abyad	567356	2586868	307	
OM07-04	vein	some kind of alteration	Bani Karous/Al Abyad	568256	2591280	269	
OM07-05	vein	carbonate veins in serpentine	rd to Wuqbah	451254	2652948	417	dolomite, chrysotile (no peaks around 35)
OM07-06	vein	listvenite/chert	rd to Wuqbah	451254	2652948	417	
OM07-07	vein	carb & silica in serpentine, massive compared to 05, up to 10 cm thick plus huge concretion ball ~ 1 m in diameter	rd to Wuqbah	449334	2651616	472	magnesite, tiny dolomite
OM07-08	trav	eroded stratigraphic top of travertine terrace, 10 to 20 cm from highest stuff	Jill	552832	2528489	483	Calcite only
OM07-09	trav	2 meters stratigraphically below 08	Jill	552832	2528489	482	
OM07-10	trav	small globular carbonate sitting on top of the travertine sequence	Jill	552832	2528489	482	
OM07-11B	trav	three different stalagmites one meter below 09	Jill	552806	2528446		
OM07-12	vein	carbonate veins in serpentine, 1 m below stalagmites (?)	Jill	552807	2528446	481	Calcite only
OM07-13	trav?	between 11 and 12	Jill	552809	2528448	482	Calcite, tiny nub of serpentine
OM07-14	trav	very base where cars are parked	Jill	552826	2528418	478	Calcite, little bit of serpentine, (Fe?)
OM07-16	trav	top of eroded "klippe", should be oldest	duck outcrop SE of Birkat al Mawz	586007	2523245		Calcite, little bit of serpentine, (Fe?), little magnesite

Sample #	Type	Description in field notes	location	E	N	elev	Minerals identified by XRD
OM07-17	vein	carbonate vein in serpentine	duck outcrop SE of Birkat al Mawz	586007	2523245		Calcite, Dolomite, small serpentine
OM07-18	trav	travertine forming now	duck outcrop SE of Birkat al Mawz	586007	2523245		Calcite, (Fe?)
OM07-25	trav	see Anna Wall notes, near location, downslope (???)	Tuf				
OM07-26	vein	botryoidal carabonate weathering out of carbonate veins in serpentine @ sill outcrop #2, above lower end of oasis	Tuf				
OM07-27	vein	massive carbonate in wadi, well above oasis, assoc w big (<= 1 m) veins	Tuf	598089	2555805	917	dolomite, serpentine (likely some liz due to small peak at 36), calcite, possible nub of quartz?
OM07-28A	vein	talc altered peridotite in wadi, tabular body ~ 2 m wide	Tuf	598021	2555719	908	
OM07-28B	vein	talc altered peridotite in wadi, tabular body ~ 2 m wide	Tuf	598068	2555616	905	
OM07-28C	vein	low angle carbonate vein dipping 25-30° SW	Tuf	597543	2554836	883	
OM07-30A	trav	Anna Wall has location; travertine or dipslope vein in gully below Tuf	Tuf				dolomite, calcite, serpentine, quartz
OM07-30B	trav	dark grey limestone blocks within travertine	Tuf				calcite, (Fe?)
OM07-31	vein	serpentinized perid w carb veins nr 34	Wadi Mahram 2				
OM07-32	vein	serpentinized perid w carb veins nr 34	Wadi Mahram 2				
OM07-33	vein	serpentinized perid w carb veins nr 34	Wadi Mahram 2				
OM07-34A	vein	old travertine, 1.5 m above current spring level, big piece	Wadi Mahram 2	608365	2526870	551	Calcite, little dolomite/ankerite, (tiny bit of Fe?)

Sample #	Type	Description in field notes	location	E	N	elev	Minerals identified by XRD
OM07-34B	vein	small carbonate vein in perid below travertine deposits	Wadi Mahram 2	608365	2526870	551	
OM07-34C	trav	flakes of currently forming travertine	Wadi Mahram 2	608365	2526870	551	Calcite, medium unknown peak @44.7 (Fe?)
OM07-39	vein	50 cm carbonate vein in wadi wall	Wadi Lufti	634006	2571609	600	magnesite, tiny magnesian calcite?, tiny serpentine
OM07-50	vein	serpentine vein in mantle N of Nassif	Nasif				
OM07-51	perid	harzburgite host rocks to 50	Nasif				
OM07-52	vein	serp & carb veins 5 cm thick in perid	Nasif				
OM07-53	vein	carb vein in dunite, low angle dip	serp & carb veins Nassif				dolomite, smectite-kaolinite, chrysotile and lizardite probably (peak @36), clinochlore? corrensite?
OM07-54	vein	carbonate coating/veins on joints	pass betw Khafifah & Dima	646240	2537136	748	dolomite, chrysotile (peak at 2theta 24 about half that at 12), possiby some lizardite (small peak around 36), tiny calcite, clinochlore? (sort of missing peak around 6)
OM07-55	perid	"ambient" serpentinized peridotite	pass betw Khafifah & Dima	646240	2537136	748	
OM07-56	vein	coarse, gree serpentine vein 1 cm wide	pass betw Khafifah & Dima	646240	2537136	748	
OM07-57	vein	mixed serpentine and carbonate, cm scale veins	pass betw Khafifah & Dima	646240	2537136	748	
OM07-58	vein	perid with mm scale carbonate on joints	pass betw Khafifah & Dima	647831	2537682	915	
OM07-59	vein	4 mm carbonate potato chips in serpentine, several photos	Wadi Dhuli	667398	2542689	414	
OM07-59B							

Sample #	Type	Description in field notes	location	E	N	elev	Minerals identified by XRD
OM07-60	trav	travertine grading downward into carbonated dunite next to road, at beginning of small wadi leading to the center of the universe; Anna Wall has the location	near center of universe				Magnesite, Dolomite, serpentine (probably chrysotile?), Calcite? (doesn't quite hit it, but couldn't find anything better…perhaps magnesian??)
OM07-61A	vein	50 m W of Batin camp, next to 4WD track, 1 m thick erosional remnant	Batin camp	671367	2536263	522	Magnesite, Dolomite only
OM07-61B	vein	different textural types near top of spine leading SW fro 61A	Batin camp	671367	2536263	522	Goethite, Dolomite, Fe? (44.7), small amount of serpentine
OM07-61C	vein	different textural types near top of spine leading SW fro 61A	Batin camp	671367	2536263	522	Dolomite, Magnesite, tiny amount of serpentine
OM08-01	vein	veins in serp	Falayj	608957	2529931		Calcite; serp (liz and/or chr?); med peak @44.7 (Fe?)
OM08-02A	conglomerate	cgl; carb-cemented alluvial fan; A=blob of cement "oozing"from outcrop 1.5m above wadi floor					Dolomite; tiny quartz, tiny serpentine, tiny feldspar(?)
OM08-03	trav	dino teeth in a vein	Janelle campsite?	598150	2555495		Dolomite, ferroan(?)/ankerite; some calcite
OM08-04	vein	massive vein(?); Massive carbonate from surficial(?) deposit	Janelle campsite?	598138	2555487		Dolomite
OM08-153	conglomerate	"terrace" (alluvium)	Wadi Nasif	598061	2555623		magnesite; talc; dolomite; serp
OM08-154	vein	vein	Wadi Nasif	598059	2555661		dolomite
OM08-155	conglomerate	cgl terrace	Wadi Nasif	598042	2555681		
OM08-156	trav	"terrace"	Wadi Nasif	598024	2555726		magnesite; talc; dolomite; tiny serp
OM08-157	vein	vein	Wadi Nasif	598022	2555723		dolomite

Sample #	Type	Description in field notes	location	E	N	elev	Minerals identified by XRD
OM08-158	trav	terr (trav w/ pebbles?); carb-cemented conglomerate w/ mostly pebble sized clats, ~70% clasts	Bahla	530006	2542670		
OM08-200	trav	trav; recently formed travertine 20m SE of recorded waypoint	Kharma (aka Death)	600173	2528469		
OM08-201	vein	vein in perid; carb-veined perid, big chunk	Kharma (aka Death)	600090	2528421		calcite, small serpentine, v small peak @44.7 (Fe?)
OM08-201A	vein	thin sect from 201					
OM08-201B	vein	thin sect from 201					
OM08-202B	conglomerate	cgl; B=cm-sized gravel in carb matrix above chemically deposited layer A; ame location as OM08-200	Kharma (aka Death)	600173	2528469		
OM08-203	trav	trav(?) plain overlying cgl; top of cheically deposited "plain" above coarse cgl, like 202E	Kharma (aka Death)	600147	2528452		
OM08-204D	vein	veins in orange-weatherd perid with lots of tiny carb veins	Kharma (aka Death)	599562	2528435	534	dolomite, serpentine (probably chrysotile), goethite?, MAYBE chromite??
OM08-206A	vein	veins in weathered perid; 206: "preconceived notions" = mm-scale carb veins in weathered perid w/many pxte dikes or bands on low part of wall along big wadi, across from palm oasis	Quraytayn	596373	2531272	566	calcite, serpentine (probably chr and some liz, but some peaks are obscured by other mins), tiny quartz, small peak at 44.7 (Fe?)

Sample #	Type	Description in field notes	location	E	N	elev	Minerals identified by XRD
OM08-206D	vein	veins in weathered perid; 206: "preconceived notions" = mm-scale carb veins in weathered perid w/many pxte dikes or bands on low part of wall along big wadi, across from palm oasis	Quraytayn	596373	2531272	566	cc, serpentine (most like chr, but liz 100pk around 26 would be obscured by cc; peak at 19 unusually low), quartz, enstatite
OM08-206I	vein	veins in weathered perid; 206: "preconceived notions" = mm-scale carb veins in weathered perid w/many pxte dikes or bands on low part of wall along big wadi, across from palm oasis	Quraytayn	596373	2531272	566	serp (lizardite & clinochrysotile?). Plenty of olivine in thin section - why not in XRD?
OM08-210	vein	veins from roadcut just N of W Khafifa/Dima Pass	Qafifa/Dima pass	647967	2537823	884	Dolomite; serpentine (chrysotile?); aragonite
OM08-211	vein	thick carb vein	Qafifa/Dima pass	647967	2537823	884	Magnesite (ferroan?), some dolomite (ferroan/ankerite?), some serp
OM08-213	fresher peridotite	"fresh" harz below cgl	Wadi Dhuli	667296	2542415	412	Serp (chr & lizardite- peaks at 38&46 actually not missing for this one!); enstatite; peakt 44.7 (Fe?)
OM08-214	vein	veins in heavily fractured per	Wadi Dhuli	667379	2542684	421	
OM08-215	vein	big steep vein, from horizontal vein	Wadi Dhuli	667331	2542932	394	calcite; small aragonite; tiny nub of serp
OM08-216	vein	similar to 215	Wadi Dhuli	667331	2542928	394	Calcite; dolomite; aragonite
OM08-217	conglomerate	non-carb-cemented cgl	Wadi Dhuli	667323	2542947	396	serp; dolomite (ferroan/ankerite?); quartz
OM08-218	trav	stalactite above pool	Wadi Dhuli	667340	2543071	399	
OM08-219A	conglomerate	cgl; gravel and coarse cgl w/ carb cement at pool	Wadi Dhuli	667340	2543071	399	serp; calcite; dolomite (ferroan/ank?); aragonite; hydromagnesite?; hematite and the like??
OM08-219B	conglomerate	cgl; gravel and coarse cgl w/ carb cement at pool	Wadi Dhuli	667340	2543071	399	calcite; some serp

Sample #	Type	Description in field notes	location	E	N	elev	Minerals identified by XRD
OM08-220	conglomerate	un-cemented cgl	Wadi Dhuli	667340	2543071	399	serp; dolomite (ferroan/ankerite?); aragonite; possibly chloritoid? (messy xrd)
OM08-221	vein	vein; laminated carb	Wadi Dhuli	671581	2535758	525	
OM08-222A	vein	laminated carb ("sills" in per)	Wadi Dhuli	671581	2535758	525	
OM08-222B	vein	laminated carb ("sills" in per)	Wadi Dhuli	671581	2535758	525	
OM08-223B	vein	big vein, massive	near camp (which camp?)				magnesite, tiny bit of dol
OM08-223C	vein	big vein, botrioydal	near camp (which camp?)				magnesite; some magnesian calcite; tiny dolomite
OM08-226	trav	stalactite over spring	Shangrila Spring	676421	2536283	591	
OM08-227	trav	trav from wadi wall above spring	Shangrila Spring	676441	2536067	574	
OM08-401	trav	trav, cgl; Carb-cemented conglomerate from highest terrace, just above veins (transitional?); forms transect w/404 and 405	Falayj	608601	2527050		
OM08-402	vein	Vein; vein carbonate ~20cm below OM08-401; Upper Terrace at Falayj	Falayj	608601	2527050		
OM08-404	trav	trav, some clasts; carb from terrace w/ mostly mm-scale clasts; Mid-level terrace at Falayj	Falayj	608403	2527059		
OM08-406	trav	karsty trav; karsty, not many clasts	Duck	586349	2523218		
OM08-408	trav	trav; top of mid-level (lower level?) terrace jutting out as islands in modern drainage	Duck	586089	2523083		
OM08-409	trav	trav (drainage plain @Duck); carbonate from plain of current spring drainage	Duck	585927	2522933		

Sample #	Type	Description in field notes	location	E	N	elev	Minerals identified by XRD
OM08-412	trav	trav; very hard (scratches/sparks w/ rock hammer), yellow inside and out	Kharma (aka Death)	599602	2528134		dolomite; tiny serp; teeny cc peak?
OM08-413	trav	Stalagmite from main spring at Falayj	Falayj	608370	2526679		
OM08-414	trav	trav; Upper level of South Falayj; Large travertine area south of 'main' falayj spring area	South Falayj	608551	2525874		
OM08-415	trav	trav; Mid-level of South Falayj	South Falayj	608429	2525929		
OM08-416	trav	trav; lower level of South Falayj	South Falayj	608279	2525960		
OM08-418	trav	Taken above main spring	Mazara	637015	2553395		
OM08-419	conglomerate	Conglomerate terrace	Mazara	637015	2553395		
OM08-421	trav	trav; No springs were found in this area	Lizq	625531	2518393		dolomite, some calcite
OM08-422	fresher peridotite	serp from irrigation ditch	South Falayj	608420	2525929		serp; clinchlore
OM08-423	fresher peridotite	serp from irrigation ditch (renumbered, originally Krevor labeled as 421)	South Falayj	608420	2525929		serp; hydrogrossular; calcite; clinochlore
OM08-450	vein	vein; chalky white massive carbonate vein (weathers orange)	Duck	584622	2525018		magnesite; some magnesian calcite; some dolomite
OM08-452	trav	trav; Flat piece from top surface of section of 1.5m thick carbonate over veined peridotite	Duck	584446	2524269		
OM08-453	trav	trav, some clasts; Already broken block containing pebble-sized clasts, under overhang, from mid to lower part of same section as OM08-452	Duck	584446	2524269		

Sample #	Type	Description in field notes	location	E	N	elev	Minerals identified by XRD
OM09-05	vein	tc-serp carb in first MOD spot	W. Mansah mtn - first spot	620560	2585129	431	?
OM09-07	listvenite	carb-list w/green vugs in 1st MOD spot; contact between OM09-06 (light grey-green meta-peridotite w/ coarse carb) and OM09-08	W. Mansah mtn - first spot	620560	2585129	431	Mostly dolomite, small amount of what appears to be kaolinite, some very small calcite peak, no quartz peak
OM09-08	listvenite	calc list w/ orange and red bands	W. Mansah mtn - first spot	620560	2585129	431	Dolomite and quartz, some kaolinite, some calcite
OM09-09	listvenite	crumbly tc-schist (NO TS)	W. Mansah mtn - first spot	620560	2585129	431	No talc!, Serp (lizardite, maybe clinochrysotile), dolomite, calcite
OM09-11	listvenite	listvenite, 5-10m below contact with perid	W. Mansah mtn - main band	621536	2585653	641	Magnesite and quartz
OM09-12	listvenite	transitional green and orange schistose rock, 1.5m below contact with dark black Hz	W. Mansah mtn - main band	621536	2585653		Antigorite, chrysotile, magnesite, quartz, dolomite, tiny clinochlore
OM09-13	fresher peridotite	black Hz from hanging wall (transitional), 1m above contact with listvenite	W. Mansah mtn - main band	621536	2585653		Chrysotile, chromite, clinochlore
OM09-14	fresher peridotite	Hz float from above contact (more normal looking Hz)	W. Mansah mtn - main band	621536	2585653	nearby ?	Forsterite, chrysotile, clinoenstatite, enstatite (ferroan)
OM09-15	listvenite	float from upper list forming summit, above Hz band, silicified, vuggy	W. Mansah mtn - main band	621536	2585653	nearby ?	large quartz peak, small mgs peak, very small peaks for dol and cc
OM09-16	listvenite	veined list in subcrop	W. Mansah mtn - main band	621635	2585426	606	Big magesite and quartz peaks, tiny dolomite peak
OM09-18	listvenite	mylonite textured carb list	W. Mansah mtn - main band	621621	2585312	584	Magnesite and quartz
OM09-19	listvenite	heavily veined carb-list float, prob from upper list band; on hike down	W. Mansah mtn - main band	?	?		
OM09-20	listvenite	heavily veined carb-list float, prob from upper list band; on hike down	W. Mansah mtn - upper band	?	?		Dolomite and quartz

Sample #	Type	Description in field notes	location	E	N	elev	Minerals identified by XRD
OM09-27	listvenite	listvenite - typical	W. Mansah mtn - main band	621700	2585400	approx or nearby	n
OM09-28	listvenite	listvenite - green spots	W. Mansah mtn - main band	621700	2585400	approx or nearby	Magnesite and quartz, tiny dolomite
OM09-29	listvenite	listvenite - near vugs	W. Mansah mtn - main band	621700	2585400	approx or nearby	?
OM09-30	listvenite	listvenite - pink breccia	W. Mansah mtn - main band	621700	2585400	approx or nearby	big dolomite peak, small magnesite, smaller quartz nub of cc
OM09-65C-MS	listvenite	list. - Nasir spot	UTM approx estimate	601980	2602749		calcite and dolomite
OM09-66C-MS	listvenite	list. - Nasir spot	UTM approx estimate	601980	2602749		Dolomite, quartz, small cc, small greenalite (or kaolinite possibly)
OM09-67C-MS	listvenite	list. - Nasir spot	UTM approx estimate	601980	2602749		Quartz, Dolomite, tiny cc
OM09-68C-MS	listvenite	list. - Nasir spot	UTM approx estimate	601980	2602749		?
OM09-69C-MS	listvenite	list. - Nasir spot	UTM approx estimate	601980	2602749		Dolomite and quartz
OM09-71C-MS	listvenite	list. - Nasir spot	UTM approx estimate	601980	2602749		?
OM09-73C-MS	listvenite	list. - Nasir spot	UTM approx estimate	601980	2602749		Huge clean dolomite peak, small quartz peak
OM09-74C-MS	listvenite	list. - Nasir spot	UTM approx estimate	601980	2602749		N
OM09-75C-MS	listvenite	list. - Nasir spot	UTM approx estimate	601980	2602749		Big dolomite peak, small quartz, smaler cc, tiny peak by serp/kao area but can't match other peaks well
OM09-121	vein	schistose serp-carb-Tc(?) at head of trav dipslope	Misht - Very rough guess of utm	487630	2575950		No Talc (missing 100 peak around 10); Dolomite, serp (chr or liz), calcite (but peaks are shifted slightly left)

Sample #	Type	Description in field notes	location	E	N	elev	Minerals identified by XRD
OM09-122	vein	mixed silicate and carb vein (talc?)	Misht	487630	2575950		No talc, dolomite, chrysotile, calcite
OM09-123	vein	veined perid blocks in trav and footwall of trav	Misht	487630	2575950		Calcite, chrysotile
OM09-127	vein	veined perid blocks in trav and footwall of trav	Misht	487630	2575950		N
OM09-129	vein	veined perid blocks in trav and footwall of trav	Misht	487630	2575950		big Calcite and chrysotile, small quartz, ankerite, magnesite;RERUN: big calcite, big lizardite (good match wrt peak location and rel heights except for missing 70pks), med olivine, med ankerite, possible nub of quartz or graphite
OM09-130	vein	veined perid blocks in trav and footwall of trav	Misht	487630	2575950		big calcite, med-chrysotile, tiny ankerite?
OM10-01	fresher peridotite	Dark harzburgite, dark red on weathered surface; below listvenite (samples 02, 03)	W. Mansah mtn Mtn, upper band	621579	2585709	606	Big serp (could be antigorite? But missing 40pks), big olivine, med, enstatite (ferroan)
OM10-02	listvenite - transitional	Transitional ugly dark green and yellowish and red, somewhat crumbly (Photo 6)	W. Mansah mtn Mtn, upper band	621579	2585709	606	mgs, chr, TALC, dol
OM10-03	listvenite	orange-red listvenite above contact (Photo 7)	W. Mansah mtn Mtn, upper band	621579	2585709	606	mgs, qtz
OM10-04	listvenite	Pink listvenite	W. Mansah mtn Mtn, upper band	621550	2585663	637	mgs, chr, dol, unkown @ 2theta=42
OM10-05	listvenite - transitional	Grey-green transitional, more crumbly (2 pieces); ~1m above OM10-04	W. Mansah mtn Mtn, upper band	621550	2585663	637	serp
OM10-06	fresher peridotite	Black harzburgite; ~ 2m above and left of OM10-05	W. Mansah mtn Mtn, upper band	621550	2585663	637	serpentine (peak@12 much higher than @24->chr or atg; peaks@35-36 could be due to liz/atg of just ol+mgt), olivine, possible mgt

Sample #	Type	Description in field notes	location	E	N	elev	Minerals identified by XRD
OM10-07	fresher peridotite	even fresher hz, about 1m further still from contact	W. Mansah mtn Mtn, upper band	621550	2585663	637	serpentine (appears to be antigorite gvien small size of peak@19), olivine +/- magnetite
OM10-08	fresher peridotite	dunite above hz. Relatively low density	W. Mansah mtn Mtn, upper band	621550	2585663	637	pure lizardite? (good peak locations and ratios for many peaks, but still missing the 70peaks)
OM10-09A	listvenite	pale greenish vugs coating red listvenite, sometimes with minty green spots, black oxides	W. Mansah mtn, listw cap				A: almost entirely dol, B: dol, tiny en?
OM10-10	listvenite	minty green spots	W. Mansah mtn, listw cap				qtz, dol, cc
OM10-11	listvenite	layered vuggy stuff; greenish, orangish, white – green stuff coats breccias chunks, orange around that and in between – several photos	W. Mansah mtn, listw cap				dol
OM10-12	listvenite	brecciated listvenite coated with greenish cc (?), orange and white layers next to that; Collected at far end of the ridge	W. Mansah mtn, listw cap				qtz, dol, tiny cc
OM10-13	listvenite	listwanitized pyroxenite vein	behind W. Mansah mtn	619705	2588676		
OM10-14	listvenite	listvenite (orange stuff) in which the pyroxenite vein was contained	behind W. Mansah mtn	619705	2588676		dol, small qtz
OM10-15	listvenite	Big chunk of listvenite – greenish stuff inside may be fuchsite?	behind W. Mansah mtn	619454	2588738	294	Rough look, dol med qtz** are 15 & 16 switched in xrd data?
OM10-16	metasediment	Whitish weathering rock just below 15	behind W. Mansah mtn	619454	2588738	294	are 15 & 16 switched in XRD data??
OM10-17	metasediment	Metasediment	behind W. Mansah mtn	619454	2588738	294	qtz, tiny kaol

Sample #	Type	Description in field notes	location	E	N	elev	Minerals identified by XRD
OM10-18	metasediment	stuff between metasediment and listvenite dipping 48° to 15° W of N (Photo 29)	behind W. Mansah mtn	619454	2588738	294	qtz, tiny kaol, nub of cc
OM10-19	listvenite	listvenite ~ 1m from contact	behind W. Mansah mtn	619454	2588738	294	dol, qtz, cc
OM10-20	listvenite	listvenite ~3m from contact; foliation in listvenite 60° to SE 160°	behind W. Mansah mtn	619454	2588738	294	dol, qtz, cc
OM10-21	metasediment	amphibolite under listvenite	behind W. Mansah mtn	623689	2585245	488	large hornblende, med-large plag, med clinochlore, small clay (illite?), small tremolite?
OM10-22	metasediment	metasomatized amphibolite? (Photo 37) Looks like listvenite, but a bit more purplish than usual	behind W. Mansah mtn	623689	2585245	488	large quartz, med-large kaol, med dolomite, med unidentified peak @30.9(right of where mgs should be), small illite
OM10-23	metasediment	brecciated (fault between amph & list?), coarse-grained, vuggy	behind W. Mansah mtn	623689	2585245	488	Huge dolomite, v small calcite, nub of clinochlore/illite?, nub of "enargite"=Cu3AsS4??
OM10-24	listvenite	listvenite above red band	behind W. Mansah mtn	623689	2585245	488	dol, qtz, cc
OM10-25	listvenite	red listvenite with green spots		621010	2584498	301	mgs, qtz, dol
OM10-26	listvenite	similar to 25; higher density of green spots a little upstream	W. Mansah mtn Mtn near wadi base	621013	2584573	307	magnesite, quartz, dolomite
OM10-27	listvenite	Grey carb in reddish-weathering matrix	Wadi Hawasina	485806	2599524		cc, qtz, "feldspar"
OM10-28	metasediment	more finely brecciated than OM10-27	Wadi Hawasina	485806	2599524		cc, qtz, med "feldspar" (albite)
OM10-29	metasediment	mostly carb, with fine dark veins; similar to 27,28	Wadi Hawasina	485806	2599524		cc, qtz, "feldspar"
OM10-30	metasediment	similar to 27, but more little veins in carb	Wadi Hawasina	485806	2599524		cc, qtz, "feldspar"

Sample #	Type	Description in field notes	location	E	N	elev	Minerals identified by XRD
OM10-31	metasediment	fine brecciated reddish rock with strong alignment of texture	Wadi Hawasina	485806	2599524		cc, strange XRD!
OM10-32	metasediment	Grey carb in reddish matrix; reddish brown matrix extends into carb clasts as veins	Wadi Hawasina	485806	2599524		cc, qtz, small "feldspar"
OM10-33A	vein	greener perid w/ cc veins	Misht travertines	487639	2575818	637	cc, serp, unkown @ 2theta=45
OM10-33B	vein	greenish soft serp – maybe talc?	Misht travertines	487639	2575818	637	
OM10-34A	vein	OM10-34 A-G “apartment buildings” i.e., nice carb networks in serp; 34A has visible relict enstatite	Misht travertines	487524	2575999		serp, cc, mgt? (messy spectrum , lowish counts)
OM10-34B	vein	OM10-34 A-G “apartment buildings” i.e., nice carb networks in serp	Misht travertines	487524	2575999		serp, cc, mgt? (messy spectrum , lowish counts), Lizardite?
OM10-34C	vein	OM10-34 A-G “apartment buildings” i.e., nice carb networks in serp	Misht travertines	487524	2575999		serp, cc, mgt? (messy spectrum , lowish counts) Mn-dol
OM10-34D	vein	OM10-34 A-G “apartment buildings” i.e., nice carb networks in serp	Misht travertines	487524	2575999		N
OM10-34E	vein	OM10-34 A-G “apartment buildings” i.e., nice carb networks in serp	Misht travertines	487524	2575999		N
OM10-34F	vein	OM10-34 A-G “apartment buildings” i.e., nice carb networks in serp	Misht travertines	487524	2575999		N
OM10-34G	vein	OM10-34 A-G “apartment buildings” i.e., nice carb networks in serp	Misht travertines	487524	2575999		N
OM10-35	fresher peridotite	ambient harzburgite	Misht travertines	487524	2575999		olivine, chrysotile, enstatite
OM10-36	fresher peridotite	Hz in streambed 6m upstream of 0 on chain	Shumayt	486059	2588469	674	N

Sample #	Type	Description in field notes	location	E	N	elev	Minerals identified by XRD
OM10-37	vein	mixed serp & dol veins above Shumayt	Shumayt	486016	2588521	698	N
OM10-38A	listvenite?	apartments, dark green flakes, dark veins [illegible "f---t--g/y" = feathery?] black in lighter grey	Wadi Bani Omar	484064	2632409		
OM10-38B	listvenite?	similar, nice veins, Peter thinks this sample has fewer holes	Wadi Bani Omar	484064	2632409		Calcite, tiny hematite?
OM10-38C	listvenite?	light yellow-green with black speckles and white chunks/veins	Wadi Bani Omar	484064	2632409		
OM10-38apts	listvenite?	"apartment complexes"	Wadi Bani Omar	484064	2632409		N
OM10-39A	metasediment?	dark grey cc-rich micaceous rock	Wadi Bani Omar	484730	2632393		large calcite, small quartz, tiny aragonite?
OM10-39B	metasediment?	picked up nearby 39A	Wadi Bani Omar	484730	2632393		huge calcite, small quartz
OM10-40	metasediment?	collected at outcrop, but similar to OM10-39A; in contact with peridotite	Wadi Bani Omar	484981	2632374		large calcite, med (calcian?) dolomite, small serpentine (chr?)
OM11-01	fresher peridotite	Partially serpentinized wallrock near wide deformed vein of light-colored carbonate	Tuf	597539	2554844	884	Large serpentine (liz best but not perfect match), med olivine
OM11-02	listvenite	orange-weathering, greyish/purplish/greenish inside, deformed carbonated perid in R-lateral fault	Tuf	597539	2554844	884	N
OM11-03	listvenite	Orangish/pinkish carbonate in same gully/fault; contains brown bands	Tuf	597547	2554840	882	Large mgs,, med talc (but 40 peak is taller than 100 peak!), med-sm serp, smallsh dolomite, diopside(?)
OM11-04	altered peridotite	purplish brown serpentinite wall rock (by Peter's foot in photo 9)	Tuf	597550	2554818	879	Large dol, large serp, med mgs, possible olivine (med may be buried in broad serp peak)

Sample #	Type	Description in field notes	location	E	N	elev	Minerals identified by XRD
OM11-05	altered peridotite	Serpentinite blob in carb band	Tuf	597550	2554818	902	Large mgs, med dol, med-sm talc, med-sm serp
OM11-06 A, B	altered peridotite	2 samples of zoned veins in serpentinite by old house; zoned serpentinite veins, going out from center: green, black, purple, orange. Purplish layer is very thin and less pronounced in A than in B	Tuf	598022	2555728	902	Large serp (looks most like liz, but there is a subpeak around 36.6 I can't match, possibly olivine); med dol
OM11-07	fresher peridotite	serp at contact w/ more altered pink rocks; black veinlets align with fault	Tuf	598022	2555728	902	large serp, med-large olivine
OM11-08 A, B	listvenite	pink altered perid sheared at contact w/serpentinite; A has more of shear zone, B has more of wall rock	Tuf	598022	2555728	902	Magnesite, dolomite, serpentine (chr/liz); peak not well-accounted for at 2-theta=43, possible minor serp peaks near, but this is pretty large
OM11-09	listvenite	Pink altered perid, ~ 20cm SW of previous sample	Tuf	598022	2555728	902	Large mgs, med talc, small serp, small dol
OM11-10	listvenite	Piece of pink altered peridotite with chromite band (Dipping ESE to SE at ~30°)	Tuf	598022	2555728	902	Large mgs, med talc, med-small dol, tiny serp
OM11-11	altered peridotite	peridotite wall rock from western contact of pink stuff; - heavily veined wall, some of it looks like OM09-206I (i.e., distinct green, orange, and black stripes)	Tuf	598022	2555728	902	big serpentine peaks, looks like mix of lizardite and chrysotile, smal l dolomite; unidentified peak @ 30.3 near 100 peak for diop but not great
OM11-12	listvenite	Red carbonate-looking rock	Tuf	598022	2555728	902	Magnesite, dolomite, possible nub of clinochlore/kaolinite?
OM11-13	altered peridotite	island of less altered peridotite near OM11-07to09	Tuf	598022	2555728	902	large mgs, med dol, med talc, small serp

Sample #	Type	Description in field notes	location	E	N	elev	Minerals identified by XRD
OM11-14	listvenite	Carbonate just above OM11-12 that weathers even more like limestone	Tuf	598022	2555728	902	Large mgs, small dol, small unidentified peak slightly right of where cc peak would be (magnesian cc??)
OM11-15	listvenite	Similar to OM11-14, but contains abundant chromite	Tuf	598022	2555728	902	Large mgs. Large dol, med clinochlore, small peak (mg-rich cc or diop??)
OM11-16	listvenite	Red apt buildings	Tuf	598022	2555728	902	Large mgs, med-small dol, small serp, tiny talc
OM11-17	listvenite	Whitish orange rock just above 16	Tuf	598022	2555728	902	Large mgs, small dol, small serp, tiny talc
OM11-18	altered peridotite	Serp wall rock next to 17	Tuf	598022	2555728	902	Large serp (most like liz), large dol, small tough to match peak (mg-rich cc?? Diop??)
OM11-19	fresher peridotite	Large island of fresher peridotite near 7-8-9	Tuf	598022	2555728	902	Large olivine, large serp
OM11-20	fresher peridotite	Black peridotite in plain at mouth of wadi below trav terraces; Black outside, dark grey inside, lots of pyroxene grains flashing on weathered surface	Falayj	608334	2525825	521	Large serp, large clinoenstatite, med-large olivine
OM11-21	fresher peridotite	Black peridotite in wall under travertine, next to where stalactites oozing out	Falayj	608373	2525832	536	large serp, large clinoenstatite
OM11-23 (note: skipped 22)	vein	sort of vuggy-looking peridotite near OM11-21, at top of peridotite under travertine; many more veins	Falayj	608373	2525832	536	large calcite, med serpentine (chr + liz), possible tiny graphite(???) or more likely just minor liz peak
OM11-24	fresher peridotite	pyroxenite vein from near garden of speleothems	Falayj	608373	2525832	536	large cpx, large serp, med olivine

Sample #	Type	Description in field notes	location	E	N	elev	Minerals identified by XRD
OM11-25	vein	Light green schistose altered peridotite with calcite in matrix and cut by white calcite veins; makes up ~10x4.5m (exposed height of wall) area of altered peridotite under the travertine. Has cobbles of less altered, dark brown peridotite in it	Falayj	608344	2525859	526	huge calcite, relatively tiny serpentine
OM11-26	vein	more of the “altered peridotite” green stuff (next to pretty crystals and vugs)	Falayj	608344	2525859	526	huge calcite, med serpentine
OM11-27	fresher peridotite	A-C Peridotite cobbles cemented on top of trav for exposure age dating (BY WHOM again?)	Falayj	608415	2525852	549	N
OM11-28	altered peridotite	Several (4) jigsaw pieces of rounded blocks of altered peridotite surrounded by more altered veins (carb?)	Nasif	641011	2534171	711	huge serp, med (but obscured) olivine, med dolomite, small cpx(?)
OM11-29	altered peridotite	intact piece from edge of rounded blocks of altered peridotite surrounded by more altered veins, next to 28, 30, 31	Nasif	641011	2534171	711	N
OM11-30	altered peridotite	small pieces of rounded blocks of altered peridotite surrounded by more altered veins	Nasif	641011	2534171	711	large serp (need chr for peak at 43.2), large olivine, med-sm dolomite;
OM11-31	altered peridotite	3 jigsaw pieces of rounded blocks of altered peridotite surrounded by more altered veins	Nasif	641011	2534171	711	large serp (need chr for peak at 43.2), large olivine, med-sm dolomite;
OM11-32	fresher peridotite	dunite wall rock ~1 m south of carbonate lens	Nasif	641011	2534171	711	Large serp (chr? lizardite missing 70peak at 46.3 also prob @38.56), forsterite

Sample #	Type	Description in field notes	location	E	N	elev	Minerals identified by XRD
OM11-33	fresher peridotite	Dunite (?) wall rock with lots of veins (serp?) ~ 10m N of carb lens	Nasif	641011	2534171	711	Large serp (chr? lizardite missing 70peak at 46.3, but 60pk might explain med sm peak @42), large olivine, small pyroxene
OM11-34	fresher peridotite	Hz wall rock some m N of carb lens (no veins)	Nasif	641011	2534171	711	big serp, big olivine (100&83pks reversed in size…liz/ant?), med enstatite
OM11-35	altered peridotite		Nasif	641011	2534171	711	N
OM11-36	altered peridotite	Rounded brown peridotite block in black and sometimes green veins	Nasif	640948	2534203	713	Big serp (all 3??..ant pk @53.9? Chr pk@42.9?), olivine (but again reversed), enstatite? (good match for peaks at 30-31 for mg enstatite, but missing 100pk@28, maybe som other px)
OM11-37	altered peridotite	huge chunk from rounded blocks in matrix	Nasif	640925	2534244	714	N
OM11-38	altered peridotite	zoned vein from same spot as OM11-37	Nasif	640925	2534244	714	Large serp (may need ant to explain peak at 36.6 and liz to explain peak @35.9 since fo missing other peaks, but similarly large peak at 54 missing), maghemite (or possibly mgt), medium dolomite
OM11-39	metasediment	phyllite from top of ridge	W. Mansah mtn Mtn	621057	2585970	599	large quartz, small clinochlore & muscovite
OM11-40	metasediment	Little pieces of cream-colored marble in the phyllite	W. Mansah mtn Mtn	621043	2585898	578	huge calcite, tiny quartz, possible nub of dolomite
OM11-41	metavolcanic	Finer-grained grey/green shale-like rock further down section	W. Mansah mtn Mtn	620879	2585914	505	Clinochlore, tremolite?, plag?, epidoite?, cummingtonite??

Sample #	Type	Description in field notes	location	E	N	elev	Minerals identified by XRD
OM11-42	metasediment	Phyllite/schist w/ white nodules and wavy layers	W. Mansah mtn Mtn	620770	2585818	467	huge quartz, small muscovite, tiny clinochlore, teeny hematite?
OM11-43	metasediment	Red weathering layers, schistose	W. Mansah mtn Mtn	620754	2585634	427	large calcite, med quartz, teeny clinochlore
OM11-44	metasediment	red limestone (that sort of looks like listvenite on the weathered surface :{) occurs as layers in the red schist like 43	W. Mansah mtn Mtn	620743	2585473	424	large calcite, med ankerite, med quartz, teeny cliochlore
OM11-45	metasediment	Dark grey limestone, coarse-grained, some pebbly clasts; weathers red	W. Mansah mtn Mtn	620740	2585436	420	large calcite, med quartz, teeny clinochlore
OM11-46	metasediment	Red quartzite in wadi as boulder	W. Mansah mtn Mtn	620727	2585391	416	Quartz, possible nub of calcite
OM11-47	metasediment	Dark red cherty stuff with slicken lines	W. Mansah mtn Mtn	621003	2585094	377	v large quartz, large dolomite, small kaolinite
OM11-48	metasediment	Layered green-grey sediment	W. Mansah mtn Mtn	621086	2585006	365	v large quartz, large calcite, small illite, clinochlore
OM11-49	metavolcanic	Green-grey massive rock w/ white vein and blobby structure à Altered pillow basalt?	W. Mansah mtn Mtn	621109	2584926	359	(messy spectrum) plag, calcite quartz, cpx, clinochlore, serp??, olivine??, enstatite??
OM11-50	metasediment	Layered sediment dipping to NW (NW side of wadi)	W. Mansah mtn Mtn	621103	2584887	354	huge quartz, small calcite, teeny nub of clinochlore, unID nub @24.0
OM11-51	metasediment	On other side of wadi, almost vertical dip	W. Mansah mtn Mtn	621103	2584887		huge quartz, nub calcite, unID nub @24.0
OM11-52	listvenite	multiple listvenite samples for fuchsite (red listvenite with green spots from same place as OM10-26, which contained fuchsite)	W. Mansah mtn Mtn	621013	2584563	321	N
OM11-53	metasediment	(Cretaceous?) Conglomerate in pass	Fanja	621486	2592904	508	huge quartz, small calcite, nub of smectite-kaol?

Sample #	Type	Description in field notes	location	E	N	elev	Minerals identified by XRD
OM11-54	metasediment	conglomerate/listvenite unconformity on boulder in drainage	Fanja	620188	2592649	284	Serp (antigorite?), med magnesite & dol
OM11-55	listvenite	Very funny colored, light, sage-green altered Hz w/ soft, white carb(?) veins; low density	Amqat	615553	2593140	240	Large calcite, large dolomite, med-sm quartz
OM11-56	listvenite	massive, chalky, white vein	Amqat	615685	2593075	235	
OM11-57	listvenite	pink altered dunite. Low density	Amqat	615685	2593075	235	large magnesite, med-lg serpentine (liz), small dol
OM11-58	altered peridotite	heavily altere Hz, low density, fine-grained pink & white, with harder pale green veins	Amqat	615685	2593075	235	large magnesite, large serp, med (obscured) olivine, small dol, tiny talc
OM11-59	altered peridotite	green altered peridotite from across the road	Amqat	615685	2593075	235	large serp, large olivine, small dol
OM11-60	metasediment	Cretaceous sandstone (?) uncomformably overlying listvenite. “ss” is largely massive and clast-free, has rounded qtz pebbles in some places, some clasts look a little worryingly angular.	Fanja	614786	2594264	304	quartz, dolomite, small calcite, tiny kaol
OM11-61			Fanja				N
OM11-62	listvenite	Very red weathering, fairly hard rock, grey inside for very fresh samples; 10 paces from S end of outcrop on W wall	Fanja roadcut, W side	614001	2594544	234	large quartz, large dolomite
OM11-63	listvenite	Buff, highly weathered, w/ fine dark stripes; 19 paces FSEO	Fanja roadcut, W side	614002	2594557		large dolomite, large serpentine, large (obscured) olivine; possible unidentified peaks around 50 (look bigger than expected for liz + dol)

Sample #	Type	Description in field notes	location	E	N	elev	Minerals identified by XRD
OM11-64	listvenite	purply pink stuff; 33 PFSEO	Fanja roadcut, W side	614005	2594578		dolomite, serpentine (may include both liz and antig based on peaks at 35.7 and 36.6 but these could also be due to chromite or maghemite (35.7) or hercynite (36.6) and small peak around 30 matches maghemite while the usual peaks are missing for liz & atg), unidentified peaks at 33.5, 50.6, 51)
OM11-65	altered peridotite	red stuff; 47 PFSEO	Fanja roadcut, W side	614007	2594598		(calcian?) magnesite, serpentine (may include both liz and antig based on peaks at 35.7 and 36.6 but these could also be due to oxides), dolomite
OM11-66	altered peridotite	red stuff w. light greenish-grey slicken lines; 53 PFSEO	Fanja roadcut, W side	614008	2594607		Big lizardite, med magnesite, unidentified double peak around 51
OM11-67	altered peridotite	green alterd peridotite; pretty scuzzy, criss-crossed with white carb veins; 57 PFSEO	Fanja roadcut, W side	614009	2594612		Big lizardite, small maghemite (main peak is same as liz, but minor peaks match som tiny otherwise unidentified peaks), possible antigorite and/or olivine
OM11-68	altered peridotite	orange and purple rock; Purple more coherent pieces break/crumble along very orange weathered cracks; transitional between greenish rocks and purple rocks; 70 PFSEO	Fanja roadcut, W side	614011	2594631		large serpentine (lizardite, possible antigorite), med dolomite, small magnesite, maghemite (or halite (potassian))

Sample #	Type	Description in field notes	location	E	N	elev	Minerals identified by XRD
OM11-69	altered peridotite	purple w/ mm-scale criss-crossing grey veins; 74 PFSEO	Fanja roadcut, W side	614011	2594637		Lizardite (mising usual peaks), possible antigotite (peat at 36.6), med dolomite, maghemite or halite
OM11-70	altered peridotite	orange listvenite; some regions of apartment buildings, white carb veins, low sub-horizontal ~ 6m vein of green stuff à fuchsite??; 80 PFSEO	Fanja roadcut, W side	614012	2594646		big calcite, big ankerite, med serpentine, med-large chromite (peaks for maghemite, olivine also in this area), small hematite, small quartz, several unidentified (would arsenopyrite be consistent w/XRF?)
OM11-71	altered peridotite	low sub-horizontal ~ 6m vein of green stuff → fuchsite?? From OM11-70 listvenite	Fanja roadcut, W side	614012	2594646		same as 70
NORTH END OF OUTCROP (W WALL)		103 paces from south end of outcrop	Fanja roadcut, W side	614016	2594678	229	
OM11-72	listvenite	fuchsite (?) from listvenite boulder below N end of outcrop. (Location approximate)	Fanja roadcut, W side	614016	2594678		Huge dol, large calcite
SOUTH END OF OUTCROP (E WALL)		Location of south end of outcrop	Fanja roadcut, E side	614079	2594482	216	
OM11-73	altered peridotite	pinkish altered dunite w/ chromite vein; greenish brown larger blocks in this stuff weathering out like rounded boulders. (Note: avoid chromite vein for bulk chem); 7 PFSEO	Fanja roadcut, E side	614078	2594493	217	Magnesite, Serpentine (liz explains peak at 35.8 - actually more likely CHROMITE PEAK, but missing peak at 46)

Sample #	Type	Description in field notes	location	E	N	elev	Minerals identified by XRD
OM11-74	altered peridotite	Purple rock, greenish, soft slicken lines → Talc-bearing?; 33 PFSEO	Fanja roadcut, E side	614075	2594536	219	Magnesite, Serpentine (liz explains peak at 35.8, but missing peak at 46). No talc in XRD
OM11-75	altered peridotite	Green, slippery rock (Talc?); 34 PFSEO	Fanja roadcut, E side	614075	2594537	219	Magnesite, Serpentine (probably both liz and antigorite, based on double peak at 35.8, 36.6 but no other major fo peaks, but the usual missing peaks for both). No talc in XRD
OM11-76	altered peridotite	Pink block in the green stuff	Fanja roadcut, E side	614075	2594537	219	Magnesite, Serpentine (probably both liz and antigorite, based on double peak at 35.8, 36.6 but no other major fo peaks, but the usual missing peaks for both).
OM11-77	altered peridotite	pink band above green stuff; 36 PFSEO	Fanja roadcut, E side	614075	2594541	220	Magnesite, Serpentine (probably lizardite); Magnesite is largest peak in powder from thin section cuttings, but missing from powder from piece broken off hand sample with a rock hammer
OM11-78	altered peridotite	Fine(?) green, ~1m above contact w/ pink; 39 PFSEO	Fanja roadcut, E side	614074	2594545	220	Serpentine (liz missing peak at 46, ant missing 3 peaks @14,15,17, but might explain peak @36.6 (partially obscured by liz peak)), dolomite

Sample #	Type	Description in field notes	location	E	N	elev	Minerals identified by XRD
OM11-79	altered peridotite	Weird light green rock w/ black stripes, some very shiny, glossy surfaces; 47 PFSEO	Fanja roadcut, E side	614073	2594558	221	Serpentine (liz, possibly chr too - and/or magnetite, possibly antigorite too - and/or hercynite). Cuttings/dry chips doesn't seem to matter
OM11-80	altered peridotite	brownish-green; 49 PSEO	Fanja roadcut, E side	614073	2594562	221	Lizardite (missing peak at 46.3, 56.1)
OM11-81	altered peridotite	white magnesite vein; 58 PSEO	Fanja roadcut, E side	614072	2594576	222	Magnesite. Tinies nubs of serpentine, calcite.
OM11-82	altered peridotite	peridotite intruded by gabbro? (meta- everything of course); 80 PSEO	Fanja roadcut, E side	614069	2594612	224	Serpentine (possibly all three, but distinguishing peaks could also be attributed to oxides, e.g. chromite for liz, hercynite for atg), hydrotalcite - large peak just left of first serp peak, but missing very first peak around 5
OM11-83	altered peridotite	meta-gabbro?; NO, CHROMITE ORE DEPOSIT	Fanja roadcut, E side	614069	2594612	224	Spinel (ferrian), lizardite, hydrotalcite (missin peak @5)
OM11-84	altered peridotite	yellowish purplish greyish peridotite; 86 PSEO	Fanja roadcut, E side	614069	2594622	225	Serpentine (possibly all three, but distinguishing peaks could also be attributed to oxides, e.g. chromite for liz, hercynite for atg), hydrotalcite - large peak just left of first serp peak, but missing very first peak around 5
OM11-85	altered peridotite	whitish-yellow vein in OM11-84;, ~15cm thick	Fanja roadcut, E side	614069	2594622	225	Hydrotalcite, magnesite, serpentine (possibly all 3 types)

Sample #	Type	Description in field notes	location	E	N	elev	Minerals identified by XRD
OM11-86	altered peridotite	purple peridotite w/ small black veins and yellow-green-brown blocks and veins (part of this on sample); 88 PSEO	Fanja roadcut, E side	614068	2594625	225	Serpentine (liz missing peak at 46, ant missing 3 peaks @14,15,17, but might explain peak @36.6 (partially obscured by liz peak)), magnesite, dolomite, maghemite(?)
OM11-87	altered peridotite	Purple altered peridotite	Fanja roadcut, E side	614068	2594630	225	Calcite, ankerite, lizardite, quartz, hercynite(?) or antigorite, some un-identified peaks
OM11-88	altered peridotite	listvenite vein in purple peridotite; 2 pieces, 1 incl contact	Fanja roadcut, E side	614068	2594630	225	huge calcite, small ankerite, very small serp
OM11-89	altered peridotite	contact between purple & listvenite	Fanja roadcut, E side	614068	2594630	225	huge calcite, med-sm dolomite, small serpentine
OM11-90	listvenite	brown listvenite near contact	Fanja roadcut, E side	614068	2594630	225	huge calcite, small quartz, tiny ankerite
OM11-91	listvenite	apartment buildings (small holes) in listvenite	Fanja roadcut, E side	614068	2594630	225	huge calcite, tiny ankerite, possible blip of goethite
OM11-92	listvenite	veins & vugs in listvenite (2 pieces)	Fanja roadcut, E side	614068	2594630	225	huge calcite, unidentified blip of something at 26.5
OM11-93	listvenite	orange listvenite (pretty normal-looking listvenite); 95 PFSEO; UTM interpolated	Fanja roadcut, E side	614070	2594634	226	Quartz, dolomite, calcite
End		End of listvenite outcrop, faulted against green sediment	Fanja roadcut, E side	614077	2594652	228	
OM11-94	altered peridotite	Pink altered peridotite w. dark green spots; containing a tump(??) of less altered brown peridotite surrounded by a thin black rim. Sampled about 1m below photos 63 & 64 (but from part that is less red)	Al-Abyad	568249	2591291	254	large magnesite, large talc (but 40 pk taller than 100pk!), small serp, small dol

Sample #	Type	Description in field notes	location	E	N	elev	Minerals identified by XRD
OM11-95	altered peridotite	Rounded peridotite remnants in pink altered peridotite. (5 pieces, some for display)	Al-Abyad	568249	2591291	254	large magnesite, large talc (but 40 pk taller than 100pk!), small serp, small dol
OM11-96	altered peridotite	zoned veins in heavily altered part between blocks; green (serp?) and white (carb?). (2 pieces)	Al-Abyad	568249	2591291	254	large magnesite, large talc (but 40 pk taller than 100pk!), small serp, small dol
OM11-97	altered peridotite	center of less altered blocks	Al-Abyad	568249	2591291	254	large serp, large olivine, large cpx(?), tiny talc
OM11-98	altered peridotite	pink heavily altered perid (no remnant blocks), from near OM11-95	Al-Abyad	568249	2591291	254	large magnesite, large talc (but 40 pk taller than 100pk!), small dol
OM11-99	altered peridotite	dark black-green perid from upstream of this highly altered zone	Al-Abyad	568249	2591291	254	huge lizardite (but still missing the 70pks), small enstatite
OM11-100	altered peridotite	layered serp & carb vein (on edge of sample) along pink, weathered perid	Al-Abyad	568249	2591291	254	N
OM11-101	fresher peridotite	fresher peridotite from back by car	Al-Abyad	568704	2590125	283	N

Appendix 2. Clean chemistry procedures

(Adapted from LDEO clean lab procedures as written up by Jason Jweda)

Dissolution of Silicate Rock Powders

1) Weigh an empty pre-cleaned Teflon beaker (wrap in Al foil and shoot with electro-static gun) and then re-zero the balance.

2) Add ~0.2 g (range: 0.19 – 0.21 g) of rock powder to beaker.

3) Weigh the beaker with the sample.

4) In fume hood, add 3 ml conc. HNO_3 + 1.5 ml HF. Seal tightly

5) Heat on hotplate for ~12 hr (overnight) at 140°C.

6) Check to see if dissolution is complete (dissolved samples should be white in color). If dissolution is complete, sonicate for ~20 minutes.

a) If dissolution is incomplete, sonicate and heat as necessary to dissolve samples.

7) Un-cap beakers and air dry beakers on hotplate at 120°C for ~3 hr (be careful to un-cap beakers in correct sequence…laminar air flow in hotplate boxes).

8) When dry, allow the samples to cool and then add 1 mL of DD conc. HNO_3 to the cap of the beakers and carefully pour into beakers. Add 1 mL of DD conc. HNO_3 to each beaker, sonicate for ~10 min, and then heat on hotplate for ~12 hr. (overnight) at 120°C.

9) Un-cap beakers and air dry on hotplate at 120°C for ~3 hr.

10) Add 2 mL of DD 6 N HCl + 0.2 N HF, cap beakers, and then sonciate for ~10 min to break up the samples.

11) Heat on hotplate at 120°C overnight.

a) If solid residues remain, sonicate for ~40 min. If solids still remain, add another 2 ml of DD 6 N HCl + 0.2 N HF. Seal beakers and heat on hotplate at 120°C for 30 minutes, then sonicate for 30 minutes.

12) Un-cap beakers, wipe droplets from outside of beakers, and dry on hotplate at 120°C for ~3 hr.

13) When dry, cap the beakers and allow them to cool.

Procedure – Tru-Spec Column Chemistry

1) Take the dried samples from the dissolution step and add 1 mL of 1 N HNO_3 to each beaker.

2) Cap beakers, sonicate for 20 min, and heat on hotplate at 90°C for ~1-2 hours.

3) Allow beakers to cool and then transfer to bullets and centrifuge samples for ~25 minutes.

4) Concurrently prepare Pb columns for Tru-Spec chemistry:

a) Add QD water to resin and brake up fine particles by shaking.

b) Pipette off fine particles from top of water surface.

c) Prepare column stand by rinsing with DI water and putting parafilm across the top of the stand. Cut holes in parafilm for columns.

d) Rinse off pre-cleaned Pb columns to for Tru-Spec column chemistry. Clean Pb columns by putting columns in a large Teflon beaker with DD 6 N HCl (re-used for cleaning) and sonicating for ~10 minutes and then rinse columns off with QD. Also put columns in a large Teflon beaker with DD 1 N HNO3 (re-used for cleaning) and sonicating for ~10 minutes and then rinse columns off with QD.

e) Add QD water to columns (bottom first and then top, avoiding any bubbles in stem of column).

f) Add Tru-Spec resin (rinsed resin with 3N HNO_3 and then QD 3x; pipette off floating particles) up to the neck of the columns.

g) Allow resin to settle and pipette off excess.

5) Collecting in a waste beaker, fill column with 1 full reservoir of QD water.

6) Make DD 1 N HCl (41.667 mL of 6 N HCl with 208.333 mL of QD).

7) Add 1 full reservoir of DD 1 N HCl to the columns to wash away REEs (2 times).

8) Add 300 µL of QD water to the columns to wash the HCl from the columns.

9) Add 300 µL of DD 1 N HNO_3 to pre-condition the columns (3 times).

10) Change the waste beakers with the original sample Teflon beakers and load centrifuged samples by carefully pipetting the supernatant avoiding the solid particles. Remember to keep beaker caps facing down.

11) Add 500 μL of DD 1 N HNO_3 to the columns to elute the cation cut (Rb and Sr) (3 times).

12) Collecting in new beakers (labeled REE cut), add 330 μL of DD 1 N HCl (3 times).

13) After all of the clean REE cut solution has been collected, cap beakers and store properly with label and polyvinyl chloride wrap.

14) Cover the columns with wrap and leave for cleaning.

15) Dry down both the cation cut and the REE cut at 120°C on the hotplate for ~3-4 hours.

16) Clean the Tru-Spec columns by rinsing with QD to remove resin and then putting columns in a 6 N HCl re-usable cleaning solution bath. Sonicate columns for ~10 minutes and then store columns in QD water.

Sr Column Chemistry

1) Add 0.5 mL of DD 3 N HNO_3 to the cation cut from the REE separation.

2) Heat to 110°C on the hotplate for ~1-2 hours to dissolve samples.

3) Transfer dissolved samples to bullets and centrifuge for ~20 minutes.

4) Concurrently prepare the 30 μL volume Sr columns with 0.5 mL volume reservoirs (hand made from shrink tubing):

a) Clean out previously used Sr columns (small columns) with QD water and removing the resin.

b) Clean Sr columns by putting them in a 6 N HCl bath and sonicating for ~15 minutes and then rinsing them off with QD.

b) Prepare column stand by rinsing with DI water and putting parafilm across the top of the stand. Cut holes in parafilm for columns.

c) Add QD water to columns (bottom first and then top, avoiding any bubbles in stem of column).

d) Add Sr resin up to the neck of the columns.

e) Allow resin to settle and pipette off excess.

5) Collecting in waste beakers, add 1 full reservoir of QD water to wash away any Sr in the columns (3 times).

6) Make DD 3 N HNO_3 (49.670 mL of DD 15.1 N HNO_3 and 200.330 mL of QD water), and then add 1 full reservoir of 3 N HNO_3 to condition the columns.

7) Collecting in the original sample beakers, load the samples by pipetting the supernatant from the centrifuged solutions

8) Add 330 µL of 3 N HNO_3 to the columns to collect Rb and other cations (3 times).

9) Collecting in new pre-cleaned beakers (labeled pure Sr cut), add 1 full reservoir of QD to elute pure Sr (3 times).

10) After all of the clean Sr cut solution has been collected, cap beakers and store properly with label and polyvinyl chloride wrap.

11) Clean Sr columns by dumping the resin with QD and then put Sr columns in a 6 N HCl bath and sonicate for ~15 minutes.

12) Dump the 6 N HCl for re-use in cleaning and store Sr columns in QD water.

13) Dry down the Sr samples. Add 2 drops of conc. HNO3, sonicate, and then dry to a drop. Then add 8 uL of 6 N HCl and keep in beaker until loaded onto filament.

14) After Sr samples have been measured by TIMS, add 20 uL of conc. HNO3 to the beakers, dry to drop, add 500 uL of 6 N HCl, heat for 5 min., sonicate, and transfer to bullets for storage.

Appendix 3. All clumped isotope data

Year	spec #	Sample ID	Type	Mineral	Rxn	Acid T, C	δ13C (PDB)	stdev	δ18O (SMOW)	stdev
2009	6	Carrara	std	Calcite	offline	25	2.357	0.003	39.628	0.009
2009	14	OM07-08	trav (old)	Calcite	offline	25	-12.836	0.002	36.748	0.007
2009	22	OM07-34c	trav (young)	Calcite	offline	25	-26.120	0.002	25.178	0.007
2009	30	eBOC	HG	HG		HG	-11.055	0.003	55.581	0.011
2009	38	OM07-54	vein	Dolomite	offline*	90	-2.019	0.002	48.166	0.004
2009	46	OM09-27	listvenite	Dolomite	offline*	90	0.802	0.003	33.949	0.008
2009	54	OM09-130	vein	Calcite	offline	25	-11.409	0.002	36.897	0.006
2009	62	BOC	HG	HG		HG	-10.674	0.001	29.526	0.010
2009	70	OM08-01-cc	vein - mixed carb	Calcite	offline	50	-10.230	0.002	37.840	0.011
2009	78	Carrara	std	Calcite	online	25	2.344	0.004	39.636	0.011
2009	86	OM07-17-dol	vein - mixed carb	Dolomite	offline*	50	0.343	0.002	43.704	0.005
2009	94	OM08-01-dol	vein - mixed carb	Dolomite	offline*	50	-10.173	0.002	37.789	0.006
2009	102	OM07-61a-dol	vein - mixed carb	Dolomite	offline*	50	-4.933	0.003	45.923	0.014
2009	115	OM09-18	listvenite	Magnesite	offline	80	-1.816	0.002	32.242	0.005
2009	123	BOC	HG	HG		HG	-10.842	0.003	41.973	0.016
2009	131	OM09-16	listvenite	Magnesite	offline	80	-1.644	0.001	30.931	0.006
2009	139	OM09-75	listvenite	Dolomite	offline*	50	0.186	0.002	33.490	0.003
2009	147	OM07-61a-mgs	vein - mixed carb	Magnesite	offline	80	-8.666	0.003	43.225	0.002
2009	156	OM07-07-mgs	vein - mixed carb	Magnesite	offline	80	-9.944	0.002	40.832	0.010
2011	443	eBOC	HG	HG		HG	-10.840	0.001	58.119	0.007
2011	465	eBOC	HG	HG		HG	-10.550	0.003	62.752	0.010
2011	474	TV01	std	Calcite	online	90	2.555	0.003	30.466	0.006
2011	483	OM08-206D	vein	Calcite	online	90	-9.003	0.003	37.286	0.005
2011	492	Carrara - offline 1	std	Calcite	offline	90	2.260	0.003	36.759	0.004
2011	501	OM08-200	trav (young)	Calcite	online	90	-19.824	0.002	26.817	0.004
2011	510	OM10-11	listvenite (crust)	Dolomite	online	90	-5.718	0.003	31.067	0.005
2011	519	TV01 offline1	std	Calcite	offline	90	2.564	0.002	29.993	0.005
2011	528	BOC	HG	HG		HG	-10.950	0.006	29.544	0.011
2011	546	Carrara - offline2	std	Calcite	offline	90	2.211	0.002	36.946	0.004
2011	555	Carrara	std	Calcite	online	90	2.341	0.002	37.302	0.003
2011	564	ht-5	mgs cal - exp	Magnesite	offline	90	-25.685	0.002	15.579	0.003
2011	574	OM10-38B	listvenite? (Bani Omar)	Calcite	online	90	-6.762	3.677	33.475	1.546
2011	583	OM07-34C	trav (young)	Calcite	online	90	-25.539	0.002	23.231	0.003
2011	593	OM10-34B	vein	Calcite	online	90	-9.090	0.002	36.313	0.005
2011	602	eBOC	HG	HG		HG	-10.945	0.003	60.230	0.004
2011	622	playa	mgs cal - playa	Magnesite	offline	90	4.282	0.002	25.168	0.007

Appendix 3. All clumped isotope d

Year	spec #	Sample ID	δ47	stdev	Δ47	stdev	st err	δ48	Δ48	stdev	Δ47 HG corr.	Δ47 acid corr.	Δ48 excess
2009	6	Carrara	20.08	0.08	-0.34	0.03	0.009	35.83	6.81	0.33	0.328	0.328	0.61
2009	14	OM07-08	2.54	0.07	-0.16	0.02	0.007	28.97	5.77	0.40	0.662	0.662	0.69
2009	22	OM07-34c	-21.85	0.06	-0.30	0.03	0.011	1.22	0.89	0.24	0.709	0.709	0.33
2009	30	eBOC	22.39	0.07	-0.64	0.03	0.010	73.31	12.03				
2009	38	OM07-54	24.55	0.06	-0.10	0.02	0.007	55.89	9.69	0.24	0.549	0.630	0.22
2009	46	OM09-27	12.95	0.07	-0.28	0.03	0.011	23.19	5.48	0.43	0.452	0.533	1.34
2009	54	OM09-130	4.02	0.07	-0.21	0.04	0.013	29.11	5.61	0.15	0.594	0.594	0.50
2009	62	BOC	-3.16	0.08	-0.84	0.01	0.005	10.67	1.77				
2009	70	OM08-01-cc	6.12	0.07	-0.19	0.01	0.005	31.53	6.14	0.42	0.594	0.625	0.64
2009	78	Carrara	20.14	0.07	-0.28	0.04	0.013	35.72	6.69	0.20	0.392	0.392	0.50
2009	86	OM07-17-dol	22.41	0.07	-0.11	0.02	0.006	46.41	9.18	0.24	0.556	0.587	1.25
2009	94	OM08-01-dol	6.09	0.08	-0.23	0.03	0.010	31.22	5.94	0.14	0.557	0.588	0.49
2009	102	OM07-61a-dol	19.45	0.06	-0.08	0.02	0.009	51.79	10.10	0.40	0.607	0.638	1.30
2009	115	OM09-18	8.54	0.07	-0.44	0.03	0.009	17.71	3.41	0.29	0.321	0.390	0.16
2009	123	BOC	9.04	0.08	-0.76	0.02	0.008	41.37	7.71				
2009	131	OM09-16	7.39	0.07	-0.44	0.02	0.008	14.37	2.70	0.26	0.327	0.396	0.00
2009	139	OM09-75	11.85	0.07	-0.32	0.02	0.007	21.56	4.77	0.35	0.419	0.450	0.89
2009	147	OM07-61a-mgs	13.02	0.06	-0.16	0.02	0.008	44.00	7.82	0.24	0.575	0.643	0.29
2009	156	OM07-07-mgs	9.38	0.07	-0.18	0.02	0.007	38.69	7.32	0.65	0.583	0.652	0.65
2011	443	eBOC	25.16	0.02	-0.57	0.02	0.008	76.02	9.80				
2011	465	eBOC	30.04	0.02	-0.56	0.01	0.004	86.87	11.11				
2011	474	TV01	11.30	0.01	-0.14	0.03	0.010	12.36	1.61	0.12	0.602	0.683	0.77
2011	483	OM08-206D	6.71	0.01	-0.25	0.01	0.004	27.90	3.73	0.15	0.519	0.600	0.88
2011	492	Carrara - offline 1	17.09	0.02	-0.36	0.02	0.008	26.90	3.71	0.15	0.317	0.398	1.00
2011	501	OM08-200	-14.13	0.01	-0.26	0.03	0.009	3.69	0.20	0.19	0.678	0.759	0.48
2011	510	OM10-11	3.73	0.01	-0.27	0.03	0.011	13.64	1.75	0.11	0.523	0.604	0.74
2011	519	TV01 offline1	10.85	0.02	-0.13	0.02	0.009	11.48	1.66	0.21	0.612	0.693	0.93
2011	528	BOC	-3.41	0.02	-0.82	0.03	0.012	10.03	1.16				
2011	546	Carrara - offline2	17.28	0.02	-0.31	0.02	0.006	27.23	3.68	0.23	0.369	0.450	0.92
2011	555	Carrara	17.72	0.02	-0.34	0.04	0.015	28.06	3.80	0.20	0.327	0.408	0.93
2011	564	ht-5	-31.02	0.01	-0.55	0.03	0.009	-21.09	-2.78	0.13	0.505	0.586	0.69
2011	574	OM10-38B	3.33	0.02	-0.26	0.06	0.023	17.35	1.81	0.19	0.538	0.619	0.33
2011	583	OM07-34C	-23.23	0.01	-0.34	0.03	0.009	-5.13	-1.61	0.12	0.662	0.743	-0.20
2011	593	OM10-34B	5.65	0.01	-0.26	0.03	0.009	25.04	2.81	0.11	0.517	0.598	0.33
2011	602	eBOC	27.14	0.01	-0.58	0.03	0.011	80.01	9.51				
2011	622	playa	7.70	0.03	-0.12	0.04	0.012	-0.23	-0.61	0.10	0.656	0.737	0.17

Year	spec #	Sample ID	Type	Mineral	Rxn	Acid T, C	δ13C (PDB)	stdev	δ18O (SMOW)	stdev
2011	632	OM10-15	listvenite	Dolomite	online	90	-0.306	0.004	33.485	0.005
2011	650	eBOC	HG	HG		HG	-10.695	0.003	63.097	0.006
2011	659	mgs-250R	mgs cal - exp	Magnesite	offline	90	-19.437	0.002	7.529	0.003
2011	671	mgs-150R	mgs cal - exp	Magnesite	offline	90	-21.012	0.002	10.636	0.005
2011	680	OM10-26 R2	listvenite	Magnesite	offline	90	0.078	0.003	34.214	0.002
2011	691	TV01 - offline 3	std	Calcite	offline	90	2.589	0.004	30.104	0.004
2011	703	AT03-44-7 x3	mgs cal -listvenite	Magnesite	offline	90	-3.912	0.003	29.342	0.005
2011	712	BOC	HG	HG		HG	-10.212	0.003	29.092	0.003
2011	721	playa R	mgs cal - playa	Magnesite	offline	90	4.236	0.003	25.099	0.004
2011	730	Carrara - offline3	std	Calcite	offline	90	2.427	0.002	36.754	0.005
2011	739	16I2 x3 "R"	mgs cal - amphibolite faci	Magnesite	offline	90	-6.682	0.003	18.675	0.004
2011	748	OM09-19 mgs	listvenite	Magnesite	offline	90	0.245	0.003	33.631	0.005
2011	758	eBOC	HG	HG		HG	-10.307	0.002	60.412	0.005
2011	767	Carrara	std	Calcite	online	90	2.340	0.003	37.288	0.004
2011	776	OM08-206D R	vein	Calcite	online	90	-8.986	0.002	37.285	0.004
2011	789	OM10-03 RR	listvenite	Magnesite	offline	90	-2.331	0.003	31.742	0.004
2011	798	mgs 150 R	mgs cal - exp	Magnesite	offline	90	-20.590	0.002	10.945	0.004
2011	807	mgs 250 R	mgs cal - exp	Magnesite	offline	90	-19.111	0.003	7.300	0.004
2011	817	OM10-26 R2 R	listvenite	Magnesite	offline	90	0.101	0.004	34.077	0.010
2011	826	OM09-19 dol R	listvenite	Dolomite	online	90	0.715	0.248	34.216	0.053
2011	835	TV01	std	Calcite	online	90	2.544	0.002	30.506	0.003
2011	844	OM10-34B R	vein	Calcite	online	90	-8.926	0.004	36.302	0.005
2011	862	OM09-19 mgs R	listvenite	Magnesite	offline	90	0.071	0.002	34.091	0.004
2011	871	AT03-44-7 x3 R	mgs cal -listvenite	Magnesite	offline	90	-3.684	0.003	28.952	0.006
2011	880	ht-5 R	mgs cal - exp	Magnesite	offline	90	-25.177	0.002	14.933	0.005
2011	889	OM10-03 R3	listvenite	Magnesite	offline	90	-2.509	0.005	32.237	0.009
2011	899	BOC	HG	HG		HG	-10.250	0.004	29.222	0.004
2011	908	OM10-11 R	listvenite (crust)	Dolomite	online	90	-5.611	0.002	30.988	0.004
2011	917	OM10-15 R	listvenite	Dolomite	online	90	-0.285	0.002	33.377	0.003
2011	926	eBOC	HG	HG		HG	-10.744	0.003	60.247	0.008
2012	1	eBOC	HG			HG	-10.790	0.008	58.068	0.016
2012	10	#1 Carrara	std	Calcite	offline	90	2.380	0.008	36.745	0.013
2012	435	OM11-43	ms	Calcite	online	90	-2.496	0.003	29.219	0.006
2012	463	Carrara	std	Calcite	online	90	2.268	0.007	36.916	0.016
2012	472	TV01	std	Calcite	online	90	2.514	0.010	30.074	0.015
2012	481	OM11-45	ms	Calcite	online	90	-0.166	0.010	30.080	0.014
2012	490	OM11-47	ms	Dolomite	online	90	-4.534	0.005	30.390	0.011

Year	spec #	Sample ID	δ47	stdev	Δ47	stdev	st err	δ48	Δ48	stdev	Δ47 HG corr.	Δ47 acid corr.	Δ48 excess
2011	632	OM10-15	11.32	0.02	-0.35	0.04	0.013	18.51	1.84	0.18	0.371	0.452	0.20
2011	650	eBOC	30.21	0.02	-0.59	0.02	0.008	86.54	10.15				
2011	659	mgs-250R	-33.14	0.02	-0.78	0.04	0.013	-39.78	-6.17	0.20	0.270	0.351	-0.30
2011	671	mgs-150R	-31.53	0.02	-0.71	0.04	0.012	-32.94	-5.23	0.14	0.331	0.412	-0.23
2011	680	OM10-26 R2	12.45	0.02	-0.32	0.02	0.005	20.49	2.37	0.10	0.397	0.478	0.48
2011	691	TV01 - offline 3	10.95	0.01	-0.16	0.02	0.009	11.07	1.04	0.19	0.582	0.663	0.36
2011	703	AT03-44-7 x3	3.61	0.02	-0.43	0.03	0.012	8.61	0.11	0.17	0.344	0.425	-0.25
2011	712	BOC	-3.12	0.02	-0.80	0.01	0.004	7.77	-0.21				
2011	721	playa R	7.58	0.02	-0.12	0.03	0.010	-0.81	-1.05	0.21	0.649	0.730	-0.20
2011	730	Carrara - offline3	17.26	0.02	-0.34	0.03	0.010	25.62	2.47	0.18	0.333	0.414	-0.08
2011	739	16l2 x3 "R"	-9.82	0.02	-0.61	0.01	0.005	-15.44	-3.19	0.20	0.268	0.349	-0.45
2011	748	OM09-19 mgs	12.08	0.01	-0.28	0.02	0.007	18.45	1.49	0.12	0.443	0.524	-0.14
2011	758	eBOC	27.99	0.01	-0.55	0.03	0.012	79.40	8.60				
2011	767	Carrara	17.67	0.01	-0.39	0.02	0.008	26.38	2.18	0.18	0.282	0.363	-0.47
2011	776	OM08-206D R	6.76	0.02	-0.22	0.04	0.012	26.55	2.40	0.17	0.554	0.635	-0.27
2011	789	OM10-03 RR	7.69	0.02	-0.28	0.02	0.006	14.06	0.84	0.15	0.479	0.560	-0.22
2011	798	mgs 150 R	-30.85	0.02	-0.73	0.03	0.009	-32.65	-5.54	0.20	0.305	0.386	-0.58
2011	807	mgs 250 R	-33.03	0.02	-0.75	0.02	0.009	-40.74	-6.72	0.21	0.297	0.378	-0.72
2011	817	OM10-26 R2 R	12.35	0.03	-0.31	0.02	0.006	19.44	1.60	0.28	0.413	0.494	-0.15
2011	826	OM09-19 dol R	13.18	0.02	-0.32	0.03	0.010	19.79	1.64	0.11	0.394	0.475	-0.16
2011	835	TV01	11.28	0.01	-0.19	0.03	0.009	11.27	0.46	0.20	0.544	0.625	-0.24
2011	844	OM10-34B R	5.81	0.02	-0.25	0.02	0.006	24.52	2.33	0.25	0.523	0.604	-0.08
2011	862	OM09-19 mgs R	12.35	0.02	-0.30	0.03	0.011	19.76	1.89	0.08	0.424	0.505	0.09
2011	871	AT03-44-7 x3 R	3.44	0.02	-0.44	0.04	0.013	8.11	0.37	0.19	0.344	0.425	0.08
2011	880	ht-5 R	-31.26	0.01	-0.65	0.03	0.009	-23.70	-4.18	0.11	0.393	0.474	-0.38
2011	889	OM10-03 R3	7.99	0.03	-0.30	0.03	0.010	15.55	1.35	0.12	0.458	0.539	0.10
2011	899	BOC	-3.02	0.02	-0.79	0.03	0.010	8.45	0.21				
2011	908	OM10-11 R	3.76	0.01	-0.27	0.02	0.007	12.62	0.89	0.19	0.522	0.603	0.02
2011	917	OM10-15 R	11.25	0.02	-0.34	0.03	0.010	18.19	1.73	0.08	0.389	0.470	0.14
2011	926	eBOC	27.37	0.02	-0.56	0.02	0.008	79.79	9.27				
2012	1	eBOC	25.14	0.07	-0.51	0.06	0.021	91.78	24.73				
2012	10	#1 Carrara	17.20	0.06	-0.27	0.06	0.020	32.62	9.38	0.82	0.320	0.401	0.12
2012	435	OM11-43	4.80	0.06	-0.41	0.06	0.019	11.85	3.60	0.86	0.312	0.393	-0.03
2012	463	Carrara	17.21	0.05	-0.33	0.03	0.011	33.20	9.61	0.87	0.254	0.335	0.20
2012	472	TV01	10.82	0.06	-0.11	0.04	0.015	15.07	5.10	1.25	0.582	0.663	0.59
2012	481	OM11-45	7.96	0.06	-0.38	0.04	0.015	15.14	5.16	1.07	0.315	0.396	0.64
2012	490	OM11-47	4.11	0.06	-0.29	0.05	0.018	15.50	4.94	0.95	0.457	0.538	0.32

Year	spec #	Sample ID	Type	Mineral	Rxn	Acid T, C	δ13C (PDB)	stdev	δ18O (SMOW)	stdev
2012	499	OM11-48	ms	Calcite	online	90	-0.571	0.007	28.987	0.017
2012	508	OM10-14	listvenite	Dolomite	online	90	-1.773	0.007	28.470	0.021
2012	524	#4 TV01	std	Calcite	offline	90	2.694	0.006	29.398	0.012
2012	533	#5 ht-5	mgs cal - exp	Magnesite	offline	90	-25.623	0.006	15.233	0.008
2012	542	#19 mgs-250	mgs cal - exp	Magnesite	offline	90	-19.140	0.005	7.051	0.009
2012	551	Carrara	std	Calcite	online	90	2.222	0.006	36.950	0.012
2012	560	OM10-20	listvenite	Dolomite	online	90	-0.427	0.007	35.095	0.013
2012	572	BOC	HG			HG	-10.953	0.006	28.496	0.013
2012	590	#8 OM09-18	listvenite	Magnesite	offline	90	-1.583	0.010	31.567	0.021
2012	599	#9 OM10-02	listvenite	Magnesite	offline	90	-0.675	0.007	31.898	0.014
2012	608	#3 Carrara	std	Calcite	offline	90	2.441	0.006	35.736	0.015
2012	627	TV01	std	Calcite	online	90	2.401	0.006	30.101	0.017
2012	636	OM09-20-c	listvenite	Dolomite	online	90	0.954	0.007	33.950	0.015
2012	645	#10 OM10-04	listvenite	Magnesite	offline	90	-3.386	0.004	32.168	0.010
2012	654	BOC	HG			HG	-9.987	0.002	29.813	0.005
2012	663	#22 TV01	std	Calcite	offline	90	2.714	0.008	29.322	0.016
2012	672	eBOC	HG			HG	-10.493	0.009	57.579	0.020
2012	681	Carrara	std	Calcite	online	90	2.188	0.001	36.798	0.006
2012	690	OM10-14 R	listvenite	Dolomite	online	90	-1.724	0.003	28.407	0.006
2012	699	OM10-20 R	listvenite	Dolomite	online	90	-0.498	0.007	35.085	0.015
2012	708	OM09-20-c	listvenite	Dolomite	online	90	1.020	0.002	33.855	0.006
2012	717	TV01	std	Calcite	online	90	2.458	0.006	29.948	0.014
2012	726	#20-ht-5	mgs cal - exp	Magnesite	offline	90	-25.568	0.006	15.225	0.012
2012	735	#14 OM09-16 R	listvenite	Magnesite	offline	90	-1.076	0.006	30.139	0.008
2012	744	BOC	HG			HG	-10.651	0.008	29.392	0.016
2012	753	#16 OM09-16	listvenite	Magnesite	offline	90	-0.863	0.005	31.786	0.019
2012	763	#12 Carrara	std	Calcite	offline	90	2.858	0.008	36.035	0.018
2012	772	#24 mgs-250	mgs cal - exp	Magnesite	offline	90	-19.388	0.003	7.195	0.004
2012	781	OM09-20-f	listvenite	Dolomite	online	90	0.757	0.006	34.671	0.016
2012	790	#31 OM10-04 R	listvenite	Magnesite	offline	90	-3.856	0.005	32.678	0.016
2012	799	#15 OM09-18 R	listvenite	Magnesite	offline	90	-1.641	0.007	31.406	0.016
2012	808	#29 OM10-03-s	listvenite	Magnesite	offline	90	-2.627	0.008	31.988	0.021
2012	817	eBOC	HG			HG	-10.327	0.006	58.715	0.030
2012	826	#34 OM11-17	listvenite	Magnesite	offline	90	-5.218	0.005	37.335	0.012
2012	835	#23 TV01	std	Calcite	offline	90	2.546	0.006	29.648	0.010
2012	844	#28 OM11-94	listvenite	Magnesite	offline	90	1.743	0.007	21.802	0.013
2012	862	#33 OM09-15	listvenite	Magnesite	offline	90	-2.632	0.008	31.682	0.014

Year	spec #	Sample ID	δ47	stdev	Δ47	stdev	st err	δ48	Δ48	stdev	Δ47 HG corr.	Δ47 acid corr.	Δ48 excess
2012	499	OM11-48	6.44	0.07	-0.41	0.05	0.019	11.92	4.11	1.29	0.295	0.376	0.46
2012	508	OM10-14	4.85	0.06	-0.32	0.04	0.014	9.07	2.29	0.58	0.420	0.501	-0.59
2012	524	#4 TV01	10.37	0.05	-0.07	0.05	0.017	11.55	2.92	0.85	0.639	0.720	-0.63
2012	533	#5 ht-5	-31.62	0.04	-0.81	0.04	0.012	-27.47	-8.57	0.39	0.326	0.407	-1.55
2012	542	#19 mgs-250	-33.51	0.06	-0.90	0.05	0.018	-50.42	-16.22	0.68	0.252	0.333	-2.98
2012	551	Carrara	17.18	0.06	-0.34	0.05	0.019	33.20	9.54	0.82	0.242	0.323	0.13
2012	560	OM10-20	12.85	0.07	-0.24	0.05	0.019	28.50	8.56	1.23	0.411	0.492	0.42
2012	572	BOC	-4.49	0.05	-0.79	0.04	0.015	9.37	2.58				
2012	590	#8 OM09-18	8.13	0.05	-0.31	0.05	0.016	19.16	6.25	1.23	0.390	0.471	0.64
2012	599	#9 OM10-02	9.40	0.05	-0.25	0.05	0.016	19.37	5.80	0.84	0.438	0.519	0.14
2012	608	#3 Carrara	16.29	0.05	-0.23	0.04	0.015	30.23	9.00	1.08	0.376	0.457	0.39
2012	627	TV01	10.73	0.05	-0.12	0.04	0.014	14.25	4.23	1.13	0.573	0.654	-0.05
2012	636	OM09-20-c	13.02	0.04	-0.27	0.04	0.014	23.63	6.01	0.71	0.373	0.454	-0.81
2012	645	#10 OM10-04	7.10	0.03	-0.19	0.03	0.010	18.89	4.82	0.72	0.542	0.623	-0.72
2012	654	BOC	-2.24	0.04	-0.78	0.03	0.012	13.22	3.83				
2012	663	#22 TV01	10.34	0.06	-0.04	0.05	0.017	11.69	3.21	1.02	0.669	0.750	-0.38
2012	672	eBOC	25.00	0.04	-0.47	0.03	0.011	90.52	24.49				
2012	681	Carrara	16.99	0.07	-0.34	0.06	0.022	32.12	8.79	0.64	0.242	0.323	-0.34
2012	690	OM10-14 R	4.85	0.03	-0.31	0.03	0.011	8.68	2.03	0.59	0.432	0.513	-0.74
2012	699	OM10-20 R	12.78	0.06	-0.22	0.04	0.013	28.74	8.82	0.88	0.427	0.508	0.61
2012	708	OM09-20-c	13.00	0.06	-0.26	0.06	0.020	23.19	5.75	0.30	0.385	0.466	-0.95
2012	717	TV01	10.61	0.08	-0.14	0.07	0.024	13.73	4.02	0.79	0.553	0.634	-0.12
2012	726	#20-ht-5	-31.57	0.05	-0.80	0.04	0.014	-26.67	-7.74	0.96	0.338	0.419	-0.94
2012	735	#14 OM09-16 R	7.17	0.05	-0.34	0.06	0.020	14.47	4.40	0.61	0.366	0.447	0.05
2012	744	BOC	-3.29	0.05	-0.77	0.04	0.012	12.67	4.11				
2012	753	#16 OM09-16	9.08	0.05	-0.28	0.04	0.014	19.22	5.88	0.66	0.409	0.490	0.25
2012	763	#12 Carrara	16.92	0.06	-0.30	0.04	0.014	29.53	7.73	1.06	0.283	0.364	-0.69
2012	772	#24 mgs-250	-33.58	0.04	-0.87	0.04	0.014	-49.86	-15.92	0.50	0.283	0.364	-2.83
2012	781	OM09-20-f	13.54	0.05	-0.27	0.03	0.012	25.85	6.78	0.66	0.363	0.444	-0.64
2012	790	#31 OM10-04 R	7.14	0.04	-0.20	0.03	0.010	20.74	5.65	0.68	0.531	0.612	-0.39
2012	799	#15 OM09-18 R	7.90	0.04	-0.32	0.04	0.014	17.33	4.76	0.89	0.379	0.460	-0.36
2012	808	#29 OM10-03-s	7.59	0.04	-0.25	0.04	0.013	19.58	5.85	0.86	0.462	0.543	0.12
2012	817	eBOC	26.31	0.03	-0.45	0.03	0.009	94.14	25.68				
2012	826	#34 OM11-17	10.52	0.07	-0.12	0.06	0.021	35.04	10.62	0.67	0.578	0.659	0.71
2012	835	#23 TV01	10.46	0.04	-0.08	0.03	0.010	12.93	3.81	1.17	0.620	0.701	-0.12
2012	844	#28 OM11-94	1.40	0.03	-0.52	0.03	0.011	-8.68	-2.47	0.78	0.239	0.320	-0.54
2012	862	#33 OM09-15	7.23	0.04	-0.30	0.03	0.011	18.62	5.50	0.73	0.409	0.490	0.03

Year	spec #	Sample ID	Type	Mineral	Rxn	Acid T, C	δ13C (PDB)	stdev	δ18O (SMOW)	stdev
2012	871	#35 OE150	mgs cal - exp	Magnesite	offline	90	-24.267	0.005	12.739	0.014
2012	880	#36 OE200	mgs cal - exp	Magnesite	offline	90	-17.643	0.005	7.572	0.007
2012	889	BOC	HG			HG	-9.800	0.007	30.562	0.014
2012	898	#38 OM11-17 R	listvenite	Magnesite	offline	90	-4.972	0.003	37.020	0.010
2012	908	#37 OM11-94 R	listvenite	Magnesite	offline	90	1.858	0.008	21.654	0.017
2012	917	Carrara	std	Calcite	online	90	2.196	0.004	36.783	0.015
2012	926	OM09-20-f R	listvenite	Dolomite	online	90	0.713	0.004	34.613	0.017
2012	935	#39 OM09-11 R	listvenite	Magnesite	offline	90	-0.114	0.009	32.133	0.014
2012	944	#44 OM09-15 R	listvenite	Magnesite	offline	90	-2.155	0.003	30.962	0.009
2012	953	eBOC	HG			HG	-10.581	0.004	58.566	0.012
2012	962	#32B OM09-11	listvenite	Magnesite	offline	90	1.349	0.006	33.725	0.012
2012	971	#41 OE150 R	mgs cal - exp	Magnesite	offline	90	-24.173	0.005	12.554	0.012
2012	980	#42 playa_new	mgs cal - natural	Magnesite	offline	90	2.393	0.005	25.322	0.010
2012	998	M223	mgs cal - exp	Magnesite	online	90	-14.846	0.007	30.868	0.012
2012	1007	#45 OE200 R	mgs cal - exp	Magnesite	offline	90	-17.929	0.006	7.942	0.010
2012	1016	#43 playa_new R	mgs cal - natural	Magnesite	offline	90	2.449	0.006	25.123	0.013

Year	spec #	Sample ID	δ47	stdev	Δ47	stdev	st err	δ48	Δ48	stdev	Δ47 HG corr.	Δ47 acid corr.	Δ48 excess
2012	871	#35 OE150	-32.78	0.05	-0.84	0.04	0.014	-33.78	-10.16	0.67	0.309	0.390	-1.43
2012	880	#36 OE200	-31.53	0.05	-0.84	0.05	0.016	-47.81	-14.54	0.52	0.286	0.367	-2.01
2012	889	BOC	-1.30	0.06	-0.76	0.04	0.016	16.13	5.25				
2012	898	#38 OM11-17 R	10.41	0.05	-0.15	0.05	0.016	34.38	10.59	0.75	0.538	0.619	0.85
2012	908	#37 OM11-94 R	1.34	0.09	-0.54	0.07	0.024	-11.40	-4.93	1.33	0.216	0.297	-2.26
2012	917	Carrara	17.02	0.04	-0.31	0.05	0.016	32.40	9.09	0.45	0.273	0.354	-0.11
2012	926	OM09-20-f R	13.43	0.03	-0.28	0.02	0.008	24.74	5.81	0.36	0.352	0.433	-1.31
2012	935	#39 OM09-11 R	10.17	0.06	-0.26	0.04	0.016	20.36	6.33	0.69	0.414	0.495	0.39
2012	944	#44 OM09-15 R	7.01	0.04	-0.27	0.04	0.014	16.17	4.47	0.40	0.444	0.525	-0.33
2012	953	eBOC	25.91	0.02	-0.44	0.02	0.006	93.78	25.64				
2012	962	#32B OM09-11	13.17	0.07	-0.28	0.06	0.022	23.84	6.64	0.91	0.364	0.445	-0.24
2012	971	#41 OE150 R	-32.83	0.07	-0.79	0.06	0.021	-34.64	-10.68	0.67	0.364	0.445	-1.72
2012	980	#42 playa_new	5.98	0.04	-0.08	0.03	0.009	0.51	-0.12	0.55	0.674	0.755	-0.68
2012	998	M223	-5.57	0.04	-0.42	0.04	0.014	17.57	6.10	0.88	0.432	0.513	0.92
2012	1007	#45 OE200 R	-31.44	0.05	-0.84	0.05	0.019	-46.36	-13.77	0.75	0.287	0.368	-1.63
2012	1016	#43 playa_new R	5.86	0.05	-0.06	0.04	0.014	0.01	-0.24	0.62	0.697	0.778	-0.66